

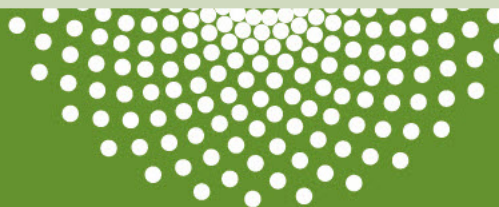


Volume 56 - 2024

ISSN 2452-3216

Procedia

Structural Integrity



Structural Integrity and Reliability of Advanced Materials obtained trough Additive Manufacturing (SIRAMM23)

**Guest editors:
Roberto Brighenti
Liviu Marsavina
Aleksandar Sedmak
Filippo Berto
Lubos Nahlik**

Available online at
www.sciencedirect.com

ScienceDirect



Structural Integrity and Reliability of Advanced Materials obtained through Additive Manufacturing (SIRAMM23)

Editorial

Liviu Marsavina^{a*}, Roberto Brighenti^b, Aleksandar Sedmak^c,

Lubos Nahlik^d, Filippo Berto^e

^a University Politehnica Timisoara, Department of Mechanics and Strength of Materials, Blvd. M. Viteazu 1, Timisoara 300222, Romania

^b University of Florence, Department Civil and Environmental Engineering, Via di S. Marta 3, 50139 Florence, Italy

^c University of Belgrade, Faculty of Mechanical Engineering, Kraljice Marije 16, 11120 Belgrade, Serbia

^d Czech Academy of Sciences, Institute of Physics of Materials, Žitkova 22, 616 62 Brno, Czech Republic

^e University Sapienza Roma, Department of Chemical Engineering Materials Environmen, Via Eudossiana 18, 00184 Roma, Italy

The International Conference on Structural Integrity and Reliability of Advanced Materials obtained through Additive Manufacturing (SIRAMM23), was organized at the University Politehnica Timisoara, Romania, in cooperation with *TC13: EDUCATION AND TRAINING* and *TC15: STRUCTURAL INTEGRITY OF ADDITIVE MANUFACTURED COMPONENTS* of the European Structural Integrity Society (ESIS), March 8th-11th 2023 as the final conference of the European Twinning project on ***Structural Integrity and Reliability of Advanced Materials obtained through additive Manufacturing***, H2020-WIDESPREAD-2018-03 under the grant agreement No. 857124.

The general aim of the conference was to promote international collaboration and share current knowledge on the structural integrity and design of additively manufactured (AM) materials and the related disciplines. Of particular interest is understanding the role of AM printing conditions and parameters on the final reliability and safety of the obtained materials, a crucial aspect especially for AM materials used in load bearing applications.

© 2023 The Authors. Published by Elsevier B.V.

This is an open access article under the CC BY-NC-ND license (<https://creativecommons.org/licenses/by-nc-nd/4.0>)

Peer-review under responsibility of the SIRAMM23 organizers

* Corresponding author. Tel.: +40726397635.

E-mail address: liviu.marsavina@upt.ro

The conference was attended (in hybrid mode) by 177 participants from 23 different countries. We had 8 keynote lectures provided by highly recognized researchers in the field of Additive Manufacturing and Structural Integrity: prof. Geert de Schutter (Gent University, Belgium), prof. Noy Cohen (Technion, Haifa, Israel), prof. Sara Bagherifard (Polytechnic of Milano, Italy), prof. Giulia Scalet (University of Pavia, Italy), prof. Katia Bertoldi (Harvard University, Boston, USA), prof. Vadim Silberschmidt (Loughborough University, UK), prof. Luca Susmel (University of Sheffield, UK), prof. Jan Torgersen (TU Munchen, Germany) and a presentation provided by dr. Dana Dragomir from NCP Romania related to the financing opportunities offered by Widening and ERA calls in Horizon Europe.

At the SIRAMM23 conference were presented 67 papers in specific sessions dedicated to the following topics:

- Characterization of AM polymer-based materials,
- Characterization of AM metallic materials
- Modeling and simulation of AM materials and processes
- Characterization of AM metallic materials and composites
- AM in bio-related applications, health, and medicine
- Applications and advancements in AM materials and structures

Among the presented papers, 26 were selected for publication in a Special Issue of the Structural Integrity Procedia Journal dedicated to the SIRAMM23 conference.

As Guest Editors of this Conference Proceedings, we wish to thank all authors for their valuable contributions in the advancement of knowledge in the field of AM from an engineering perspective.

The guest Editors of **Procedia Structural Integrity** SIRAMM23 Conference Proceedings:

Liviu Marsavina, University Politehnica Timisoara, Romania
Roberto Brighenti, University of Florence, Italy
Aleksander Sedmak, University of Belgrade, Serbia
Lubos Nahlik, IPM Brno, Czech Republic
Filippo Berto, University Sapienza Roma, Italy



Structural Integrity and Reliability of Advanced Materials obtained through Additive Manufacturing (SIRAMM23)

Additive manufacturing for orthopedic implants: morphological and material characterization of SLM thin Ti6Al4V samples

Francesca Danielli^a, Francesca Berti^a, Adelaide Nespoli^b, Valentina Lo Presti^a, Edoardo Sironi^a, Davide Ninarello^{a,b}, Tomaso Villa^a, Lorenza Petrini^{c*}

^aLaBS-Laboratory of Biological Structure Mechanics – Department of Chemistry, Materials and Chemical Engineering "Giulio Natta", Politecnico di Milano, Piazza Leonardo da Vinci 32, Milano 20133, Italy

^bNational Research Council, Institute of Condensed Matter Chemistry and Technologies for Energy, Via Previati 1/E, Lecco 23900, Italy

^cDepartment of Civil and Environmental Engineering", Politecnico di Milano, Piazza Leonardo da Vinci 32, Milano 20133, Italy

Abstract

In the last decades, the orthopedic industry has increasingly adopted Additive Manufacturing (AM) technologies, such as selective laser melting, to produce custom devices. Given their novelty with respect to discrete-size implants, New 2017/745 Medical Device Regulation introduced the need for safety and quality demonstration of such unique devices, a non-trivial task since no defined criteria state how to test them. In this scenario, numerical analyses can be a robust tool for the intended purposes as long as the reliability of the numerical models is verified in terms of geometry reconstruction and material assignment. The latter need has to deal with the peculiarities of AM in the production of lattice structures, distinctive features of this new generation of devices conceived to mimic bone morphology. Indeed, the struts of such structures have diameters of hundreds of microns, which approach AM accuracy limit. If, on the one hand, the issues related to AM production are well-known, on the other hand, it is not yet fully understood how to deal with them if thin struts are manufactured. Given the still questionable research area and starting from the few literature findings, this study aims to provide an exhaustive morphological and material characterization of Ti6Al4V thin struts produced by selective laser melting, supporting experimental activities with numerical analyses. The importance of investigating together their morphology and mechanical behavior will be highlighted: morphological analyses will constitute the first step to assess the quality of the manufactured samples and to correctly interpret the experimental results of static and fatigue tests. In this light, the differences with respect to the mechanical properties of both machined samples and thick AM samples will be outlined. The outcomes of this research will be fundamental for the development of reliable FE models of lattice-based devices.

© 2023 The Authors. Published by Elsevier B.V.

This is an open access article under the CC BY-NC-ND license (<https://creativecommons.org/licenses/by-nc-nd/4.0>)

Peer-review under responsibility of the SIRAMM23 organizers

* Corresponding author. Tel.: +39 02 2399 4307; fax: +39 02 2399 4286.

E-mail address: lorenza.petrini@polimi.it

Keywords: Fatigue tests; Finite element analysis; Morphological analyses; Selective laser melting; Static tests; Thin struts; Ti6Al4V ELI

1. Introduction

Nowadays, the advantages of AM applied to the orthopedic industry are well recognized. The production of a new generation of custom devices is an outstanding example: lattice structures are conceived both to design lightweight implants, reducing the risk of stress-shielding, and to mimic the trabecular bone, enhancing the implant osteointegration within the surrounding bone tissue. These devices are commonly produced using Selective Laser Melting (SLM) as a manufacturing process and Ti6Al4V alloys as metallic powder. Contrary to traditional manufacturing processes, such as machining, AM allows the production of custom devices fitting complex anatomies. Unlike discrete-size devices, there are no defined methodologies to assess the safety and quality of custom implants, given their unique shapes and dimensions. Finite Element (FE) modeling of implantable devices is a viable option as long as the FE model reliability is verified in terms of geometry reconstruction and assignment of material properties. As for the latter, the characterization of the struts involved in the implants' lattice structures is still an open issue and is hindered by their dimensions approaching the accuracy limit of AM technologies. For instance, the minimum printable strut diameter is about 200 μm (Yang et al., 2021). Therefore, uncertainties in their manufacturing arise, affecting the final product morphology and mechanical properties. Internal and surface defects (e.g., porosity and surface roughness) may be present, and their effect on the material properties is particularly relevant, given the struts dimensions in the order of hundreds of microns. Recent works (Hossain et al., 2021; Murchio et al., 2021a) highlighted a significant discrepancy between thin struts and samples with dimensions in the order of centimeters or bigger. The reasons behind these findings are many and not yet fully understood, making this field still open to further investigations. Given the introduced evidence, morphology and mechanical behavior (both static and fatigue) of AM thin struts should be investigated together. As for the fatigue behavior, if its characterization has been exhaustively conducted on traditional manufacturing Ti6Al4V, the same cannot be stated for AM samples. The emerging literature findings assess that the fatigue life of AM materials is lower with respect to the conventional ones due to, for instance, internal and surface defects introduced by AM (Edwards & Ramulu, 2014; Greitemeier et al., 2016; Nakatani et al., 2019; Pegues et al., 2018; Persenot et al., 2019). However, to the best of the authors' knowledge, the majority of literature works deal with samples having dimensions in the order of centimeters (e.g., diameter > 3 mm), but very few works (Murchio et al., 2021a) have investigated smaller samples (e.g. diameter < 1 mm), object of the current work. Thus, this study aims to provide an exhaustive morphological and material characterization of Ti6Al4V thin struts produced via SLM, coupling experimental and computational approaches. This is a preliminary but fundamental step in the design process of orthopedic patient-specific implants. In particular, the reference application of this work is an implant for the talus substitution, as discussed by the authors research group (Danielli, Berti, et al., 2023).

2. Materials and Methods

2.1. Design and fabrication of the material specimens

Cylindrical specimens were designed as shown in Fig. 1a. A diameter of 0.6 mm was chosen based on both the minimum printable dimension (0.2 mm) (Yang et al., 2021), and an average thickness of bone trabeculae (0.2 mm-1 mm) (Ho et al., 2013; Turunen et al., 2020). The samples were manufactured at the CNR-ICMATE laboratories (Lecco, Italy) using SLM technology. A Renishaw AM400 printer was exploited, and a biomedical grade Ti6Al4V ELI powder was used as raw material (spherical particles 15-45 μm). The manufacture was conducted with a spot diameter of 70 μm at the focal point, a layer thickness (t) of 30 μm , a hatching distance (H) of 65 μm , and a laser power (P) of 200 W (pulsed-wave emission mode). Due to the laser pulsed functioning, the scanning speed (v) was calculated as the ratio between the laser point distance (75 μm) and the laser exposure time (50 μs). Therefore, the laser energy density ($E = P/(t \cdot h \cdot v)$) was calculated equal to 68 J/mm^3 . The meander strategy was chosen as a scanning

strategy, and the process was carried out in a reduced build volume ($78 \cdot 78 \cdot 55 \text{ mm}^3$) on a Ti-based platform. Before processing, vacuum was applied (oxygen level lower than 500 ppm), the build chamber was filled with Argon, and no preheating was applied to the build platform. Three batches of material specimens were manufactured, different for the print direction with respect to the build platform (45° , 60° , 90° , Fig. 1b). The angles were chosen based on the struts inclinations of the trabecular cells commonly used for orthopedic devices (Olivares, 2022) and compatibly with the AM limits (Yang et al., 2021). As for the latter constraint, the minimum printable inclination angle is 20° . The specimens were placed 3 mm above the build plate using supports, to ensure a better heat transfer and keep them in place during the process. Additionally, a second set of supports was introduced for the 45° -samples (Fig. 1c). After the manufacture, the specimens were subjected to heat treatment (850°C for 2 hours followed by slow cooling in furnace) to avoid, or at least minimize, the presence of residual stresses. Finally, no surface treatment was performed on the specimens (Fig. 1d).

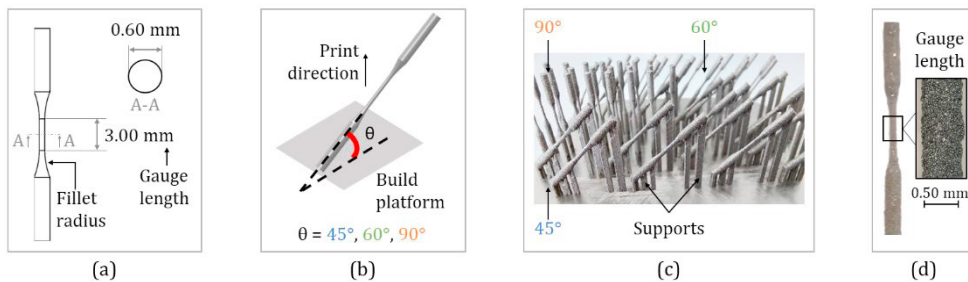


Fig. 1. (a) CAD drawing of the cylindrical samples; (b) Schematic representation of the printing process to highlight the inclination (θ) of the samples with respect to the build platform and the print direction; (c) Batches of the printed samples manufactured in Ti6Al4V through the SLM technology; (d) Example of a printed sample, with a detail about the gauge length.

2.2. Morphological characterization

The inaccuracies of AM fabrication have been outlined by the literature, and they are more evident in the presence of thin samples. In addition to the dimensions, the final product is affected by its orientation with respect to the build platform (Murchio et al., 2021a). Therefore, a deep morphological characterization is needed before performing mechanical tests. Thus, the quality of the printed samples was investigated by performing the following analyses.

- Density measurements were carried out to assess the presence of internal pores. Using the Gibertini E 50 S/2 analytical scale, the density of three samples (ρ_{SAMPLE} , g/cm^3) for each batch was calculated exploiting the Archimedes principle and compared with the one of a machined Ti6Al4V ELI alloy (ρ_{REF} , g/cm^3). From the calculated density, the porosity of the AM sample can be calculated as $1 - (\rho_{\text{SAMPLE}} / \rho_{\text{REF}})$ [%].
- Lateral images were acquired with the *WILD Stereomicroscope* (7x magnification) to measure the Gauge Length (GL) of three samples for each batch and processed with the imaging software *NISELEMENTS AR Analysis* (Nikon Instruments, Melville, NY, USA);
- Profilometry analyses were performed using the *Olympus Lext Laser Microscope* (10x magnification): 2D height-maps were acquired to evaluate the surface roughness of the samples (the average roughness, R_a , was calculated). One sample for each batch was analyzed, and for each sample, the roughness of four sides was evaluated by rotating the sample of about 90° along its axis. Five measurements for each side were performed;
- Three samples for each batch were used to evaluate the cross-section; three sections for each specimen were made along the GL, 500 μm equally spaced along the specimen axis. The cut portions were embedded in epoxy resin and polished. Images were acquired using the *WILD Stereomicroscope* (32x magnification) and processed using the imaging software *ImageJ* (Wayne Rasband, National Institutes of Health, USA).

2.3. Material characterization: static tests

Static uniaxial tensile tests were performed under displacement control on three specimens for each batch until failure, using an *Instron E3000 ElectroPulse* machine. The final aim of the tests is to calculate the elastic modulus and the yield stress of the material based on the deformation of the only GL (the portion of the sample at constant cross-section, Fig. 1a), avoiding the contribution of the fillet radius (the portion of the sample at variable cross-section, Fig. 1a). Due to the small size of the specimens, extensometers could not be applied to measure the deformation of the GL. Therefore, experimental tests were coupled with numerical analyses: FE models of the samples were developed considering the actual dimensions of the samples (2.2), and the experimental tests were numerically replicated using *Abaqus/CAE 2020* (Dassault Systèmes, Vélizy-Villacoublay, France). Based on the experimental force-displacement curves and the results of the simulations, the elastic modulus (E) was calculated as follows:

$$\alpha = \frac{u_{GL}^{FEA}}{u_{TOT}^{FEA}} \quad \varepsilon_{GL} = \frac{u_{TOT}^{EXP}}{L_0} \cdot \alpha \quad \sigma^{EXP} = \frac{F^{EXP}}{A_0} \quad E = \frac{\sigma^{EXP}}{\varepsilon_{GL}} \quad (1)$$

where: α is the percentage of displacement of the only GL, u_{TOT}^{FEA} is the displacement applied in the FE simulation, u_{GL}^{FEA} is the resulting numerical displacement of the GL, ε_{GL} is the deformation of the GL, u_{TOT}^{EXP} is the experimental applied displacement (the distance between the grips of the testing machine), L_0 is the GL initial length (the value was assigned based on the measures described in 2.2), σ^{EXP} is the experimental stress on the GL, F^{EXP} is the force recorded during the experimental test, A_0 is the GL initial cross-section area (the value was assigned based on the measures described in 2.2). The elastic modulus of the samples was calculated as the slope of the line interpolating the elastic portion of the stress-strain curve, and the yield stress was determined based on the 0.2% offset method: the interpolation line is offset by 0.002 of the strain and its intersection with the stress-strain curve is the yield stress.

As compared to the previous work published by the authors (Danielli, Berti, et al., 2023), the calculation of the static material properties has been performed considering not only the effective cross-section area of the manufactured samples but also their effective gauge length, which was previously assumed to be equal to the nominal dimension.

2.4. Material characterization: preliminary fatigue tests

Tensile-tensile fatigue tests were performed under force control using an *Instron E3000 ElectroPulse* machine with the following parameters: load ratio $0 < F_{MIN}/F_{MAX} < 1$, mean force $F_{MEAN}=40$ N, frequency $f=60$ Hz. Since this was a preliminary investigation, fatigue tests were conducted to construct only the finite life fatigue curve of Wöhler diagram, following the ISO 12107 standard (ISO 12107:2012, 2012). Moreover, only the 60°- and the 90°-samples were tested. Three load levels were considered for both batches, and five specimens were tested for each level.

Tests were conducted until either specimen failure or runout ($5 \cdot 10^5$). The runout was chosen based on the final aim of the project within which the current study falls: the design of a talus prosthesis. Considering the walking activity as a cyclic load and assuming an average of 10^6 steps/year, the time needed to reach an almost fully-osteointegration of the implant is about half a year ($5 \cdot 10^5$ cycles), during which it is reasonable to assume that the prosthesis is the only element bearing the body weight, without the support of the surrounding bone tissue. This condition represents the worst-case scenario to be investigated during the fatigue analysis. Finally, Scanning Electron Microscope (SEM) images of the fracture surfaces were acquired using a *Zeiss LEO 1430 SEM* (300x magnification). Two surfaces were analyzed for each batch, one for the highest load level and one for the lowest.

3. Results

3.1. Morphological characterization

The density measures showed no significant differences among the three batches (4.33 ± 0.01 g/cm³), leading to an overall samples porosity with respect to a fully solid machined Ti6Al4V ELI (density of 4.42 g/cm³) of 2%. The measurements of the GL outlined a significant mismatch with respect to the length in the nominal model (3 mm, Fig. 2a). Namely, the relative difference was found to increase with the increase of the sample inclination: about 40% for

the 45°-sample and about 60% for the 90°-sample. The results of the profilometry analysis were analyzed by distinguishing between the samples downskin and upskin surfaces. The former is the surface directed towards the build platform, while the latter is the 180°-opposite one. This distinction can be made for inclined samples, while no differentiation can be made for the vertical samples since no lateral surface faces the build platform. The relative difference between the downskin surface roughness and the upskin one was higher for the 45°-samples (the upskin is about 55% less rough than the downskin) with respect to the 60°-ones (the upskin is about 40% less rough as compared to the downskin). For both the 45°- and 60°-samples, the surface roughness of the other two surfaces fell within the range defined by the downskin and upskin surfaces. As for the 90°-samples, no significant differences were found for the four lateral views, and the average surface roughness fell within the range defined by the downskin and upskin surfaces of the 45°- and 60°-samples (Fig. 2c). Finally, the actual cross-section areas underrated the nominal one (0.283 mm²). The lower relative difference was found for the 45°-samples (3%), while the higher one for the 90°-samples (20%). Besides the values, the shapes were observed. The mismatch from the nominal circular shape was found to increase as the sample inclination decreased. The 90°-samples exhibit an almost circular shape, the 45°-samples a drop-like shape with the tip in the downskin surface, while the 60°-samples an intermediate shape (Fig. 2b).

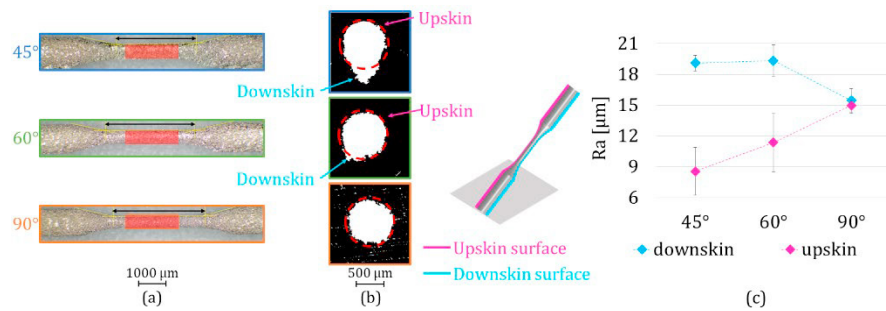


Fig. 2. (a) Actual gauge lengths (black lines) compared with the nominal ones (red rectangles); (b) Actual cross-sections (white images) compared with the nominal ones (dashed red lines). The downskin and upskin surfaces are highlighted for the 45°- and 60°-samples; (c) Average surface roughness (R_a) measured on the upskin and downskin surfaces (45°- and 60°-samples), and on two arbitrary surfaces (90°-samples).

3.2. Material characterization: static tests

The results of the static tensile tests are reported in Fig. 3: for each batch, the average stress-strain curves out (Fig. 3c) of three tests were derived from the experimental force-displacement (Fig. 3b) curves and were used for the calculation of the elastic modulus and the yield stress (Table 1). The tests performed on the same sample batches are repeatable, as shown by the slight standard deviation (vertical black lines) of both the force-displacement and stress-strain curves. Moreover, no significant differences exist among the stress-strain curves for the different batches.

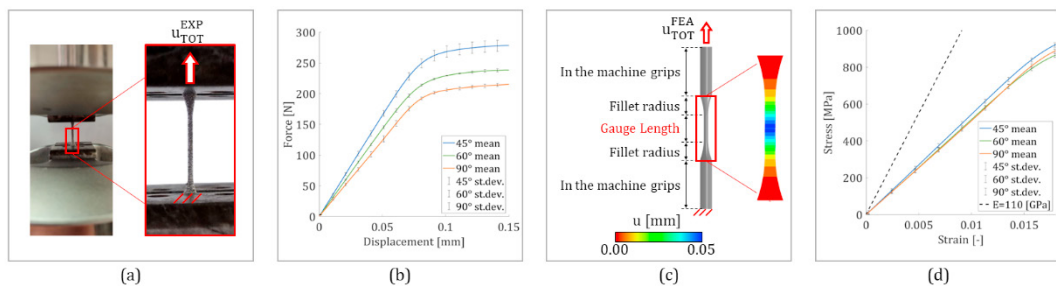


Fig. 3. (a) Static tensile test; (b) Force-displacement curves recorded during the experiments: average values and standard deviations; (c) Simulation of the experiment with a detail of the displacement field in the gauge length and in the filler radii; (d) Stress-strain curves for the gauge length: average values and standard deviations. The dashed black line is representative of the mechanical behavior of both thick AM Ti6Al4V samples (Material Data Sheet - SLM Ti6Al4V ELI, n.d.) and machined Ti6Al4V samples (Material Data Sheet - Ti6Al4V ELI, n.d.).

The quantitative results of the analyses reported in paragraphs 3.1 and 3.2 are summarized in Table 1.

Table 1. Main results obtained from the morphological analyses and from the static tests for each samples batch.

Quantity	45°-sample	60°-sample	90°-sample
Density [g/cm ³]	4.327±0.043	4.320±0.030	4.3240±0.031
Gauge length [mm]	4.307±0.219	4.781±0.129	4.908±0.184
Ra side 1 [μm] – Downskin	19.106±0.750	19.333±1.530	15.462±1.126
Ra side 2 [μm]	18.028±1.625	19.886±2.961	15.157±0.766
Ra side 3 [μm]	14.118±2.991	19.082±3.116	14.362±0.748
Ra 4 side [μm] – Upskin	8.557±2.329	11.352±2.810	14.993±0.765
Cross-section area [mm ²]	0.276±0.011	0.253±0.005	0.221±0.011
Elastic modulus [GPa]	72.9±2.3	70.2±2.2	69.1±2.8
Yield Stress [MPa]	968.1±28.9	898.7±3.5	936.5±17.9

3.3. Material characterization: preliminary fatigue tests

The results of the fatigue tests and the reconstructed finite life fatigue curve of Wöhler diagram are shown in Figure 4a. SEM images of the fracture surfaces are shown in Figure 4b. The tear zone (yellow dashed line) is located near the upskin surface for the 45°- and 60°-samples, while no preferential areas are identified for the 90°-samples. The red arrows indicate potential crack nucleation sites.

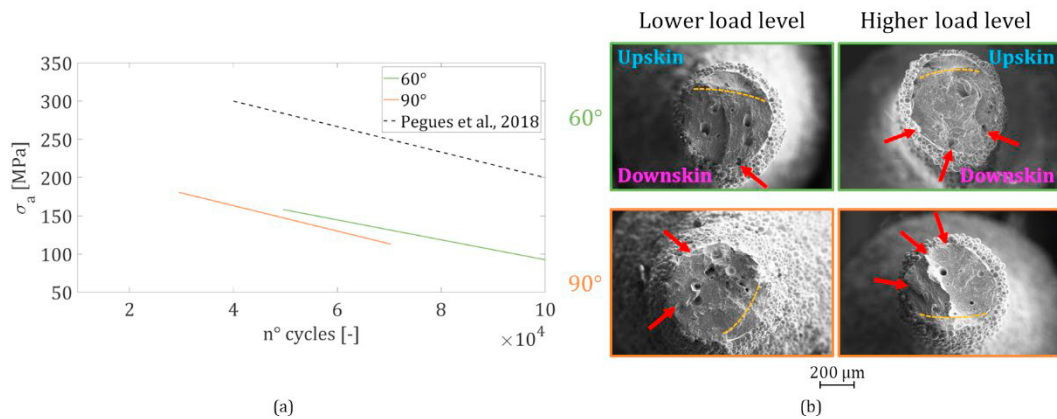


Fig. 4. (a) Finite life fatigue curve of Wöhler diagram (alternating stress as function of the number of cycles) for 60°- and 90° samples. The dashed black line is representative of the mechanical behavior of thick AM Ti6Al4V samples (Pegues et al., 2018); (b) Fracture surfaces at the lower and higher load levels. The dashed yellow lines delineate the tear surfaces, while the red arrows indicate potential crack nucleation sites.

4. Discussion and conclusions

AM has been recognized with great potential in the personalized medicine industry. It is currently a well-established technology for the production of lattice-based orthopedic prostheses. The trabeculae involved in the lattice structures are characterized by small dimensions that approach the accuracy limit of AM technologies, hindering a high-fidelity manufacture of the structures with respect to the conceived model. Many works in the literature clearly state how the final AM product may present several defects, such as internal porosity and surface roughness. Based on this evidence, they aim to study the peculiarities of AM production by investigating geometry and mechanical behavior of the final product. However, very few works focused on the characterization of thin struts, and a comprehensive overview of

their characterization is still lacking. Thus, the current study aimed to raise the main issues in the characterization of thin struts by proposing a pipeline fitting in the context of designing an orthopedic prosthesis.

Starting from the morphological analyses, the samples density was measured to estimate the presence of internal pores. The results are in line with works that studied the influence of AM process parameters on the occurrence of defects in Ti6Al4V samples, finding an internal porosity of 1%-5% (Gong et al., 2015; Khorasani et al., 2019).

As for the dimensional measurements, the discrepancy between the nominal and the actual length of the GL (more than 40%) is an issue not raised by the literature, despite its relevance in the material characterization. For instance, the authors of the current work did not question the effective GL in their recent work (Danielli, Berti, et al., 2023), leading to a misinterpretation of the experimental tests and a wrong calculation of the elastic modulus of the previously tested samples, which still belonged to the same batches of the specimens of the current study. On the contrary, the mismatch of the cross-section areas (5%-20% lower with respect to the nominal one) and the surface roughness (in the range of 14-17 μm) are evidence pointed out by the works in the literature (Murchio et al., 2021a), whose results are in line with the ones obtained in the current work. Moreover, these quantities are affected by the sample inclination with respect to the build platform. For instance, as the inclination decreases (e.g., 45°), the cross-section areas assume a "drop-like" shape, where the elongated portion is directed towards the build platform. Moreover, the difference in the surface roughness between the downskin and the upskin surfaces is more evident for lower-angle samples. Both evidences can be attributable to not optimal heat dissipation and gravitational force during the printing process.

The results obtained from the morphological analyses highlight how the nominal model produced of an AM sample cannot be considered for further investigations, such as FE analyses, especially if its dimensions approach AM accuracy limit. Moreover, the morphology of the final product is strictly affected by the sample inclination with respect to the build platform.

Looking at the static tests, the primary outcome was a decrease of about 40% for the elastic modulus with respect to both thick AM Ti6Al4V samples (*Material Data Sheet - SLM Ti6Al4V ELI*, n.d.) and machined Ti6Al4V samples (*Material Data Sheet - Ti6Al4V ELI*, n.d.): an average value of 70 GPa was obtained in contrast with 110 GPa-120 GPa. The observed reduction is consistent with the literature findings (Danielli, Ciriello, et al., 2023; Dzugan et al., 2018; Murchio et al., 2021a). For instance, both (Dzugan et al., 2018) and (Murchio et al., 2021b) characterized SLM Ti6Al4V samples (0.6 mm diameter), obtaining an elastic modulus of about 60 GPa and 80 GPa, respectively. Thus, it is possible to state that the results reported in the current work fall within the literature range. Finally, the authors did not find significant differences among the 45°, 60°- and 90°-samples, suggesting that the print direction does not affect the elastic modulus. The wrong assumption on the dimension of the gauge length in (Danielli, Berti, et al., 2023) led to an apparent dependence of the elastic modulus from the inclination, which the current results have disclaimed.

The results of the fatigue tests outlined a reduction of 20%-40% for the limit stress within $5 \cdot 10^4$ - 10^5 cycles with respect to the results of (Nakatani et al., 2019; Pegues et al., 2018), in which SLM Ti6Al4V samples (3 mm-6 mm diameter) were tested. Moreover, the results of the current work agree with the study of (Murchio et al., 2021a), where the limit stress within $5 \cdot 10^4$ - 10^5 cycles was about 100-180 MPa for 90°-samples (L-PBF Ti6Al4V samples with 0.6 mm diameter). Looking at the SEM images of the fracture surfaces, it is reasonable to assume that for the 60°-samples, the tear zone is close to the upskin surface, while the source for the crack propagation is close to the downskin surface. On the contrary, the 90°-samples do not show specific areas as possible sources of crack nucleation. However, how the surface roughness affects the fatigue life of AM thin samples needs to be deeply investigated.

To conclude, AM uncertainties in producing thin struts and their effect on the morphology and mechanical properties are currently unclear. The preliminary finding of the current study aimed to highlight the main related issues by proposing a methodology for their evaluation. Looking at the biomedical context, a deep insight into geometrical and material properties of these structures is crucial in view of correctly describing the mechanics of AM lattice-based prostheses. Moreover, this is an unavoidable task if FE models are used as predictive tools of the implants behavior.

References

- Danielli, F., Berti, F., Nespoli, A., Colombo, M., Villa, T., La Barbera, L., & Petrini, L. (2023). Towards the development of a custom talus prosthesis produced by SLM: design rules and verification. *Journal of Mechanical Science and Technology*. <https://doi.org/10.1007/s12206-022-2109-z>
- Danielli, F., Ciriello, L., La Barbera, L., Rodriguez Matas, J. F., & Pennati, G. (2023). On the need of a scale-

- dependent material characterization to describe the mechanical behavior of 3D printed Ti6Al4V custom prostheses using finite element models. *Journal of the Mechanical Behavior of Biomedical Materials*, 140. <https://doi.org/10.1016/j.jmbbm.2023.105707>
- Dzuga, J., Seifi, M., Prochazka, R., Rund, M., Podany, P., Konopik, P., & Lewandowski, J. J. (2018). Effects of thickness and orientation on the small scale fracture behaviour of additively manufactured Ti-6Al-4V. *Materials Characterization*, 143(April), 94–109. <https://doi.org/10.1016/j.matchar.2018.04.003>
- Edwards, P., & Ramulu, M. (2014). Fatigue performance evaluation of selective laser melted Ti-6Al-4V. *Materials Science and Engineering A*, 598, 327–337. <https://doi.org/10.1016/j.msea.2014.01.041>
- Gong, H., Rafi, K., Gu, H., Janaki Ram, G. D., Starr, T., & Stucker, B. (2015). Influence of defects on mechanical properties of Ti-6Al-4V components produced by selective laser melting and electron beam melting. *Materials and Design*, 86, 545–554. <https://doi.org/10.1016/j.matdes.2015.07.147>
- Greitemeier, D., Dalle Donne, C., Syassen, F., Eufinger, J., & Melz, T. (2016). Effect of surface roughness on fatigue performance of additive manufactured Ti-6Al-4V. *Materials Science and Technology (United Kingdom)*, 32(7), 629–634. <https://doi.org/10.1179/1743284715Y.0000000053>
- Ho, J. T., Wu, J., Huang, H. L., Chen, M. Y. C., Fuh, L. J., & Hsu, J. T. (2013). Trabecular bone structural parameters evaluated using dental cone-beam computed tomography: Cellular synthetic bones. *BioMedical Engineering Online*, 12(1). <https://doi.org/10.1186/1475-925X-12-115>
- Hossain, U., Ghouse, S., Nai, K., & Jeffers, J. R. T. (2021). Mechanical and morphological properties of additively manufactured SS316L and Ti6Al4V micro-struts as a function of build angle. *Additive Manufacturing*, 46, 102050. <https://doi.org/10.1016/j.addma.2021.102050>
- ISO 12107:2012. (2012).
- Khorasani, A. M., Gibson, I., Awan, U. S., & Ghaderi, A. (2019). The effect of SLM process parameters on density, hardness, tensile strength and surface quality of Ti-6Al-4V. *Additive Manufacturing*, 25, 176–186. <https://doi.org/10.1016/j.addma.2018.09.002>
- Material Data Sheet - SLM Ti6Al4V ELI. (n.d.). https://www.slm-solutions.com/fileadmin/Content/Powder/MDS/MDS_Ti-Alloy_Ti6Al4V__ELI_0719_EN.pdf
- Material Data Sheet - Ti6Al4V ELI. (n.d.). <https://www.upmet.com/sites/default/files/datasheets/ti-6al-4v-eli>
- Murchio, S., Dallago, M., Zanini, F., Carmignato, S., Zappini, G., Berto, F., Maniglio, D., & Benedetti, M. (2021a). Additively manufactured Ti-6Al-4V thin struts via laser powder bed fusion: Effect of building orientation on geometrical accuracy and mechanical properties. *Journal of the Mechanical Behavior of Biomedical Materials*, 119(March), 104495. <https://doi.org/10.1016/j.jmbbm.2021.104495>
- Murchio, S., Dallago, M., Zanini, F., Carmignato, S., Zappini, G., Berto, F., Maniglio, D., & Benedetti, M. (2021b). Additively manufactured Ti-6Al-4V thin struts via laser powder bed fusion: Effect of building orientation on geometrical accuracy and mechanical properties. *Journal of the Mechanical Behavior of Biomedical Materials*, 119. <https://doi.org/10.1016/j.jmbbm.2021.104495>
- Nakatani, M., Masuo, H., Tanaka, Y., & Murakami, Y. (2019). Effect of Surface Roughness on Fatigue Strength of Ti-6Al-4V Alloy Manufactured by Additive Manufacturing. *Procedia Structural Integrity*, 19, 294–301. <https://doi.org/10.1016/j.prostr.2019.12.032>
- Olivares, M. A. (2022). *Design, modeling and characterization of lattice structures for orthopedic implant applications*.
- Pegues, J., Roach, M., Scott Williamson, R., & Shamsaei, N. (2018). Surface roughness effects on the fatigue strength of additively manufactured Ti-6Al-4V. *International Journal of Fatigue*, 116, 543–552. <https://doi.org/10.1016/j.ijfatigue.2018.07.013>
- Persenot, T., Burr, A., Martin, G., Buffiere, J. Y., Dendievel, R., & Maire, E. (2019). Effect of build orientation on the fatigue properties of as-built Electron Beam Melted Ti-6Al-4V alloy. *International Journal of Fatigue*, 118, 65–76. <https://doi.org/10.1016/j.ijfatigue.2018.08.006>
- Turunen, M. J., Le Cann, S., Tudisco, E., Lovric, G., Patera, A., Hall, S. A., & Isaksson, H. (2020). Sub-trabecular strain evolution in human trabecular bone. *Scientific Reports*, 10(1). <https://doi.org/10.1038/s41598-020-69850-x>
- Yang, X., Ma, W., Gu, W., Zhang, Z., Wang, B., Wang, Y., & Liu, S. (2021). Multi-scale microstructure high-strength titanium alloy lattice structure manufactured: Via selective laser melting. *RSC Advances*, 11(37), 22734–22743. <https://doi.org/10.1039/d1ra02355a>



International Conference on Structural Integrity and Reliability of Advanced Materials
obtained through Additive Manufacturing (SIRAMM23)

A technique for estimation of cyclic stress-strain curves using an optical strain measurement and its application to additively manufactured AlSi10Mg

Radim Halama^{a*}, Zbyněk Paška, Ajay Vignesh Natarajan^a, Jiří Hajnýs^b

^aDepartment of applied mechanics, FME, VŠB-Technical University of Ostrava, 17.listopadu 2172/15, Ostrava, Czech Republic

^bDepartment of Machining, Assembly and Engineering Metrology, FME, VŠB-Technical University of Ostrava, 17.listopadu 2172/15, Ostrava, Czech Republic

Abstract

The article describes a new accelerated technique for estimation of cyclic stress-strain curves of cyclically stable materials based on a full-field measurement of strain during low-cycle testing on a large amplitude of loading. Any optical method suitable for capturing the strain contours on the curved part of the specimen during cyclic loading is applicable in the approach developed. In this study, the digital image correlation method is used to measure the deformation on the curved part of the specimen. The technique is presented on chosen results of low-cycle fatigue tests performed on AlSi10Mg printed with selective laser melting technology. Proportional loading cases were performed in tension-compression and pure torsion. The case of non-proportional loading was realized in the form of 90 degree out-of-phase tests. The stress-strain behavior is evaluated using a standard procedure and an accelerated technique with a good correlation for the three loading cases.

© 2023 The Authors. Published by Elsevier B.V.

This is an open access article under the CC BY-NC-ND license (<https://creativecommons.org/licenses/by-nc-nd/4.0>)

Peer-review under responsibility of the SIRAMM23 organizers

Keywords: Accelerated testing; cyclic stress-strain curve; low-cycle fatigue; non-proportional loading; DIC; full-field measurement.

* Corresponding author. Tel.: +420-59-732-1288; fax: +420-59-691-6490.

E-mail address: radim.halama@vsb.cz

1. Introduction

Selective laser melting (SLM) is an additive manufacturing (AM) technology used to print functional parts from metallic powders using a high-energy laser beam. AM brings freedom in complex geometry and enhanced possibilities of design as bionic structures. Light structures can be produced by application of a lattice structure; see the review of Obadimu and Kourousis (2021). The fatigue properties of AM materials must be considered when evaluating materials for industrial use. Compared to the static tensile properties of the parts produced by AM, fatigue performance is less reported in recent research studies, especially in the low cycle domain; see Brandl et al. (2012) and Raja et al. (2022).

The AlSi10Mg alloy is one of the most popular materials used in light structures produced by SLM and commonly used in the aviation and automotive industries due to its high heat resistance and fatigue properties, see Glodež (2020). Influence of scanning strategies on the stress-strain behavior and its prediction by a crystal plasticity model is studied for instance in Chakrabarty and Chakraborty et al. (2023). Crack propagation properties of additively manufactured AlSi10Mg were explored in Chakrabarty and Sahu et al. (2023). The possibility of heat treatment to reduce the residual stresses, that are natural in the AM process, keeping the cellular microstructure is studied by Měsíček et al. (2022).

In computational fatigue analysis, the cyclic stress-strain curve is an important material characteristic, which is usually constructed by an approximation of stress peaks from low-cycle fatigue tests performed for particular (plastic) strain amplitudes. This paper shows a new possibility of estimating the cyclic stress-strain curve using full-field data from optical measurement of strain on the curved part of the specimen. The first example of such an application was described by Halama et al. (2017). The procedure described in this study was applied to two proportional loading cases performed under tension-compression and pure torsion, and to the 90 degree out-of-phase axial-torsion test.

Nomenclature

b_{0-3}	parameters of the four-parametric approximation function
G	shear modulus
R	radius of the curved part of the specimen
Y	coordinate of the DIC point in the Y-direction
Z	coordinate of the DIC point in the Z-direction
Y_0, Z_0	optimized parameters
$\varepsilon_1, \varepsilon_2, \varepsilon_3$	principal strains
ε_{eqv}	equivalent strain calculated according to von Mises
$\varepsilon_{ap}, \gamma_{ap}$	axial plastic strain amplitude, shear plastic strain amplitude
σ_a, τ_a	axial stress amplitude, shear stress amplitude

2. Accelerated technique description

The selective laser melting is an expensive manufacturing technology. The limitation in build space dimensions requires to carefully plan number of parts and their orientation. In anisotropy investigation, one needs a lot of specimens for monotonic and fatigue testing. Therefore, it is necessary to obtain maximum information from each test, and the accelerated technique of cyclic stress-strain curve estimation is very beneficial.

2.1. Main idea

In a standard uniaxial strain-controlled fatigue test, the amplitude of the axial strain and the mean strain in the gauge part are kept constant throughout the fatigue test. However, in the rounded part, the cross-sectional area of the specimen is larger and that is why there are lower stress and strain magnitudes. The history of strain can be measured optically using the digital image correlation (DIC) method. A simplified illustration of this procedure is shown in Figure 1(a). Figure 1(b) shows two hysteresis loops for two selected points on the curved part of the sample. For evaluation, the axial stress is considered as a nominal stress in the given cross section and the axial strain corresponds directly to the Y-component of the Cauchy strain tensor. The upper hysteresis loop is an example of an extreme condition: the signal noise is significant; the stresses are low, and the plastic deformation does not develop significantly. The bottom hysteresis loop shows the result of material behaviour close to the gauge part of the specimen (the strain amplitude measured by an extensometer in the gauge part is 1.5%). By capturing the strain history and evaluating the peaks together with the stress, one can obtain a cyclic stress-strain curve of the material. However, some corrections are necessary to achieve good correlation with the conventional cyclic stress-strain curve, as will be shown within this paper.

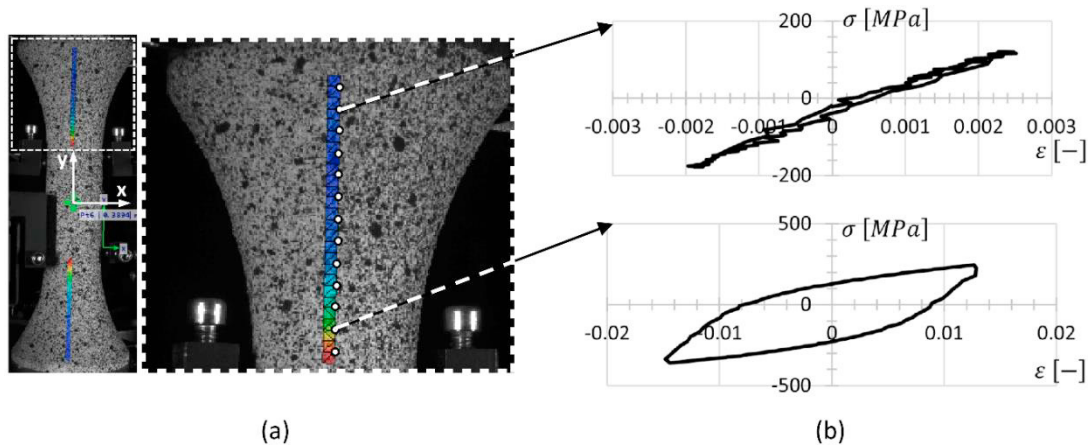


Fig. 1. Example of DIC measurement evaluation: (a) representation of several selected points on the curved part of the specimen; (b) each point corresponds to one hysteresis loop.

2.2. Procedure

In this work, Alpha software of the X-Sight company was used. However, any DIC software can be applied that enables capturing the history of the strain components. The basic procedure consists of the following steps:

- 1) Determine the amplitude of the load in the middle of the life of the specimen.
- 2) Create a network of points in the DIC software at which the components of the strain tensor will be calculated (marked as DIC points in the following text).
- 3) Determine the positions of the DIC points on the curved part of the specimen in the given coordinate system and find the border between the gauge (cylindrical) part and the curved part (Fig. 2).

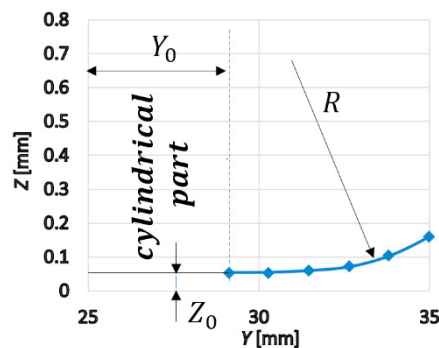


Fig. 2. Identification of the border between the gauge part and the curved part during the DIC measurement evaluation.

The circle equation can be used to find the border between the gauge part and the curved part of the specimen:

$$Z_{approximation} = Z_0 + \sqrt{R^2 - (Y - Y_0)^2} \quad (1)$$

where R is the radius of curvature ($R = 40$ mm in our study), and Z_0, Y_0 are the optimized values (least squares). The plane $Z - Y$ of the reference coordinate system should contain the specimen axis.

4) Based on knowledge of the parameters describing the curved part DIC points by equation (1), assign the cross-sectional characteristics to them. The stress amplitude is calculated as a nominal stress amplitude.

5) Find the mid-life cycle and calculate the amplitude of the response variable (strain). It is noticed that each DIC point has a different quantity of strain amplitude. It is advisable to take into account the occurrence of multi-axial strain by calculating the equivalent strain value for each evaluated point, e.g. according to the von Mises hypothesis:

$$\varepsilon_{eqv} = \frac{\sqrt{2}}{3} \sqrt{[(\varepsilon_1 - \varepsilon_2)^2 + (\varepsilon_3 - \varepsilon_1)^2 + (\varepsilon_2 - \varepsilon_3)^2]} \quad (2)$$

where $\varepsilon_1, \varepsilon_2, \varepsilon_3$ are principal strains. It is recommended to measure the strain field on both curved parts of the specimen and calculate the averaged strain amplitude.

3. Experiments

The AlSi10Mg is an aluminium alloy, which does not show a strain rate sensitivity. Based on the fact, two proportional loading cases and one nonproportional loading case were considered with a harmonic signal of strain. This helps to get more accurate evaluation of stress and strain amplitudes. In this contribution, the three fatigue tests will be described in detail, the rest of fatigue tests used in the conventional way of cyclic stress-strain curve determination will be described in a separate scientific paper.

3.1. Specimens manufacturing

The thin-walled tubular specimen was designed in accordance with the ASTM E2207 standard as shown in Figure 3. The outer diameter of the tubular specimen is 14 mm, while the inner diameter is 11.5 mm. The gauge part length was selected as 28 mm.

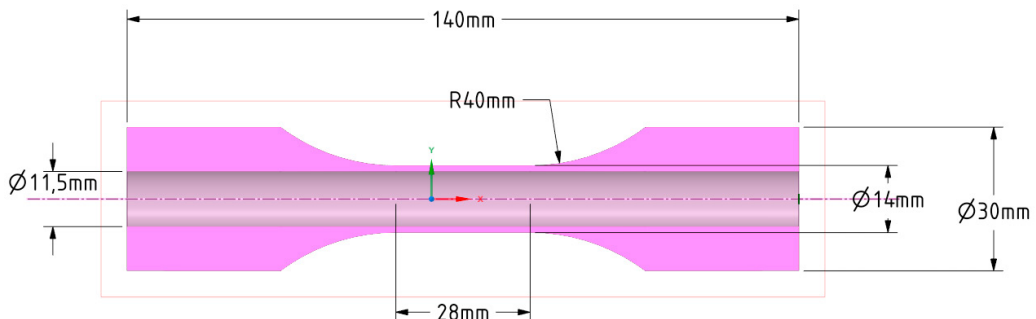


Fig. 3. Scheme of specimen geometry.

For fabricating specimens, the Renishaw 3D printer, namely AM400 type, was used. All the specimens were tested in as-built state. The most important printing parameters used during the AM process are reported in Table 1. The 90° orientation of the sample indicates its position in the printer chamber during the production process. The specimens were printed with 350 W laser power, a scanning speed of $1150 \text{ mm}\cdot\text{s}^{-1}$ and a layer thickness of $30 \mu\text{m}$. The 'Meander' scanning strategy was applied, which is the most used strategy for specimens with small cross-sections. During fabrication, the chamber was filled with argon with purity 5.0 to prevent oxidation. The building platform was preheated to 170°C to reduce residual stresses during the AM process.

Table 1. Printer setting parameters for the production of fatigue specimens.

Specimens orientation	3D printing strategy	Laser power (W)	Laser rate ($\text{mm}\cdot\text{s}^{-1}$)	Layer thickness (μm)	Preheating of building platform ($^\circ\text{C}$)
90°	"meander"	350	1150	30	170

3.2. Low-cycle fatigue testing

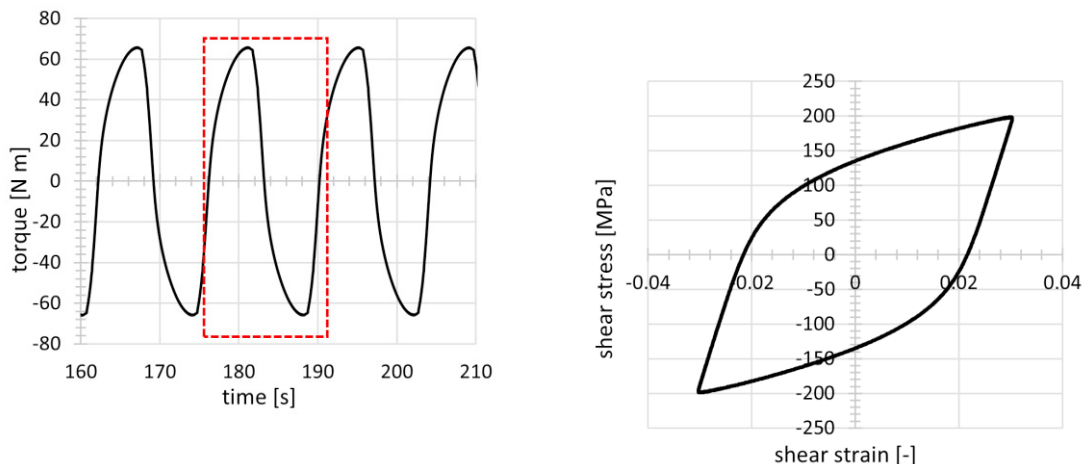
All the three loading cases were realized using the Epsilon Tech 3550 biaxial extensometer for controlling the axial/shear strain in the gauge part (25 mm gauge length). Time-periods in the tension-compression and pure torsion tests were 6 s and 14 s respectively. In the non-proportional loading case, the strain rate was 1 %/s. Equivalent strain amplitudes in the middle-life were: 1.5 % (push-pull), 1.75 % (torsion) and 1.25 % (nonproportional). Two cameras with a resolution of 2.3 Mpx and a frame rate of 20 fps were used in a 3-D measurement arrangement.

4. Results

This chapter presents the results obtained by the accelerated fatigue test evaluation methodology. The resulting cyclic stress-strain curves are compared with the data obtained by conventional approach (ASTM E2207).

4.1. Torsion case

In the pure torsion case, the symmetric shear strain cycle generated the waveform of the response quantity (torque). The time history of torque in the mid-life of the specimen is shown in Fig.4(a), whereas the corresponding



hysteresis loop is highlighted in Fig.4(b). The line segment in the first quadrant of the loop determines the shear modulus $G = 23651$ MPa.

(a) (b)

Fig. 4. (a) the torque waveform in response to the deformation load on the specimen; (b) the hysteresis loop corresponding to the 13th load cycle.

The result of the proposed technique applied to the torsional fatigue test is shown in Fig.5, where the amplitude of shear strain vs the amplitude of shear stress is presented. In the same graph, the linear part (elastic domain) is represented by the shear modulus. The results of the evaluation of the stress-strain data from the upper and the bottom parts of the specimen correlate very well with the conventional cyclic stress-strain curve (evaluated accordingly with the ASTM 2207 standard).

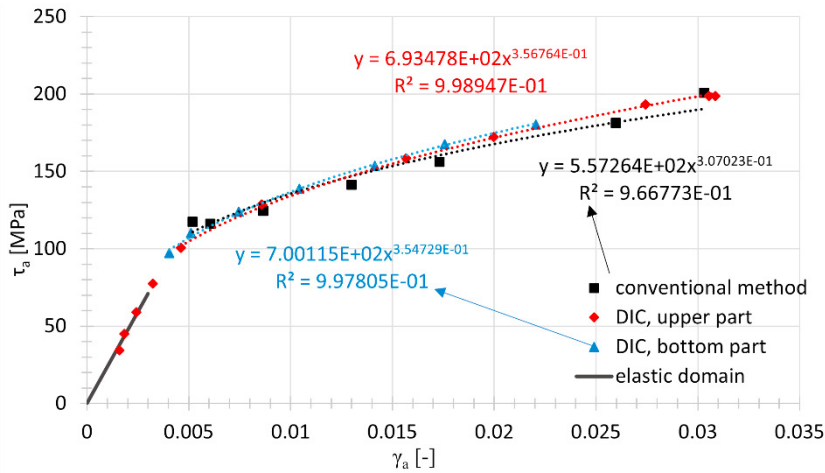
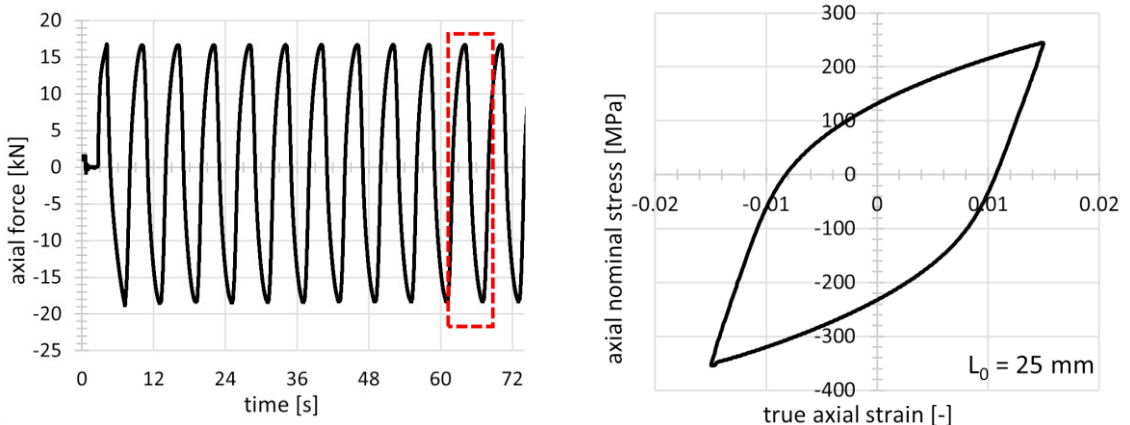


Fig. 5. Cyclic strain curve for the case of symmetric torsional loading obtained by DIC measurements on the curved part of the specimen.

The Fig.5 shows that the first few points with the lowest stress value lie in the elastic region of deformation. Consequently, a fairly good agreement with the results obtained by the conventional method on cylindrical specimens can be seen.

4.2. Tension-compression case

From the test machine recordings in the push-pull case, the force versus time dependence is available as shown in Fig.6(a). The 11th cycle, which corresponds to the half-life of the specimen, is highlighted in the same figure.



(a) (b)

Fig. 6. Results of tension-compression fatigue test: (a) the axial force time-history; (b) the hysteresis loop corresponding to the 11th load cycle.

Fig. 6(b) shows the shape of the hysteresis loop corresponding to the 11th load cycle, for which the axial strain was determined using the extensometer. From the stable hysteresis loop, the amplitude of the axial stress and the amplitude of the axial strain can be determined and thus a single point on the cyclic strain curve can be obtained, see Fig. 7.

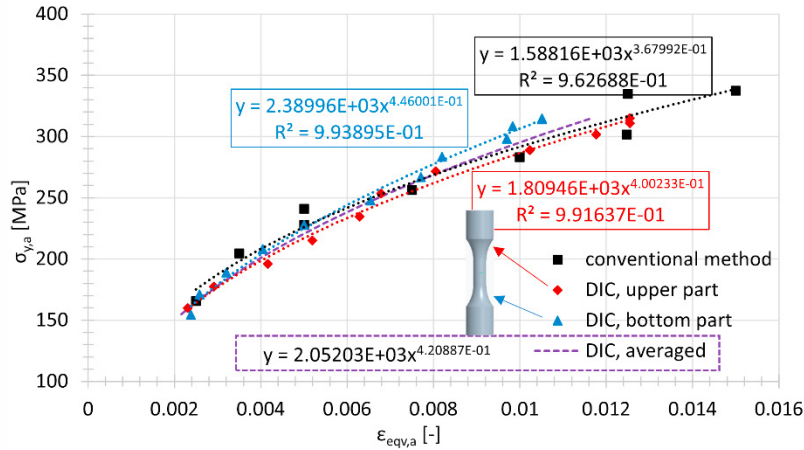


Fig. 7. Cyclic stress-strain curve of tension-compression case corrected for the effect of multi-axial strain.

It is worth noting that the curve for the upper and lower part of the specimen was obtained from a single fatigue test. Each point in the 'conventional method' corresponds to a fatigue test performed under a specific level of strain amplitude.

4.3. Nonproportional loading case

The waveforms of the loading quantities for the tension-compression/torsion loading are harmonic and are offset by 90° from each other. The test was set so that the amplitude of the equivalent strain was 1.25 % and the shape of the load path was circular. When the axial force reaches its maximum/zero value, the torque has a zero/minimum magnitude (phase shift 90°). This fact can be exploited, and the test can be independently evaluated at these specific time points, regardless of the existence of biaxial tension. Fig. 8(a) shows a comparison of the results obtained from the DIC (axial stress) with the results of the fatigue tests obtained conventionally. Again, the results for the upper and lower curved parts of the specimen are shown. The approximation in this case is made by using a non-linear function of Chaboche type. The approximation function has the following form

$$\sigma_a(\varepsilon_{ap}) = b_0 + b_1\varepsilon_{ap} + b_2(1 - e^{-b_3\varepsilon_{ap}}), \tag{3}$$

where b_i ($i = 0, 1, 2, 3$) are the unknown parameters optimised by a non-linear least squares method, σ_a is the stress amplitude and ε_{ap} is the axial plastic strain amplitude. The results obtained for the shear stress component are shown in Fig. 8(b). The approximation by a nonlinear function is denoted here as "DIC, upper/bottom part approx.". The "DIC, averaged" mark then shows the resulting cyclic stress-strain curve obtained by the proposed technique. The parameters obtained from the approximation function (3) considering the axial / shear stress and strain components are summarised in Table 2.

Table 2. Resulting parameters of the approximation of the cyclic stress-strain curve for the 90° out of phase test.

Component	b_0 [MPa]	b_1 [MPa]	b_2 [MPa]	b_3 [-]
axial	166.7	5929.9	100.8	436.6
shear	126.0	9914.3	105.5	1731.9

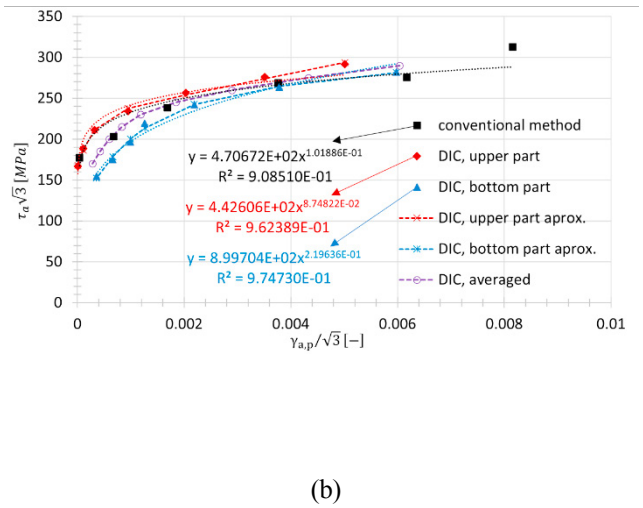
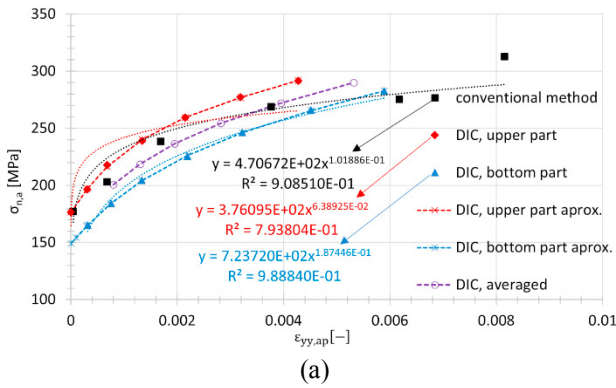


Fig. 8. Cyclic stress-strain curve reconstructed considering (a) the axial strain; (b) the shear strain.

5. Conclusions

The paper presents the accelerated fatigue testing procedure in terms of obtaining multiple points of the cyclic stress-strain curve from a single experiment using an optical method. The procedure was presented in three loading cases performed on an AlSi10Mg alloy prepared by selective laser melting technology. The best candidate for wide application of the accelerated technique in technical practice is the digital image correlation (DIC), which is the most popular optical method in mechanics and was successfully applied in this study. The resulting cyclic stress-strain curves correlate very well with the conventional ones. In the case of the nonproportional loading, the axial as well as shear component of stress/strain can be considered with comparable results. The technique is not limited just to the fatigue area; it can be beneficially applied to creep testing of various materials as described in Halama et al. (2022).

Acknowledgements

This research work was supported by the project financed from the Czech Science Foundation under the registration number 23-05338S.

References

- Brandl, E., Heckenberger, U., Holzinger, V., 2012. Additive manufactured AlSi10Mg samples using Selective Laser Melting (SLM): Microstructure, high cycle fatigue, and fracture behavior. *Materials & Design* 34, 159-169.
- Glodež, S., Klemenc, J., Zupanič, F., Vesenjak, M., 2020. High-cycle fatigue and fracture behaviours of SLM AlSi10Mg alloy. *Transactions of Nonferrous Metals Society of China (English Edition)* 30(10), 2577-2589.
- Halama, R., Gál, P., Paška, Z., Sedlák, J., 2017. A New Accelerated Technique for Validation of Cyclic Plasticity Models, 22nd Conference on Machine Modeling and Simulation, Sklené Teplice, Slovakia. *MATEC Web of Conferences* 157(2):05008.
- Halama, R., Kourousis, K., Pagáč, M., Paška, Z., 2022. Cyclic plasticity of additively manufactured metals. In: *"Cyclic Plasticity of Metals"*, In: Motlagh, H.J. and Roostaei, A. A. (Eds.). Elsevier: Amsterdam, pp. 397.
- Chakrabarty, A., Chakraborty, P., Jain, R., Sahu, V.K., Gurao, N.P., Bar, H.N., Khutia, N., 2023. Influence of Scanning and Building Strategies on the Deformation Behavior of Additively Manufactured AlSi10Mg: CPFEM and Finite Element Studies. *Metals and Materials International*, in press.
- Chakrabarty, A., Sahu, R., Kumar, A., Bar, H.N., Hitzler, L., Khutia, N., 2023. Finite element evaluation of fracture toughness and crack propagation in LB-PBF AlSi10Mg. *Continuum Mechanics and Thermodynamics* 35(2), 677-697.
- Měsíček, J., Čegan, T., Ma, Q.P., Halama, R., Skotnicová, K., Hajnyš, J., Juřica, J., Krpec, P., Pagáč, M., 2022. Effect of artificial aging on the strength, hardness, and residual stress of SLM AlSi10Mg parts prepared from the recycled powder. *Materials Science and Engineering A* 855, 143900.

- Obadimu, S.O., Kourousis, K.I., 2021. Compressive behaviour of additively manufactured lattice structures: A review. *Aerospace*, 2021, 8(8), 207.
- Raja, A., Cheethirala, S.R., Gupta, P., Nilesh, J. V., Jayaganthan, R. 2022. A review on the fatigue behaviour of AlSi10Mg alloy fabricated using laser powder bed fusion technique. *Journal of Materials Research and Technology* 17, 1013-1029.

Structural Integrity and Reliability of Advanced Materials obtained through Additive Manufacturing (SIRAMM23)

Comparative analysis of ABS materials mechanical properties

Zorana Golubovic^{a*}, Božica Bojovic^a, Ljubiša Petrov^b, Aleksandar Sedmak^a, Aleksa Milovanović^b, Žarko Mišković^a, Miloš Milošević^b

^a University of Belgrade, Faculty of Mechanical Engineering, Belgrade, Serbia

^b Innovation Centre of Faculty of Mechanical Engineering, Belgrade, Serbia

Abstract

Additive Manufacturing (AM) has shown rapid development during the last decades. More commonly known as 3D printing, this technology offers significant benefits for the fabrication of physical models with complex geometries. This technology started as a valuable tool for prototyping purposes but is considered for general manufacturing due to the production cycle shortening and less (if none) material waste. Out of seven possible AM technologies, this research covers three of them, namely: Fused Deposition Modeling (FDM), Stereolithography (SLA), and Digital Light Processing (DLP). Although, ABS thermoplastic material is a thoroughly researched AM material, a new resin material also called ABS is an interesting object for research. Hence, the aim of this paper is to acquire the tensile properties of this material and to compare them to the “original” ABS thermoplastic material.

© 2023 The Authors. Published by Elsevier B.V.

This is an open access article under the CC BY-NC-ND license (<https://creativecommons.org/licenses/by-nc-nd/4.0>)

Peer-review under responsibility of the SIRAMM23 organizers

Keywords: Additive Manufacturing, FDM, SLA, DLP, ABS, ABS resin, mechanical testing

1. Introduction

All Additive Manufacturing (AM) technologies share a bottom-up approach to manufacturing, i.e., an object is built “from scratch” until it’s finished in a layer-by-layer manner.

According to the ISO/ASTM 52900:2021 standard, there are seven types of AM technologies:

- Material extrusion, the most well-known technology is Fused Deposition Modeling (FDM),
- Vat photopolymerization, covers many sub-types such as Stereolithography (SLA) and Digital Light Processing (DLP),
- Powder bed fusion, the technology uses more robust machines and the most utilized sub-types are Selective Layer Sintering (SLS) and Selective Laser Melting (SLM),

- Directed Energy Deposition (DED),
- Material jetting,
- Binder jetting, and
- Sheet lamination.

Nomenclature

AM	Additive manufacturing
FDM	Fused Deposition Modeling
SLA	Stereolithography
DLP	Digital Light Processing
ABS	Acrylonitrile Butadiene Styrene

Generally, the most used AM technologies are Material extrusion and Vat photopolymerization, mostly due to machines' low cost and accessibility of build material. For this research, FDM, SLA, and DLP technologies were selected precisely because of the availability of these AM technologies. When it comes to AM of polymer materials, FDM is one of the most utilized technologies where thermoplastic material in the filament form is melted and extruded through a hot nozzle onto a build platform forming an object in a layer-by-layer manner (Ngo et al., 2018; Samykanon et al. 2019; Milovanović et al., 2022). For the utilization of liquid photo-reactive resins, SLA is the most frequently used AM technology. Here, photosensitive liquid resin is cured by a UV light laser beam (Voet et al., 2018). Next, DLP also belongs to Vat photopolymerization AM technology as SLA but, the difference is in the light source. Namely, in contrast to SLA the whole surface of the photopolymer resin vat meant for the light entry is exposed in a single pass (Shah et al., 2020).

AM technologies depend on CAD model creation, and most of the technologies need a CAD model in a so-called "STL" file format (abr., Standard Tessellation Language), to be then used in a dedicated slicer software for AM process preparation. The chosen parameters have an influence on final object properties, such as dimensional accuracy, surface roughness, mechanical properties, etc. Most of the technologies share the same parameters: the thickness of the printed layer, build and raster orientation, supporting material addition (for object support during AM process), laser speed and intensity, and post-processing techniques (Abeykoon et al., 2020).

The range of applications and possibilities that arise from AM are broadly diverse, leading to the introduction of more materials. As well as with "old" materials, proper characterization of a new material must be performed and compared with already available materials to estimate the benefits, if possible. In FDM, besides Polylactic Acid (PLA) material Acrylonitrile Butadiene Styrene (ABS) is mostly used thermoplastic polymer. Compared to other FDM materials, ABS stands out with good mechanical properties, but it lacks dimensional accuracy, due to unwanted material shrinking during the cooling process after extrusion. Also, ABS is a more polluting material emitting an unpleasant odor during an AM process (Ngo et al., 2018; Milovanović et al., 2019). Except for FDM use where the material is in the form of a filament, there is also a parallel material in the form of a resin. This "ABS-like" resin material is available both in SLA and DLP technologies. Applications may cover the production of objects with moderate detail performance, high strength, and in-total satisfactory functionality (Zhu et al., 2020).

In engineering, polymer materials may find proper use hence, novel research activities search for different polymer mixtures and types in order to achieve desired mechanical properties of AMed objects. The aim of this particular research is to tensile test this new "ABS-like" resin material and to compare it with standard thermoplastic ABS. In addition to mechanical tests, topography observation using optical microscopy is conducted.

2. Methodology

ABS and ABS resin specimens for tensile testing were prepared according to the ISO 527-2 standard (see Fig. 1). Five specimens were prepared for each AM technology, to achieve sufficient repeatability. FDM specimens were AMed on a Creality CR-10 Smart Pro machine (Shenzhen, China), and ABS-like resin specimens were made on an SLA (Kings 600 Pro, Shenzhen, China) and DLP machine (Creality LD-002R, Shenzhen, China). FDM and DLP

machines are desktop versions, unlike the industry-grade SLA machine used here. Another research output here is the comparison of the industrial-grade machine with desktop ones. Printing properties were set to be as similar as possible hence, specimens were fabricated with 100% infill density, with a grid infill pattern, and with a 90° orientation of rasters. All tensile tests had the same conditions, i.e., they were tested at room temperature (around 23 °C) and relative humidity of 55%.

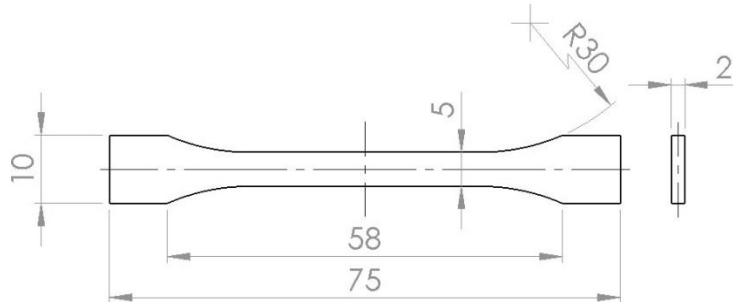


Fig. 1. Specimen geometry according to the ISO 527-2 standard (dimensions in mm)..

Tensile tests were performed on the Shimadzu AGS-X machine (Shimadzu Corp., Kyoto, Japan) equipped with a load cell of 100 kN capacity. The testing speed was set to 1 mm/min. Optical 2D and 3D microscopy were utilized after conducting tensile tests, on laboratory-grade 3D Digital Video Microscope KH-7700 (Hirox, Tokyo, Japan).

3. Results and Discussion

ABS material represents the toughened modification of styrene-acrylonitrile (SAN) copolymer, where toughening is achieved by adding the sub-microscopically small rubber particles in the coherent brittle SAN matrix (Grellmann et al., 2001). The amount and manner of dispersion of those particles have a direct influence on the morphology and materials' mechanical properties. It is already well-known that ABS resins share time-dependent behavior, i.e., their mechanical properties are influenced by the straining rate, as well as by the volume of rubber content (Bernal et al., 1995).

All tested specimens, from both of the stated materials, exhibited brittle fracture behavior (see Fig. 2, upper level). Further 2D and 3D optical microscopy analysis was conducted for topography and morphology observation. Taken images showed different textures, depending on applied printing regimes (see Fig.2, Middle and Lower level). One of the purposes of the utilization of optical microscopy is to find any defects, which would be proof of irregularities and abruptions in specimens' integrity.

On the FDM fracture surface, there is a considerable size difference in the present internal gaps, located between printed raster lines. Such a gap size inconsistency refers to uneven intra- and inter-layer bonding in the structure. This anisotropy of FDM specimens is shown in the leftmost 2D image in Fig. 2, Middle level. Naturally, when the surrounding gaps are bigger in size, the raster lines are more visible. The other two 2D images in Fig. 2, Middle level, show expected similarities in fracture surface structure on both Vat photopolymerization AM technologies. As one can see in all 2D images from Fig. 2- Middle level, there is a major difference in resolution and accuracy of both Vat photopolymerization AM technologies in contrast to FDM one.

Fig. 2- Lower level is dedicated to 3D images: here, in the leftmost image one can see the two-level fracture surface on FDM specimens. FDM specimen's 3D image gives a better insight into the fracture morphology where one can clearly see two predominately flat surfaces, separated by a ridge. This particular ridge reveals the location of probable low inter-layer bonding, which caused the separation between layers. From the 3D image, it is visible that the highest deformation is present at the ridge peak. Namely, after the inter-layer separation the closest layers receive higher loads. Hence, the highest level of ductile deformation is cited all along the ridge edge.

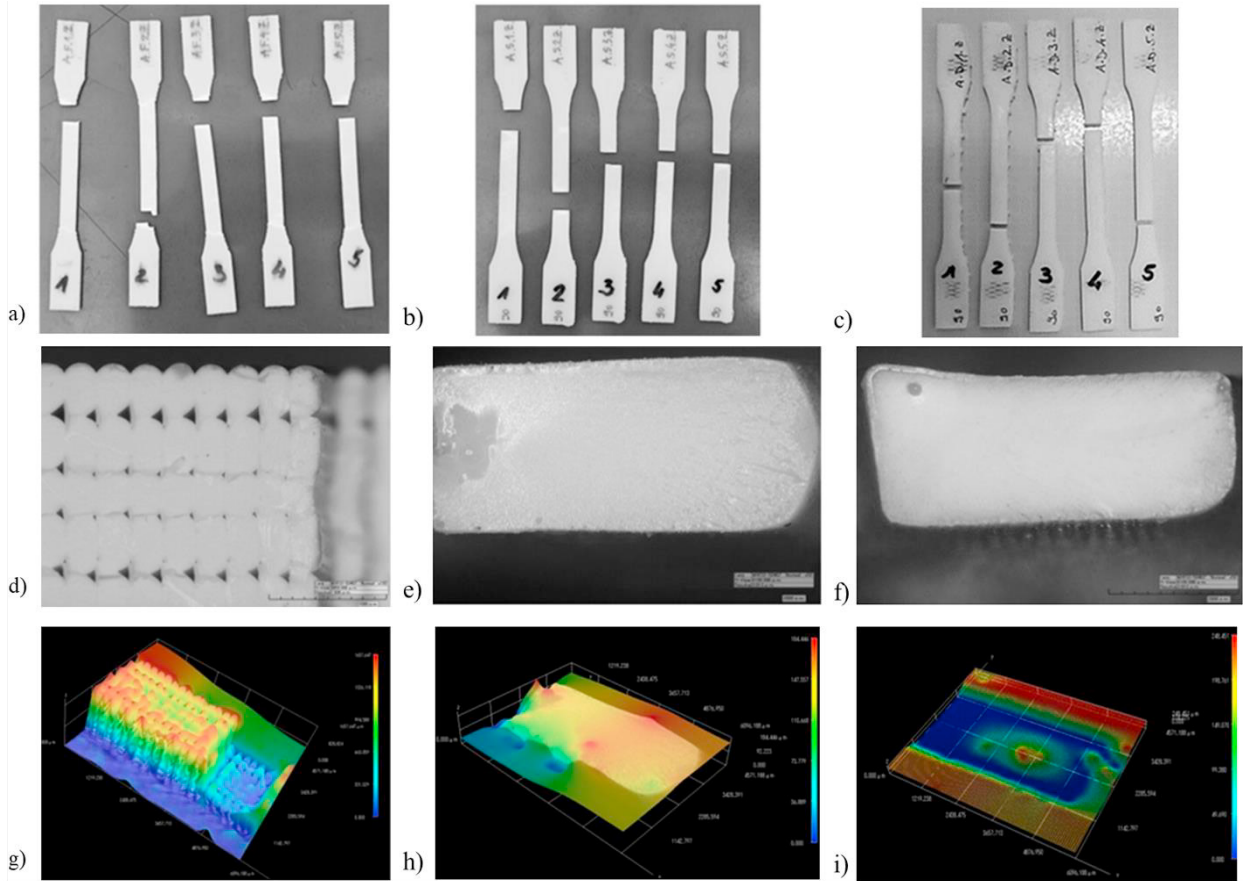


Fig. 2. Upper - Images of ISO 527-2 fractured specimens: a) FDM; b) SLA; c) DLP;
 Middle - 2D micrographs: d) FDM; e) SLA; f) DLP;
 Bottom - 3D micrograph: g) FDM; h) SLA; i) DLP (Golubović et al., 2023).

Unlike FDM, the fracture surfaces in SLA and DLP specimens are principally flat. In Fig. 2 (Middle level), the second 2D image is dedicated to SLA: here, the fracture surface is flat except for the left side where the polymer material was pulled upward for $200\ \mu\text{m}$. A better visualization of the stated can be seen on the 3D image of the SLA fracture surface, placed one image below (see Fig. 2, Lower level). Due to different refraction from the fracture surface in the 2D image, one can assume that the ductile fracture is present on most of the specimen, except for the pulled small portion of the material, where it experienced a brittle fracture. Images dedicated to DLP specimens are placed on the right-hand side in Fig. 2. The brittle fracture is present on the whole fracture surface, see 2D image (Fig. 2, Middle level). Apart from the nature of the fracture, one can also see the bubbles scattered all over the fracture surface. The irregularities in shape and size of the bubbles are better visualized in the 3D image (Fig. 2, Lower level). From the 2D image, it is also noticeable that the outer surface has a different appearance from the interior: namely, due to the post-curing of the specimens via LED lamps it is apparent that the outer surface is better polymerized than the specimen's inside. The size of the bubbles is in order of 240 microns (see 3D image). The origin of bubbles is from the shaking of the resin in the bottle, right before pouring the liquid into the vat. Due to the lower energy of the UV light source in DLP, not all the bubbles disappeared during the AM process, i.e., some got trapped inside the cured resin.

Fig. 3 represents the engineering stress-strain interpretation of all the tensile results. In order to show the repeatability of the results, the three diagrams are meant to show all the curves from tested batches. Here, one can see

that the repeatability of DLP results (Figure 3 c) is not representative. This may refer to the overall lower quality of the DLP process (in comparison with SLA in Figure 3 b, for example).

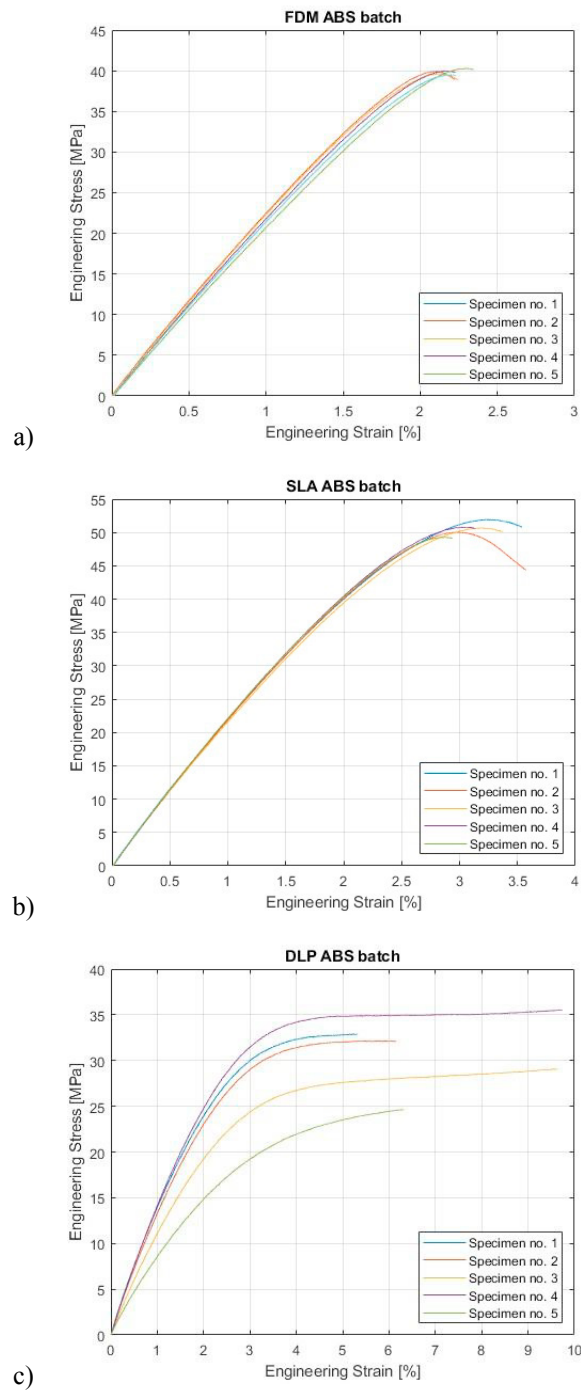


Fig. 3. The comparison between engineering stress-strain curves for ABS: a) FDM, b) SLA and c) DLP printed specimens.

Tensile results from both standard ABS and ABS resin material, using these three mentioned AM technologies, vary significantly (see Fig. 4). In general, AM parts obtained from the extrusion process have overall better mechanical properties than parts created from the polymerization of resin material. But SLA specimens here have higher UTS than FDM ones. However, DLP tensile results show lower UTS than FDM’s (see Figs. 3 and 4). This advantage of SLA can be explained by finer materials’ structure due to higher UV laser energies during the AM process. On the other hand, the lower energy of LCD projected UV light and the existence of bubbles in the resin created highly anisotropic DLP specimens. Hence, the UTS values significantly depend upon the AM technology utilized, even though the material is the same. Here, the SLA proved to be better than the other two AM technologies (see Fig. 3). Regarding the elastic modulus, the SLA values are quite similar to the FDM ones. This statement may be visualized as the overlap of both average curves in their linear regions (see Fig. 3). However, the DLP’s elastic modulus is distinctly lower. Quantitative values of elastic modulus are shown in Fig. 4. DLP has proven that it is a better option regarding the maximum strain and elongation at break (see Fig. 4). Their overall elongation is more than double in value, compared to the other two observed AM technologies. Hence, the DLP is sufficiently tougher although the material used is the same photosensitive resin as in the SLA process. One may conclude that the utilized AM technology has an effect on overall strain values.

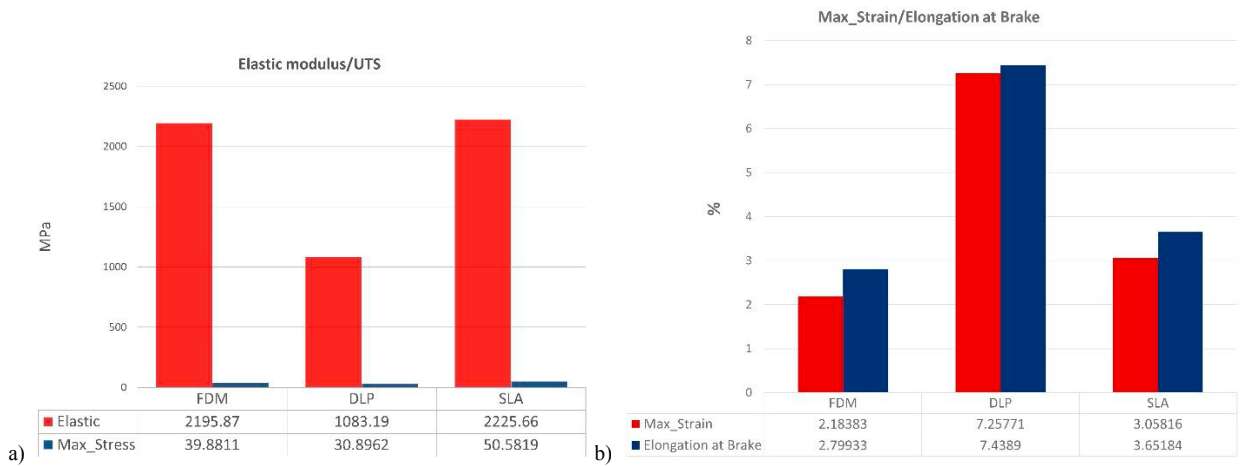


Fig. 4. a) Elastic modulus and UTS chart, and b) maximum strain and elongation at break chart.

The absorbed energy during the tensile process was also monitored here. Worth pointing out is that this absorbed energy is interpreted as an area underneath the stress-strain diagrams from Fig. 3. Hence, DLP’s value is approx. 1.09 J while the value for SLA and FDM are 0.43 J and 0.73 J, respectively. Therefore, this information goes along with the fact that DLP’s can strain more than the other two. This may also be influenced by the post-printing process that DLP specimens underwent. As additional info, the DLP specimens appeared more rubber-like when touched than the SLA ones.

4. Conclusions

Both tensile properties and fracture surface morphology of standard ABS filament and novel resin material has been analyzed, leading to a more comprehensive understanding of the differences between the two. In tensile tests, all the tested materials experienced predominantly brittle behavior upon fracture. FDM and SLA have been shown to have similar elastic modulus, with quantitative values around 2.2 GPa. The presence of bubbles in DLP specimens has shown its effect on the elastic modulus namely, these defects decrease the property value. Regarding UTS, the SLA has proven to be the best AM technology of the monitored three. One should not forget that the SLA device used here is an industry-grade machine, in contrast to desktop FDM and DLP devices. However, the DLP has higher overall elongation and higher total energy absorption.

The general conclusion is that ABS resin material has shown its benefits in comparison with well-known standard ABS material used in FDM technology. Depending on the Vat photopolymerization technology used, the ABS resin material may offer higher elongation and energy absorption or it can exhibit higher strength. In that sense, SLA technology provides AM parts with better tensile strength, while DLP enables tougher components.

Acknowledgements

This research was financially supported by the Ministry of Science, Technology Development and Innovation of the Republic of Serbia by Contract No. 451-03-47/2023-01/200105 from 03.02.2023. This research is supported also by European Union's Horizon 2020 research and innovation program "SIRAMM", under grant agreement No. 857124.

References

- Ngo, T.D., Kashani, A., Imbalzano, G., Nguyen, K.T.Q., Hui, D., 2018. Additive manufacturing (3D printing): A review of materials, methods, applications and challenges. *Compos. Part B Eng.*, 143, 172–196
- Samykano, M., Selvamani, S.K., Kadirgama, K., Ngui, W.K., Kanagaraj, G., Sudhakar, K., 2019. Mechanical property of FDM printed ABS: influence of printing parameters, *The International Journal of Advanced Manufacturing Technology*, 102, 2779–2796. <https://doi.org/10.1007/s00170-019-03313-0>
- Milovanović, A., Golubović, Z., Babinský, T., Šulák, I., Mitrović, A., 2022. Tensile Properties of Polypropylene Additively Manufactured by FDM. *Structural Integrity and Life* Vol. 22, No 3, pp. 305–308
- Voet, V.S.D., Strating, T., Schnelting, G.H.M., Dijkstra, P., Tietema, M., Xu, J., Woortman, A.J.J., Loos, K., Jager, J., Folkersma, R., 2018. Biobased Acrylate Photocurable Resin Formulation for Stereolithography 3D Printing, *ACS Omega* 2018, 3, 1403–1408. doi: 10.1021/acsomega.7b01648
- Shah, D.M., Morris, J., Plaisted, T.A., Amirkhizi, A.V., Hansen, C.J., 2020. Highly Filled Resins for DLP-based Printing of Low Density, High Modulus Materials, *Additive Manufacturing*, doi: <https://doi.org/10.1016/j.addma.2020.101736>
- Abeykoon, C., Sri-Amphorn, P., Fernando, A., 2020. Optimization of fused deposition modeling parameters for improved PLA and ABS 3D printed structures, *International Journal of Lightweight Materials and Manufacture*, 3, 284-297. <https://doi.org/10.1016/j.ijlmm.2020.03.003>
- Milovanović, A., Milošević, M., Mladenović, G., Likozar, B., Čolić, K., Mitrović, N., 2019. Experimental Dimensional Accuracy Analysis of Reformer Prototype Models Produced by FDM and SLA 3D Printing Technology, in "Experimental and Numerical Investigations in Materials Science and Engineering". In: Mitrović, N., Milošević, M., Mladenović, G. (Ed.). Springer, Cham, pp. 84-95.
- Zhu, Z.H., Zhang, N., Wang, T., Hao, M.Y., 2020. Short Review of Polymer Composites for 3D Printing, *IOP Conf. Ser.: Mater. Sci. Eng.* 758 012046. doi: 10.1088/1757-899X/758/1/012046
- W. Grellmann et al. (eds.), 2001. *Deformation and Fracture Behaviour of Polymers*, Springer-Verlag Berlin Heidelberg. ISBN: 978-3-662-04556-5
- Bernal, C. R., Frontini, P. M., Sforza, M., & Bibbó, M. A. 1995. Microstructure, deformation, and fracture behavior of commercial ABS resins. *Journal of Applied Polymer Science*, 58(1), 1–10. doi:10.1002/app.1995.070580101
- Golubović, Z., Danilov, I., Bojović, B., Petrov, Lj., Sedmak, A., Mišković, Ž., Mitrović, N., 2023. Comprehensive mechanical examination of ABS and ABS-like polymers additively manufactured by material extrusion and vat photopolymerization processes, *Polymers*, 15(21), 4197; <https://doi.org/10.3390/polym15214197>



International Conference on Structural Integrity and Reliability of Advanced Materials
obtained through Additive Manufacturing (SIRAMM23)

Computational Modeling of Directed Energy Deposition of Titanium Aluminide Plate Geometries

Balichakra Mallikarjuna^{a,*}

^aDepartment of Production Engineering, National Institute of Technology Tiruchirappalli, Tamil Nadu, India

Abstract

In this work, transient thermomechanical analysis of the laser-based Directed Energy Deposition (DED) process was carried out to predict melt pool dimensions, thermal cycles and residual stress during Titanium Aluminide (TiAl) plate deposition. The predicted melt pool length, width, and depth increased as the laser power was increased from 250 W to 350 W at a constant travel speed of 15 mm/s. The melt pool length increased from 0.425 mm to 0.55 mm, while the depth increased from 0.1 to 0.29 mm, and the width increased from 0.412 to 0.5 mm. The plate's edges (tracks 1 and 6) were found to experience a slightly higher temperature than the middle tracks, which may contribute to higher thermal gradients at the edges. The highest Principal stress of 140 MPa was found in track 1. The magnitude of Principal stresses diminished as track deposition progressed from track 2 to 6 due to the variation of the thermal gradient along the tracks.

© 2023 The Authors. Published by Elsevier B.V.

This is an open access article under the CC BY-NC-ND license (<https://creativecommons.org/licenses/by-nc-nd/4.0>)

Peer-review under responsibility of the SIRAMM23 organizers

Keywords: γ -TiAl Alloy; Laser Metal Deposition; Melt Pool; Thermal Cycles; Residual Stress

1. Introduction

Metal Additive Manufacturing (MAM) is an innovative process wherein the digital data in the form of a Computer-Aided Design (CAD) file is used to build a prototype or fully functional components without fixtures and tooling,

* Corresponding author. Tel.: +91 8310 405 141; fax: +0-000-000-0000 .

E-mail address: mallubalichakra@gmail.com and mallik@nitt.edu

unlike traditional manufacturing processes. MAM is based on depositing the parts by layer-by-layer of material addition. The component or part is created layer-by-layer; the next layer is deposited over the previously deposited under the heat or chemicals (Bandyopadhyay, 2016). MAM technologies such as Directed energy deposition (LENS, DMD, DM3D, Beam, etc.) and Powder Bed Fusion (SLM, DMLS, Renishaw, SLS, Trumpf etc.,) processes have revolutionised the manufacturing business in recent times (Diepold et al., 2020). However, MAM technologies face several technological problems, such as limited choice of materials, slow process speed, lack of available industrial standards, accuracy and reliability (Bhavar et al., 2017). MAM uses a laser or electron beam or plasma as a heat source to melt the powders during material layer-upon-layer deposition. DED techniques such as Laser Engineered Net Shaping (LENS) use a laser to melt the powders coming from the nozzles. Where a focused laser beam creates the melt pool on the substrate. Then the powders are injected into the melt pool (powder size is between 40 to 150 μm) via nozzles (Liu Weiping and John DuPont, n.d.). The series of beads (solidified melt pools) result in a layer. A successive layer is deposited by incrementing the laser head in the z-axis by a layer thickness. DED processes involve complex thermal behaviour in each melting pool and in the layers. The melt pool and thermal history significantly affect the microstructure, mechanical properties, residual stress, and distortion of the end part. To understand all these intrinsic variables, researchers have carried out a thermomechanical analysis of the DED process on the deposited parts (Balichakra et al., 2016; Hazarika et al., 2016; Kamara et al., 2011; Marimuthu et al., 2013; Roberts et al., 2009, 2012). Thereby eliminating the number of experiments required for the deposition of the TiAl parts (Balichakra et al., 2019; Bandyopadhyay & Traxel, 2018; Manvatkar et al., 2011). The LENS processes various materials such as titanium alloy, H13 tool steel, stainless steel, composites etc. (Murr et al., 2009; J. Wang et al., 2019; L. Wang et al., 2008). Neela et al. (2009), carried out process modelling of the LENS process. They study the influence of process parameters on thermal behaviour, mechanical properties, and build quality. This study concluded that overheating of the top layers can be avoided by reducing the heat input during the deposition of these layers. Manvatkar et al. (2011), carried out a 3D transient thermal finite element analysis to predict cooling rates, thermal cycling during deposition, and melt pool dimensions. The predicted temperatures were used to correlate with the hardness of the sample. Pratt et al. (2008) investigated the residual stress development in LENS-deposited samples both numerically and experimentally. The specimens were deposited at different laser powers, scan speeds and powder feed rates. Their investigation showed that laser velocity does not contribute significantly to residual stress development, while laser power strongly influences residual stress development. The melt pool and temperature prediction in the DED process were reported. The melt pool size at the edges is more significant than inside the wall (Mallikarjuna et al., 2021). Several researchers reported predicting the melt pool, thermal cycles, residual stress, and distortion in the directed energy deposited parts (Abdullah & Anwar, 2020; Hajjalizadeh & Ince, 2020; Mallikarjuna & Reutzel, 2022; Shen & Chou, 2012; Zhang et al., 2016).

Towards this end, the current work presents result of the thermomechanical modelling of directed energy deposited γ -TiAl plate geometries. This work attempted to predict the melt pool, thermal history and residual stress in γ -TiAl plate geometries.

2. Methodology

2.1 Thermomechanical analysis

This work uses a sequencing method to simulate the thermomechanical analysis. First, the transient thermal analysis is carried out to predict the temperatures. Secondly, mechanical analysis is carried out by importing body temperatures (through LDREAD) from thermal analysis. For both the analysis, necessary initial conditions, material properties and boundary conditions were used. To perform the thermomechanical analysis, ANSYS macros are created, which consist of necessary elements, boundary conditions and properties. Finally, results are extracted from thermal and mechanical analyses such as temperature history, melt pool and stresses, respectively. The Coupled field scheme of thermo-mechanical analysis is represented in Fig 1. The material properties, boundary conditions, and governing equations are found elsewhere (Balichakra et al., 2019). The thermomechanical analysis was carried out for the plate geometry. The details of the process parameters used are presented in Table 1.

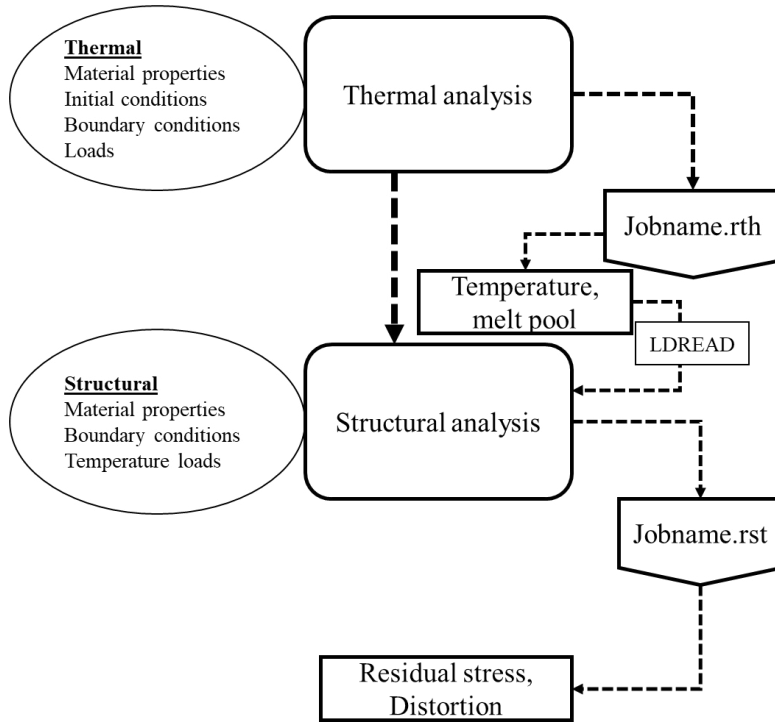


Fig. 1. Simulation scheme used for thermal and structural analysis of plate in ANSYS software

Table 1. Process parameters considered

Process parameter	Value
Layer height, Length of layer (mm)	0.25 mm, 20 mm
No. of tracks, Width of each track (mm)	6, 0.5 mm
Laser beam diameter and Overlap percentage (mm)	0.5 mm, 0%
Laser power (W)	250, 300, 350
Travel speed (mm/s)	10, 15, 20
Scanning pattern	Bidirectional

3. Results and discussions

3.1 Effect of laser power and travel speed on melt pool dimensions

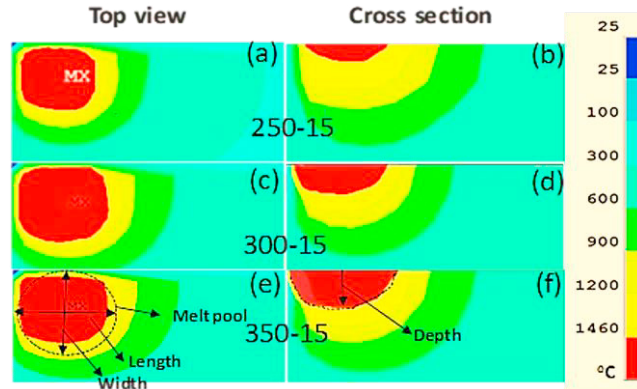


Fig. 2. Predicted melt pool top and cross-sectional view while deposition of layer 2 and track 3 at constant velocity (V) = 15 mm/s and different laser power (a) and (b) 250 W; (c) and (d) 300 W; (d) and (e) 350 W (Mallikarjuna, 2020).

Fig.2. Shown the melt pool FE contours predicted for varying laser power at constant travel speed. The red colour in the melt pool contour indicates the molten region where the liquidus temperature is greater than the 1460 °C of the TiAl material. The melt pool length, width, and depth increased as the laser power was increased from 250 W to 350 W at a constant velocity of 15 mm/s. The melt pool length increased from 0.425 mm to 0.55 mm, while the depth increased from 0.1 to 0.29 mm, and the width increased from 0.412 to 0.5 mm. This increase in melt pool dimensions with the increase in laser power can be attributed to the higher energy available at increasing powers to melt the powder. However, melt pool size (length, width, and depth) decreased for varying travel speeds (10, 15, 20 mm/s) at a constant laser power of 300 W. This can be attributed to the fact that the powders were less exposed under the laser.

3.2 Thermal cycling during deposition of plate

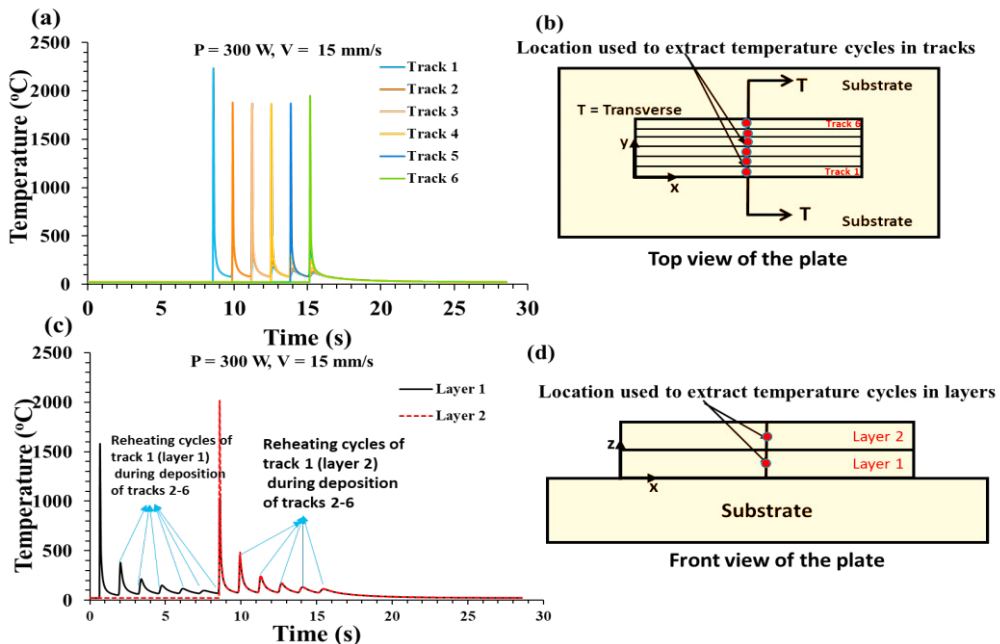


Fig 3. (a) and (c) Peak thermal history in tracks and layers of the plate for $P = 300$ W, $V = 15$ mm/s and (b) and (d) Locations used to extract temperatures of respective tracks and layers (Mallikarjuna, 2020).

The thermal history of the six tracks as a function of time for bidirectional scanning is shown in Fig. 3(a). It can be observed that the peak temperature in the plot is 2176 °C in track 1 (From Fig. 3(a)). The temperature then attains a uniform average temperature of 1826 °C in the middle tracks (2, 3, 4, and 5). However, in the last track (track 6), the temperature increases to 1899 °C. It can be seen that the edges experience a slightly higher temperature than the middle tracks and this may contribute to higher thermal gradients at the edges.

3.3 Influence of laser power and travel speed on residual stress distribution in the plate

The effect of laser power on the first Principal stress for the bidirectional scan was investigated. The Principal stress increases from 196 to 237 MPa with increased laser power (250 to 350 W) at a constant travel speed (15 mm/s). This is because the high laser power induces higher thermal gradients in the plate. Similarly, the effect of travel speeds at constant laser power on the first Principal stress for a bidirectional scan was studied. The Principal stress slightly decreases from 239 to 215 MPa as the travel speed increases from 10 to 20 mm/s at a constant laser power of 300 W. The lower exposure time reduces the thermal gradients. It can be concluded that the laser power has shown more dominance in the magnitude of residual stress formation than the travel speed.

4. Conclusion

The computational modelling of directed energy deposition of TiAl plate geometries was carried out. The results indicate that the melt pool dimensions increased as the laser power increased from 250 to 350 W and decreased as the travel speed increased from 10 to 20 mm/s. The edges of the plate experienced slightly higher temperatures (track 1-2176 °C and track 6-1899 °C) than the middle tracks. The Principal stress slightly decreases from 239 to 215 MPa as the travel speed increases from 10 to 20 mm/s at a constant laser power of 300 W. The lower exposure time reduces the thermal gradients. The laser power has shown more dominance over the magnitude of Principal stress formation than the travel speed.

Acknowledgements

The author thanks the Computation Fluid Dynamics Lab, National Institute of Technology Karnataka, Surathkal, India, for providing the computational facility to run the simulation.

Reference

- Abdullah, F. M., & Anwar, S. (2020). Thermomechanical simulations of residual stresses and distortion in electron beam melting with experimental validation for Ti-6Al-4V. *Metals*, 10(9), 1151.
- Balichakra, M., Bontha, S., Krishna, P., & Balla, V. K. (2019). Prediction and validation of residual stresses generated during laser metal deposition of γ titanium aluminide thin wall structures. *Materials Research Express*, 6(10), 106550. <https://doi.org/10.1088/2053-1591/ab38ee>
- Balichakra, M., Bontha, S., Krishna, P., Das, M., & Balla, V. K. (2016). Understanding thermal behavior in laser processing of titanium aluminide alloys. *Proceedings of 6th International & 27th All India Manufacturing Technology, Design and Research Conference (AIMTDR-2016)*, 73–77.
- Bandyopadhyay, A. (2016). Laser engineering net shaping of microporous Ti6Al4V filters. *Frontiers in Mechanical Engineering*, 2(10), 1–9. <https://doi.org/10.3389/fmech.2016.00009>
- Bandyopadhyay, A., & Traxel, K. D. (2018). Invited review article: Metal-additive manufacturing-modeling strategies for application-optimized designs. *Additive Manufacturing*, 22(7), 758–774. <https://doi.org/10.1016/j.addma.2018.06.024>
- Bhavar, V., Kattire, P., Patil, V., Khot, S., Gujar, K., & Singh, R. (2017). A review on powder bed fusion technology of metal additive manufacturing. *Additive Manufacturing Handbook: Product Development for the Defense Industry*, 251–261. <https://doi.org/10.1201/9781315119106>
- Diepold, B., Vorlaufer, N., Neumeier, S., Gartner, T., & Göken, M. (2020). Optimization of the heat treatment of additively manufactured Ni-base superalloy IN718. *International Journal of Minerals, Metallurgy and Materials*, 27(5), 640–648.

- Hajjalizadeh, F., & Ince, A. (2020). Short review on modeling approaches for metal additive manufacturing process. *Material Design & Processing Communications*, 2(2), 0–2. <https://doi.org/10.1002/mdp2.56>
- Hazarika, B., Mallikarjuna, Krishna, P., Balla, V. K., & Bontha, S. (2016). Numerical modelling of laser additive manufacturing processes. *NAFEMS India Regional Conference*, 8, 30–31.
- Kamara, A. M., Marimuthu, S., & Li, L. (2011). A numerical investigation into residual stress characteristics in laser deposited multiple layer waspaloy parts. *Journal of Manufacturing Science and Engineering*, 133(3), 031013. <https://doi.org/10.1115/1.4003833>
- Liu Weiping and John DuPont. (n.d.). Fabrication of Titanium Aluminide Matrix Composites by Laser Engineered Net Shaping. *Atlantic*, 124–132.
- Mallikarjuna. (2020). *Effect of process variables on residual stress and microstructure in laser additive manufacturing of γ -TiAl alloy* [NATIONAL INSTITUTE OF TECHNOLOGY KARNATAKA]. <https://idr.nitk.ac.in/jspui/handle/123456789/16897>
- Mallikarjuna, B., Bontha, S., Krishna, P., & Balla, V. K. (2021). Characterization and thermal analysis of laser metal deposited γ -TiAl thin walls. *Journal of Materials Research and Technology*, 15(12), 6231–6243. <https://doi.org/10.1016/j.jmrt.2021.10.133>
- Mallikarjuna, B., & Reutzel, E. W. (2022). Reclamation of intermetallic titanium aluminide aero-engine components using directed energy deposition technology. *Manufacturing Review*, 9(27), 1–21. <https://doi.org/10.1051/mfreview/2022024>
- Manvatkar, V. D., Gokhale, A. A., Reddy, G. J., & Venkataramana, A. (2011). Estimation of melt pool dimensions, thermal cycle, and hardness distribution in the laser-engineered net shaping process of austenitic stainless steel. *Metallurgical and Materials Transactions A*, 42A. <https://doi.org/10.1007/s11661-011-0787-8>
- Marimuthu, S., Clark, D., Allen, J., Kamara, A. M., Mativenga, P., Li, L., & Scudamore, R. (2013). Finite element modelling of substrate thermal distortion in direct laser additive manufacture of an aero-engine component. *Proceedings of the Institution of Mechanical Engineers, Part C: Journal of Mechanical Engineering Science*, 227(9), 1987–1999. <https://doi.org/10.1177/0954406212470363>
- Murr, L. E., Gaytan, S. M., Ceylan, A., Martinez, E., Martinez, J. L., Hernandez, D. H., Machado, B. I., Ramirez, D. a., Medina, F., Collins, S., & Wicker, R. B. (2009). Characterization of titanium aluminide alloy components fabricated by additive manufacturing using electron beam melting. *Acta Materialia*, 58(5), 1887–1894. <https://doi.org/10.1016/j.actamat.2009.11.032>
- Roberts, I. A., Wang, C. J., Esterlein, R., Stanford, M., & Mynors, D. J. (2009). A three-dimensional finite element analysis of the temperature field during laser melting of metal powders in additive layer manufacturing. *International Journal of Machine Tools and Manufacture*, 49(12–13), 916–923. <https://doi.org/10.1016/j.ijmachtools.2009.07.004>
- Roberts, I. A., Wang, C. J., Kibble, K. A., Stanford, M., Mynors, D. J., & Kingdom, U. (2012). *Numerical and experimental studies on the laser melting of steel plate surfaces. 2–5.*
- Shen, N., & Chou, K. (2012). Thermal modeling of electron beam additive manufacturing process – powder sintering effects. *Proceedings of the ASME 2012 International Manufacturing Science and Engineering Conference June 4-8, 2012, Notre Dame, Indiana, USA*, 1–9.
- Wang, J., Pan, Z., Wei, L., He, S., Cuiuri, D., & Li, H. (2019). Introduction of ternary alloying element in wire arc additive manufacturing of titanium aluminide intermetallic. In *Additive Manufacturing* (Vol. 27, pp. 236–245). <https://doi.org/10.1016/j.addma.2019.03.014>
- Wang, L., Felicelli, S., Gooroochurn, Y., Wang, P. T., & Horstemeyer, M. F. (2008). Optimization of the LENS® process for steady molten pool size. *Materials Science and Engineering A*, 474(1–2), 148–156. <https://doi.org/10.1016/j.msea.2007.04.119>
- Zhang, J., Liou, F., Seufzer, W., & Taminger, K. (2016). A coupled finite element cellular automaton model to predict thermal history and grain morphology of Ti-6Al-4V during direct metal deposition (DMD). *Additive Manufacturing*, 11(Dmd), 32–39. <https://doi.org/10.1016/j.addma.2016.04.004>



+ Structural Integrity and Reliability of Advanced Materials obtained through Additive Manufacturing (SIRAMM23)

Effect of Fillers on Mechanical Properties of FDM printed PLA Components

Cristina Vălean^a, Dan Ioan Stoia^{a*}, Carmen Opreș^a, Emanoil Linul^{a*}

^aPolitehnica University Timisoara, Mihai Viteazul no.1, Timisoara 300222, Romania

Abstract

Fused Deposition Modelling (FDM) is the most accessible additive technology nowadays, because it combines the low cost and simplicity of the machine with the low cost and availability of the thermoplastic polymers. This class of polymers are however limited and in order to increase the application range of the products, mixing polymeric matrix with various fillers can be a solution.

The purpose of this study is to identify the effect of the functional fillers incorporated in PLA thermoplastic on the mechanical properties of the obtained components. In addition, the layer orientation in relation to the loading direction will be considered as a study variable. All samples were manufactured under the same conditions using the same FDM machine. The effect of carbon / glass fibers and bronze particle fillers on the PLA matrix in comparison with the pure PLA filament was evidenced by tensile and flexural testes. The results were then interpreted based on the two criteria: filler type and layer deposition in accordance to the loading direction. It was determined that regardless of the type of test (tensile or flexural), the mechanical behavior is strongly influenced by the type of filler in the matrix. The most ductile behavior was showed by the pure PLA samples, and the most brittle by the PLA reinforced with carbon fibers.

© 2023 The Authors. Published by Elsevier B.V.

This is an open access article under the CC BY-NC-ND license (<https://creativecommons.org/licenses/by-nc-nd/4.0>)

Peer-review under responsibility of the SIRAMM23 organizers

Keywords: PLA fillers, Tensile, Flexural, Carbon fibers, Glass fibers, Bronze particles.

* Dan Ioan STOIA, * Emanoil LINUL. Tel.: +40256403631

E-mail address: dan.stoia@upt.ro, emanoil.linul@upt.ro

1. Introduction

Due to the possibility of obtaining complex parts with a high dimensional precision, additive manufacturing (AM) technology has gained a lot of attention in recent years compared to traditional technologies [1-3]. Among the AM technologies, the Fused Deposition Modelling (FDM) process is by far the most developed and used process [4]. This aspect is due to the friendly handling, low costs, acceptable precision and high properties of the printed components [5, 6]. FDM works with many thermoplastic materials, however, the most used is polylactic acid (PLA) [7].

The integration of the agricultural by-products in PLA filaments was approached by Cali et al [8]. The natural fillers in the biocompatible matrix opens the possibility of filaments to be used in biomedical field. The hemp and hemp inflorescences mixture in PLA matrix provide to the new composite significant improvements in elastic properties and density.

The changings in hardness, density, tensile strength and melting temperature were presented by Lohar et al [9] in accordance to the addition of bio fillers in the PLA matrix. The wall nut shell powder, egg shell powder, white marble powder and combination of those were used as fillers in PLA matrix, producing composites that impact the properties of PLA. One of the most impacted properties are the elongation at break and the hardness of the new composites. These properties are enhanced by the presence of the bio fillers.

Mei-Po et al [10] conduct tensile, flexural and impact properties of PLA reinforced with bamboo charcoal for food storage applications. An important aspect was observed, regarding the mechanical properties: the properties increase until a threshold value of 7.5 wt.% charcoal particles is reached, leading to the necessity of limiting the percentage of filler in mixture.

Graphite was used as filler in PLA polymer matrix by Zerankeshi et al [11]. Acting as a reinforcement phase, the composite exhibit significant better printability and mechanical properties. Also, the thermal properties of the PLA-graphite mixture were enhanced in comparison with untainted PLA. Some authors develop mathematical models of failure probability of PLA with and without fillers starting from static tensile testing [12]. The presence of the alumina particles in the polymeric matrix lowers the tensile strength both in raw filament and on the printed samples.

The integration of nickel powder in the PLA matrix was approached by some authors [13]. They use the scanning electron microscopy for analyzing the uniformity of the particle distribution in the structure of the composite and reveal that some composites are not suitable to become filaments for 3D printing. The best results in this case were recorded for a 5% of nickel particles in the PLA volume.

A comprehensive review work on the effect of presence of different fillers on PLA matrix was conducted by Joseph Arockiam et al [14]. Here, the mechanical and thermal properties of polylactic acid filaments containing various types of fillers were examined. Among considered fillers were: carbon fiber, microcrystalline cellulose, core-shell rubber, accelyted tannin, hemp hurn, cellulose nanofibers, continuous flax fiber, hemp and harakeke, wood, diatomaceous earth, bamboo fibers, talc, cork and ABS. Al results are presented in comparison with the untainted PLA materials but no comparison between the fillers was done. Therefore, this paper presents a comparison between several types of fillers (glass/carbon fibers and bronze particles) and pure PLA. The investigations are carried out under tensile and flexural loads.

Nomenclature

AM	Additive Manufacturing
FDM	Fused Deposition Modelling
PLA	polylactic acid
PLA+GF	polylactic acid + glass fibres
PLA+CF	polylactic acid + carbon fibres
PLA+BP	polylactic acid + bronze particles

3D	three-dimensional
----	-------------------

1. Materials and methods

The materials used in study are commercially available filaments of pure PLA and PLA mixed with three types of fillers: short glass fibers, short carbon fibers and bronze particles, named in the article PLA+GF, PLA+CF and PLA+BP respectively. The PLA+GF is composed of a PLA matrix (85%) and glass fibers (15%), the PLA+CF is composed of a PLA matrix (85-90%) and carbon fibers (15-10%) and the PLA+BP has more than 80% metal particles [15]. The size of the fibers and bronze particles have a wide range, according to our own measurements: glass fibers 200-300 μm , carbon fibers 100-300 μm , bronze particles 5-30 μm . All filaments were 1.75 mm in diameter, semicrystalline and possessed similar processing temperatures (below 230 $^{\circ}\text{C}$), according to their manufacturers.

The 3D printing was conducted on Makerbot Sketch printer using the following parameters: extruder temperature – 220 $^{\circ}\text{C}$, build plate temperature – 50 $^{\circ}\text{C}$, layer height – 0.1 mm, infill density – 95%, infill pattern – linear, nozzle diameter – 0.4 mm, printing velocity: – 35 mm/s.

The microscopic images of the samples were obtained using Olympus BX51M microscope at 100 \times magnification. The images in the Figure 1 represent the surface morphology of each representative sample.

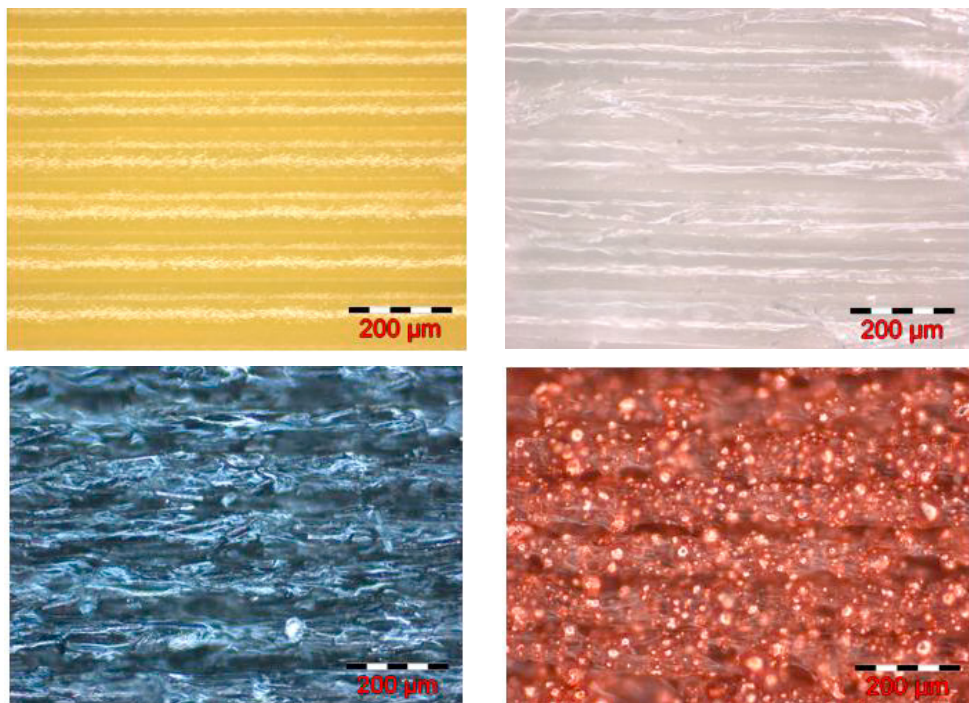


Fig. 1. Microscopic images 100 \times , of the printed structures: (a) pure PLA, (b) PLA+GF, (c) PLA+CF, (d) PLA+BP

The tensile and flexural tests of the samples were performed according to ISO 527-1:19 standard [16] for tensile tests and ASTM D 790:17 [17] for flexural, on 5 kN Zwick Roell testing machine. The tests were carried out at a loading velocity of 2 mm/min, in control of the displacement, at room temperature.

2. Results and discussions

3.1 Tensile results

Figure 2 shows tensile stress-strain and energy-strain curves of 3D-printed samples. It is observed that the investigated samples fracture both at different levels of stresses and strains (Figure 2a). The curves do not show a settlement zone, the linear-elastic zone starting from the beginning of the stress-strain curves. However, the slope of stress-strain curves differs significantly with the material type, with the exception of PLA and PLA+CF samples where almost overlapping slopes are obtained. The most brittle behavior is presented by the PLA+CF samples, and the most ductile by the non-reinforced PLA samples. The other two categories of samples are found between the two behaviors, the first (PLA+GF) showing a quasi-brittle tendency to fracture, and the second (PLA+BP) a slightly ductile one. The PLA samples are the only ones that show a yield zone after reaching the maximum stress, the other samples fracture brittle immediately after the maximum point.

Figure 2b shows major differences between the types of material tested in terms of the capacity of the samples to absorb energy until fracture. It can be seen that the samples show different variations of the energy with the strain, especially in the amplitude of the curves. The only similarity is found between the PLA and PLA+CF samples, which show more than half an overlap of the curves. However, the maximum level of fracture energy is in favor of PLA samples. Like the stress-strain curves, the samples from PLA+GF and PLA+BP show a lower energy-strain curve behavior than the other two materials (PLA and PLA+CF).

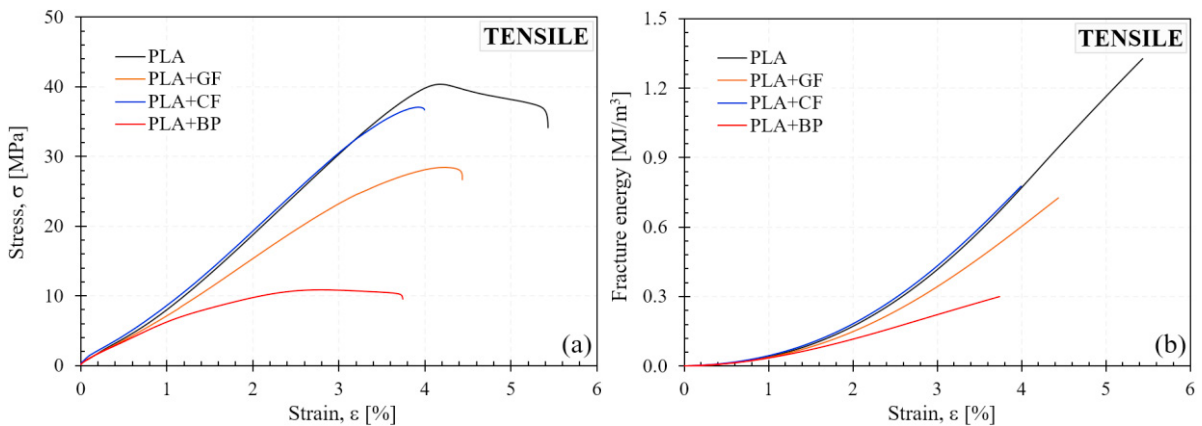


Fig. 2. Tensile stress-strain (a) and energy-strain (b) curves of printed samples

From both Figure 2a and Figure 3a, it can be easily seen that the PLA samples have the best strength properties. These are followed in order by the PLA+CF, PLA+GF and PLA+BP samples. The percentage difference between the first two materials (PLA and PLA+CF) is 21.6%, and between the extremes (PLA and PLA+BP) is 72.8%. The closest results are found between the PLA+GF and PLA+CF samples, obtaining differences of only 14.7%. Stress at break is slightly lower than tensile strength, the only exceptions being registered in the case of PLA and PLA+BP samples where differences of around 9%, respectively 25% are obtained. The other two materials show differences between the two strength properties (tensile strength and stress at break) of 3.3% (PLA+GF) and 1.6% (PLA+CF).

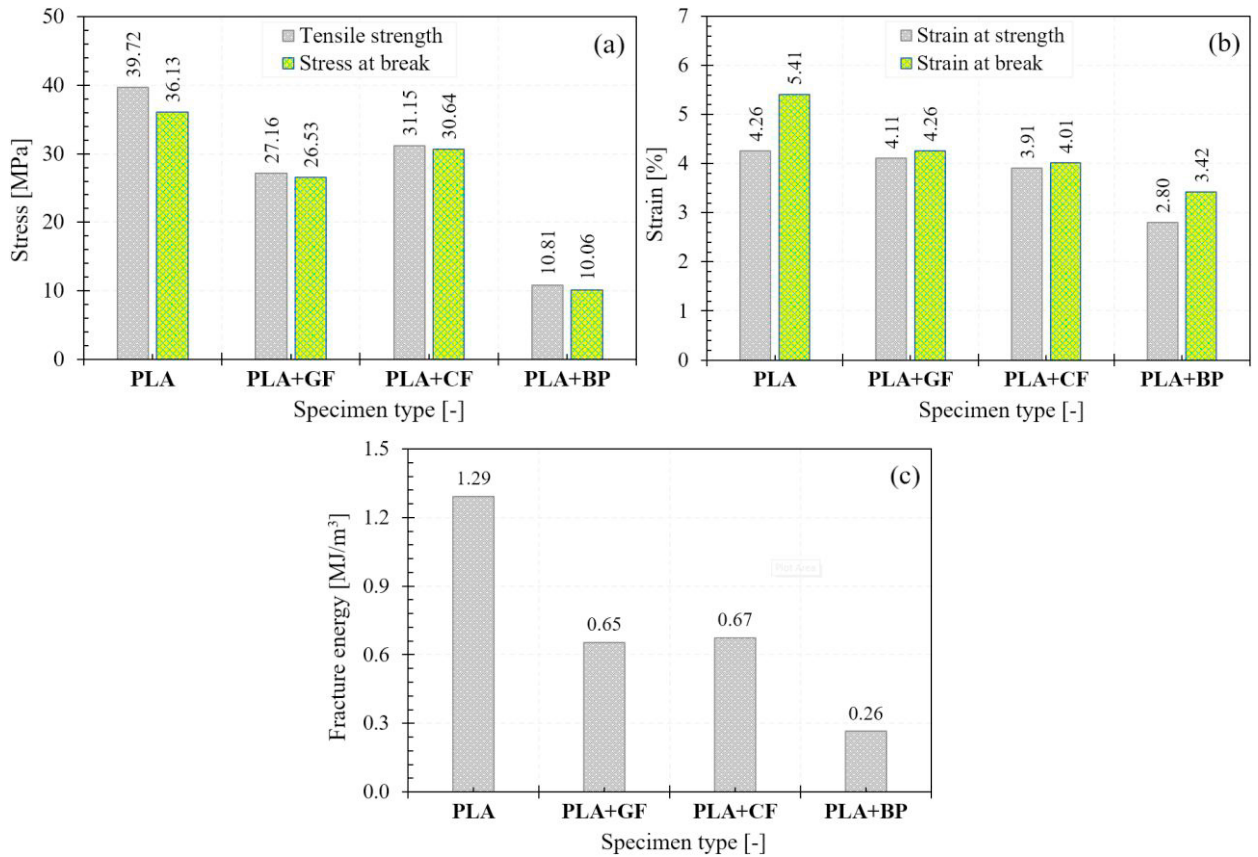


Fig. 3. The variation of strength (a), strain (b) and energy (c) properties with the filament type

Figure 3b shows that strain at strength extremes (maximum and minimum values) are represented, such tensile strength, also by the PLA (5.41%) and PLA+BP (3.42%) samples. In this case, differences of over 36% were obtained between PLA and PLA+BP. The same two materials show the biggest difference between strain at strength and strain at break (27.0% for PLA and 22.2% for PLA+BP). At the opposite pole, differences below 3.5% are obtained for PLA+GF and PLA+CF samples. Considering that the fracture energy is given by the area under the stress-strain curves, the PLA samples show significantly higher values than the other configurations. More precisely, PLA absorbs up to 47.9% more energy than the sample in second place and 79.5% more than the sample in last place. The PLA+GF and PLA+CF samples absorb approximately the same amount of energy, the values being slightly favorable (3%) for the PLA+CF material.

From tensile results, a clear domination of pure PLA properties is observed. The fillers prove to decrease consistently the mechanical strength and dramatically the fracture energy. This effect can be put on the discontinuity created in the PLA matrix, induced by the presence of the filler material. The bond between the filler fiber/particle and the matrix seems to be weaker than the bond inside the polymeric matrix. Also, it can be observed that carbon and glass fillers, which are in almost the same percentage in the mixture, produce similar property loss comparing to pure PLA. Also, the bronze filler in a much higher percentage is further decreasing the properties in a significant manner.

3.2 Flexural results

From Figure 4a it can be seen that the flexural stress-strain of printed samples shows a very different behavior depending on the type of filament used. All the curves show a linear-elastic zone, followed by the yield of the material and finally its fracture. The samples from PLA+BP show a settlement zone (up to around 0.4% strain), while the other types of configurations (PLA, PLA+GF and PLA+CF) do not highlight such a zone. It seems that the low stiffness of the samples induces this rather obvious and pronounced area. Moreover, the PLA+BP samples also present the shortest linear-elastic region, at the opposite pole are the PLA+CF samples with the most extensive area. Regarding the fracture zone, the samples from PLA+CF show a quasi-brittle behavior, the other samples a ductile behavior. In this sense, due to the lack of filament reinforcements and the defects induced by them (gaps or cracks in the matrix), the samples made of unreinforced PLA show a pronounced deformation until fracture. The presence of reinforcements (GF, CF and BP) in the polymer matrix considerably accelerates the fracture of the samples at low levels of strains. Significant differences between the four types of samples are also observed in the flexural energy absorption-strain curves (Figure 4b). Due to the pronounced plastic deformation (Figure 4a), unreinforced PLA samples absorb the largest amount of energy. The PLA+BP samples are identified at the opposite pole. It was found that in the area of small deformations, below 1%, the curves almost overlap.

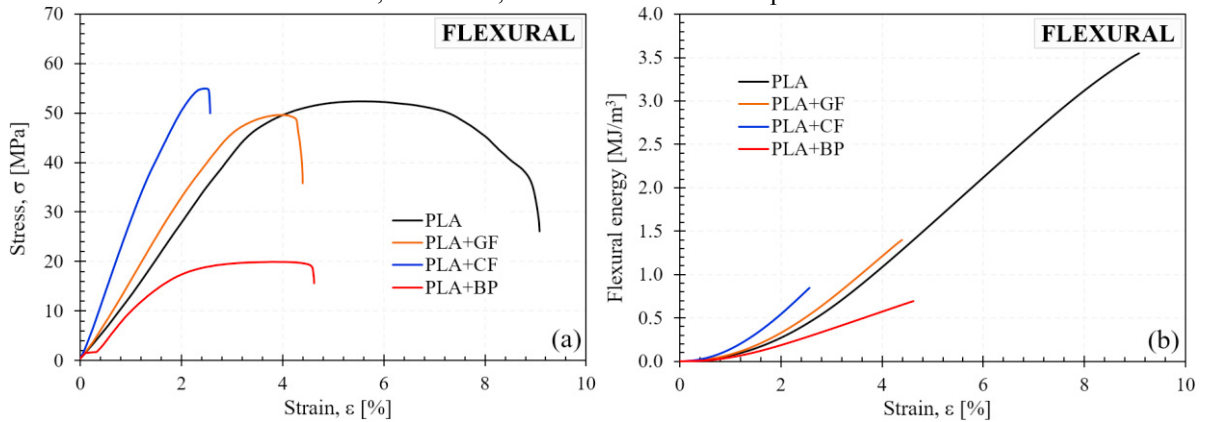


Fig. 4. Flexural stress-strain (a) and energy-strain (b) curves of printed samples

The highest flexural modulus values are recorded for the PLA+CF samples, and the lowest for the PLA+BP samples (Figure 5a). Thus, in this case differences of over 56% are obtained between the two types of samples. Smaller but still considerable differences are also obtained between the first and second material. Thus, PLA+CF shows flexural modulus values over 43% higher than PLA+GF. Between PLA+GF and PLA samples, the difference is only 10% in favor of PLA+GF. The CFs in the matrix provide stiffness to the sample when this is loaded perpendicular to the direction of deposition. The CFs are relatively longer and stiffer than GFs and therefore the elastic properties are superior for this filler.

The strength properties follow somewhat the same pattern as the elastic ones, with the observation that in this case the order of stress values is reversed between the PLA+GF and PLA samples (Figure 5b). This time, the differences between the first three materials are much smaller than in the case of flexural modulus. Thus, differences in terms of flexural strength of 5.9% are obtained between PLA+CF and PLA samples, respectively of 10.6% between PLA+CF and PLA+GF. Also, the PLA samples reinforced with BPs show the lowest flexural strength values, over 64% lower than the PLA+CF samples. Due to the different fracture mode (quasi-brittle or ductile), the biggest differences between flexural strength and stress at break are obtained for PLA samples (50.2%), and the smallest differences for PLA+CF samples (4.7%).

The high values of the elastic properties (flexural modulus) and strength (flexural strength and stress at break) of the PLA+CF samples are replaced by low values of the strain properties (Figure 5c). In this case, the PLA samples show the highest strain at strength, followed in order by the PLA+GF, PLA+BP and finally PLA+CF samples. The biggest difference is obtained between PLA and PLA+CF samples (53.7%), and the smallest between PLA+GF and PLA+BP (5.5%). As for the size of the values, strain at break largely follows the same order as strain at strength, the PLA samples showing the highest value, respectively PLA+CF the lowest.

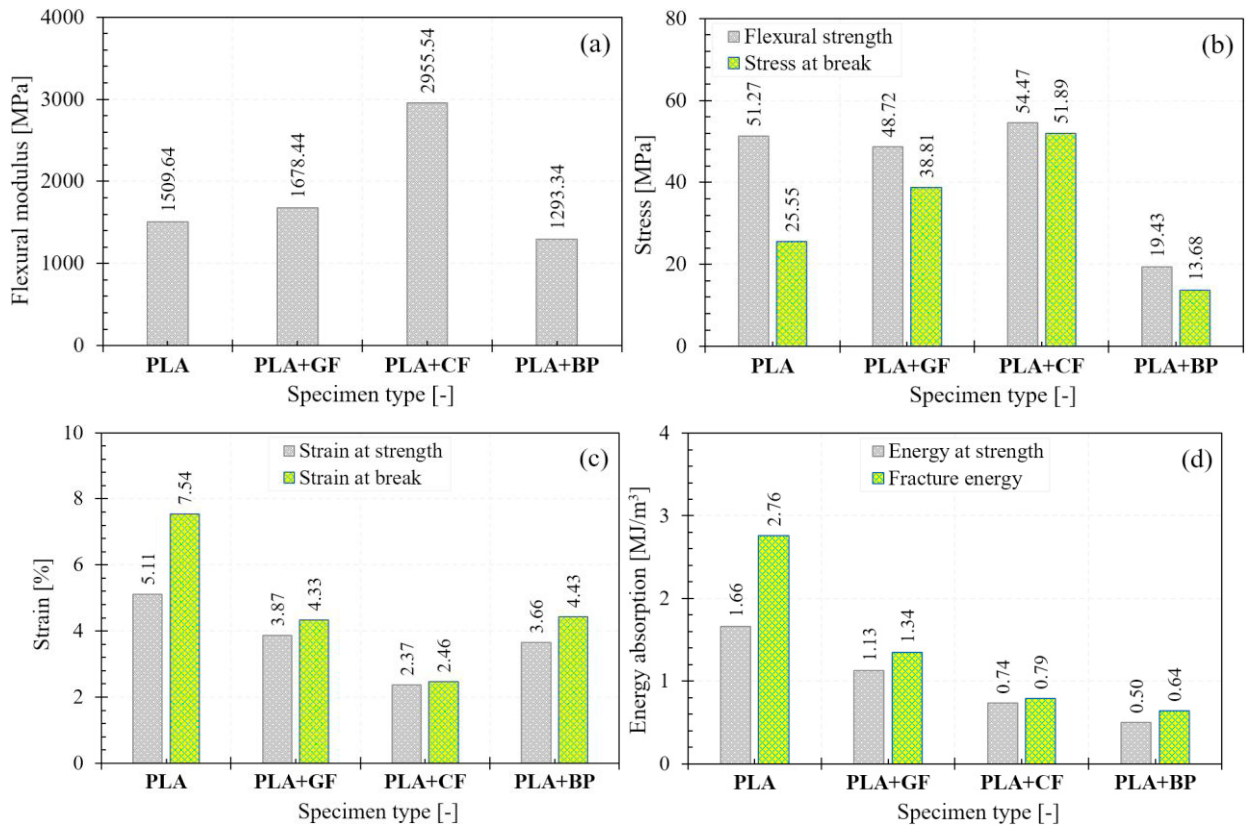


Fig. 5. The variation of flexural modulus (a), strength (b), strain (c) and energy (d) properties with the type of sample

Due to the extension of the stress-strain curve (see Figure 4a), and also the area under this curve, the unreinforced PLA samples show the highest fracture energy (2.76 MJ/m³, Figure 5d). The lowest energy values are identified for the PLA+BP samples, where decreases of up to 77% are recorded compared to the PLA samples. Between the two types, there are PLA+GF and PLA+CF samples with fracture energy values of 1.34 and 0.79 MJ/m³, respectively. Energy at strength shows a pattern similar to fracture energy, obtaining differences of 70% between the extreme values. The biggest differences between fracture energy and energy at strength are found for PLA samples (39.8%), and the smallest in the case of PLA+CF samples (6.5%). This aspect is given by the ductile behavior (PLA), respectively quasi-brittle (PLA+CF) of the matrix of the investigated samples.

3. Conclusions

The paper investigates the mechanical behavior of pure and reinforced PLA samples. For this purpose, the pure PLA and PLA reinforced with glass fibers (PLA+GF), carbon fibers (PLA+CF) and bronze particles (PLA+BP) were tested in tensile and three-point bending. After analyzing the results, the following can be concluded:

- the best strength properties are given by the pure PLA in tensile and PLA+CF in bending.
- the largest strains, both in tension and in bending, are found for the pure PLA, which prove to be more ductile.
- due to the quasi-brittle matrix, the PLA+CF material presents the highest stiffness.
- in both tensile and bending, pure PLA possess the highest fracture energy, due to its ductility manifested by an extension of the plastic zone until fracture.

Therefore, the choice of the material type (unreinforced or reinforced) is important to be made in accordance to the functional loading conditions.

Acknowledgements

This paper was financially supported by the Project “Network of excellence in applied research and innovation for doctoral and postdoctoral programs / InoHubDoc”, project cofounded by the European Social Fund financing agreement no. POCU/993/6/13/153437.

References

- [1] DI Stoia, L Marşavina, E Linul, Correlations between process parameters and outcome properties of Laser-Sintered Polyamide, *Polymers* 11 (11), 2019, 1850.
- [2] DA Şerban, AV Coşa, G Belgiu, R Negru, Failure Locus of an ABS-Based Compound Manufactured through Photopolymerization, *Polymers* 14 (18), 2022, 3822.
- [3] DI Stoia, L Marsavina, E Linul, Mode I fracture toughness of polyamide and alumide samples obtained by selective laser sintering additive process, *Polymers* 12 (3), 2020, 640.
- [4] L Marşavina, C Vălean, M Mărghitaş, et al., Effect of the manufacturing parameters on the tensile and fracture properties of FDM 3D-printed PLA specimens, *Engineering Fracture Mechanics* 274, 2022, 108766.
- [5] CF Popa, T Krausz, SV Galatanu, et al., Numerical and experimental study for FDM printed specimens from PLA under IZOD impact tests, *Materials Today: Proceedings* 78, 2023, 326-330.
- [6] DI Stoia, L Marsavina, E Linul, Mode I critical energy release rate of additively manufactured polyamide samples, *Theoretical and Applied Fracture Mechanics* 114, 2021, 102968.
- [7] C Vălean, L Marşavina, M Mărghitaş, et al., The effect of crack insertion for FDM printed PLA materials on Mode I and Mode II fracture toughness, *Procedia Structural Integrity* 28, 2020, 1134-1139.
- [8] LM Cali, G Pascoletti, M Gaeta, G Milazzo, R Ambu, New filaments with natural fillers for FDM 3D printing and their applications in biomedical field, *Procedia Manufacturing*, Volume 51, 2020, Pages 698-703.
- [9] DV Lohar, AM Nikalje, PG Damle, Development and testing of hybrid green polymer composite (HGPC) filaments of PLA reinforced with waste bio fillers, *Materials Today: Proceedings*, Volume 62, Part 2, 2022, Pages 818-824.
- [10] MP Ho, KT Lau, H Wang, D Hui, Improvement on the Properties of Polylactic Acid (PLA) using Bamboo Charcoal Particles, *Composites Part B* (2015), doi: 10.1016/j.compositesb.2015.05.048.
- [11] MM Zerankeshi, SS Sayedain, M Tavangarifard, R Alizadeh, Developing a novel technique for the fabrication of PLA-graphite composite filaments using FDM 3D printing process, *Ceramics International*, Volume 48, Issue 21, 2022, Pages 31850-31858
- [12] A Smirmov, P Peretyagin, N Nikitin, Assessment Effect of Nanometer-Sized Al₂O₃ Fillers in Polylactide on Fracture Probability of Filament and 3D Printed Samples by FDM. *Materials* 2023, 16, 1671.
- [13] E Mackiewicz, T Wejrzanowski, B Adamczyk-Cieślak, GJ Oliver, Polymer–Nickel Composite Filaments for 3D Printing of Open Porous Materials. *Materials* 2022, 15, 1360.
- [14] AJ Arockiam, K Subramanian, RG Padmanabhan, R Selvaraj, DK Bagal, S Rajesh, A review on PLA with different fillers used as a filament in 3D printing. *Materials Today: Proceedings*, Volume 50, Part 5, 2022, Pages 2057-2064.
- [15] Web site: <https://filament2print.com/gb/>, accessed on 20.10.2023
- [16] ISO 527-1:2019, *Plastics — Determination of tensile properties — Part 1: General principles*, 2019.
- [17] ASTM D790-17, *Standard Test Methods for Flexural Properties of Unreinforced and Reinforced Plastics and Electrical Insulating Materials*, 2017.



Structural Integrity and Reliability of Advanced Materials obtained through Additive Manufacturing (SIRAMM23)

Effect of Post-processing Techniques on the Surface Roughness of Laser Powder Bed Fusion Processed AlSi12 Alloy

Sai Kumar Balla^a, Manjaiah Mallaiah^{a,*}, Anand Kumar Subramaniyan^b

^aAdditive Manufacturing Laboratory, Department of Mechanical Engineering, National Institute of Technology, Warangal – 506004, India

^bAdditive Manufacturing Research Laboratory, Department of Mechanical Engineering, Indian Institute of Technology, Jammu – 181221, India

Abstract

The Additive manufacturing (AM) process, especially laser powder fusion (LPBF), could print complex medical implants directly from computer-aided design (CAD) data. LPBF offers numerous benefits compared to traditional methods, such as efficient customized product development, complex shape creation, and lighter components that save time and costs. AM also have some challenges that are usually addressed, such as poor surface quality, physical properties, residual stresses and fatigue. These challenges prevent AM parts from being used in real-life applications. Surface roughness is a significant issue in many forms of additive manufacturing because of the layer-by-layer deposition process. This study aims to understand better the roughness generated during the laser powder bed fusion process. In LPBF, metal powders are melted by a focused laser beam to create each component layer. Despite its ability to produce fine details using a variety of metal powders, LPBF is one of the most widely used metal AM processes across various industries, including the automobile, aerospace, and medical fields. However, there are complex physical phenomena in LPBF that contribute to roughness. This study seeks to understand LPBF and explore post-processing techniques to improve the surface roughness of additively manufactured parts. The processing techniques, including traditional machining, wire electro-discharge machining, chemical anodizing, abrasive flow finishing and laser polishing, are customarily applied to resolve these issues. This study has complied with various post-processing techniques and their implementation. The effects of different post-processing techniques on additive-manufactured Al12Si are discussed in detail. Micro-milling significantly reduces surface irregularity topography, peaks and roughness. Micro-milling reduced average surface roughness (S_a) by up to 99% and a minimal increase in surface hardness compared to WEDMed, chemical anodizing, sandblasting, and as-printed parts. The study found that micro-milling is a promising approach for finishing complex metallic additively manufactured parts with minimal complexity.

© 2023 The Authors. Published by Elsevier B.V.

This is an open access article under the CC BY-NC-ND license (<https://creativecommons.org/licenses/by-nc-nd/4.0>)

Peer-review under responsibility of the SIRAMM23 organizers

* Corresponding author. Tel.: +91-9740847669;

E-mail address: Manjaiah.m@nitw.ac.in

Keywords: Laser powder bed fusion; Sand blasting; Chemical anodizing; Wire EDM; Micro milling, Surface roughness

1. Introduction

Additive manufacturing (AM), also known as 3D printing, is a revolutionary technology that has transformed how we design and produce objects (Diegel et al., 2019). This process allows for creation of complex geometries and unique shapes that are difficult to produce using traditional manufacturing methods. Additive manufacturing has entered many industries, including aerospace, medical, and automotive. The laser powder bed fusion (LPBF) process is one of the most promising metal AM processes, which offers a more efficient and cost-effective solution for producing complex geometries. LPBF uses a high-powered laser to selectively melt and fuse metal powders layer by layer to create a solid object. It allows for creating intricate designs with high accuracy, reducing the amount of material wasted in the production process (Thompson et al., 2016). Aluminium alloys are a popular material for additive manufacturing using LPBF because of their unique properties i.e., they are lightweight, have high strength, and exhibit excellent corrosion resistance. AlSi12 is a eutectic alloy with a small difference in melting and solidification temperatures, resulting in excellent thermal properties and good thermal resistance (Suzuki et al., 2021). AlSi12 is an ideal material for joining metal pieces together, such as welding and extrusion processes. The applications include fabricating thin-walled parts such as heat exchangers (Siddique et al., 2015) and other industrial-grade prototypes. Evidently, LPBF processed AlSi12 alloys reveals better strength than Evidently, LPBF processed AlSi12 alloys reveal better strength than conventionally manufactured alloys because solute Si in supersaturated solid solution inhibits work hardening strength (Takata et al., 2020). LPBF provides a better opportunity to fabricate these eutectic alloys even complicated shapes, with ease, but the surface quality is still a concern. Surface roughness in additively manufactured components is higher than conventionally manufactured components due to the staircasing effect formed by layer-by-layer manufacturing and partially melted particles. The surface roughness of the as-built components by the LPBF process is approximately 10-28 μm (Li et al., 2018; Spierings et al., 2011). Surface roughness is notably important and requires a smooth surface to eliminate premature failure from cracking in many applications. Surface roughness is an important factor for initiating fatigue failure, especially in LPBF processed components (Teimouri et al., 2022) and parts with poor surface quality effects the fatigue performance. To improve the surface quality, LPBF-processed alloys are subjected to various methods like process parameters optimization, adopting post-processing techniques such as polishing, machining, shot peening, sandblasting etc. Some authors have attempted to reduce the surface roughness by optimizing the process parameters such as laser power, scanning speed, hatch spacing, layer thickness, and scanning strategy (Cao et al., 2021; Liu et al., 2019). The other method to improve the surface quality of LPBF processed components is by adopting post-processing techniques. Subramaniyan et al. have reduced the surface roughness of LPBF processed AlSi10Mg alloy by endorsing shot peening and with different heat treatments. They concluded that shot peening helps reduce surface roughness by 50% compared to as-built samples (Kumar et al., 2021). Lesyk et al. investigated the effect of shot peening on the surface quality of In718 alloy fabricated by the LPBF process (Lesyk et al., 2021), and it was concluded that shot peening helps in reducing surface roughness by approximately 48% due to new wavy surface formation due to severe plastic deformation. Further, another interesting study on pulsed electro-polishing of In718 alloy showed beneficial effects (Shrivastava et al., 2021). Polishing more reduces surface roughness compared to shot peening and shot blasting for AlSi10Mg alloy processed by LPBF (Sagbas et al., 2021). Since polishing is a material removal technique from the final component whereas shot peening is a cold plastic deformation process which produces compressive stresses resulting in plastic deformation which improves the surface quality and texture. Kaynak and Tascioglu tried to describe finish machining as an effective post-processing technique to reduce the surface roughness of LPBF-produced Inconel 718 alloy and achieved a reduction of 92% in surface roughness compared with as-built conditions (Kaynak & Tascioglu, 2023). Campos et al. investigated the effect of micro milling on the surface roughness of LPBF processed Ti6Al4V, producing better surface compared to initial conditions (de Oliveira Campos et al., 2020). Better surface quality is produced due to micro milling, lower ductility, and elevated hardness leads to less plastic flow during cutting. Varghese and Mujumdar studied the micro-milled surface roughness and forces acting on surface during machining on LPBF processed Ti6Al4V alloy and concluded that surface roughness increased by increasing depth of cut due to increase in shear forces and chip

loading on the surface (Varghese & Mujumdar, 2021). It is evident from the literature that, most of researchers have worked on implementation of shot peening as post processing technique for improving the surface quality of LPBF processed components and limited work has been conducted on other post processing methods. As stated earlier, there is a need for improving the surface quality of LPBF processed components. The present study focused on effect of different post processing techniques on surface quality of LPBF processed AlSi12 alloy and evaluated the surface roughness of the AlSi12 alloy by comparing it with as-built conditions.

2. Experimentation

2.1. LPBF process

AlSi12 alloy samples are fabricated using a DMP Flex 100 LPBF (3D Systems, USA) machine which uses a 100 W optical fibre laser with a build volume of $100 \times 100 \times 30 \text{ mm}^3$. The powder size of $5\text{--}45 \text{ }\mu\text{m}$ with good flowability used to fabricate the cubes with dimensions $10 \times 10 \times 10 \text{ mm}^3$ as designed are shown in Fig. 1 (a) and manufactured using the LPBF process. The laser interaction with powder particles during the fabrication is shown in Fig. 1 (b) The AlSi12 samples are fabricated using optimal conditions and process parameters used are laser power of 90 W, layer thickness of $30 \text{ }\mu\text{m}$, scanning speed of 600 mm/s, hatch spacing of 0.06 mm with hexagonal scanning strategy. The samples are fabricated in an inert atmosphere with an oxygen content of less than 1000 ppm to prevent them from oxidation during fabrication. The manufactured samples are kept for cooling in the manufacturing chamber at room temperature and samples are cleaned using the vacuum cleaner to remove any unwanted particles from the substrate and sample surfaces.

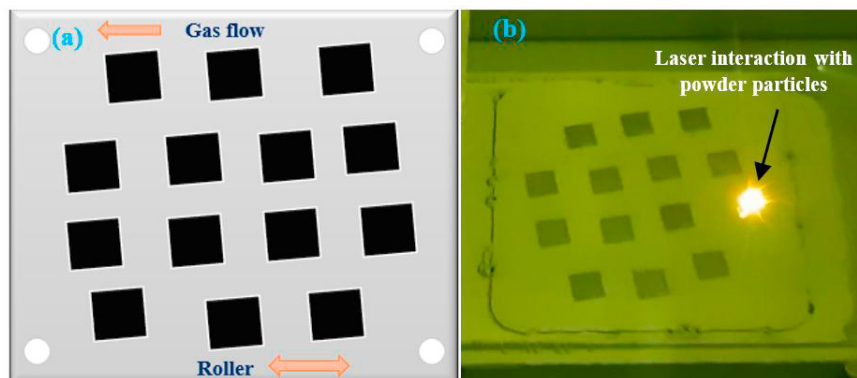


Fig. 1. (a) Designed samples in build volume; (b) Fabrication chamber of LPBF machine

2.2. Post-processing

Four post-processing operations such as sand blasting, chemical anodizing, wire electric discharge machining (Wire-EDM) and micro milling are performed on the samples to obtain different surface features as shown in Fig. 2. Sandblasting on AlSi12 alloy samples performed to remove the loosely bounded powder particles. A nozzle diameter of 6 mm and 100–120 μm stand-off distance is maintained between the samples and nozzle to ensure uniform distribution of sand particles by maintaining 6 psi pressure for sandblasting. Chemical anodizing is performed on the AlSi12 alloy surface to lay off the outer layer. 10% vol of 40% concentrated H_2SO_4 solution with distilled water is used for chemical anodizing by supplying 5 V voltage and 2.5 A current. Wire-EDM is one of the dominant unconventional machining processes and it helps remove the surface to improve the surface quality of additively manufactured components. Wire-EDM is performed with Electronica Ezeewin ES500 for different process combinations like pulse on time (T_{on}) 30,60 μSec , pulse off time (T_{off}) 3 μSec and peak current (IP) of 3,6 mA on different surfaces of the AlSi12 alloy. Also, LPBF processed AlSi12 alloy samples are machined using micro milling (DT-100i, Mikrottools Pte. Ltd., Singapore) to reduce the surface roughness from as-built condition and high spindle micro milling with spindle speed of 14000 rpm, and 20 mm feed per minute with 100 μm depth of cut used.

Tungsten carbide coated with an 8 mm diameter tool helped in removing the outer surface from the AlSi12 specimen.

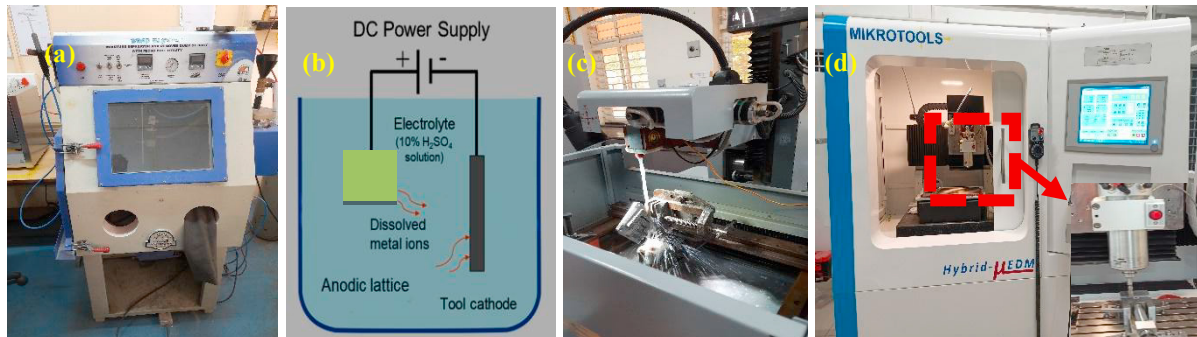


Fig. 2. Different post processing techniques adopted (a) sand blasting (b) chemical anodizing (c) wire-EDM and (d) micro milling

2.3. Surface roughness

Surface roughness was measured for as-built and post-processed AlSi12 alloy samples using a non-contact optical profilometer (Olympus DSX1000) as shown in Fig. 3. The profilometer utilizes the principles of optical light interference to scan and the surface features of the samples are calculated. Instead of using a diamond-tipped probe, optical profilometry employs light to find surface abnormalities. Using this non-contact method, a three-dimensional surface measurement is obtained. However, just like a contact stylus profilometer, all optical profilometers can display two-dimensional surface outputs. Optical profilometer provided better results with high accuracy, measuring small features than contact profilometers. In contact profilometers, the stylus is getting contact with the surface, and there are chances for surface damage, which is eliminated with non-contact optical profilometers. Roughness is calculated for scanning area of 1 mm² on the surface for all the samples and measurements were taken at 3 different locations and average is noted.



Fig. 3. Olympus DSX1000 microscope used for surface roughness measurement

3. Results and discussion

When assessing topography characteristics, surface roughness is a crucial component of surface integrity. The surface roughness (S_a) for different post processed conditions is evaluated and tabulated in Table 1 and the surface morphology is shown in Fig. 4.

Table 1. Surface average roughness (S_a) and their post-processing conditions

Condition	As-printed	Sand blasted	Chemical anodizing	Wire EDM	Micro milled
-----------	------------	--------------	--------------------	----------	--------------

S_a (μm)	22.74	9.05	11.25	3.98	0.256
-------------------------	-------	------	-------	------	-------

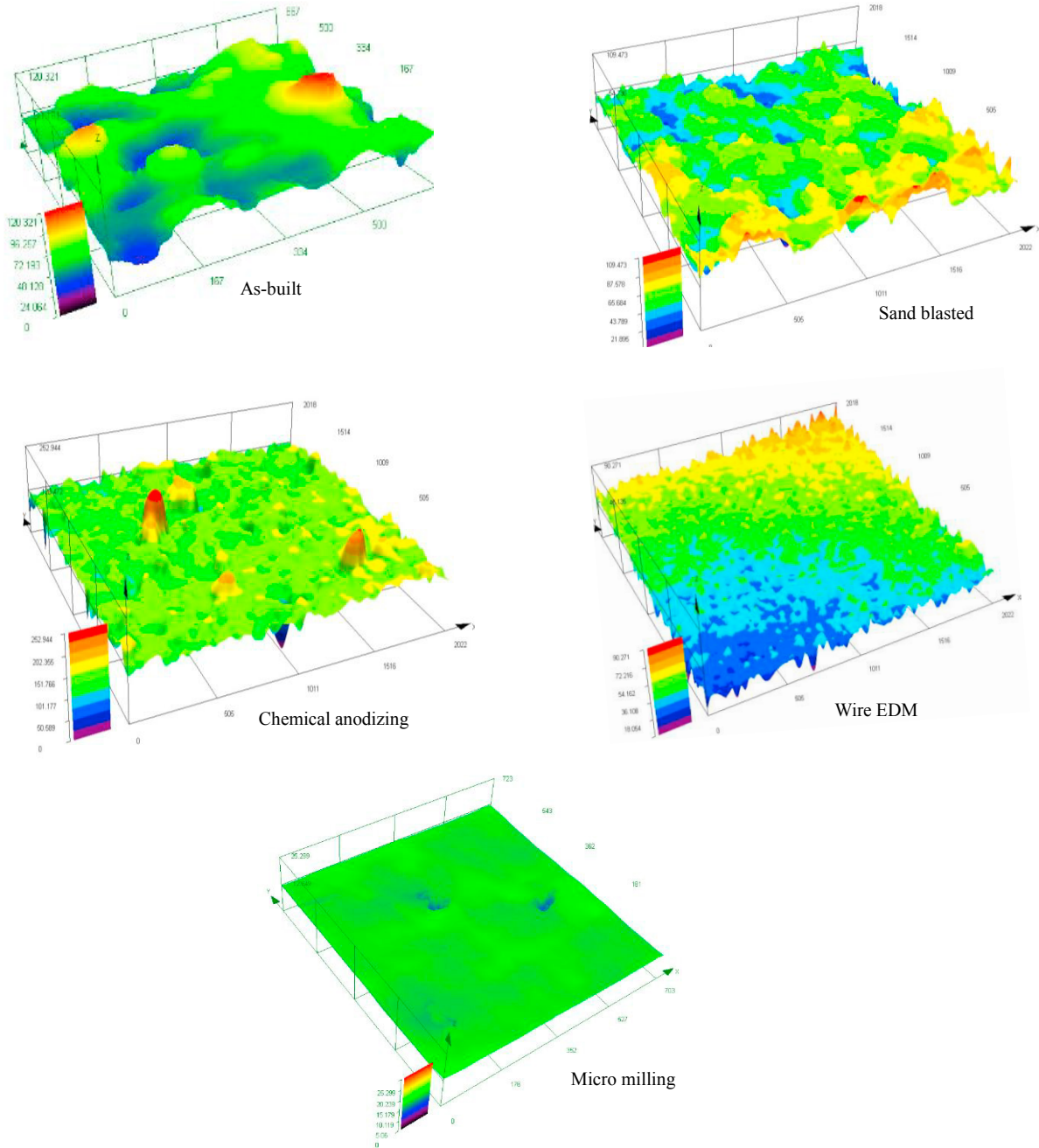


Fig. 4. 3D surface topography images of adopted post processing techniques compared with as-built AISi12 samples

3D topography of the post processed surfaces is compared with as-built surface condition and it clearly indicates in decreasing the surface roughness by reducing peak heights. In sandblasting, the sand bead particles are forced on

the surface using compressed air to smooth, clean, and remove contaminants from the rough surface. It helps in removing loosely bound unwanted particles and materials from the surface. Anodizing is an electrochemical process that creates a protective oxide layer on the surface of aluminum alloys. The oxide layer can improve the surface properties of aluminum, including its durability, corrosion resistance, and aesthetic appearance. This oxide layer can reduce surface roughness by filling in small surface defects and smoothing out the surface. Wire EDM can improve the surface roughness of aluminium alloys fabricated by LPBF by removing any excess material, such as support structures or surface irregularities, that may be present on the part after the fabrication process. This process can also help create fine features and details on the part's surface that may be difficult or impossible to achieve using the LPBF process alone. Table 1 shows that the maximum surface roughness of 22.74 μm has resulted in as-built samples, which is not applicable in industrial applications. This can be reduced to 9.05 μm and 11.25 μm using post-processing conditions sand blasting and chemical anodizing respectively. These two conditions help remove unwanted particles from the surface, which reduce the surface roughness but not effectively. The sand beads in sand blasting remove the unmelted and unbound particles from the surface and chances of producing pores, which doesn't completely eliminate the surface roughness. But in Wire EDM, the outer surface is chipped off using minimal diameter wire using optimal parameters to improve the surface quality of fabricated samples. Wire EDM offers better surface finish than other non-conventional machining processes even though machining efficiency is lower. The surface integrity is mainly affected by discharge energy, which combines pulse on time and power (Abhilash & Chakradhar, 2022). The higher discharge energy forms irregular craters due to large sparks which produce rough surface. Lower discharge energy helps create surface quality due to fewer craters and a lower surface finish is obtained using a T_{on} of 30 μSec .

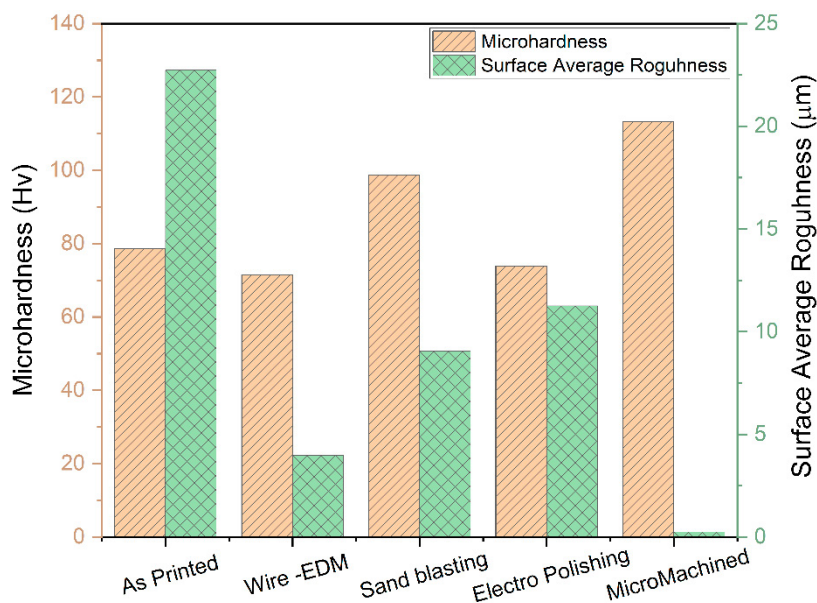


Fig. 5. Comparison of microhardness and surface roughness of post processed samples with as-built AlSi12 samples

And finally, micro milling is performed on LPBF fabricated AlSi12 alloy samples using different process parameters and observed the surface quality produced. We observed that, surface roughness is reduced with increasing spindle speed up to a certain limit and then starts increased. This is because higher spindle speed allows higher cutting speeds, resulting in smoother cuts and reduced tool marks on the surface. Increasing spindle speed beyond certain limits can generate more heat during cutting and causes material to soften or melt, increasing the surface roughness. By observing these different conditions in wire EDM as well as micro milling, the optimal condition results are reported and surface topography of better machined surface is represented in Fig. 4. and it is concluded that micro milling helps in producing better surface quality of additively manufactured AlSi12

components followed by wire EDM. Maximum peaks and valleys are observed in as-built and chemical anodizing conditions, which is unacceptable in applications. A completely smoother surface is obtained using micro milling and surface roughness of $0.256 \mu\text{m}$ is achieved successfully. Post processing helps reduce surface roughness in all conditions and reduced by 60%, 50%, 82.5% and 98.8% in sand blasting, chemical anodizing, wire-EDM and micro milling, respectively compared with as-built samples. The microhardness and surface roughness of post processed samples are compared with as-built condition for AlSi12 alloy and represented in Fig. 5. It is observed that, microhardness had increased for micro-milling and sand blasting conditions where as it had been reduced with wire-EDM and electropolishing compared to as-built AlSi12 samples. For micro milled samples, microhardness increased due to work hardening on the milled surface where as in sand blasted also helps slightly increase the microhardness of the AlSi12 alloy in the treated area due to work hardening caused by the mechanical impact of the abrasive particles. Electropolishing reduces the microhardness of the AlSi12 alloy in the treated area. This is because it selectively removes material from the surface and can remove work-hardened layers generated during prior machining or mechanical treatment and wire-EDM tends to induce localized heat-affected zones, potentially reducing microhardness.

4. Conclusions

In this experimental work, AlSi12 alloy samples are successfully fabricated using LPBF process and adopted different post-processing techniques on the surfaces to improve the surface quality of samples. The surface roughness is measured for all post-processed samples and compared it with as-built conditions to evaluate the effect of post processing on the surface roughness of LPBF-processed AlSi12 alloy components and it was concluded that:

- Post processing techniques like sand blasting, chemical anodizing, micro milling and wire EDM can be used even to improve the surface quality of AlSi12 alloy with minute features.
- Micro-milling s average surface roughness (S_a) is reduced by up to 98.8% and increased microhardness from 78.64 HV to 113.2 HV compared to as-built conditions.
- Micro-milling is a promising approach for finishing complex metallic additively manufactured parts with minimal complexity, followed by wire EDM.

References

- Abhilash, P. M., & Chakradhar, D. (2022). Effect of wire material and discharge energy on productivity and surface integrity of WEDM-processed Inconel 718. *Advances in Materials and Processing Technologies*, 8(4), 4698–4719. <https://doi.org/10.1080/2374068X.2022.2079590>
- Cao, L., Li, J., Hu, J., Liu, H., Wu, Y., & Zhou, Q. (2021). Optimization of surface roughness and dimensional accuracy in LPBF additive manufacturing Build platform. *Optics and Laser Technology*, 142(May), 107246. <https://doi.org/10.1016/j.optlastec.2021.107246>
- de Oliveira Campos, F., Araujo, A. C., Jardini Munhoz, A. L., & Kapoor, S. G. (2020). The influence of additive manufacturing on the micromilling machinability of Ti6Al4V: A comparison of SLM and commercial workpieces. *Journal of Manufacturing Processes*, 60(February 2019), 299–307. <https://doi.org/10.1016/j.jmapro.2020.10.006>
- Diegel, O., Nordin, A., & Motte, D. (2019). Additive Manufacturing Technologies. https://doi.org/10.1007/978-981-13-8281-9_2
- Kaynak, Y., & Tascioglu, E. (2023). Finish machining-induced surface roughness , microhardness and XRD analysis of selective laser melted Inconel 718 alloy. *Procedia CIRP*, 71(March), 500–504. <https://doi.org/10.1016/j.procir.2018.05.013>
- Kumar, A., Sudarshan, A., Mathias, S., Shrivastava, A., & Raghupatruni, P. (2021). Influence of post-processing techniques on the microstructure , properties and surface integrity of Al – Si – Mg alloy processed by laser powder bed fusion technique. *425*(August).
- Lesyk, D. A., Dzhemelskiy, V. V., Martinez, S., Mordiyuk, B. N., & Lamikiz, A. (2021). Surface Shot Peening Post-processing of Inconel 718 Alloy Parts Printed by Laser Powder Bed Fusion Additive Manufacturing. *Journal of Materials Engineering and Performance*, 30(9), 6982–6995. <https://doi.org/10.1007/s11665-021-06103-6>
- Li, B. Q., Li, Z., Bai, P., Liu, B., & Kuai, Z. (2018). Research on surface roughness of AlSi10Mg parts fabricated by laser powder bed fusion. *Metals*, 8(7), 1–10. <https://doi.org/10.3390/met8070524>
- Liu, Y., Liu, C., Liu, W., Ma, Y., Tang, S., Liang, C., Cai, Q., & Zhang, C. (2019). Optimization of parameters in laser powder deposition AlSi10Mg alloy using Taguchi method. *Optics and Laser Technology*, 111(March 2018), 470–480. <https://doi.org/10.1016/j.optlastec.2018.10.030>
- Sagbas, B., Gencelli, G., & Sever, A. (2021). Effect of Process Parameters on Tribological Properties of Ti6Al4V Surfaces Manufactured by

- Selective Laser Melting. *Journal of Materials Engineering and Performance*, 30(7), 4966–4973. <https://doi.org/10.1007/s11665-021-05573-y>
- Shrivastava, A., Anand Kumar, S., Nagesha, B. K., & Suresh, T. N. (2021). Electropolishing of Inconel 718 manufactured by laser powder bed fusion: Effect of heat treatment on hardness, 3D surface topography and material ratio curve. *Optics and Laser Technology*, 144(August), 107448. <https://doi.org/10.1016/j.optlastec.2021.107448>
- Siddique, S., Imran, M., Wycisk, E., Emmelmann, C., & Walther, F. (2015). Influence of process-induced microstructure and imperfections on mechanical properties of AlSi12 processed by selective laser melting. *Journal of Materials Processing Tech.*, 221, 205–213. <https://doi.org/10.1016/j.jmatprotec.2015.02.023>
- Spierings, A. B., Herres, N., & Levy, G. (2011). Influence of the particle size distribution on surface quality and mechanical properties in AM steel parts. *Rapid Prototyping Journal*, 17(3), 195–202. <https://doi.org/10.1108/13552541111124770>
- Suzuki, A., Miyasaka, T., Takata, N., Kobashi, M., & Kato, M. (2021). Control of microstructural characteristics and mechanical properties of AlSi12 alloy by processing conditions of laser powder bed fusion. *Additive Manufacturing*, 48(PA), 102383. <https://doi.org/10.1016/j.addma.2021.102383>
- Takata, N., Liu, M., Kodaira, H., Suzuki, A., & Kobashi, M. (2020). Anomalous strengthening by supersaturated solid solutions of selectively laser melted Al–Si-based alloys. *Additive Manufacturing*, 33(January), 101152. <https://doi.org/10.1016/j.addma.2020.101152>
- Teimouri, R., Sohrabpoor, H., Grabowski, M., Wyszynski, D., Skoczypiec, S., & Raghavendra, R. (2022). Simulation of surface roughness evolution of additively manufactured material fabricated by laser powder bed fusion and post-processed by burnishing. *Journal of Manufacturing Processes*, 84(June), 10–27. <https://doi.org/10.1016/j.jmapro.2022.09.045>
- Thompson, M. K., Moroni, G., Vaneker, T., Fadel, G., Campbell, R. I., Gibson, I., Bernard, A., Schulz, J., Graf, P., Ahuja, B., & Martina, F. (2016). Design for Additive Manufacturing: Trends, opportunities, considerations, and constraints. *CIRP Annals - Manufacturing Technology*, 65(2), 737–760. <https://doi.org/10.1016/j.cirp.2016.05.004>
- Varghese, V., & Mujumdar, S. (2021). Micromilling-induced surface integrity of porous additive manufactured Ti6Al4V alloy. *Procedia Manufacturing*, 53(2020), 387–394. <https://doi.org/10.1016/j.promfg.2021.06.041>



International Conference on Structural Integrity and Reliability of Advanced Materials
obtained through Additive Manufacturing (SIRAMM23)

Effect of Process Parameters on Mechanical Properties in Fused Deposition Modelling of Polyethylene Terephthalate Glycol

Balichakra Mallikarjuna^{a,*}, Vasu Mallesh^{a,*}, Musunuri Shanmukha Vardhan^b, Harshini
Gopalakrishnan Vadivudaiyanayak^b, Penjuru Gnana Sri Datta^b

^aDepartment of Production Engineering, National Institute of Technology, Tiruchirappalli, Tamil Nadu 620015, India

^bDepartment of Mechanical Engineering, Amrita School of Engineering, Amrita Vishwa Vidyapeetham, Coimbatore, India

Abstract

The current study investigates the effects of various process parameters such as extrusion temperature, printing speed, and infill density on Fused Deposition Modelling (FDM) of Polyethylene Terephthalate Glycol (PETG) parts. It was found that higher tensile, flexural, and impact strengths have been observed for the samples (S4, S5, S6) having 25% infill density. The sample with 30% infill density, 245 °C extrusion temperature, and 25 mm/s print speed has been found to have the highest ultimate tensile strength of 35.46 MPa. The compression strength is directly proportional to the infill density. The impact strength of the samples (S3, S5, S6 and S7) was highest, where the print speed was 25 mm/s.

© 2023 The Authors. Published by Elsevier B.V.

This is an open access article under the CC BY-NC-ND license (<https://creativecommons.org/licenses/by-nc-nd/4.0>)

Peer-review under responsibility of the SIRAMM23 organizers

Keywords: Fused Deposition Modelling; Polyethylene Terephthalate Glycol; Process Parameter; Mechanical Properties; Spectacle Frame;

1. Introduction

Fused Deposition Modelling (FDM) is one of the material extrusion-based additive manufacturing techniques (B Mallikarjuna et al., 2023; Mallikarjuna B, 2013; Balichakra Mallikarjuna & Reutzel, 2022). The Acrylonitrile Butadiene Styrene (ABS), Polylactic Acid (PLA), High-Density Polyethylene (HDPE) and Polyethylene Terephthalate Glycol (PETG) are common filaments used in FDM for the fabrication of various components.

* Corresponding author. Vasu Mallesha, Balichakra Mallikarjuna Tel.: +91-9611604276; +91-8310405141

E-mail address: mvasu@nitt.edu, mallik@nitt.edu

PETG is one of the market's most commonly available and widely used 3D printing filaments. PETG is commonly used for bottles, food containers, the clothing industry, medical braces, electronics, and covers. The printing temperature of PETG is 200 °C to 260 °C, 260 °C being its melting point (Gebisa & Lemu, 2018; Kristiawan et al., 2021; Reddy et al., 2015). PETG has a tensile strength of 60 MPa to 67 MPa. PETG was chosen over PLA and ABS materials due to its proper heat resistance, durability, and also UV resistance. Along with these advantages, PETG is more flexible than ABS and PLA (B Mallikarjuna et al., 2023; Mohan et al., 2017). However, processing any material on FDM is influenced by various parameters (Derise & Zulkharnain, 2020; Thrimurthulu et al., 2004). These parameters include build orientation, air gap, layer resolution, extrusion temperature, bed temperature, raster angle, print speed and extrusion speed Mwema and Akinlabi, (2020). Özen et al., 2021 optimized the tensile specimen geometry and process parameters for FDM using PETG. They focused on slicer parameters in accordance with positional failures to put forth an effective measurement of mechanical properties. A newly developed printing path was utilized to eliminate excess travel lines, resulting in a more homogeneous structure on the macroscale and fewer premature failures. ISO 527-2 and ISO-Modified are suggested to perform better by tuning the slicing parameters. Kumar et al., 2021 studied the effects of infill density and annealing on the mechanical properties of PETG via the FDM process. The infill density was varied as 25%, 50%, 75% and 100%. The samples were prepared for the hardness, tensile, impact and flexural test specimens. They had an extrusion temperature of 220 °C and a bed temperature of 60 °C. The annealing in which the printed specimen was placed on a Teflon-coated baking pan, heated above 5 °C in accordance with glass transition temperature for 60 minutes, and then cooled at room temperature. Annealed PETG have 66, 77, 90 and 97 HRC of hardness; 38, 42, 47 and 52.4 MPa of tensile strength; 68, 74, 88 and 96 J/m² of impact strength; 51, 59, 65 and 70 MPa of flexural strength for 25%, 50%, 75% and 100% infill density respectively. In conclusion, higher infill density showcased better mechanical properties. Heidari-Rarani et al., 2022 investigated the process parameters that influence the FDM deposition of PLA parts. The process parameters were used, such as infill density (20%, 40%, 60%, 80%), printing speed (20 mm/s and 40 mm/s), and layer thickness (0.1 mm and 0.2 mm). The optimal process parameters under the experimental values are layer thickness of 0.1 mm, infill density of 80% and printing speed of 40 mm/s which has an ultimate tensile strength of 34.04 MPa. Similarly, for the S/N software results, the optimal process parameters were layer thickness of 0.2 mm, infill density of 80% and printing speed of 40 mm/s which has an Ultimate Tensile Strength (UTS) of 34.54 MPa. M. A. Kumar et al., 2020 studied the effects on strength and hardness of FDM due to machine parameters when for carbon fibre-reinforced PETG thermoplastics. Srinivasan et al., 2020 examined the impact of infill density in the FDM process for PETG material. The specimen's tensile strength and surface roughness were studied when the infill density varied from 20% to 100% with an increment of 10%. The range of surface roughness varies from 3.82 µm - 2.87 µm and 17.38 MPa – 32.12 MPa for tensile strength when the infill density is varied from 20% to 100%, respectively. Guessasma et al., 2019 reported influence of the extrusion temperature on the printability of PETG was analysed. Similarly, various researchers have reported on process parameter optimization in FDM deposition of PETG material (Kadhun & Al-zubaidi, 2023; Sekaran et al., 2023; Srinivasan, Nirmal Kumar, et al., 2020; Teraiya et al., 2021). The literature review identified that optimization of the process parameters considering printing speed, extrusion temperature and infill density hadn't been studied concerning the spectacle frame fabrication.

This work used FDM to fabricate various PETG (Bedi, Mallesha, Mahesh, Mahesh, & Ponnusami, 2023; Bedi, Mallesha, Mahesh, Mahesh, Mukunda, et al., 2023) test samples under different process conditions, including infill density, extrusion temperature, and print speed. Then printed samples were investigated to understand the effect of process conditions on mechanical properties such as tensile strength, compressive strength, flexural strength and impact test.

Nomenclature

FDM	:Fused Deposition Modelling
ABS	:Acrylonitrile Butadiene Styrene
PLA	:Polylactic Acid
PETG	:Polyethylene Terephthalate Glycol
UTM	:Universal Testing Machine
UTS	:Ultimate Tensile Strength

2. Methodology

2.1 Equipment and Materials

The FDM technique (3D Cubic CUB 3.5, India) was used to build the PETG samples and prototype. The process parameters used to prepare samples are shown in Table 1. PETG is a thermoplastic polyester used as a filament for printing samples. The filament spool is white transparent, and the diameter of the wire is 1.75 mm. The melting temperature of PETG is 230–250 °C. The PETG filament was procured from e-commerce.

Table 1 Process parameters used for printing

Sample Designation	Infill Density (%)	Print Temperature (°C)	Print Speed (mm/sec)
S1	20	225	20
S2	20	235	25
S3	20	245	30
S4	25	225	25
S5	25	235	30
S6	25	245	20
S7	30	225	30
S8	30	235	20
S9	30	245	25

2.2 Testing and characterization

The tensile test samples were prepared according to the ASTM 'D638' standard. This test method uses dumbbell-shaped specimens with 25 mm or 50 mm gauge lengths. The FDM-printed PETG samples' tensile test was carried out using a Uniaxial Tensile Test machine (H25KT, Tinius Olsen, 2007). The FDM-printed tensile samples are shown in Fig. 1 (a). The compression test was fabricated following the ASTM 'D695' standard, as shown in Figure 1 (b).

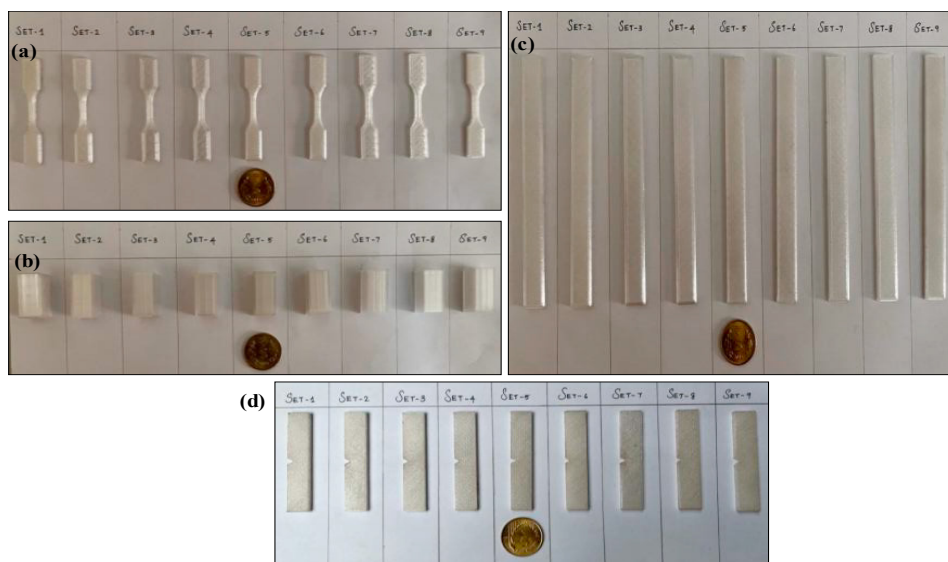


Fig. 1. FDM Printed samples of (a) tensile specimen; (b) compression specimen; (c) flexural specimen; (d) impact specimens.

The specimen is a cube with dimensions 12.7 x 12.5 x 25.4 mm³. The flexural strength of samples was built with a size of 3.2 x 12.7 x 127 mm according to ASTM D790 standard and tested in UTM-Electronic type. The printed sample's picture is shown in Fig. 1 (c). Finally, the impact sample prepared following the ASTM D256 standard is shown in Fig. 1 (d). The standard specimen dimensions are 63.5 mm x 12.7 mm with a notch of 22.5 degrees and a radius of 0.25 mm.

3. Results and discussions

3.1 Tensile Strength

The Ultimate Tensile Strength (UTS) of 9 different samples varies from 24.9 MPa to 36 MPa, as shown in Fig. 2. A least tensile strength has been noted for S1, i.e., 20%, 225 °C and 20 mm/s and the highest for S9, i.e., 30%, 245 °C and 25 mm/s. It can be observed that with an increase in infill density, there is an increase in ultimate tensile strength. S1, S2 and S3 have the least infill density of 20% and display the least UTS compared to the other 6 specimens. The same trend can be noted for the other two process parameters. The difference in the UTS is minimal in S4 and S9; this implies that we can achieve almost similar UTS with less infill density.

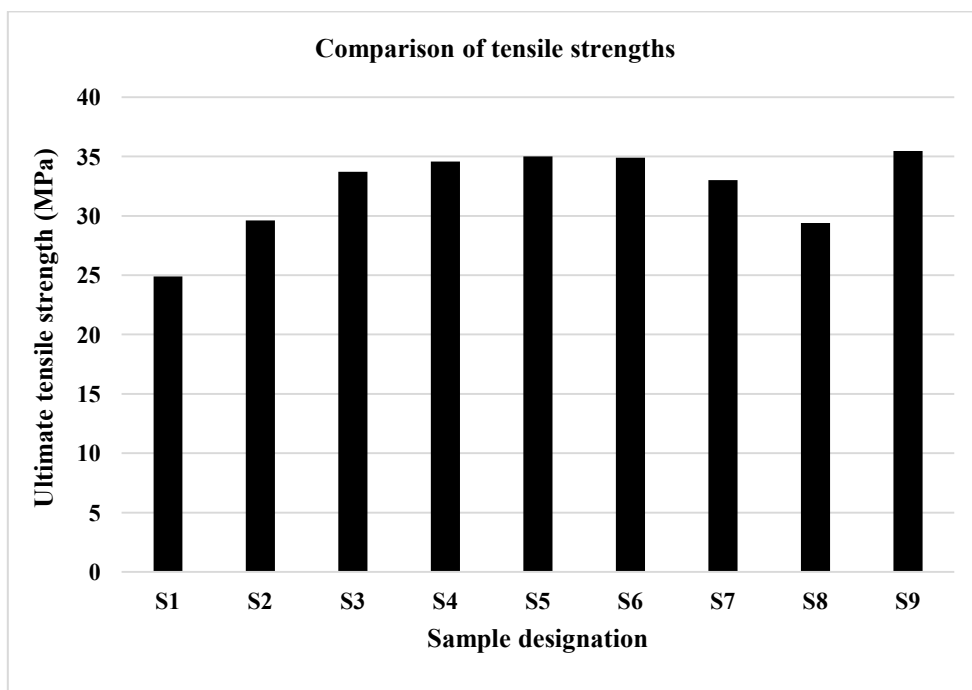


Fig. 2. Comparison of tensile strengths of various samples built under process conditions.

3.2 Flexural Strength

The flexural strength varies from 46.7 MPa to 54.8 MPa, as presented in Fig. 3. The Highest flexural strength has been observed for S8 and the least for S7, which have the same infill density of 30%. It was found that the S3, S6, and S8 have shown the highest flexural strength. Also, S4, S5, and S6 have better strength in the other two groups (S1, S2, S3 and S7, S8, and S9). It was observed that the specimen's flexural strength is more than tensile strength.

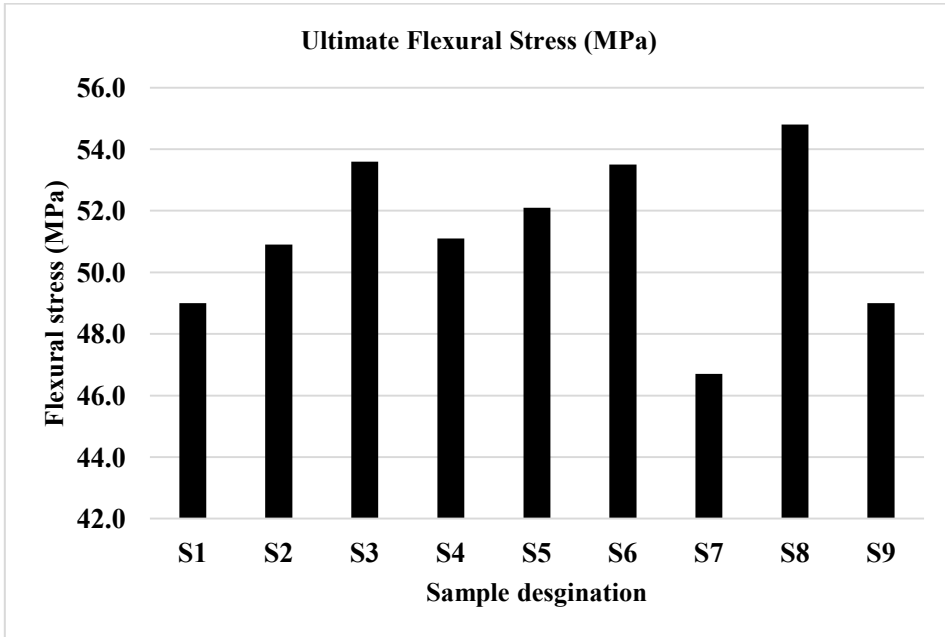


Fig.3. Comparison ultimate flexural stress of various samples built under process conditions.

3.3. Compression Test

The maximum compression load for PETG specimen hold ranges from 1.08 kN to 2.1 kN in Fig 4. Highest compression strength has been observed for S9 and least for S1. The compression strength has been observed to be directly proportional to the infill density.

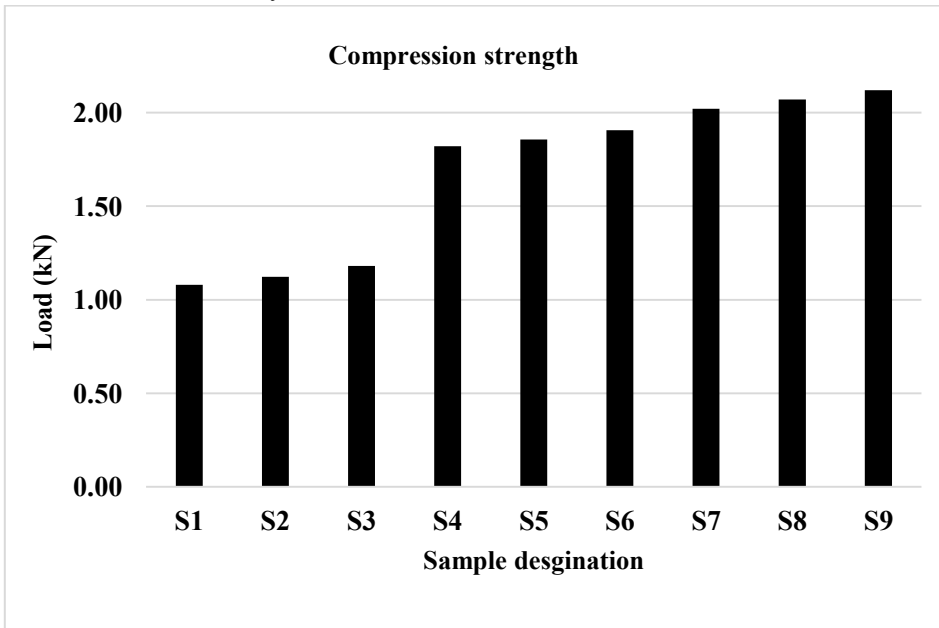


Fig. 4. Comparison of compression test results.

3.4. Impact strength

Impact strength of PETG specimen has been observed to be either 23.6 J/m or 34.3 J/m, as shown in Fig.5. Higher impact strength has been recorded for specimen S3, S5, S6 and S7 with a density of 25%.

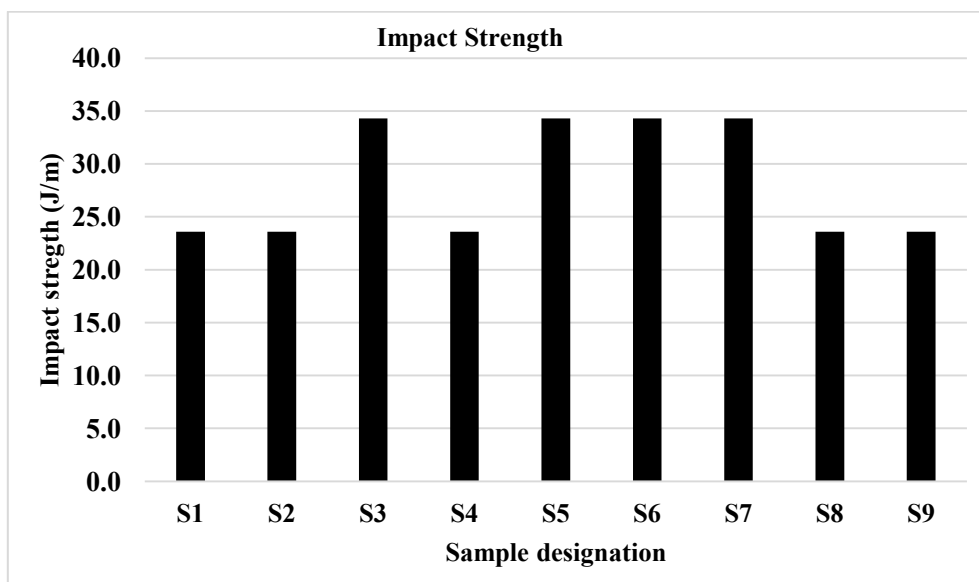


Fig.5. Impact strength.

Conclusions

The following conclusions can be drawn from this study:

- The least tensile strength has been noted for S1, with 24.9 MPa (20%, 225 °C and 20 mm/s) and the highest tensile strength of 35.46 MPa for S9 (30%, 245 °C and 25 mm/s).
- The highest compression strength has been observed for S9 (2.1 kN) and the least for S1 (1.08 kN). The compression strength is directly proportional to the infill density.
- The impact strength of the samples (S3, S5, S6 and S7) was highest, where the print speed was 25 mm/s.
- The samples S4, S5, and S6 have shown better mechanical properties than the counterpart S1, S2, S3, S7, S8, and S9 samples.
- Optimized process parameters would be used to fabricate the spectacle frame prototype via the FDM process in the future work.

Acknowledgements

The authors would like to thank the additive manufacturing lab, Mechanical Engineering Department, Amrita Vishwa Vidyapeetham, Coimbatore and National Institute of Technology Tiruchirappalli Tamil Nadu, India.

References

- Bedi, S. S., Mallesha, V., Mahesh, V., Mahesh, V., Mukunda, S., Negi, S., & Ponnusami, S. A. (2023). Thermal characterization of 3D printable multifunctional graphene-reinforced polyethylene terephthalate glycol (PETG) composite filaments enabled for smart structural applications. *Polymer Engineering and Science*, June, 1–16. <https://doi.org/10.1002/pen.26409>
- Bedi, S. S., Mallesha, V., Mahesh, V., Mahesh, V., & Ponnusami, S. A. (2023). Investigation of low-percentage graphene reinforcement on the

- mechanical behaviour of additively manufactured polyethylene terephthalate glycol composites. *Journal of Thermoplastic Composite Materials*, 0(0), 1–21. <https://doi.org/10.1177/08927057231188025>
- Derise, M. R., & Zulkharnain, A. (2020). Effect of infill pattern and density on tensile properties of 3D printed polylactic acid parts via fused deposition modeling (FDM). *International Journal of Mechanical & Mechatronics Engineering IJMME-IJENS*, 20(02), 54–63. <https://doi.org/http://dx.doi.org/10.1177/0954406219856383>
- Gebisa, A. W., & Lemu, H. G. (2018). Investigating effects of fused-deposition modeling (FDM) processing parameters on flexural properties of ULTEM 9085 using designed experiment. *Materials*, 11(4), 1–23. <https://doi.org/10.3390/ma11040500>
- Guessasma, S., Belhabib, S., & Nouri, H. (2019). Printability and tensile performance of 3D printed polyethylene terephthalate glycol using fused deposition modelling. *Polymers*, 11(7). <https://doi.org/10.3390/polym11071220>
- Heidari-Rarani, M., Ezati, N., Sadeghi, P., & Badrossamay, M. R. (2022). Optimization of FDM process parameters for tensile properties of polylactic acid specimens using Taguchi design of experiment method. *Journal of Thermoplastic Composite Materials*, 35(12), 2435–2452. <https://doi.org/10.1177/0892705720964560>
- Kadhun, A. H., & Al-zubaidi, S. (2023). Effect of the infill patterns on the mechanical and surface characteristics of 3D printing of PLA , PLA + and PETG materials. *Chemengineering*, 7(3), 46.
- Kristiawan, R. B., Imaduddin, F., & Ariawan, D. (2021). A review on the fused deposition modeling (FDM) 3D printing: Filament processing, materials, and printing parameters. *Open Engineering*, 11(1), 639–649. <https://doi.org/https://doi.org/10.1515/eng-2021-0063>
- Kumar, K. S., Soundararajan, R., Shanthosh, G., Saravanakumar, P., & Ratteesh, M. (2021). Augmenting effect of infill density and annealing on mechanical properties of PETG and CFPETG composites fabricated by FDM. *Materials Today: Proceedings*, 45, 2186–2191. <https://doi.org/10.1016/j.matpr.2020.10.078>
- Kumar, M. A., Khan, M. S., & Mishra, S. B. (2020). Effect of machine parameters on strength and hardness of FDM printed carbon fiber reinforced PETG thermoplastics. *Materials Today: Proceedings*, 27, 975–983. <https://doi.org/10.1016/j.matpr.2020.01.291>
- Mallikarjuna B, J. christiyan K. G. (2013). Innovative modeling and rapid prototyping of turbocharger impeller. *International Conference on Advanced Materials, Manufacturing, Management & Thermal Sciences (AMMMT-2013)*, 2(9), 1426–1432.
- Mallikarjuna, B., Pachipulusu, B., Shivashankar, H., Jayachristiyan, K. G., & Jayanth, N. (2023). A review on the melt extrusion-based fused deposition modeling (FDM): background , materials , process parameters and military applications. *International Journal on Interactive Design and Manufacturing (IJIDeM)*, 17(2), 1–14.
- Mallikarjuna, Balichakra, & Reutzell, E. W. (2022). Reclamation of intermetallic titanium aluminide aero-engine components using directed energy deposition technology. *Manufacturing Review*, 9(27), 1–21. <https://doi.org/10.1051/mfreview/20220204>
- Mohan, N., Senthil, P., Vinodh, S., & Jayanth, N. (2017). A review on composite materials and process parameters optimisation for the fused deposition modelling process. *Virtual and Physical Prototyping ISSN:*, 12(1), 45–59. <https://doi.org/10.1080/17452759.2016.1274490>
- Özen, A., Auhl, D., Völlmecke, C., Kiendl, J., & Abali, B. E. (2021). Optimization of manufacturing parameters and tensile specimen geometry for fused deposition modeling (FDM) 3D-printed PETG. *Materials*, 14(5), 2556.
- Reddy, A. B., Siva, G., Reddy, M., Sudhakar, K., Manjula, B., Sinha, S., & Sadiku, E. R. (2015). Polyethylene terephthalate-based blends: Natural rubber and synthetic rubber. In *Poly(Ethylene Terephthalate) Based Blends, Composites and Nanocomposites* (pp. 75–98). <https://doi.org/https://doi.org/10.1016/C2013-0-19172-6>
- Sekaran, J. J. G., Pragadish, N., Valsakumari, M., & Ravikumar, S. (2023). Characterization of fused deposition modeling components fabricated at different print orientations. *Engineering Research Express*, 5(4), 025019.
- Srinivasan, R., Nirmal Kumar, K., Jenish Ibrahim, A., Anandu, K. V., & Gurudhevan, R. (2020). Impact of fused deposition process parameter (infill pattern) on the strength of PETG part. *Materials Today: Proceedings*, 27, 1801–1805. <https://doi.org/10.1016/j.matpr.2020.03.777>
- Srinivasan, R., Ruban, W., Deepanraj, A., Bhuvanesh, R., & Bhuvanesh, T. (2020). Effect on infill density on mechanical properties of PETG part fabricated by fused deposition modelling. *Materials Today: Proceedings*, 27(3), 1838–1842. <https://doi.org/10.1016/j.matpr.2020.03.797>
- Teraiya, S., Vyavahare, S., & Kumar, S. (2021). Experimental investigation on influence of process parameters on mechanical properties of PETG parts made by fused deposition modelling. In H. K. Dave & D. Nedelcu (Eds.), *Advances in Manufacturing Processes* (pp. 283–293). Springer Singapore.
- Thrimurthulu, K., Pandey, P. M., & Reddy, N. V. (2004). Optimum part deposition orientation in fused deposition modeling. *International Journal of Machine Tools and Manufacture*, 44(8), 585–594. <https://doi.org/10.1016/j.ijmactools.2003.12.004>



Structural Integrity and Reliability of Advanced Materials obtained through Additive Manufacturing (SIRAMM23)

Effect of the notch opening angle on the quasi-static behavior of PLA and carbon fibers reinforced PLA realized through Fused Deposition Modelling

Estera Vălean^{a,*}, Pietro Foti^b, Seyed Mohammad Javad Razavi^b, Liviu Marșavina^a, Filippo Berto^c

^aDepartment of Mechanics and Strength of Materials, University Politehnica Timisoara, Timisoara 300222, Romania

^bDepartment of Mechanical and Industrial Engineering, MTP Gløshaugen, Norwegian University of Science and Technology, Trondheim 7491, Norway

^cDepartment of Chemical Materials Environment Engineering, Sapienza University, Roma, Italy

Abstract

Additive manufacturing provides significant advantages over conventional manufacturing. Among the others, the almost unconstrained freedom in the geometrical design for this technology can be pointed out. However, the geometrical complexness of such components requires for adequate tools to assess both their fracture behavior and fatigue life. A suitable solution for such a design challenge is to rely on the so-called local approaches whose main advantage is to consider a local parameter to evaluate the behavior of the entire component; besides, such methods have the advantage that their critical value can be assumed to be independent on both the overall geometry of the component and the loading conditions. With this purpose, the present work investigates the fracture behavior of notched specimens made of PLA and carbon fiber reinforced PLA realized through additive manufactured technique. The specimen's geometry considered is smooth and double notched while the notch opening angles varies between 30 and 120 degrees. The results of the experimental campaign have been summarized through the averaged strain energy density (SED) method, an energy-based local approach, widely proved to be a valid tool to investigate both fracture in static condition and fatigue failure. The critical value of SED has been obtained through the stress-strain curve of smooth specimens for the two studied materials. After the determination of the control volume characteristic length, R_0 , the data have been summarized in terms of averaged SED values. The critical loads for the different geometries and the different materials considered are predicted by the method with an average error of $\pm 7\%$.

© 2023 The Authors. Published by Elsevier B.V.

This is an open access article under the CC BY-NC-ND license (<https://creativecommons.org/licenses/by-nc-nd/4.0>)

Peer-review under responsibility of the SIRAMM23 organizers

* Corresponding author.

E-mail address: estera.valean@student.upt.ro (E. Vălean)

2452-3216 © 2023 The Authors. Published by ELSEVIER B.V.

This is an open access article under the CC BY-NC-ND license (<https://creativecommons.org/licenses/by-nc-nd/4.0>)

Peer-review under responsibility of the SIRAMM23 organizers

10.1016/j.prostr.2024.02.037

Keywords: Additive manufacturing; Fracture; Fused Deposition Modelling; local approaches.

1. Introduction

Fused Deposition Modeling (FDM) is an additive manufacturing (AM) process that involves the extrusion of material from a nozzle to realize 3D parts from plastic materials. Ease of use, prototyping accuracy, and low cost make it a widely used AM technique. In FDM, a filament of thermoplastic printing material is melted through a printer extrusion die and deposited line by line and layer by layer on a heated printing plate. Producing a printed structure involves generating a digital design of the model via 3D design software and running it through the printer until the complete model is reproduced (Vaezi et al. 2013; Song et al 2017; García Plaza et al. 2019). Despite the advantages of this process, if the process parameters are not optimized problems may arise such as poor adhesion or large process-induced defects leading to detrimental effects on the mechanical performance with failures facilitated by the delamination between different layers. Nowadays, FDM is mainly used in dealing with thermoplastic materials such as polylactic acid (PLA). Due to its excellent properties and low cost, PLA has evolved as perhaps the most widely used material in 3D printing. It is a biodegradable, recyclable and compostable thermoplastic polymer with high strength and high modulus, which has proven its potential to replace many conventional polymers in various industrial applications (Farah et al. 2016; Savioli Lopes et al. 2012). It is worth noting that FDM can be exploited also to build components made of materials such as metals, ceramics or cermets employing high-filled polymers during the FDM process followed by post-processing phases to achieve the final component, (Spiller et al. 2022¹; Spiller et al. 2022²). Other materials of high interest for FDM process are fiber reinforced polymers. However, such reinforced materials are still a field of research due to the high variability of mechanical performance that can be achieved depending on the process parameters (Ajay Kumar et al. 2020; Durga et al. 2019; Marsavina et al. 2022).

Besides the variety of materials that can be used through AM and the flexibility of AM processes in production of highly complex components, proper tools are still required to assess fracture behavior and fatigue life, (Mohammadzadeh et al. 2019; Foti et al. 2023). The so-called local approaches provide a suitable solution being their critical values independent of both the overall geometry of the component and the loading conditions. With this purpose, the present work investigates through an energetic local approach the fracture behavior of AM notched specimens made of PLA and carbon fiber reinforced PLA.

2. Fundamentals of the strain energy density

Among local approaches, the strain energy density (SED) method, as proposed by Lazzarin et al. (2001, 2002), is an energy-based local approach widely validated to assess fracture both in static and dynamic conditions (Foti et al. 2020). The SED method is founded on the idea that brittle fracture happens when the total elastic energy, averaged over a given control volume, reaches a critical value. According to the method hypothesis, both the critical SED value and the characteristic length, R_0 , defining the control volume represent material properties; they are indeed independent on both the local geometrical conditions and on the loadings mode, even if the shape and the location of the control volume depends on them (for further details, see Foti et al. 2021). It is worth highlighting that, under the assumption of ideally brittle material, the critical SED value, $\bar{W}_c = W_c$, can be estimated through the conventional ultimate tensile strength, σ_{UTS} , of a smooth specimen:

$$\bar{W}_c = \frac{\sigma_{UTS}^2}{2E} \quad (1)$$

Thanks to the absence of stress gradients, in the case of smooth specimens no information are needed regarding the control volume characteristic length. On the other hand, when geometrical discontinuities are present in the

material, the application of the SED method cannot disregard the determination of the control volume characteristic length. Due to the independency of the control volume characteristic length and of the SED critical value on the geometry, both can be determined if the loads to fracture are known for the same material according to two different geometrical conditions. This led to the development of analytical solutions for the determination of R_0 such as the following ones that gives R_0 for static conditions as a function of the ultimate tensile strength and of the fracture toughness, K_{IC} , (Lazzarin et al. 2005; Yosibash et al. 2004):

$$R_0 = \frac{(1+\nu)(5-8\nu)}{4\pi} \left(\frac{K_{IC}}{\sigma_{UTS}} \right)^2 \quad \text{plane strain} \quad (2)$$

$$R_0 = \frac{(5-3\nu)}{4\pi} \left(\frac{K_C}{\sigma_{UTS}} \right)^2 \quad \text{plane stress} \quad (3)$$

The concepts presented in the above constitute the basic idea of the method; for further insights on the method analytical framework and applications, we recommend the works of Radaj et al. 2013 and Berto et al. 2014.

3. Materials and methods

The materials considered in this work are polylactic acid (PLA, Silver - Prusa Polymers) and carbon fiber reinforced polylactic acid (PLA-CF, Sunlu - containing short CF (<20%)). Prusa MK3 printer was used to realize the specimens. 3D printing software was used to set the printing parameters, such as raster angle, head speed, temperature and so on. The temperature of the nozzle and the built platform was controlled at around 60°C and 215°C, respectively. An infill density of 100% is defined in the printing software with raster angles of ± 45 degrees for the infill, while the orientation position of the part on the built platform was 0°. The tests have been carried out in displacement control mode (2 mm/min) using an electromechanical testing machine (Model: Zwick Roell 005) with a maximum load of 5 kN. The Young's modulus, E , ultimate tensile strength, σ_{UTS} , and strain at break, ε_b , were obtained considering three smooth specimens per material according to ISO 527-1 (2012) while the fracture loads were obtained for notched specimens with changing the notch opening angles 2α , as reported in Fig. 1, considering five specimens per geometrical condition and material.

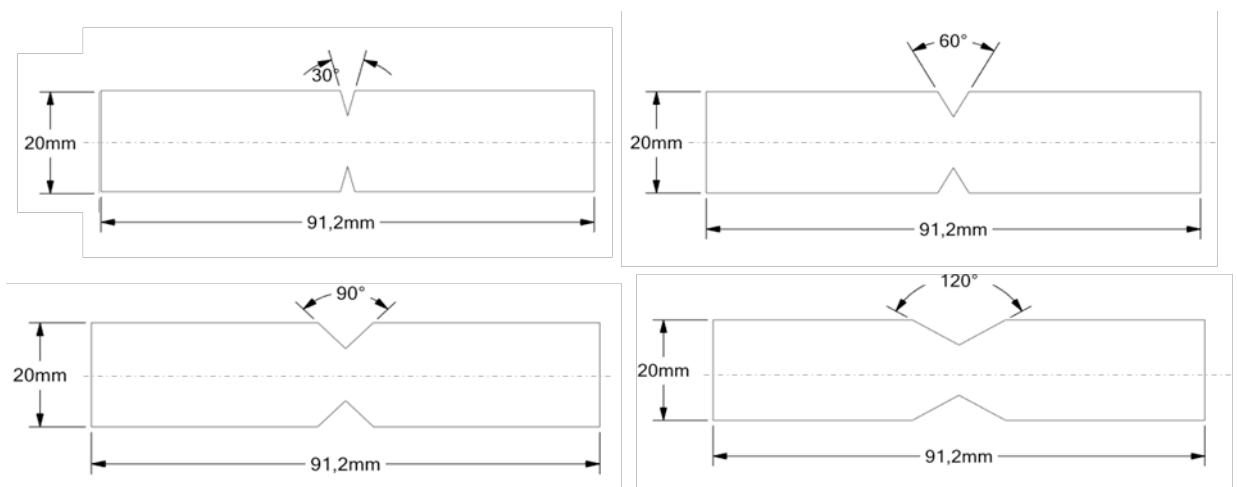


Fig. 1. Geometries of the test V-notched specimens tested under tension. All specimens are 4 mm thick.

4. Results and discussion

The experimental setup and the average stress - strain diagrams are shown in Fig. 2. Particularly, PLA specimens present a more brittle behavior with respect to PLA-CF. The mechanical properties are provided in Table 1.

Table 1. Average of the experimental results, for smooth specimens.

Average	PLA	PLA-CF
E [MPa]	3250.6	3203.3
σ_{UTS} [MPa]	41.59	33.48
ϵ_b [MPa]	2.28	4.32

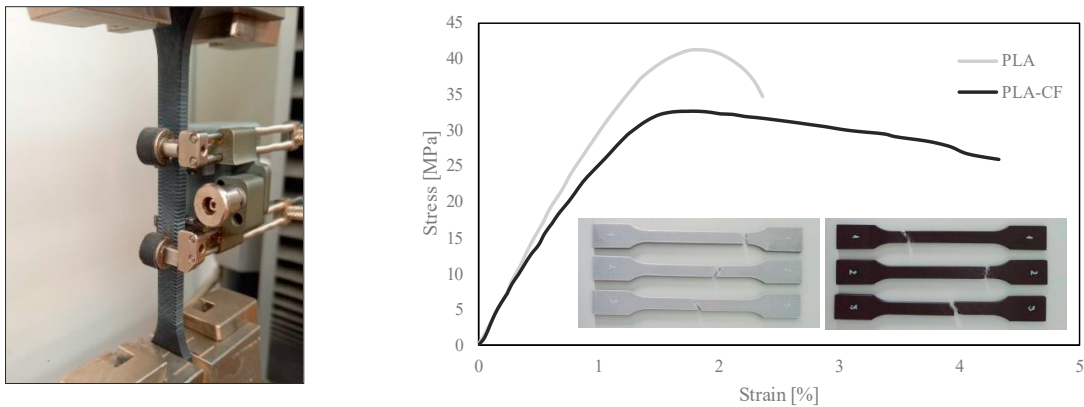


Fig. 2. a) Example showing one dog bone specimen that was tested under tensile loading and b) average stress -strain curves for PLA and PLA-CF.

Fig. 3 reports the force - displacement curves for the notched specimens together with the critical load to failure vs. notch opening angle. It is worth highlighting that the unreinforced material over performed with respect to the reinforced one for both smooth and notch specimens. No clear trend can be observed with changing the notch opening angle; however, both materials present a minimum of the critical load to failure at 60°. The test results, in terms of load to failure, are summarized in Table 2.

Table 2. Summary of the experimental results, in terms of load to failure, for V - notched specimens.

	PLA				PLA-CF			
	30°	60°	90°	120°	30°	60°	90°	120°
No. Sample	Fmax[N]	Fmax[N]	Fmax[N]	Fmax[N]	Fmax[N]	Fmax[N]	Fmax[N]	Fmax[N]
1	1513	1203	1288	1711	938	743	796	1049
2	1498	1217	1329	1691	921	736	794	1015
3	1483	1181	1279	1705	915	743	852	1062
4	1441	1228	1270	1742	906	734	835	1036
5	1560	1195	1386	1704	925	752	818	1063
Average	1499	1205	1310	1711	921	742	819	1045

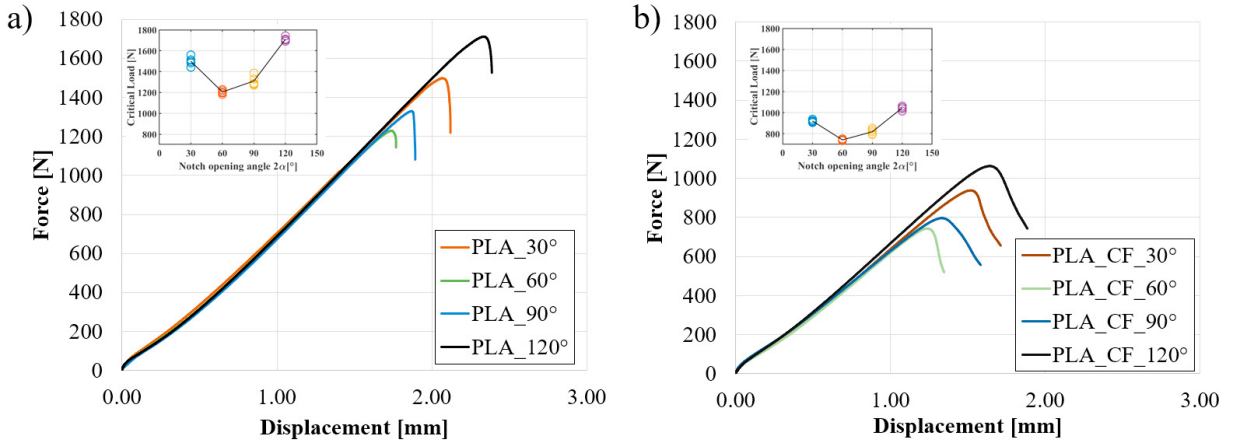
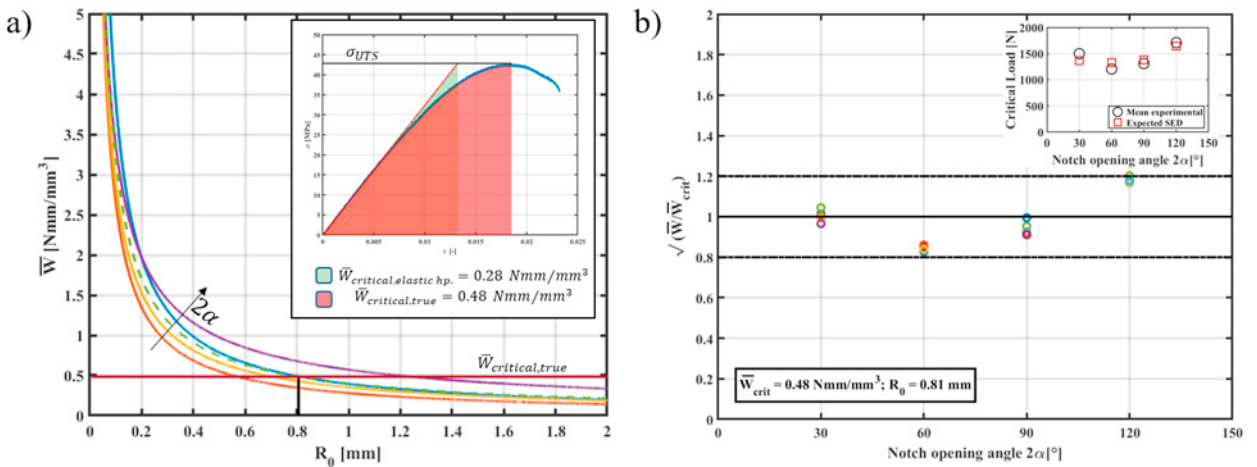


Fig. 3. Force vs displacement curves for notched specimens under tensile loading: a) PLA; b) PLA-CF.

The results have been summarized in terms of SED value as shown in Fig. 4. In particular, Fig. 4 a) and c) show the procedure considered to determine the control volume characteristic length R_0 ; due to the variability that can be seen in the results also for specimens having the same nominal geometry, R_0 has been determined by minimizing the error in the SED summary of the results. Due to the behavior shown by both materials, it was not possible to consider them as brittle and an equivalent elastic model had to be established. Therefore, the critical strain energy density, determined through the smooth specimens, was evaluated considering the true strain – true stress curve of the material leading for PLA to $\bar{W}_{critical,true} = 0.48 \text{ Nmm/mm}^3$ and $R_0 = 0.81\text{mm}$ while for PLA-CF to $\bar{W}_{critical,true} = 0.41 \text{ Nmm/mm}^3$ and $R_0 = 0.30\text{mm}$. According to the explained procedure, the critical loads for the different geometries and the different materials considered are predicted by the method with an average error of $\pm 7\%$; besides, as it is possible to see from Fig. 4 b) and d), the method predicts a minimum of the critical load to failure for 60° , in agreement with the experimental results.



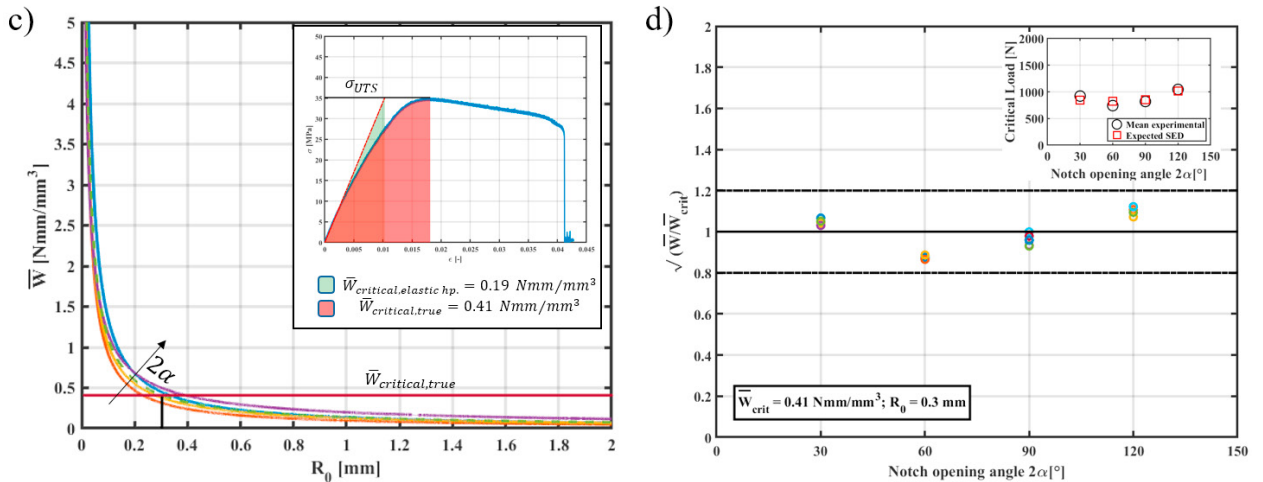


Fig. 4. a) SED vs. R_0 trend with critical SED value as determined from smooth specimens and b) SED summary for PLA specimens with experimental and predicted fracture load; c) SED vs. R_0 trend with critical SED value as determined from smooth specimens.

5. Conclusions

In this work the behavior of PLA and PLA-CF specimens realized through FDM process and weakened by V-notches has been investigated in mode I loadings condition while changing the notch opening angle through the use of SED method. The critical SED value, considered for the application of the method, have been evaluated through the true strain – true stress curve; the ductile behavior shown by both materials required for the consideration of an equivalent elastic material for a consistent application of the method. It has been shown that, considering an equivalent elastic material, the method is able to predict the expected fracture load with an average error of $\pm 7\%$ considering both sets of specimens; besides, in agreement with the experimental results, the method predicts a minimum of the critical load to failure for 60° .

Acknowledgements

The project leading to these results has received funding from the European Union's Horizon 2020 research and innovation program under grant agreement No. 857124.

References

- Ajay Kumar, M., Khan, M.S., Mishra, S.B., 2020. Effect of fused deposition machine parameters on tensile strength of printed carbon fiber reinforced PLA thermoplastics, *Materials Today: Proceedings* 27, 1505–1510.
- Berto, F., Lazzarin, P., 2014. Recent developments in brittle and quasi-brittle failure assessment of engineering materials by means of local approaches, *Mater. Sci. Eng. R Reports*, 75(1), 1-48.
- Durga, V., Rajiv, P., Navya Geethika, V., 2019. Effect of Fused Deposition Modelling (FDM) Process Parameters on tensile Strength of Car-bon Fibre PLA, *Materials Today: Proceedings* 18, 2012-2018.
- Farah, S., Anderson, D.G., Langer, R., 2016. Physical and mechanical properties of PLA, and their functions in widespread applications – a comparative review. *Advanced Drug Delivery Reviews* 107, 367-392.
- García Plaza, E., López, P.J.N., Torija, M.Á.C., Muñoz, J.M.C., 2019. Analysis of PLA geometric properties processed by FFF additive manufacturing: Effects of process parameters and plate-extruder precision motion. *Polymers*, 11, 1581.
- Foti, P., Berto F., 2020. Evaluation of the Effect of the TIG-Dressing Technique on Welded Joints through the Strain Energy Density Method, *Procedia Structural Integrity*, 25, 201-208.

- Foti, P., Razavi, S.M.J., Ayatollahi, M.R., Marsavina, L., Berto, F., 2021. On the application of the volume free strain energy density method to blunt V-notches under mixed mode condition, *Engineering Structures*, 230, 111716.
- Foti, P., Razavi, S.M.J., Fatemi, A., Berto F., 2023. Multiaxial fatigue of additively manufactured metallic components: A review of the failure mechanisms and fatigue life prediction methodologies, *Progress in Materials Science*, 137, 101126.
- Lazzarin, P., Zambardi, R., 2001. A finite-volume-energy based approach to predict the static and fatigue behavior of components with sharp V-shaped notches. *Int J Fract*, 112(3), 275–98.
- Lazzarin, P., Zambardi, R., 2002. The equivalent strain energy density approach re-formulated and applied to sharp V-shaped notches under localized and generalized plasticity. *Fatigue Fract Eng Mater Struct.*; 25(10), 917–28.
- Lazzarin, P., Berto, F., 2005. Some expressions for the strain energy in a finite volume surrounding the root of blunt V-notches. *Int J Fract*. 135(1–4), 161–85.
- Lazzarin, P., Berto, F., 2005. From Neuber's elementary volume to Kitagawa and Atzori's diagrams: An interpretation based on local energy. *Int J Fract*, 135(1–4), 33–8.
- Marsavina L., Valean C., Marghitas M., Linul E., Razavi S.M.J., Berto F., Brighenti R., 2022. Effect of the manufacturing parameters on the tensile and fracture properties of FDM 3D-printed PLA specimens, *Engineering Fracture Mechanics*, 274, 108766.
- Mohammadizadeh, M., Imeri, A., Fidan, I., Elkelany, M., 3D printed fiber reinforced polymer composites - Structural analysis, *Composites Part B: Engineering* Volume 175, 15 October 2019, 107112.
- Radaj, D., Vormwald, M., 2013. Advanced methods of fatigue assessment. *Advanced Methods of Fatigue Assessment* (Vol. 9783642307).
- Savioli Lopes, M., Jardini, A.L., Maciel Filho, R., Poly (Lactic Acid) Production for Tissue Engineering Applications, *Procedia Eng.*, 42 (2012), pp. 1402-1413.
- Song, Y., Li, Y., Song, W., Yee, K., Lee, K.Y., Tagarielli, V., L., 2017. Measurements of the mechanical response of unidirectional 3D-printed PLA. *Mater Des*, 123, 154–64.
- Spiller, S., Berto F., Razavi, S., M.J., 2022¹. Mechanical behavior of Material Extrusion Additive Manufactured components: an overview. *Procedia Structural Integrity*, 41, 158–174.
- Spiller, S., Kolstad S.O., Razavi, S.M.J., 2022². Fabrication and characterization of 316L stainless steel components printed with material extrusion additive manufacturing, *Procedia Structural Integrity*, 42, 1239-1248.
- Vaezi, M., Seitz, H., Yang, S., 2013. A review on 3d micro-additive manufacturing technologies. *The International Journal of Advanced Manufacturing Technology* 67(5–8):1721–1754
- Yosibash, Z., Bussiba, A., Gilad, I., 2004. Failure criteria for brittle elastic materials. *Int J Fract*, 125(1957), 307–33.
- ISO 527-1, 2012. *Plastics-Determination of Tensile Properties-part 1: General Principles*. International Organization for Standardization; ISO: Geneva, Switzerland, 23.



Structural Integrity and Reliability of Advanced Materials obtained through Additive Manufacturing (SIRAMM23)

Enhanced fatigue performance of laser directed energy deposition fabricated Ti6Al4V alloy using laser shock peening

Sapam Ningthemba Singh^{a*}, Ashish B. Deoghare^a

^aDepartment of Mechanical Engineering, National Institute of Technology Silchar, 788010, India

Abstract

Additively manufactured parts generally have lower fatigue life than their wrought counterparts as a result of the nature of deposition, defects, extreme thermal gradients, and residual stresses generated during the process. The present study explored a high-layer thickness laser-directed energy deposition (LDED) of Ti6Al4V and enhancing its fatigue life by using laser shock peening (LSP). Significant improvements in the fatigue life in samples 1 and 4 were observed for the LDED+LSPed samples as compared to only LDED samples. However, for samples 2 and 3, a slight decrease in fatigue life were observed for LDED+LSPed samples. This can be due to the presence of internal defects on the LDED+LSPed samples or surface cracks or uneven distribution of LSP on the surfaces. A ductile mode of fatigue failure was observed with multiple cracks (both point and line cracks) on the failed surface. River lines with multiple tributaries as well as striation regions with clear signs of incremental crack growth were also observed. The present paper presented the high layer thickness LDED for faster part fabrication and enhanced fatigue life using LSP as a post-processing method. This will help in reducing the manufacturing time while also improving the fatigue life as compared to other AM processes.

© 2023 The Authors. Published by Elsevier B.V.

This is an open access article under the CC BY-NC-ND license (<https://creativecommons.org/licenses/by-nc-nd/4.0>)

Peer-review under responsibility of the SIRAMM23 organizers

Keywords: Laser shock peening; laser directed energy deposition; fatigue behavior; additive manufacturing; Ti6Al4V.

* Corresponding author.

E-mail address: sapamthemba@gmail.com and sapam_rs@mech.nits.ac.in

1. Introduction

Additive manufacturing (AM) is a manufacturing process where the material is deposited in a layer by layer fashion according to the design data. It can process polymers, composites, ceramics, and metallic materials. Powder bed fusion (PBF) and directed energy deposition (DED) are two major types of AM processes for processing metallic materials. While the PBF process offers higher dimensional accuracies than the DED process, the DED process has the ability to fabricate parts with much higher layer thickness as compared to the PBF process (Singh and Deoghare 2022; Dávila et al. 2020). Increasing layer thickness can significantly improve the material deposition rate and hence, the manufacturing lead time. Ti6Al4V alloy is one of the widely used materials in the aerospace, biomedical, and automobile industries, having excellent mechanical properties such as strength-to-weight ratio, toughness, fatigue, and ductility properties (S. Liu and Shin 2019). However, due to poor machinability and difficulties in processing Ti6Al4V, AM of Ti6Al4V is gaining attention in the manufacturing world (Arrazola et al. 2009). The applications of Ti6Al4V alloy in the aerospace, biomedical and automotive industry has been reported in the literature (Tamayo et al. 2021; Z. Liu et al. 2021; Duraiselvam et al. 2014; Froes et al. 2004). The design freedom and ability to fabricate complex parts, the laser AM of Ti6Al4V has been investigated extensively in the literature. It is reported that post-processing of additively manufactured parts is important to obtain a smooth and regular surface as the surface roughness of the additively manufactured Ti6Al4V parts is more than those of the parts obtained from casting (de Oliveira Campos et al. 2020). It is also reported that the properties of Ti6Al4V parts manufactured by PBF and DED process are competitive to that of cast materials and other additively manufactured parts (Baufeld, Biest, and Gault 2010). However, the fatigue performance of additively manufactured parts is generally lower than that of wrought counterparts (Sterling et al. 2015). It is also reported that the as-built samples have lower fatigue performance than those of machined samples of the additively manufactured samples (Le et al. 2020).

The fatigue performance of additively manufactured Ti6Al4V alloy can be improved by employing various post-processing operations, including heat treatment, hot isostatic pressing (HIP), shot peening, laser shock peening (LSP), etc. (Cao et al. 2018; Li et al. 2016; Kahlin et al. 2020). After such post-processing, some fatigue performances were more than those of the wrought parts (Li et al. 2016). This has further been supported by the findings from (Günther et al. 2017). A smoother surface is favorable for a higher fatigue performance and rough surfaces should be reduced to a possible and reasonable level (Bagehorn, Wehr, and Maier 2017; Pegues et al. 2018). LSP is one of the promising post-processing methods that induce compressive residual stress (CRS) on surfaces with or without the application of an overlay layer and protective layer. Internal defects on the prepared samples were the main reasons for the part failure during the ultra-high cycle fatigue of Ti6Al4V samples manufactured by the selective laser melting (SLM) process (Jiang et al. 2021). Improvement in fatigue life after LSP was observed for different AM processes such as SLM, PBF, electron beam melting (EBM), etc. (Jin et al. 2020; Aguado-Montero et al. 2022; Kahlin et al. 2020).

With all these advances, the scientific literature available in this research area is mostly focused on the powder PBF-based AM processes. Most of the available information is on the thin layer thickness process. With DED, the layer thickness can be significantly increased (more than 1 mm). The research on the fatigue performance of high layer thickness is limited, and further research is needed with regards to the high layer thickness LDED process as well as enhancing the fatigue life with post-processing methods such as LSP. The present paper is focused on the fatigue life enhancement of Ti6Al4V alloys manufactured by the LDED process using the LSP process.

Nomenclature

AM	additive manufacturing
ASTM	American Society for Testing and Materials
CRS	compressive residual stress
CNC	computer numerical control
DED	directed energy deposition
EDM	electrical discharge machining
HIP	hot isostatic pressing
LDED	laser directed energy deposition
LPBF	laser powder bed fusion

LSP	laser shock peening
PBF	powder bed fusion
SLM	selective laser melting
SEM	scanning electron microscope

2. Methods and materials

The fatigue samples were prepared in the Meltio M450 DED machine according to the ASTM E-466/22 standard with the process parameters given in Table 1. Ti6Al4V wire alloy of 1 mm diameter was supplied for an average layer thickness of 1.2 mm during the deposition process. Constant Argon gas was supplied to prevent immediate oxidation during the deposition process. Air conditioning was also maintained in the printing chamber. An initial periphery deposition around the fatigue samples was adopted and then an alternate 45° deposition pattern was used in between the layers. The fabricated samples were separated from the substrate by using wire-cut electrical discharge machining (wire-cut EDM). The surfaces were machine and polished with grit sizes ranging from 100 to 2200 to obtain a crack-free, flat polished surface before the fatigue test and LSP process. Fig. 1(a) shows as-printed samples, Fig. 1(b) shows the machined surface and Fig. 1(c) shows the polished samples.

One set of samples was subjected to the LSP process. The fatigue samples were peened two times on both sides using a Litron Nd:YAG laser of 1064 nm wavelength with a laser diameter of 0.8 mm, and a spot overlapping of 60%. A pulse width of 6 ns and repetition rate of 10 Hz with a maximum energy of 370 mJ was applied. To provide the maximum possible pressure, an overlay of water was provided. A sacrificial layer of black tape was provided to minimize material ablation on the Ti6Al4V alloy. Fig. 2 shows the LSP setup where a focusing lens is used to focus the laser from the deflecting lens on the samples, as shown in Fig. 2(a). The sample is kept inside a tray controlled by CNC. A constant stream of water is supplied, as seen in Fig. 2(b). The LSPed samples are shown in Fig. 2(c). The fatigue test was conducted on both sets of samples: (a) LDED only and (b) LDED+LSPed samples under the load of 650 MPa and a load ratio -1 with 5 Hz frequency for sample numbers 1, 2, and 4. For sample no. 3, different frequency ranges (5 Hz, 10 Hz, and 15 Hz) were used to test the reaction of the samples under different frequencies. The fractured surfaces were analyzed using a scanning electron microscope (SEM) to study the fractography and microstructural details.

Table 1. Process parameters used during the LDED process.

Dataset no.	1	2	3	4
Power (W)	800	850	900	950
Speed (mm/s)	10	10	13	13
Layer thickness (mm)	1.2			
Wire diameter (mm)	1			
Deposition pattern	Alternative 45° deposition with initial periphery deposition			

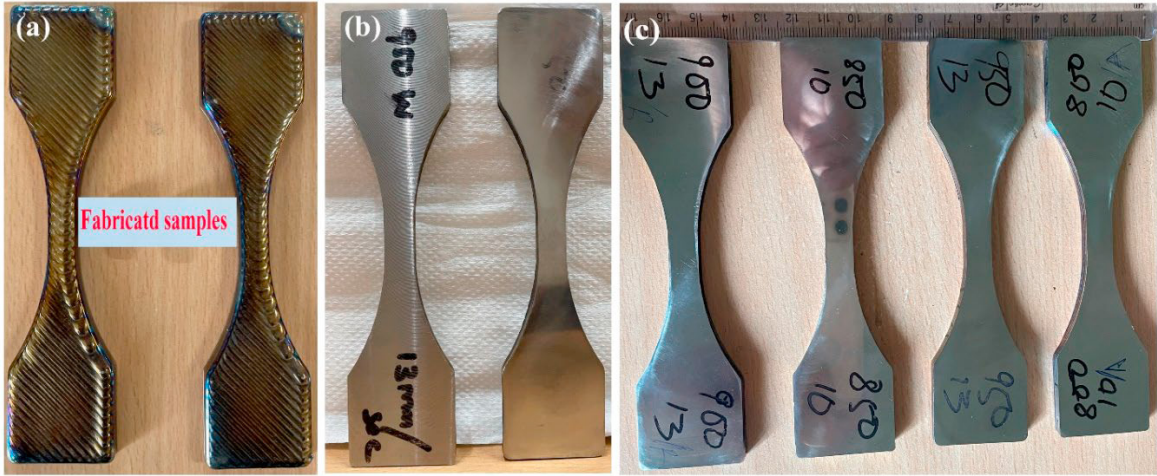


Fig. 1. (a) Fabricated fatigue samples (b) machined samples and (c) polished fatigue samples.

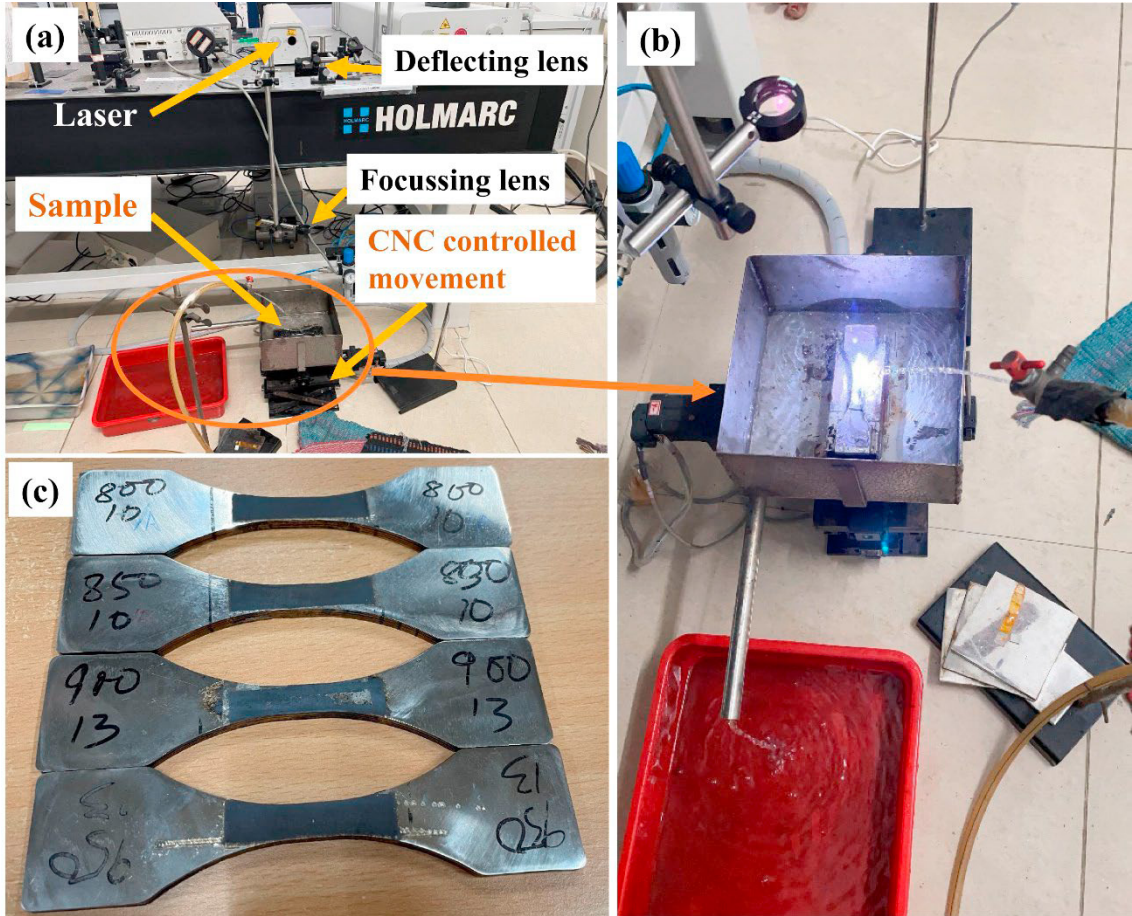


Fig. 2: (a) LSP setup, (b) LSP of the samples, (c) LSPed samples.

3. Results and discussions

The initial microscopic inspection of the fabricated samples revealed surface micro-cracks which are common to AM and welding processes. These cracks were not visible to visual inspections. Upon polishing, these cracks were eliminated and a polished surface without cracks were obtained before the fatigue testing. Isolated and very small voids were observed on the interface between the deposition pattern and the initial boundary deposition. Such voids can act as a crack initiation point. There was a 61.4% increase in fatigue life from sample no. 1 to 2, followed by a 15.6% decrease from sample no. 2 to 3 and 25.7% from sample no. 3 to 4 in LDED-only samples as seen in Fig. 3(a). The increase in the fatigue life is mainly due to an increase in laser power, allowing for more proper melting and re-melting of the successive layers. However, further increasing the laser power results in slower cooling of the fabricated parts, resulting in coarser microstructures that are not favorable for fatigue life (Amine, Newkirk, and Liou 2014; Farshidianfar, Khajepour, and Gerlich 2016). Higher laser power encourages more deformation, and a higher heating/cooling cycle induces more unwanted stresses. This is the reason for the reduced fatigue life in sample no. 3&4.

Significant improvement in the fatigue life in samples 1 (56.51%) and 4 (39.26%) was observed for the LDED+LSPed as compared to samples without LSP. However, for samples 2 and 3, a slight decrease of 0.99% and 11.40%, respectively were observed for LDED+LSPed samples as compared to the LDED-only samples. The primary reason for the decrease in fatigue life is the gaps observed in samples 2&3 in the LSPed area, as shown in Fig. 3(a). Another reason can be due to internal defects on the LDED+LSPed samples, surface cracks, or due to uneven distribution of LSP on the surfaces. Even though the samples of the same process parameters were prepared in one go, there are still chances that microstructure and void distribution can be different, resulting in different fatigue life.

The mode of fatigue failure was prominently ductile mode of failure. Multiple cracks and voids were observed during the fractography of the fractured surfaces. River lines, voids (dimples), striations, and cracks were observed as seen in Fig. 3(b). No significant difference in the fracture pattern was observed between the LDED-only samples and LDED+LSPed samples, as seen in Fig. 4. This shows the effects of LSP are limited to surfaces and near-surface only which is in agreement with the results in the literature (X. Zhang et al. 2022; Hareharen et al. 2023; Bai et al. 2023). The fatigue performance is within the range of existing literature (M. Zhang et al. 2018; Ghouse et al. 2018). This is significant considering the high layer thickness adopted in the current study.

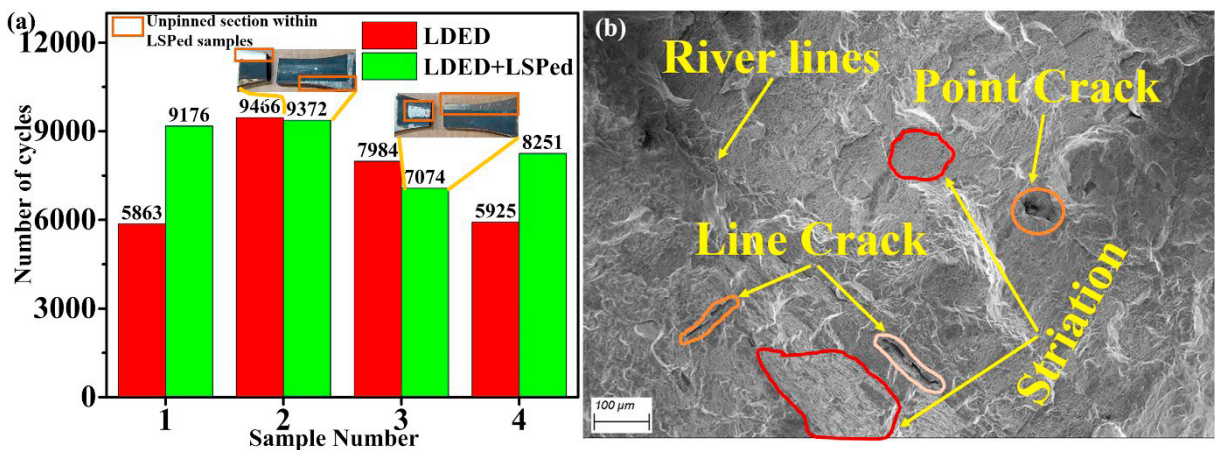


Fig. 3: (a) fatigue life of LDED and LDED+LSPed samples, and (b) SEM image of fractured surface.

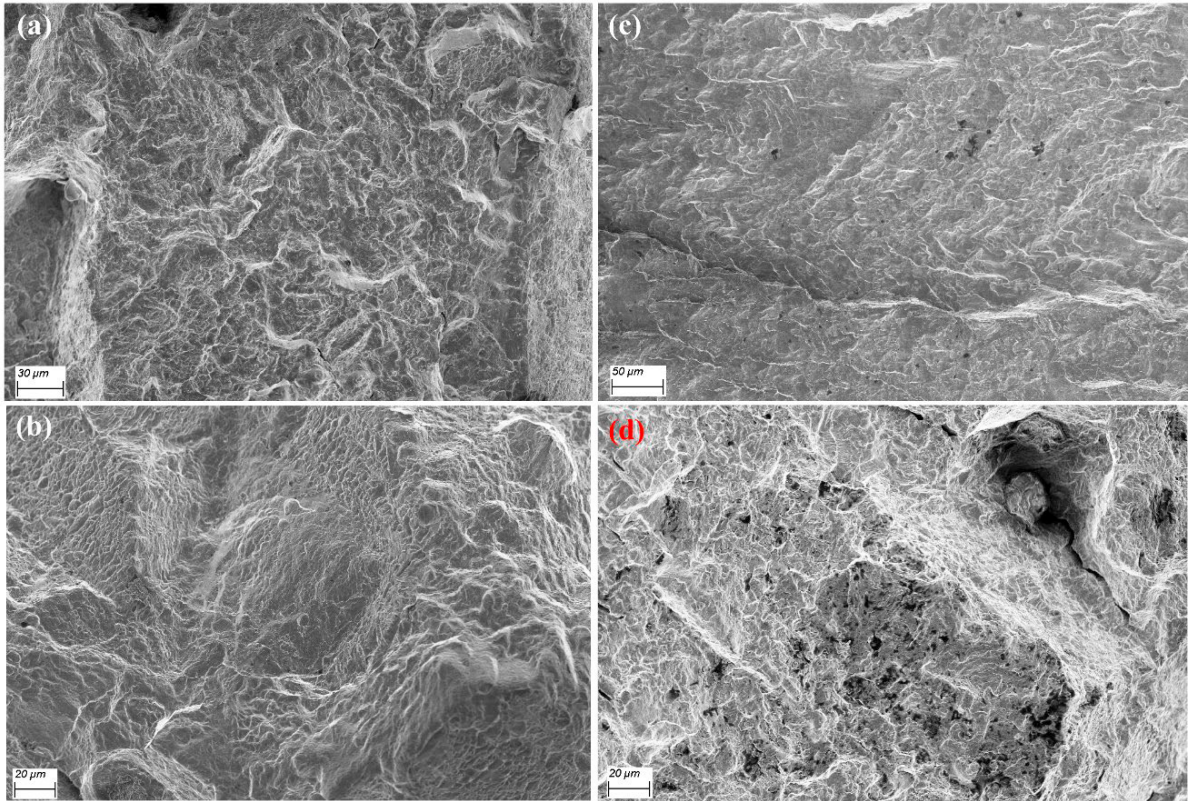


Fig. 4: SEM images of the fractured surfaces in (a&b) LDED only and (c&d) LDED+LSPed fractured surface.

4. Conclusions

This research explored the high-layer thickness AM of Ti6Al4V alloy using the LDED process and enhancing the fatigue performance of these fabricated parts by using the LSP process. The surface micro-cracks were eliminated after polishing. These cracks are common to both AM and welding processes due to extreme temperature gradients. The fatigue life of the samples increased at first as the power increased, but a decreasing trend was observed due to longer cooling time, leading to coarser grains. Significant improvement in the fatigue life in samples 1 (56.51%) and 4 (39.26%) was observed for the LDED+LSPed. However, for samples 2 and 3, a slight decrease of 0.99% and 11.40%, respectively, in fatigue life, were observed for LDED+LSPed samples as compared to the LDED-only samples. Gaps seen in the LSPed area in samples 2 and 3 were the primary reason for the decrease in fatigue life. Internal defects and voids are also another reason for the decreased fatigue life.

Acknowledgments

The authors thank the Ministry of Education, Government of India, and Indovation Lab, NIT Silchar for providing financial and material support. The authors also thank CFM, VIT Vellore for allowing access to the LSP system. The authors acknowledge the advanced manufacturing lab, weld and corrosion lab, NIT Silchar for optical microscope and polishing facility, CIF IIT Guwahati for SEM facility, and Material characterization lab IIT Hyderabad fatigue testing facility.

References

- Aguado-Montero, Santiago, Carlos Navarro, Jesús Vázquez, Fernando Lasagni, Sebastian Slawik, and Jaime Domínguez. 2022. “Fatigue Behaviour of PBF Additive Manufactured Ti6Al4V Alloy after Shot and Laser Peening.” *International Journal of Fatigue* 154 (January): 106536. <https://doi.org/10.1016/j.ijfatigue.2021.106536>.
- Amine, Tarak, Joseph W. Newkirk, and Frank Liou. 2014. “An Investigation of the Effect of Direct Metal Deposition Parameters on the Characteristics of the Deposited Layers.” *Case Studies in Thermal Engineering* 3 (July): 21–34. <https://doi.org/10.1016/j.csite.2014.02.002>.
- Arrazola, P. J., A. Garay, L. M. Iriarte, M. Armendia, S. Marya, and F. Le Maître. 2009. “Machinability of Titanium Alloys (Ti6Al4V and Ti555.3).” *Journal of Materials Processing Technology* 209 (5): 2223–30. <https://doi.org/10.1016/j.jmatprotec.2008.06.020>.
- Bagehorn, S., J. Wehr, and H. J. Maier. 2017. “Application of Mechanical Surface Finishing Processes for Roughness Reduction and Fatigue Improvement of Additively Manufactured Ti-6Al-4V Parts.” *International Journal of Fatigue* 102 (September): 135–42. <https://doi.org/10.1016/j.ijfatigue.2017.05.008>.
- Bai, Yunjian, Guo-Jian Lyu, Yun-Jiang Wang, Tianyu Chen, Kun Zhang, and Bingchen Wei. 2023. “Laser Shock Peening Strengthens Additively Manufactured High-Entropy Alloy through Novel Surface Grain Rotation.” *Materials Science and Engineering: A*, March, 144886. <https://doi.org/10.1016/j.msea.2023.144886>.
- Baufeld, Bernd, Omer Van der Biest, and Rosemary Gault. 2010. “Additive Manufacturing of Ti-6Al-4V Components by Shaped Metal Deposition: Microstructure and Mechanical Properties.” *Materials and Design* 31 (SUPPL. 1): S106–11. <https://doi.org/10.1016/j.matdes.2009.11.032>.
- Cao, Fei, Tiantian Zhang, Matthew A. Ryder, and Diana A. Lados. 2018. “A Review of the Fatigue Properties of Additively Manufactured Ti-6Al-4V.” *JOM* 70 (3): 349–57. <https://doi.org/10.1007/s11837-017-2728-5>.
- Dávila, José Luis, Paulo Inforçatti Neto, Pedro Yoshito Noritomi, Reginaldo Teixeira Coelho, and Jorge Vicente Lopes da Silva. 2020. “Hybrid Manufacturing: A Review of the Synergy between Directed Energy Deposition and Subtractive Processes.” *International Journal of Advanced Manufacturing Technology*. Springer. <https://doi.org/10.1007/s00170-020-06062-7>.
- Duraiselvam, Muthukannan, A. Valarmathi, S. M. Shariff, and G. Padmanabham. 2014. “Laser Surface Nitrided Ti-6Al-4V for Light Weight Automobile Disk Brake Rotor Application.” *Wear* 309 (1–2): 269–74. <https://doi.org/10.1016/j.wear.2013.11.025>.
- Farshidianfar, Mohammad H., Amir Khajepour, and Adrian P. Gerlich. 2016. “Effect of Real-Time Cooling Rate on Microstructure in Laser Additive Manufacturing.” *Journal of Materials Processing Technology* 231 (May): 468–78. <https://doi.org/10.1016/j.jmatprotec.2016.01.017>.
- Froes, F. H., H. Friedrich, J. Kiese, and D. Bergoint. 2004. “Titanium in the Family Automobile: The Cost Challenge.” *JOM* 56 (2): 40–44. <https://doi.org/10.1007/S11837-004-0144-0/METRICS>.
- Ghose, Shaaz, Sarat Babu, Kenneth Nai, Paul A. Hooper, and Jonathan R.T. Jeffers. 2018. “The Influence of Laser Parameters, Scanning Strategies and Material on the Fatigue Strength of a Stochastic Porous Structure.” *Additive Manufacturing* 22 (August): 290–301. <https://doi.org/10.1016/j.addma.2018.05.024>.
- Günther, J., D. Krewerth, T. Lippmann, S. Leuders, T. Tröster, A. Weidner, H. Biermann, and T. Niendorf. 2017. “Fatigue Life of Additively Manufactured Ti-6Al-4V in the Very High Cycle Fatigue Regime.” *International Journal of Fatigue* 94 (January): 236–45. <https://doi.org/10.1016/j.ijfatigue.2016.05.018>.
- Hareharen, K., Pradeep Kumar S, T Panneerselvam, Dinesh Babu P, and N Sriraman. 2023. “Investigating the Effect of Laser Shock Peening on the Wear Behaviour of Selective Laser Melted 316L Stainless Steel.” *Optics and Laser Technology* 162 (September 2022): 109317. <https://doi.org/10.1016/j.optlastec.2023.109317>.
- Jiang, Qinghong, Shuai Li, Cong Zhou, Bi Zhang, and Yongkang Zhang. 2021. “Effects of Laser Shock Peening on the Ultra-High Cycle Fatigue Performance of Additively Manufactured Ti6Al4V Alloy.” *Optics and Laser Technology* 144 (December): 107391. <https://doi.org/10.1016/j.optlastec.2021.107391>.
- Jin, Xinyuan, Liang Lan, Shuang Gao, Bo He, and Yonghua Rong. 2020. “Effects of Laser Shock Peening on Microstructure and Fatigue Behavior of Ti-6Al-4V Alloy Fabricated via Electron Beam Melting.” *Materials Science and Engineering A* 780 (April): 139199. <https://doi.org/10.1016/j.msea.2020.139199>.
- Kahlin, M., H. Ansell, D. Basu, A. Kerwin, L. Newton, B. Smith, and J. J. Moverare. 2020. “Improved Fatigue Strength of Additively Manufactured Ti6Al4V by Surface Post Processing.” *International Journal of Fatigue* 134 (May): 105497. <https://doi.org/10.1016/j.ijfatigue.2020.105497>.
- Le, Viet Duc, Etienne Pessard, Franck Morel, and Serge Prigent. 2020. “Fatigue Behaviour of Additively Manufactured Ti-6Al-4V Alloy: The Role of Defects on Scatter and Statistical Size Effect.” *International Journal of Fatigue* 140 (November): 105811.

- <https://doi.org/10.1016/j.ijfatigue.2020.105811>.
- Li, P., D. H. Warner, A. Fatemi, and N. Phan. 2016. “Critical Assessment of the Fatigue Performance of Additively Manufactured Ti-6Al-4V and Perspective for Future Research.” *International Journal of Fatigue* 85 (April): 130–43. <https://doi.org/10.1016/j.ijfatigue.2015.12.003>.
- Liu, Shunyu, and Yung C. Shin. 2019. “Additive Manufacturing of Ti6Al4V Alloy: A Review.” *Materials and Design* 164 (February): 107552. <https://doi.org/10.1016/j.matdes.2018.107552>.
- Liu, Zhiying, Bei He, Tianyi Lyu, and Yu Zou. 2021. “A Review on Additive Manufacturing of Titanium Alloys for Aerospace Applications: Directed Energy Deposition and Beyond Ti-6Al-4V.” *JOM*. Springer. <https://doi.org/10.1007/s11837-021-04670-6>.
- Oliveira Campos, Fábio de, Anna Carla Araujo, André Luiz Jardini Munhoz, and Shiv Gopal Kapoor. 2020. “The Influence of Additive Manufacturing on the Micromilling Machinability of Ti6Al4V: A Comparison of SLM and Commercial Workpieces.” *Journal of Manufacturing Processes* 60 (December): 299–307. <https://doi.org/10.1016/j.jmapro.2020.10.006>.
- Pegues, Jonathan, Michael Roach, R. Scott Williamson, and Nima Shamsaei. 2018. “Surface Roughness Effects on the Fatigue Strength of Additively Manufactured Ti-6Al-4V.” *International Journal of Fatigue* 116 (November): 543–52. <https://doi.org/10.1016/j.ijfatigue.2018.07.013>.
- Singh, Sapam Ningthemba, and Ashish B. Deoghare. 2022. “Laser Shock Peening of Laser Based Directed Energy Deposition and Powder Bed Fusion Additively Manufactured Parts: A Review.” *Metals and Materials International*. Springer. <https://doi.org/10.1007/s12540-022-01334-1>.
- Sterling, Amanda, Nima Shamsaei, Brian Torries, and Scott M. Thompson. 2015. “Fatigue Behaviour of Additively Manufactured Ti-6Al-4 V.” In *Procedia Engineering*, 133:576–89. No longer published by Elsevier. <https://doi.org/10.1016/j.proeng.2015.12.632>.
- Tamayo, José A., Mateo Riascos, Carlos A. Vargas, and Libia M. Baena. 2021. “Additive Manufacturing of Ti6Al4V Alloy via Electron Beam Melting for the Development of Implants for the Biomedical Industry.” *Heliyon* 7 (5): e06892. <https://doi.org/10.1016/J.HELIYON.2021.E06892>.
- Zhang, Meng, Chen Nan Sun, Xiang Zhang, Jun Wei, David Hardacre, and Hua Li. 2018. “Predictive Models for Fatigue Property of Laser Powder Bed Fusion Stainless Steel 316L.” *Materials and Design* 145 (May): 42–54. <https://doi.org/10.1016/j.matdes.2018.02.054>.
- Zhang, Xiushuo, Yu’e Ma, Meng Yang, Chouting Zhou, Nanke Fu, Wei Huang, and Zhenhai Wang. 2022. “A Comprehensive Review of Fatigue Behavior of Laser Shock Peened Metallic Materials.” *Theoretical and Applied Fracture Mechanics* 122 (December): 103642. <https://doi.org/10.1016/j.tafmec.2022.103642>.

Structural Integrity and Reliability of Advanced Materials obtained through Additive Manufacturing (SIRAMM23)

Evaluation of wall thickness effect on tensile properties of injected short fiber reinforced polymers

Dan Micota^{1*}, Alexandru Isaincu², Liviu Marsavina³, Lucian Rusu⁴

^{1,3,4} Politehnica University of Timișoara, Department of Mechanics and Strength of Materials, Mihai Viteazul Blvd, No. 1, Timișoara 300222, Romania

² Politehnica University of Timișoara, Department of Steel Structures and Structural Mechanics, Ioan Curea Str, No. 1, Timișoara 300224, Romania

Abstract

The aim of this paper is to analyze the effect of increasing the wall thickness in injection molded short fiber reinforced polymer (SFRP) parts, focusing mainly on tensile strain and tensile strength, as these are the most used characteristics for structural analyses. The phenomena that makes this evaluation of interest has to do with the microstructure of SFRP injection molded parts and how the fibers get oriented along the flow direction at superficial depths with an increasingly less aligned structure down to the mid plane/surface. By increasing the injected part wall thickness the ratio between the thicknesses of highly oriented layers and poorly oriented layers decreases, thus the tensile properties of the material should suffer a decrease as well.

In order to study the mentioned hypothesis two types of materials were tested, PPA GF33 and PPS GF40, dog-bone type specimens were cut at different angles to the flow direction from injection molded plates of 2 and 3 mm wall thickness values. The tensile strains were recorded using a video extensometer and material data was calibrated using Digimat MX reverse engineering module and Ansys properties homogenization tool and finite element solver.

© 2023 The Authors. Published by Elsevier B.V.

This is an open access article under the CC BY-NC-ND license (<https://creativecommons.org/licenses/by-nc-nd/4.0>)

Peer-review under responsibility of the SIRAMM23 organizers

Keywords: wall thickness, composite materials, tensile tests

1. Introduction

The widespread use of high-performance engineering thermoplastic materials in industry is pushing for increasingly higher demands in terms of performance, efficiency and costs. Especially, in the automotive sector short

* Corresponding author. Tel.: +4-074-001-5046;.

E-mail address: dan.micota@student.upt.ro

fiber reinforced polymers (SFRP) are the chosen materials for many components and assemblies, even for many applications that in the near past were considered completely metal dependent.

This family of composite materials can offer many advantages as they blend plastic materials lightness and mass scale manufacturability with the glass or carbon fibers high mechanical properties. Thus, the preferred manufacturing technology for SFRP parts is plastic injection molding, which comes with a series of advantages but also with some challenges that need to be comprehensively understood even from design phases.

Plastic injection molding is quite advantageous as a manufacturing technology due to the good mechanical properties of the resulted parts, repeatable tolerancing and dimensional stability as well as directly out of mold desired surface finishing, reduction of technological and manipulation operations, cost efficiency as a result of mass scale production and low takt times per part. But for all its advantages plastic injection molding technology is a very complex process with a lot of interdependent parameters and variables which have to be carefully balanced to get the best results, such as molding tool design, manufacturing and materials, raw materials state and quality, process temperatures, pressures and durations, but one of the greatest influence of SFRP parts quality, strength and behavior is the design of the part itself. As the injection molding technology is based on pressurized plastic melt flow through the mold cavity and simultaneously with liquid to solid phase transformation, the resulting part presents differentiated orientation of the fibers to the melt flow direction, and not only in different areas of the parts geometry but also throughout the thickness of the parts walls Bernasconi et al. (2007), Castagnet et al. (2021), Holmström et al. (2020); Huszar et al. (2015), Jørgensen et al. (2019), Stepashkin et al. (2018). This being such an high demand process and technology, but a very complex one, there is a high research interest with some of the works referenced in this paper being Bernasconi et al. (2007), Choi & Takahashi (1992), Hassan et al. (2004); Huang et al. (2019); Isaincu et al. (2021), Lohr et al. (2018), Micota, Isaincu, & Marsavina (2021), Ogierman & Kokot (2016), Oseli et al. (2020); Şerban et al. (2012, 2016), Skourlis et al. (1998), Takahashi et al. (2014), Zhang et al. (2014), Zhao et al. (2019).

The effect of different wall thicknesses on the mechanical properties and strength of the resulted injected SFRP parts was investigated in this paper. The phenomena is that increased wall thicknesses create a higher volume mid-plane flow channel, the fibers of the material in those channels cannot be aligned in the melt flow direction by the mold walls, thus freezing in a random orientation at the moment when the tool cavity is fully filled. Throughout the parts wall thickness the percentage of highly oriented fibers in the melt flow direction is decreasing with the increase of the overall designed wall thickness.

2. Tested materials

This paper is continuing the work presented in Micota, Isaincu, & Marsavina (2021), so the same two thermoplastic materials were studied, once again provided by the Solvay group. One being a polyphthalamide (PPA) reinforced with 33% short glass fiber inclusions (GF33) and the other material a polyphenylene sulfide (PPS) with a higher quantity of the same type of inclusions, 40% (GF40). These two materials can be found under the commercial designations of AMODEL AE-4133 for the PPA and Ryton R-4-270BL for the PPS. Both materials have a semi-crystalline structure of their matrix base polymers and are included in the high-performance class of engineering plastic materials. Also, they are widely used in the automotive industry in tough work environments regarding temperatures, loads and chemical agents.

3. Experimental testing

As results obtained for this paper have been compared with ones from Micota, Isaincu, & Marsavina (2021), much of the specimen preparation and test methodology was kept the same, in order to influence as few variables as possible.

The specimens for this test campaign were obtained from square injection molding plates of PPA and PPS, measuring approximately 100mm on their sides and approximately 3.2mm thick. The tool cavity was filled via a cold runner and a side positioned fan gate, in order to uniformly distribute the flow front along the plate's length, resulting in a highly oriented fiber orientation pattern in the fill direction.

The chosen wall thickness values to be analyzed, 2 and 3.2 mm, are right in the recommended range for injection molded short fiber reinforced plastic parts, this range being in between 1 and 5 mm and is common knowledge in the plastic injection molding industry based on many years of experience and material suppliers recommendations. Some of the reasons why is not recommended to inject SFRP in molds that produce wall thicknesses lower than 1 mm include high resistance to flow of the material, increased injection pressures, accelerated wear of the molds, risk of unfilled cavities, thus making such a process very difficult from a technological point of view. On the maximum side of the recommended thickness range it is easy to inject SFRP material in molds which produce wall thickness over 5 mm but the resulting parts will have major issues with shrinkage and warpage as the part cannot be effectively cooled throughout it's cross section.

From the described plates, dog-bone tensile specimens were cut via CNC machining at different angles to the melt flow direction, according to ISO 527-2 (2016). The relatively small size of the plates has limited the tensile specimen size and the 1BA type was chosen from the standard, Fig. 1 (a). The in-cut finish of the specimens after the CNC routing was very good, so no further preparation was needed before testing. To ensure the best fiber orientation distribution for each specimen, only one was cut from each plate's central area. For each of the 2 materials a total of 30 specimens were tested, 5 for each angle/orientation (0° , 15° , 30° , 45° , 60° and 90°) compared to the melt flow direction, all specimen orientation can be seen in Fig. 1 (b).

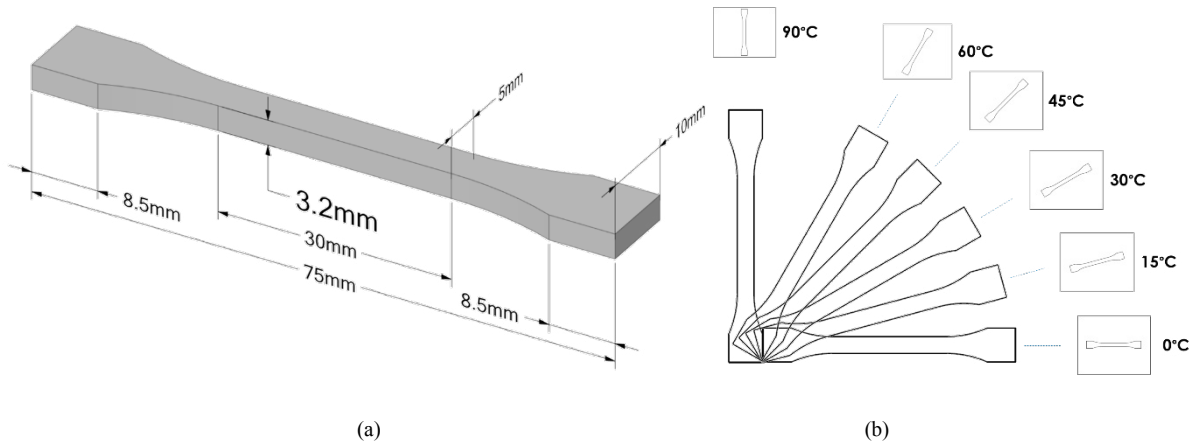


Fig. 1. (a) ISO 527-2 1BA dog-bone tensile specimen with increased thickness (3.2 mm); (b) specimen angles/orientations to the melt flow direction.

All tensile tests were performed on the same machine as for the referred lower wall thickness specimen tests, an Instron 8874 biaxial servo-hydraulic testing system, being capable of axial, torsional and combined axial-torsional loadings, but only the static axial capabilities of the machine were used for the tests. For specimen clamping the machine is equipped with Series 2742-30 kN fatigue rated hydraulic wedge grips, these allow for a precise control of the tightening pressure in order to prevent the specimens from slipping while also not crushing them. The design of the equipped grips also allows for automatic compensation in specimen thickness, maintaining a constant grip force across the test duration. The engineering axial strain of the specimens was measured with the Instron SVE1 (Standard Video Extensometer 1) 2663-822.

The rate of loading for these tests was done according to ISO 527-1 (527-1, 2016) with a constant speed of 5 mm/min and all the test were performed at room temperature. Given the high glass fiber content of both materials no necking phenomena was observed during the tests, all of the fractures being quasi-brittle.

4. Results and comparison

The results of the previously described tensile tests are presented in terms of engineering stress and strain in Fig. 2 for the PPA-GF33 material and in Fig. 3 for the PPS-GF40 material. For both materials the increased wall

thickness (3.2 mm) results are presented side by side with the lower wall thickness (2 mm) test results from Micota, Isaincu, & Marsavina, (2021), keeping also the same curves scale for a good comparison and visualization of the wall thickness influence at each orientation for both materials. As 5 specimens were tested for each material, wall thickness and orientation, only one representative curve was plotted for good graphs intelligibility.

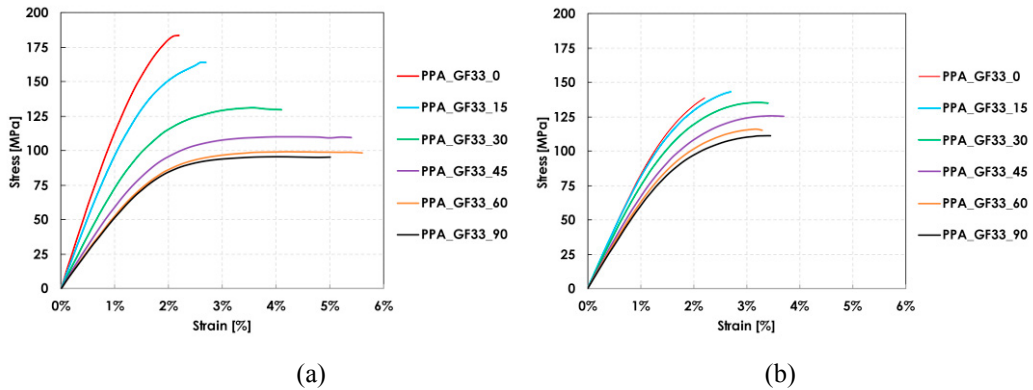


Fig. 2. Engineering stress-strain curves for PPA-GF33 with low 2 mm wall thickness (a) and increased (3.2 mm) wall thickness.

At a quick glance over the curves for PPA-GF30 it is obvious that the increase in wall thickness has a major influence over the mechanical properties of the injection molding plates specimens. One of the overall tendencies is that the strength (stress) is decreasing with the increase in wall thickness for the lower angles-oriented specimens (0° , 15°). While the strains at break are substantially decreasing with the increase in wall thickness for the higher angles-oriented specimens (30° , 45° , 60° and 90°). Average values of the stress and strains at break can be read in Table 1, together with the standard deviations and the percentual coefficient of variation, calculated for each of the 5-specimen batch. The values for Young's modulus are also in Table 1, as they are less observable from the graphs. Table 1 also contains the percentual difference compared to the values of the 2 wall thicknesses, with the proper signs for decrease (-) or increase (+) of the 3.2mm specimens values over the 2mm specimens.

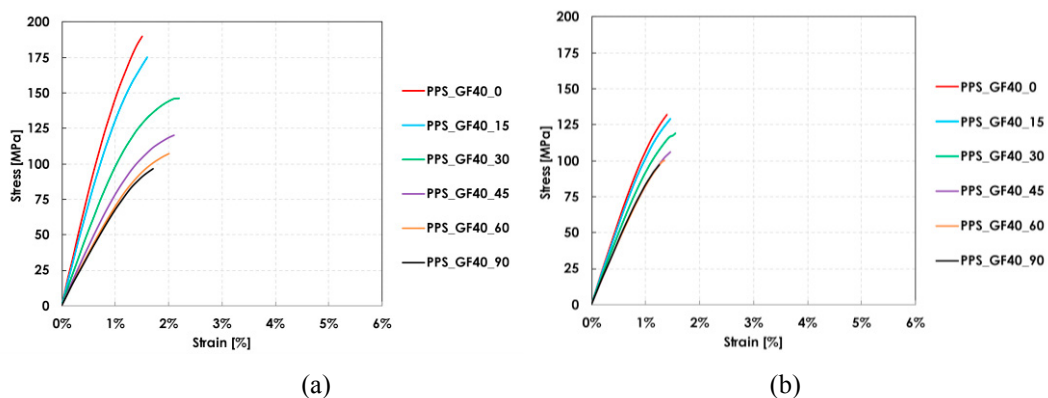


Fig. 3. Engineering stress-strain curves for PPS-GF40 with low 2 mm wall thickness (a) and increased (3.2 mm) wall thickness.

Looking over the side-by-side graphs for the 2mm and 3.2mm thick PPS-GF40 specimens from Fig.3 it can be observed that the brittleness on the thicker specimens is increased as less plasticity is present, and strain at break over the whole orientation range is significantly decreased. For this material the stress at break is also strongly reduced for the higher thickness specimens for all angles/orientations except 90° .

Another phenomenon that can be observed between the thicknesses for both materials is that the 2mm thick specimens have a wider spread of the stress-strain curves in the orientations range, while the ones for 3.2mm wall thickness are more closely grouped. This is an indication of the anisotropy of the 2 types of specimen thicknesses, high anisotropy in the orientations range for 2mm thickness and low anisotropy for increased wall thickness (3.2mm). Regardless of specimen orientation the material response to loading being similar to an extent, for the higher wall thickness specimens.

Table 1. Mean values (μ), standard deviation (σ), and coefficient of variation (CV) for the Young's modulus, tensile strength and strain at break of the increased wall thickness (3.2mm) specimens for PPA-GF33 and PPS-GF40, also the percentual difference (PD) from the lower wall thickness (2mm) specimens.

Mat.	θ (°)	Young's modulus				Tensile strength				Strain at break			
		μ (MPa)	σ (MPa)	CV (%)	PD (%)	μ (MPa)	σ (MPa)	CV (%)	PD (%)	μ (MPa)	σ (MPa)	CV (%)	PD (%)
PPA-GF33	0	8996	±210	2.3	-23.1	147	±2	1.7%	-21.3	2.83	±0.07	2.6	+28.9
	15	8797	±101	1.2	-12.8	145	±1	0.8%	-11.2	3.21	±0.12	3.7	+18.6
	30	8113	±198	2.4	+2.8	136	±2	1.6%	+3.4	3.45	±0.05	1.6	-17.6
	45	6980	±407	5.8	+7.2	125	±3	2.8%	+13.4	3.74	±0.16	4.4	-27.1
	60	6665	±228	3.4	+18.6	116	±2	1.9%	+16.9	3.33	±0.04	1.1	-39.2
	90	6363	±209	3.3	+13.3	111	±2	1.9%	+16.0	3.57	±0.12	3.4	-29.0
PPS-GF40	0	11693	±733	6.3	-26.6	134	±5	3.7%	-31.1	1.45	±0.05	3.3	-6.8
	15	11247	±389	3.5	-20.6	130	±4	3.0%	-26.4	1.49	±0.06	3.9	-10.4
	30	10074	±333	3.3	-4.3	121	±3	2.2%	-17.5	1.59	±0.08	5.1	-28.1
	45	9051	±170	1.9	+4.7	106	±4	3.8%	-12.6	1.45	±0.09	6.4	-33.3
	60	8887	±591	6.6	+18.0	101	±3	2.9%	-6.6	1.37	±0.05	3.8	-33.8
	90	9191	±243	2.6	+24.5	98	±3	3.1%	-0.2	1.28	±0.05	4.2	-28.5

5. Material modeling and calibration

With the resulted experimental data, 2 two material models have been developed and calibrated, for the PPA and PPS, similar to (Micota, Isaincu, & Marsavina, 2021), using specialized software Digimat, MX module (Digimat 2022.4 MX User's Guide Digimat MX User's Guide, 1992). This enabled the reverse engineering approach for homogenizing the matrix polymer properties with the elastic properties of the filler (GF), resulting in elasto-plastic material cards based on the Tsai-Hill fracture criterion (*Tsai-Hill Criterion*, n.d.).

The reverse engineering approach of the Digimat MX (*Digimat 2022.4 MX User's Guide Digimat MX Users Guide*, 1992) module is done by varying the material parameters presented in Table 2, each in a physical accurate range of values, until the best possible (optimized) fitting is done simultaneously on the 0°, 45° and 90° stress-strain curves (engineering values in this case), Micota, Isaincu & Marsavina, (2021). The specimen geometry, elaboration technology and filler type have also been accounted for.

Table 2. Material parameters for the Tsai-Hill model used in Digimat MX calibrations.

Material	Matrix Young's modulus [MPa]	Poisson's ratio [-]	Yield stress [MPa]	Hardening modulus [MPa]	Hardening exponent [-]	Linear hardening modulus [MPa]	Plastic strain multiplier [-]	Fiber aspect ratio [-]
PPA-GF33	3000	0.37	22.5	60	250	10	3.9	22
PPS-GF40	3450	0.41	32.5	45.05	150	10	5	25

Graphic results of the Digimat MX calibration for both materials with the increased 3.2mm specimen thickness are presented in Fig. 4. The main targets of the curve fitting calibration were the 0° orientation longitudinal curves as these contribute the most to the overall strength of the specimens/materials.

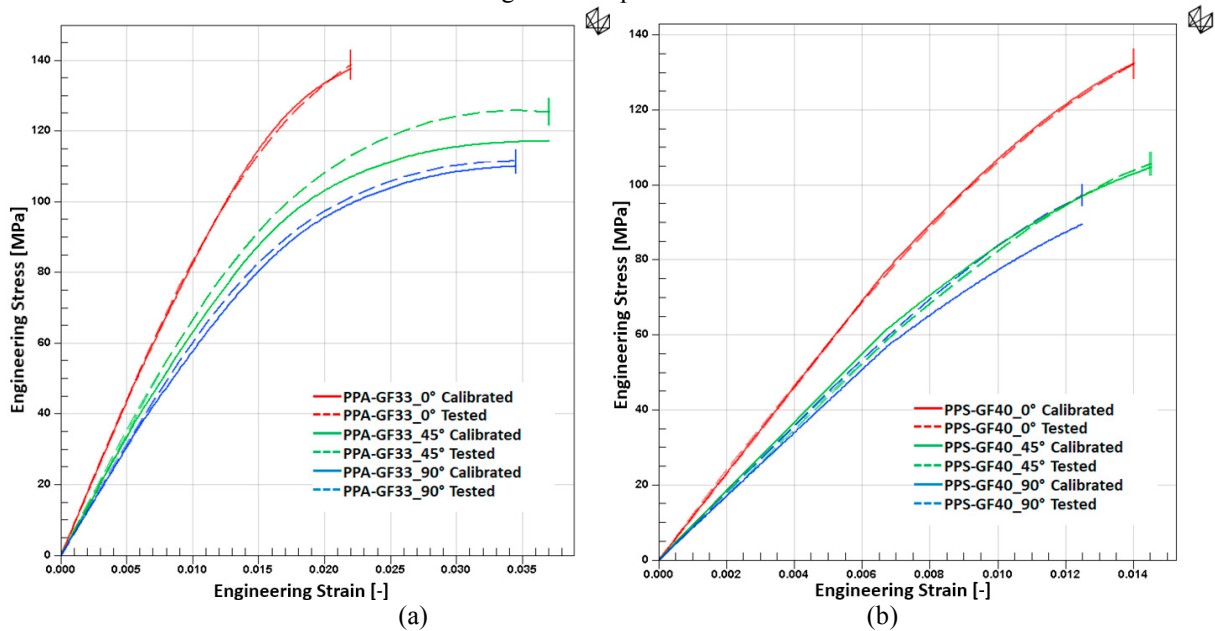


Fig. 4. Digimat calibration curves for PPA-GF33 (a) and PPS-GF40 (b) fitted at 0° , 45° and 90° orientations.

In order to build a micromechanical virtual model for each of the tested specimen type the fiber orientation tensor (FOT) data had to be obtained Isaincu et al.(2022). Injection molding simulations have been ran, using Autodesk Moldflow software Li et al.(2017), for the 3.2mm wall thickness plates with both materials. From these simulations the mesh and FOT files have been exported for the mapping process done in Digimat MAP module (*Digimat 2022.4 MAP User's Guide Digimat MAP User's Guide*, 1992). In this process the specific orientation specimen geometries (already meshed in ANSYS Mechanical) are overlaid onto the mesh of the full injected plate and elements that are detected to share the same approximate space/volume get attributed the specific differentiated value of FOT (fiber orientation tensor). This mapping process is transforming the specimen models into micromechanical structures that are composed of many areas of different oriented fibers, which also follow a stratified structure of good and poor oriented fibers throughout the specimens wall thickness. Fact that can be observed in Fig. 5 where the 0° angled 2mm thick specimen (a) presents shell-core-shell structure model, Bernasconi et al. (2007), with highly oriented fibers in the flow direction for the shell layers and poorly oriented fibers in the core layer. While the same angled specimen of the higher thickness has a skin-shell-core-shell-skin structure, in which the good orientation shell layers occupy less material/thickness percentage than the less in flow-oriented skin and core layers. Thus, explaining the reduction of in flow strength of the higher wall thickness specimens and the anisotropy difference, as the poorly oriented layers behave almost the same regardless of the loading angle.

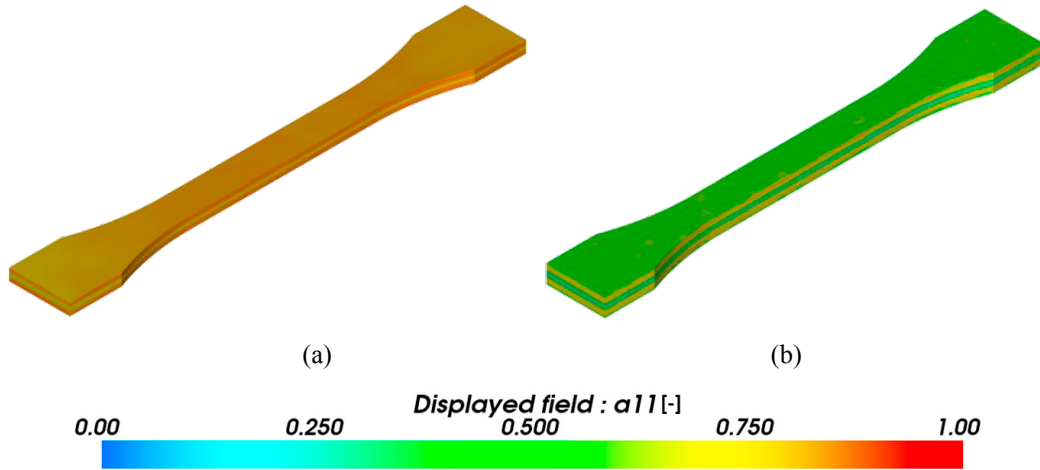


Fig. 5. Scalar field for a_{11} term of the fiber orientation tensor in the principal direction mapped at 0° orientation onto the 2mm thick specimen (a) vs. 3.2mm thick specimen (b).

The elasto-plastic material models and the FOT mapped files have all been introduced and virtually tensile loaded in ANSYS Workbench as the finite element (FEA) solver. All the tested angles specimen types and materials have been simulated and simulation results (dotted curves) vs. test results (solid curves) can be compared in Fig.6, for PPA 3.2mm thick (a) and PPS 3.2mm thick (b). Curves are plotted in force over displacement, and they share the same scale only for the force axis, as the variations in strain at break between materials are substantial.

A quite good calibration can be observed for the PPA material and not as good for the PPS, though the differences in displacement/travel between the simulation and test curves are amplified by the lower scale of the strain, this was imposed due to the more brittle behavior of the PPS-GF40 specimens.

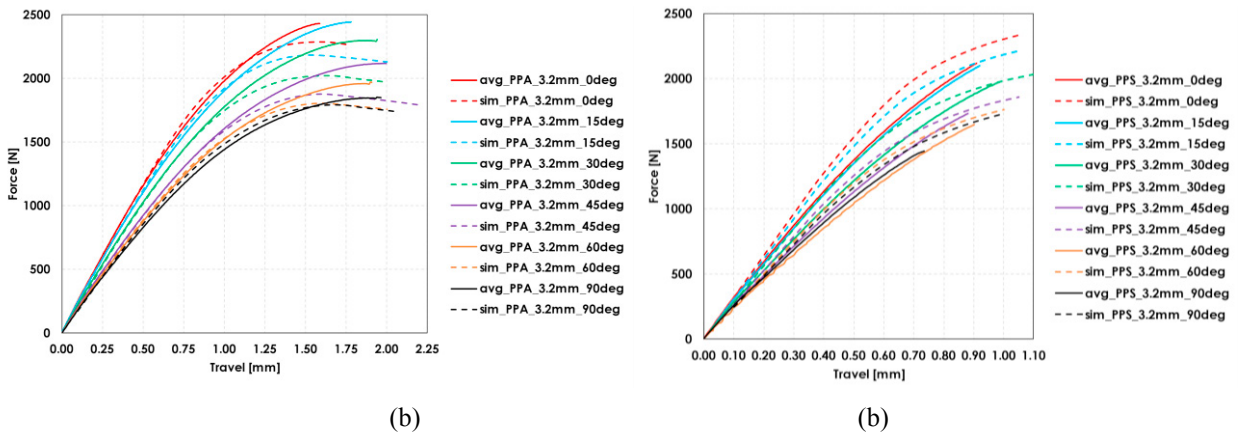


Fig. 6. Force-displacement curves of FEA validation material models at all tested orientations for PPA-GF33 (a) and PPS-GF40 (b).

6. Conclusions

This paper investigates the effects of increasing the wall thickness of SFRP injected parts and it has focused on the mechanical properties also going through material modeling and structural FEA simulations and calibrations. As

well as test results and comparisons with lower wall thickness injected plate specimens from previous work from the authors is has also detailed a comprehensive workflow for modeling and simulating SFRP injected parts/components, starting with injection molding simulations (Autodesk Moldflow), material modeling with Digimat MX, FOT mapping with Digimat MAP and FEA solver for structural simulation ANSYS Mechanical.

The main conclusions that can be drawn are the following:

- Good results were obtained from the increased specimens thickness tests considering the shape of the stress-strain curves and the small dispersion of the obtained data.
- The influence of wall thickness on the mechanical properties of SFRP injected components is substantial, growth of wall thickness leading to a general decrease in properties.
- This tendency is accentuated longitudinally in terms of rigidity and strength, and quite unobservable transversally.
- Strains at break decrease over the whole orientation range for increased wall thickness.
- The main reason for this phenomenon is due to the mid layer fountain effect, as the wall thickness increases the central melt layer that freezes last is thicker, and it freezes with an un-oriented fiber structure.
- Also, the overall anisotropy at higher wall thicknesses decreases as the difference in FOT between layers is decreased, thus the stress-strain curves are more closely spread in Y direction (stress axis).

Future directions might be the following:

- Tensile tests for both material at lower (-40°C) and higher (up to +120°C) temperatures.
- Improve the calibration of the material model using Digimat.
- Compare material model calibration results with Ansys Material Designer.
- Validate the material models using a mechanical test for an injected automotive part.

Acknowledgements

The work leading to this paper was partially supported by InoHubDoc project POCU/993/6/13/153432 and by the European Union's Horizon 2020 research and innovation program (H2020-WIDESPREAD-2018, SIRAMM) under grant agreement no. 857124. Results were disseminated in the SIRAMM project, final conference SIRAMM 23 in Timisoara, Romania. Special thanks to the Solvay Group for providing materials and support. Thanks, are also extended to Vitesco Technologies company for support in specimen elaboration, technical and specialized software support.

References

- 527-1, I. (2016). *Plastics — Determination of tensile properties — Part 1: General principles* (Vol. 2016, pp. 2–7).
- 527-2, I. (2016). *Plastics — Determination of tensile properties — Part 2: Test conditions for moulding and extrusion plastics*. 2016, 2–7.
- Bernasconi, A., Davoli, P., Basile, A., & Filippi, A. (2007). Effect of fibre orientation on the fatigue behaviour of a short glass fibre reinforced polyamide-6. *International Journal of Fatigue*, 29(2), 199–208. <https://doi.org/10.1016/j.ijfatigue.2006.04.001>
- Castagnet, S., Nadot-Martin, C., Fouchier, N., Conrado, E., & Bernasconi, A. (2021). Fatigue life assessment in notched injection-molded specimens of a short-glass fiber reinforced Polyamide 6 with different injection gate locations. *International Journal of Fatigue*, 143(September 2020), 105968. <https://doi.org/10.1016/j.ijfatigue.2020.105968>
- Choi, N. S., & Takahashi, K. (1992). Stress fields on and beneath the surface of short-fiber-reinforced composites and their failure mechanisms. *Composites Science and Technology*, 43(3), 237–244. [https://doi.org/10.1016/0266-3538\(92\)90094-J](https://doi.org/10.1016/0266-3538(92)90094-J)
- Digimat 2022.4 MAP User's Guide Digimat MAP User's Guide*. (1992). <https://simcompanion.hexagon.com>
- Digimat 2022.4 MX User's Guide Digimat MX User's Guide*. (1992). <https://simcompanion.hexagon.com>
- Hassan, A., Yahya, R., Yahaya, A. H., Tahir, A. R. M., & Hornsby, P. R. (2004). Tensile, impact and fiber length properties of injection-molded short and long glass fiber-reinforced polyamide 6,6 composites. *Journal of Reinforced Plastics and Composites*, 23(9), 969–986. <https://doi.org/10.1177/0731684404033960>
- Holmström, P. H., Hopperstad, O. S., & Clausen, A. H. (2020). Anisotropic tensile behaviour of short glass-fibre reinforced polyamide-6. *Composites Part C: Open Access*, 2, 100019. <https://doi.org/10.1016/j.jcomc.2020.100019>
- Huang, Z. M., Zhang, C. C., & Xue, Y. De. (2019). Stiffness prediction of short fiber reinforced composites. *International Journal of Mechanical Sciences*, 161–162. <https://doi.org/10.1016/j.ijmeosci.2019.105068>

- Huszar, M., Belblidia, F., Davies, H. M., Arnold, C., Bould, D., & Sienz, J. (2015). Sustainable injection moulding: The impact of materials selection and gate location on part warpage and injection pressure. *Sustainable Materials and Technologies*, 5, 1–8. <https://doi.org/10.1016/j.susmat.2015.07.001>
- Isaincu, A., Dan, M., Ungureanu, V., & Marşavina, L. (2021). Numerical investigation on the influence of fiber orientation mapping procedure to the mechanical response of short-fiber reinforced composites using Moldflow, Digimat and Ansys software. *Materials Today: Proceedings*, 45, 4304–4309. <https://doi.org/10.1016/j.matpr.2020.12.792>
- Isaincu, A., Micota, D., & Marsavina, L. (2022). On the Fracture Toughness of PPS and PPA Reinforced with Glass Fiber. *Procedia Structural Integrity*, 41(C), 646–655. <https://doi.org/10.1016/j.prostr.2022.05.073>
- Jørgensen, J. K., Andreassen, E., & Salaberger, D. (2019). The effect of fiber concentration on fiber orientation in injection molded film gated rectangular plates. *Polymer Composites*, 40(2), 615–629. <https://doi.org/10.1002/pc.24698>
- Li, K., Yan, S. L., Pan, W. F., & Zhao, G. (2017). Optimization of fiber-orientation distribution in fiber-reinforced composite injection molding by Taguchi, back propagation neural network, and genetic algorithm-particle swarm optimization. *Advances in Mechanical Engineering*, 9(9), 1–11. <https://doi.org/10.1177/1687814017719221>
- Lohr, C., Beck, B., Henning, F., Weidenmann, K. A., & Elsner, P. (2018). Process comparison on the microstructure and mechanical properties of fiber-reinforced polyphenylene sulfide using MuCell technology. *Journal of Reinforced Plastics and Composites*, 37(15), 1020–1034. <https://doi.org/10.1177/0731684418777120>
- Micota, D., Isaincu, A., & Marsavina, L. (2021). Micromechanical modeling of glass fiber reinforced plastic material. *Materials Today: Proceedings*. <https://doi.org/10.1016/j.matpr.2020.12.919>
- Micota, D., Isaincu, A., & Marşavina, L. (2021). Experimental testing of two short-fiber reinforced composites: PPA-GF33 and PPS-GF40. *Material Design and Processing Communications*. <https://doi.org/10.1002/mdp2.264>
- Ogierman, W., & Kokot, G. (2016). A study on fiber orientation influence on the mechanical response of a short fiber composite structure. *Acta Mechanica*, 227(1), 173–183. <https://doi.org/10.1007/s00707-015-1417-0>
- Oseli, A., Prodan, T., Susiç, E., & Slemenik Perše, L. (2020). The effect of short fiber orientation on long term shear behavior of 40% glass fiber reinforced polyphenylene sulfide. *Polymer Testing*, 81(August 2019). <https://doi.org/10.1016/j.polymertesting.2019.106262>
- Şerban, D. A., Maravina, L., & Silberschmidt, V. (2012). Behaviour of semi-crystalline thermoplastic polymers: Experimental studies and simulations. *Computational Materials Science*, 52(1), 139–146. <https://doi.org/10.1016/j.commatsci.2011.02.042>
- Şerban, D. A., Weissenborn, O., Geller, S., Marşavina, L., & Gude, M. (2016). Evaluation of the mechanical and morphological properties of long fibre reinforced polyurethane rigid foams. *Polymer Testing*, 49, 121–127. <https://doi.org/10.1016/j.polymertesting.2015.11.007>
- Skourlis, T. P., Pochiraju, K., Chassapis, C., & Manoochchri, S. (1998). Structure-modulus relationships for injection-molded long fiber-reinforced polyphthalamides. *Composites Part B: Engineering*, 29(3), 309–319. [https://doi.org/10.1016/s1359-8368\(97\)00011-5](https://doi.org/10.1016/s1359-8368(97)00011-5)
- Stepashkin, Chukov, D. I., Senatov, F. S., Salimon, A. I., Korsunsky, A. M., & Kaloshkin, S. D. (2018). 3D-printed PEEK-carbon fiber (CF) composites: Structure and thermal properties. *Composites Science and Technology*, 164, 319–326. <https://doi.org/10.1016/j.compscitech.2018.05.032>
- Takahashi, R., Shohji, I., Seki, Y., & Maruyama, S. (2014). Effect of fiber direction and temperature on mechanical properties of short fiber-reinforced PPS. *2014 International Conference on Electronics Packaging, ICEP 2014*, 778–781. <https://doi.org/10.1109/ICEP.2014.6826787>
- Tsai-Hill Criterion*. (n.d.).
- Zhang, K., Zhang, G., Liu, B., Wang, X., Long, S., & Yang, J. (2014). Effect of aminated polyphenylene sulfide on the mechanical properties of short carbon fiber reinforced polyphenylene sulfide composites. *Composites Science and Technology*, 98, 57–63. <https://doi.org/10.1016/j.compscitech.2014.04.020>
- Zhao, Y., Chen, Y., & Zhou, Y. (2019). Novel mechanical models of tensile strength and elastic property of FDM AM PLA materials: Experimental and theoretical analyses. *Materials and Design*, 181. <https://doi.org/10.1016/j.matdes.2019.108089>



Structural Integrity and Reliability of Advanced Materials obtained through Additive Manufacturing (SIRAMM23)

Fatigue behaviour of SLM maraging steel under variable-amplitude loading

Zbigniew Marciniak^{a,*}, Ricardo Branco^b, Wojciech Macek^c, Cândida Malça^{d, e}

^a Opole University of Technology, Department of Mechanics and Machine Design, Mikolajczyka 5, 45271 Opole, Poland

^b Department of Mechanical Engineering, University of Coimbra, CEMMPRE, ARISE, Rua Luis Reis Santos, 3030-788 Coimbra, Portugal

^c Gdansk University of Technology, Faculty of Mechanical Engineering and Ship Technology, 11/12 Gabriela Narutowicza, Gdansk 80-233, Poland

^d Department of Mechanical Engineering, Polytechnic Institute of Coimbra, Rua Pedro Nunes, Coimbra, 3030-199, Portugal

^e Centre for Rapid and Sustainable Product Development, Polytechnic Institute of Leiria, Rua de Portugal, Marinha Grande, 2430-028, Portugal

Abstract

One of the most challenging issues for additive manufactured materials is fatigue endurance. Engineering components often operate under complex, variable amplitude loadings, in which existing technological imperfections promote fatigue cracks growth and damage of elements eventually. In this study the effects of different variable-amplitude strain levels on fatigue life, 18Ni300 steel was tested. The work presents various behaviours of the material depending on the load level.

© 2023 The Authors. Published by Elsevier B.V.

This is an open access article under the CC BY-NC-ND license (<https://creativecommons.org/licenses/by-nc-nd/4.0>)

Peer-review under responsibility of the SIRAMM23 organizers

Keywords: Fatigue of material, SLM maraging steel, variable-amplitude loading

1. Introduction

Maraging steel is a special class of advanced high-strength steels, widely used in the aircraft, aerospace, military, offshore, tooling and mould making industries, due to the combination of unusual properties, namely high-strength,

* Corresponding author. Tel.: +4874498422.

E-mail address: z.marciniak@po.edu.pl

Nomenclature

ε_a	strain amplitude
σ_y	yield strength
σ_u	tensile strength
σ	stress
t	time
E	Young's modulus
N_f	number of cycles to failure
LCF	low cycle fatigue
HCF	high cycle fatigue

toughness, ductility, and weldability along with dimensional stability (Kempen K et al. 2011). Because of their martensitic matrix, these materials require a rapid quench from the austenitic region to temperatures below the martensite start temperature, which makes them particularly suited for the selective laser melting (SLM) technology. Although this alloy produced by SLM has been relatively studied in terms of microstructure features (Macek W. et al. 2022) and monotonic response for different manufacturing conditions (Branco, R. et al. 2012, Garcias J.F. et al. 2022), its behaviour under fatigue loading is not clear. Fatigue tests of SLM 18Ni300 steel have been mainly focused on determining the basic fatigue characteristics (Branco et al., 2018) but the deep understanding of fatigue behaviour under more complex loading is missing. Scientists are looking for the best fatigue parameters to effectively define the relationship between load and durability.

In the above-mentioned areas of application, most components experience variable-amplitude loading which makes them prone to fatigue failure. Under these service conditions, engineering design against fatigue requires not only a detailed knowledge on the loading history but also a deep understating of the cyclic deformation response (Marciniak Z. et al. 2008). Nevertheless, so far, very few studies have addressed the loading sequence effect and the damage accumulation mechanisms in fatigue life of maraging steel produced by selective laser melting. Thus, this paper studies the uniaxial fatigue behaviour of 18Ni300 maraging steel produced by selective laser melting under variable-amplitude loading.

2. Material and methods

The material selected for all experiments performed in this study was the 18Ni300 maraging steel produced by selective laser melting. The specimen geometries were fabricated with a vertical orientation, on the base plate, using a Concept Laser M3 linear printing system equipped with a Nd:YAG fibre laser (see Figure 1). The building strategy comprised the deposition of 40 μm thick layers, with a hatch spacing of 100 μm , at a scan speed of 200 mm/s. The nominal chemical composition of tested steel is presented in Table 1, and the mechanical properties are presented in Table 2.

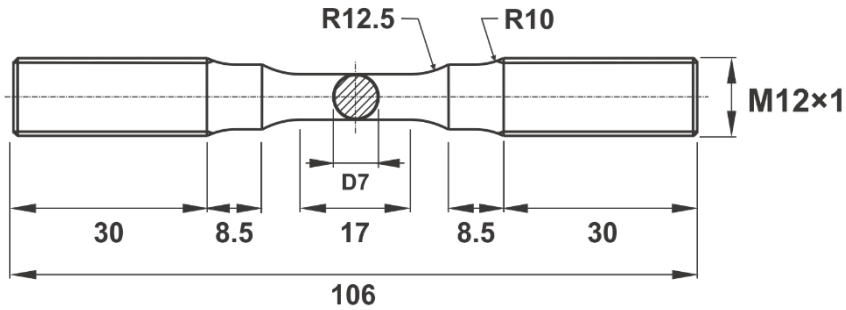


Fig. 1. Specimen geometries used in the low-cycle fatigue tests (unit: mm).

Table 1. Chemical composition (wt.%) of 18Ni300 steel manufactured by SLM.

C	Ni	Co	Mo	Ti	Al	Cr	P	Si	Fe
0.01	18.2	9.0	5.0	0.6	0.05	0.3	0.01	0.1	balance

Table 2. Mechanical properties of 18Ni300 steel manufactured by SLM.

Porosity (%)	Density (g/cm ³)	Hardness (HV1)	E (GPa)	σ_u (MPa)	σ_y (MPa)	Strain at Failure (%)
0.74±0.09	7.42	354±5	168±29	1147±13	910±11	5.12±0.001

The microstructure of the tested material is formed by grains elongated, with about 150 μm long and 35 μm width, see Fig. 2. It can also be seen martensitic needles dispersed throughout the entire surface. As expected, the laser passes are visible in the surface. Micrography shows small porosities (0.74%). Tests were performed in low-cycle fatigue (LCF) and high-cycle fatigue (HCF) regimes under fully-reversed strain-controlled conditions using cyclic sinusoidal waves on a 100 kN closed-loop servo-hydraulic testing machine (Instron).

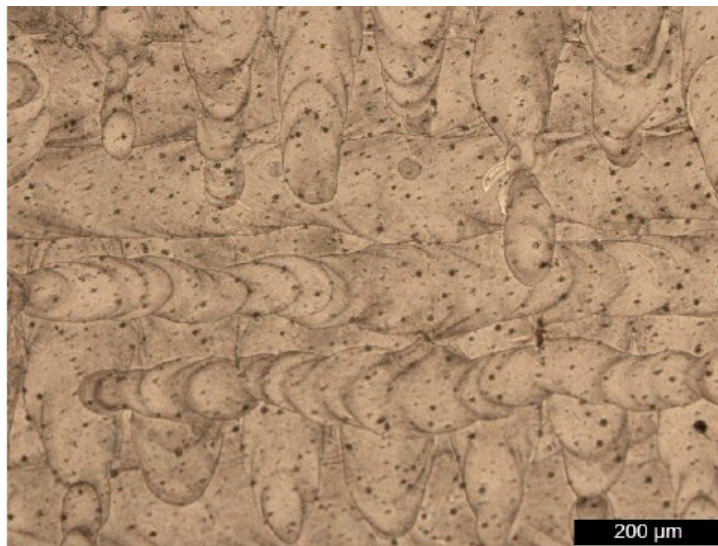


Fig. 2. Microstructure of the tested SLM 18Ni300 maraging steel. Reprinted from reference Branco et al., 2018. Low-cycle fatigue behaviour of AISI 18Ni300 maraging steel produced by selective laser melting, Metals 8(1), 32.



Fig. 3. Universal testing system Instron 8802.

The loading history consisted of two blocks of three cycles each (Fig. 4), repeated until failure. In the first block, the amplitude increased, and in the second they decreased. The amplitudes of the individual cycles were 50%, 75% and 100% of the maximum strain amplitude. The tests were carried out at four load levels at the maximum value of the strain amplitude: 1.00%, 0.75%, 0.50% and 0.35%. Twelve specimens were tested, three on each level.

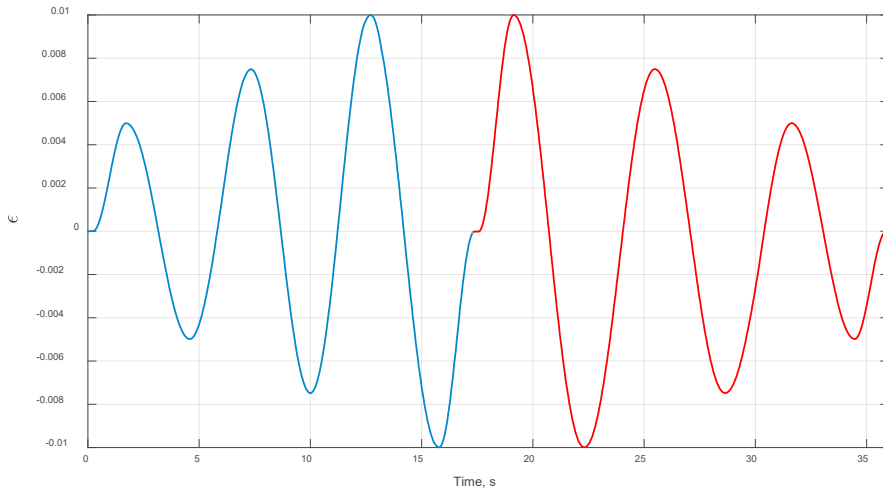


Fig. 4. The shape of the strain course carried out during the tests.

3. Results and discussion

During the tests, the deformation and stress courses were recorded continuously, as exhibited in Fig. 5, thanks to which the analysis of the behaviour of the tested samples was possible. The tests showed different transient responses of the material depending on the strain level. At the two highest load levels, the samples showed a cyclic softening behaviour (Fig. 5a), which was evident by the decrease in stress amplitude and the degeneration of the hysteresis loops throughout the test (Fig. 6). On the other hand, for the two lowest strain levels, where the value of plastic deformation was small, a stable behaviour was observed (Fig. 5b), and the stress level was constant until the crack appeared, as can be inferred from the hysteresis loops shown in Fig. 7.

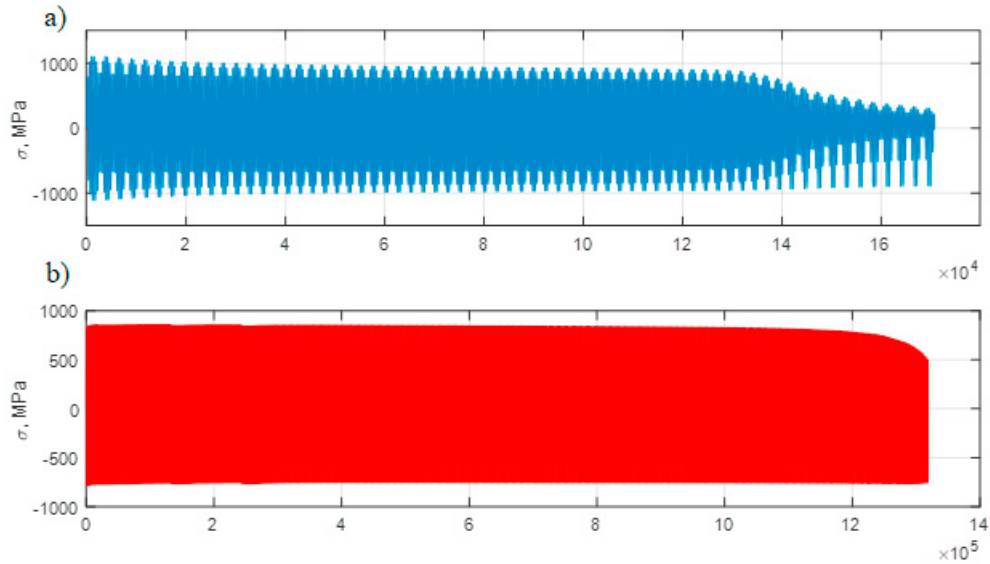


Fig. 5. Stress changes during the tests for the maximum strain amplitude: a) 1%, b) 0.5%.

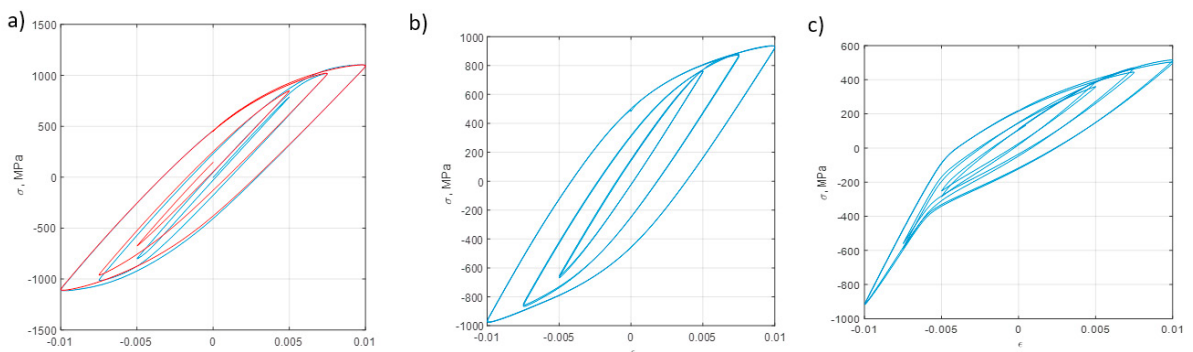


Fig. 6. Examples of the hysteresis loops collected in the tests at a maximum strain amplitude of 1% for different stages of fatigue life: a) at the beginning, b) in the middle, c) before failure.

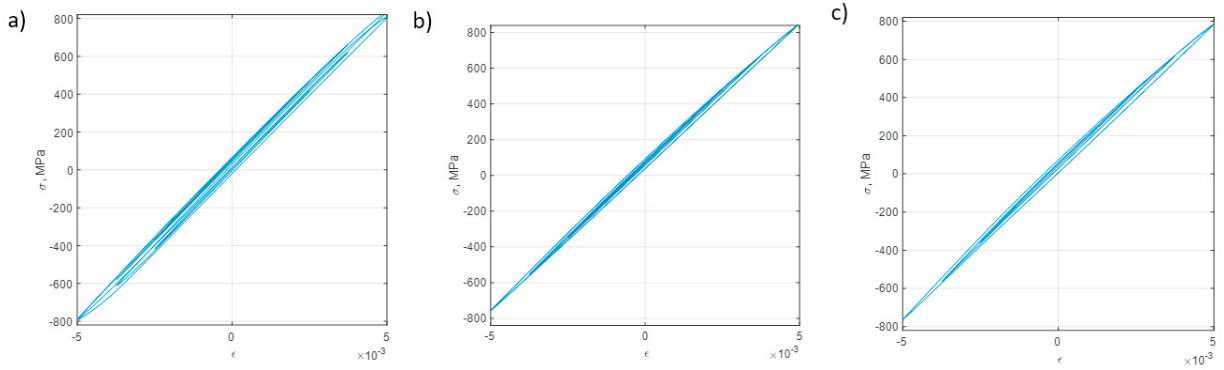


Fig. 7. Examples of the hysteresis loops collected in the tests a maximum strain amplitude of 0.5% for different stages of fatigue life: a) at the beginning, b) in the middle, c) before failure.

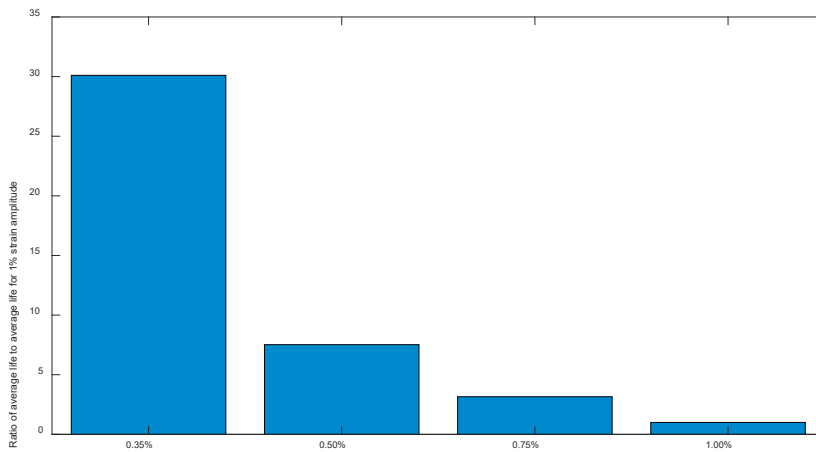


Fig. 8. Ratio of average fatigue life to average fatigue life for 1% strain amplitude.

The analysis of the obtained results showed a significant increase in durability with a decrease in the maximum strain amplitude. This behaviour can be seen in Fig. 8, which shows the ratio of the average fatigue life to the average fatigue life for a strain amplitude of 1%. Research has shown that a decrease in load amplitude by 25% resulted in an increase in durability about three times, and a 50% decrease in amplitude resulted in an increase in durability about eight times. On the other hand, reducing the amplitude value by 65% extended the durability 30 times (see Fig. 8).

4. Conclusions

Based on the obtained test results, it was noticed that for the two highest loading levels, where the maximum strain amplitude was 1.00% and 0.75%, the material cyclically softened, which was evident by about a 20% decrease in the stress amplitude, while for the other two loading scenarios, it behaved stably, i.e. the transient response was negligible. The average fatigue life increased, concerning the average fatigue life at the maximum strain amplitude of 1.00%, three times (at a strain amplitude of 0.75%), eight times (at a strain amplitude of 0.50%) and over thirty times (at a strain amplitude of 0.35%).

Acknowledgements

This research is sponsored by national funds through FCT – Fundação para a Ciência e a Tecnologia, under the project UIDB/00285/2020 and LA/P/0112/2020.

Authors also acknowledge Science and Technology Park in Opole for enabling access to fatigue test equipment.

References

- Kempen K, Yasa E, Thijs L, Kruth JP, Van Humbeeck J (2011). Microstructure and mechanical properties of selective laser melted 18Ni-300 steel. *Physics Procedia* 12, 255-263.
- Silva T, Silva F., Xavier J., Gregório A., Reis A., Rosac P., Konopik , Rundd M., Jesus M.. Mechanical Behaviour of Maraging Steel Produced by SLM. *Procedia Structural Integrity*. 45-50
- Garcias, J.F., Martins R.F., Branco R., Marciniak Z., Macek W., Pereira C., Santos C. Quasistatic and fatigue behavior of an AISI H13 steel obtained by additive manufacturing and conventional method. *Fatigue and Fracture of Engineering Materials and Structures* 44, 3384-3398
- Branco, R., Costa, J.D., Antunes, F.V., (2012). Low-cycle fatigue behaviour of 34CrNiMo6 high strength steel. *Theoretical and Applied Fracture Mechanics* 58, 28-34.
- Macek W., Martins R.F., Branco R., Marciniak Z., Szala M., Wronski S.,(2022), Fatigue fracture morphology of AISI H13 steel obtained by additive manufacturing. *International Journal of Fracture* 235, 79-98.
- Branco, R., Martins, R.F., Correia, J.A.F.O., Marciniak, Z., Macek, W., Jesus, J., 2022. On the use of the cumulative strain energy density for fatigue life assessment in advanced high-strength steels. *International Journal of Fatigue* 164, 107121.
- Branco R. Costa J.D.M., Berto F., Razavi S.M.J., Ferreira J.A.M., Capela C., Santos L., Antunes F., 2018. Low-cycle fatigue behaviour of AISI 18Ni300 maraging steel produced by selective laser melting, *Metals* 8(1), 32
- Marciniak Z, Rozumek D, Macha E (2008). Fatigue lives of 18G2A and 10HNAP steels under variable amplitude and random non-proportional bending with torsion loading. *International Journal of Fatigue* 30, 800-813.



Structural Integrity and Reliability of Advanced Materials obtained through Additive Manufacturing (SIRAMM23)

Fatigue Life and Crack Growth Rate Prediction of Additively Manufactured 17-4 PH Stainless Steel using Machine Learning

B. Kalita^{a,*}, R.C. Abhiraaj^a, R. Jayaganthan^b

^aStudent, Engineering Design Department, IIT Madras, Chennai, India-600036

^bProfessor, Engineering Design Department, IIT Madras, Chennai, India-600036

Abstract

The present work is focused on machine learning-assisted predictions of the low cycle fatigue behaviour and fatigue crack growth rate (FCGR) of 17-4 PH SS processed through L-PBF and post-processing. Various machine learning techniques reported in the literature provided a flexible approach for explaining the complex mathematical interrelationship among processing-structure-property of the materials. In the present work, four machine learning (ML) algorithms, such as K-Nearest Neighbor (KNN), Decision Trees (DT), Random Forests (RF), and Extreme Gradient Boosting (XGB) algorithms, are implemented to analyze the Fatigue Crack growth rate (FCGR) of 17-4 PH SS alloy. After optimizing the hyper parameters for these algorithms, the trained models were found to estimate the unseen data as equally well as the trained data. The four tested ML models are compared among each other over the training as well as the testing phase based on their mean squared error and R2 scores. Extreme Gradient Boosting model has performed better for the FCGR predictions providing the least mean squared errors and higher R2 scores compared to other models.

© 2023 The Authors. Published by Elsevier B.V.

This is an open access article under the CC BY-NC-ND license (<https://creativecommons.org/licenses/by-nc-nd/4.0>)

Peer-review under responsibility of the SIRAMM23 organizers

Keywords: Fatigue; 17-4 PH SS; Machine learning; Additive manufacturing.

1. Introduction

In the field of internet of things, data may now be shared and retrieved via cloud-based data storage systems from any location in the globe [1]. Thus, the introduction of advanced data collection and interpretation techniques, such as support vector mechanisms, decision trees, and random forests approaches, can address the shortcomings in the current

* Corresponding author. Tel.: +91 6000585610.

E-mail address: ed20d003@smail.iitm.ac.in

failure prediction methods, such as inconsistency in the prediction and inability to solve complex nonlinear damage mechanics [2-4]. Using a backpropagation neural network (BPNN) and extreme learning machine (ELM), Raja et al. [4] have estimated the FCGR of Al 2014 alloy and concluded that ELM better on the dataset. Nowadays, in the era of Industry 4.0, data can be shared and retrieved from anywhere around the globe using cloud-based data storage methods [5].

The term machine learning (ML) refers to the application of sophisticated algorithms developed using programming languages like Python to teach a computer to perform a given task accurately. Machine learning techniques are way too easy and flexible as compared to designing numerical equations because of their non-linear activation functions [6, 7].

2. Materials and Methods

The 17-4 PH stainless steel is a martensitic alloy that can be precipitation hardened when used in traditional manufacturing processes. Within an L-PBF process, it will exhibit up to 5% lower yield strength and 6% higher elongation [8]. Due to their popularity in various structural applications, high fatigue resistance is particularly desirable for 17-4 PH SS. Therefore, many recent studies focused on the fatigue crack initiation behavior of L-PBF 17-4 PH SS [11]. In this investigation, specimens were made from Stainless steel 17-4 PH powder that had been atomized with argon using the laser powder bed fusion (LPBF) method.

In order to build the ML models, relevant experimental Fatigue data of 17-4 PH SS alloy is collected from the literature. Electrical discharge machining (EDM) was used to create compact tension (CT) specimens from fabricated samples in the EOS M290 in an argon-shielded environment [9]. CT samples containing the same measurements were also fabricated from wrought 17-4 PH stainless steel plates as it is pertinent to contrast the mechanical characteristics of L-PBF 17-4 PH SS with its wrought equivalent. Based on the orientation of the notch in regard to the building direction, L-PBF 17-4 PH SS specimens were machined [10-12]. After machining, L-PBF 17-4 PH SS specimens were put through the heat treatment processes [13, 14]. Contrary to samples treated to 1072 MPa yield strength, 1132 MPa ultimate various deformation behaviors, the specimens treated to 1300 MPa yield strength, 1375 MPa ultimate strength, and 0.16 true fracture strain have more strength and ductility [15]. It is essential to determine the constituent phases to analyze the crack growth behavior related to microstructure because of their varied deformation characteristics. For this, the TCFE9 thermodynamic database for several kinds of steels and alloys based on Fe, including stainless steels, was used [16].

2.1. Fractography and the fatigue crack growth test (FCG)

On a testing device for servo-hydraulic systems, FCG experiments were carried out. Low-stress fatigue on CT samples under load control, at room temperature, using a sinusoidal loading waveform with a load ratio $R = 0.1$ and a frequency $f = 10$ Hz until failure experiments (also known as high cycle fatigue regime) were carried out [15]. Because pre-cracking was conducted under the same stress as for the fatigue crack growth rate testing, there won't be a crack tip plastic zone size disparity to contend with. The load amplitudes ranged from 4275 N to 1575 N. The recorded CMOD values, the load range, and the observed cycle count were used to determine the FCG rate, da/dN , and stress intensity factor ranges (ΔK), in accordance with ASTM E647. Four CT samples from each group were subjected to FCG testing to address variability.

The following variables are the key factors affecting Fatigue Crack Growth rate:

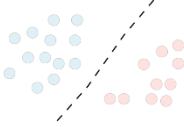
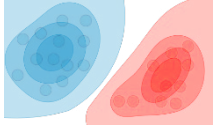
- Average stress impact (mean stress effect)
- Environment
- Short cracking effect
- Underloads and overloads

The stress-life method can be used to determine a material's fatigue life, the crack-growth method, the strain-life method, and probabilistic methodologies. It may be based on techniques for crack or life growth.

2.2. Machine Learning Techniques

With a series of data points $\{x(1), \dots, x(m)\}$ linked to a set of outcomes $\{y(1), \dots, y(m)\}$, we want to build a classifier that can learn to predict y . Prediction type - The following table provides a summary of the various categories of predictive models:

Table 1. Categories of predictive models [4, 5].

An example of a column heading	Column A (t)	Column B (t)
Goal	Directly estimate $p(y x)$	Estimate $p(x y)$ to deduce $p(y x)$
What's learned	Decision boundary	Probability distributions of the data
Illustration		
Examples	Regressions, SVMs	GDA, Naive Bayes

2.3. Hypothesis

The model we select is indicated by the letter h . The model's output for a given input value $x(i)$ is $h(x(i))$. A loss function is a function that determines how different two inputs—the anticipated value z that corresponds to the actual data value y —are from one another.

An estimator's mean squared error in statistics calculates the average squared difference between the estimated values and the actual value. The expected value of the squared error loss correlates with the risk function (loss) known as MSE. Additionally, MSE is usually always just ever positive (and not zero) due to chance or because the estimator ignored information that might have allowed for a more accurate estimate. Additionally, MSE is usually always just ever positive (and not zero) due to chance or because the estimator ignored information that might have allowed for a more accurate estimate. Machine learning refers to the typical loss on a collection of observed data as MSE as an estimate of the true MSE. Mean absolute error is a statistician's measure of errors between identically matched observations. Comparing expected data to seen data is an example of a Y vs X comparison, subsequent time to initial time, and one measuring technique to another. Thus, the absolute errors $|e_i| = |y_i - x_i|$, where $y(i)$ is the forecast and $x(i)$ is the true value, are averaged using math.

A ROC curve is produced by comparing the true positive rate (TPR) and false positive rate (FPR). The percentage of observations among all positive observations that were correctly anticipated to be positive is known as the true positive rate ($TP/(TP + FN)$). The false positive rate ($FP/(TN + FP)$) is the proportion of observations that are incorrectly projected to be positive among all negative observations. For instance, the true positive rate in a medical test is the percentage of patients who are actually diagnosed as having the disease under consideration.

2.4. Classification and Regression

It is a process of understanding and recognising ideas and objects, then classifying them into specified categories, frequently referred to as "sub-populations." Utilizing these pre-categorized training datasets, ML programs employ a range of methods to organize incoming information into important and acceptable classifications. Machine learning classifiers estimate the likelihood or probability that the data that follows will fall into one of the predetermined categories using the incoming training data.

Examining a link between independent variables (features) and a dependent variable is done through regression (outcome). It is a machine learning-based approach to predictive modelling where an algorithm is employed to forecast continuous outcomes. A very popular use of machine learning models, when it comes to supervised machine learning, is to solve regression problems. The link between independent inputs and results is taught via algorithms (dependent variable). After that, the algorithm/model is applied to predict the results of novel, previously unseen input features or to fill in missing data. For this method of training models, the features and output must be labelled data. A crucial

aspect is that the training data should be properly labelled since machine learning based regression models need to comprehend the link between input and output variables.

Regression analysis, whether used to support stock market predictions or forecast healthcare trends, can give the different organisations important information to help make decisions. Using a sort of regression approach known as polynomial regression, the relationship between the features and the outcome is modelled as an nth degree polynomial.

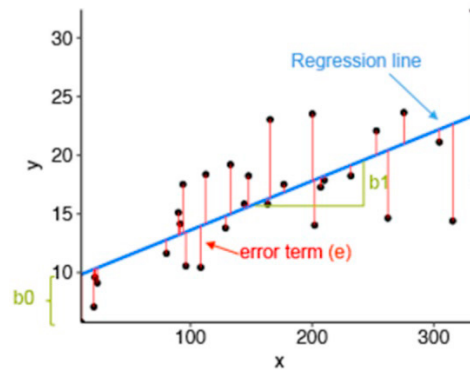


Fig. 1. : Linear regression curve [7]

2.5. Comparing ML Algorithms

ML techniques vary among themselves in terms of complexity. For instance, while neural networks employ a real-valued function of linear variable bounds, linear regression fits linear functions. More complicated models run the risk of overfitting but can produce more accurate results.

While some models such as linear regression and neural network (NN) have minimal parameters, others require more decision-making to be optimized such as Support Vector Machines (SVMs). Models vary in how quickly they can fit the required parameters. The speed at which a model can predict a given query varies between the models.

Some models are more understandable and straightforward than others (white box vs. black box models). If a model can take the inputs, and routinely get the same outputs, the model is interpretable. Interpretability poses no issue in low-risk scenarios. If a model is recommending movies to watch, that can be a low-risk task. Interpretability sometimes needs to be high in order to justify why one model is better than another.

3. Results and Discussion

Relevant experimental Fatigue data of 17-4 PH Stainless Steel has been gathered in order to create the ML model from already published and pertinent literature. For the purpose of determining the FCGR properties, conventional Compact Tension (CT) samples were made from grade 5 17-4 PH SS spherical powder. Sizes of the powder particles ranged from 15 to 45 micrometers. FCGR tests were carried out in accordance with ASTM E647 guidelines. A pre-crack of size 1mm was generated and manufactured prior to FCGR examination. V. Cain et al. observed three alternative build orientation XY, XZ, and ZX as well as post-processing methods for each orientation as-built, heat treated, and stress relieved were varied along with cyclic loading of 5 Hz and a 0.1 stress ratio under processing conditions. Following stress release, heat-treated samples were annealed at 890 °C for two hours after being soaked at 650 °C for a few hours. The data for the post-processing mentioned above were pulled from the literature while the process parameters were optimized. For the predictive study of the FCGR of 17-4 PH SS, data from the Paris law graphs are collected and used for each distinct processing and post-processing scenario. The data points which are collected are plotted for visualization during the analysis and shown in Figure. 2.

3.1. Data and description

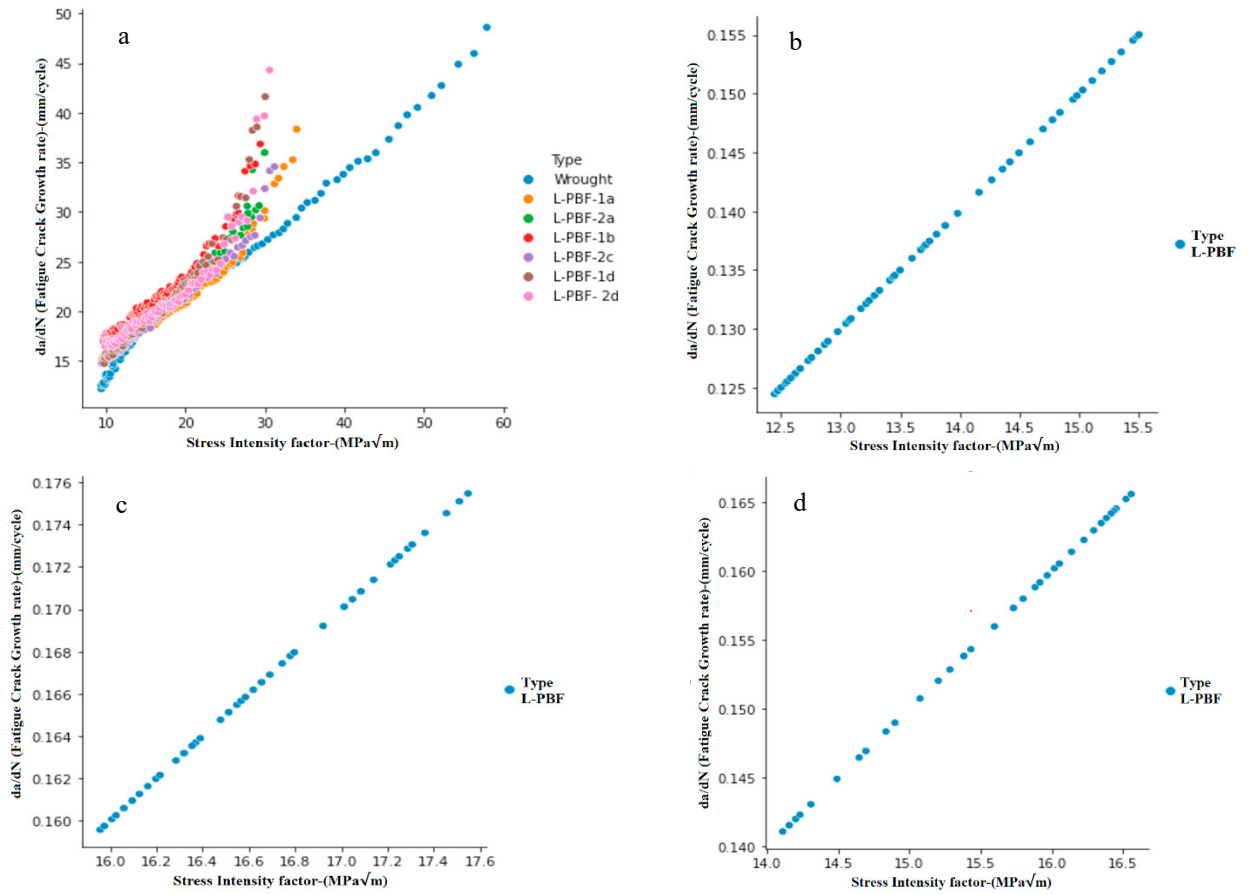


Fig. 2. SIF vs fatigue crack growth rate (a) different L-PBF studies, (b) XY, (c) XZ and (d) ZX specimen build orientation.

3.2. Prediction model

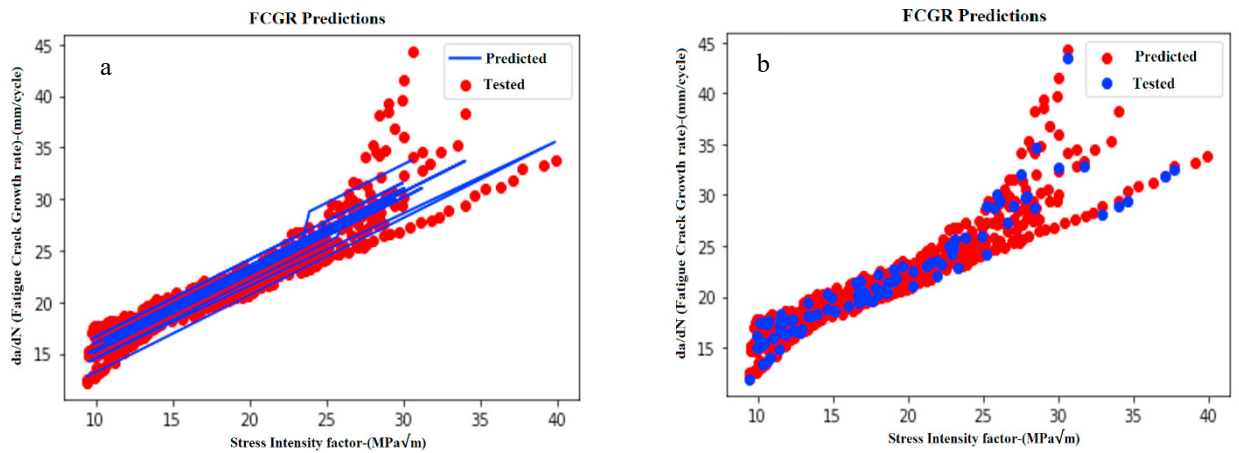


Fig. 3. Actual and prediction plots for fatigue crack growth rate predictions (a) normal plot and (b) scattered plot.

4. Conclusion

Fatigue crack growth rate behaviour of additively manufactured (fabricated by L-PBF) 17-4 PH SS alloy with respect to different specimen conditions was analyzed by using machine learning techniques. The following findings have been drawn from this study. It is suggested to calculate the growth of fatigue cracks using machine learning techniques, and the linear regression model has been used to investigate the link between the rate of fatigue crack growth and the stress intensity component. Utilizing testing data from various datasets, the trained model was verified. The findings reveal that the model can accurately predict the fatigue crack formation rate nonlinearities, and the performance of model-based fatigue crack growth is acceptable for diverse experimental results. It was observed that the Linear Regression algorithm has led to best R2 score and least mean squared error in predicting the FCGR of 17-4 PH SS alloy. In the feature importance analysis, apart from ΔK , the important parameters identified are Post Processing technique and Built Orientation for predicting the FCGR of 17-4 PH Stainless Steel alloy. Since the optimization of processing and post processing parameters are still in developing stage in metal additive manufacturing, data-driven models can help in establishing the appropriate set of input variables. An effective property predictive model can improve the understanding of FCGR mechanisms which would help to design the materials with high performance.

Acknowledgements

I would like to express my sincere gratitude towards my guide, Prof. R. Jayaganthan, Department of Engineering Design, Indian Institute of Technology Madras, for his invaluable advice and meticulous guidance throughout this project. I would also like to thank the members of the Materials Design & Additive Manufacturing lab, Department of Engineering Design, IIT Madras, for their timely advice and help during this study.

References

- Rovinelli A, Sangid MD, Proudhon H, Ludwig W. Using machine learning and a data-driven approach to identify the small fatigue crack driving force in polycrystalline materials. *npj Computational Materials*. 2018 Jul 16;4(1):35.
- Melching D, Strohmann T, Requena G, Breitbart E. Explainable machine learning for precise fatigue crack tip detection. *Scientific Reports*. 2022 Jun 9;12(1):9513.
- Konda N, Verma R, Jayaganthan R. Machine Learning based predictions of fatigue crack growth rate of additively manufactured Ti6Al4V. *Metals*. 2021 Dec 27;12(1):50.
- Raja A, Chukka ST, Jayaganthan R. Prediction of fatigue crack growth behaviour in ultrafine grained al 2014 alloy using machine learning. *Metals*. 2020 Oct 9;10(10):1349.
- Zhang L, Wang Z, Wang L, Zhang Z, Chen X, Meng L. Machine learning-based real-time visible fatigue crack growth detection. *Digital Communications and Networks*. 2021 Nov 1;7(4):551-8.
- Zhan Z, Li H. Machine learning based fatigue life prediction with effects of additive manufacturing process parameters for printed SS 316L. *International Journal of Fatigue*. 2021 Jan 1;142:105941.
- Bock, F.E.; Aydin, R.C.; Cyron, C.J.; Huber, N.; Kalidindi, S.R.; Klusemann, B. A Review of the Application of Machine Learning and Data Mining Approaches in Continuum Materials Mechanics. *Front. Mater*. 2019, 6, 1–23.
- Nezhadfar PD, Burford E, Anderson-Wedge K, Zhang B, Shao S, Daniewicz SR, Shamsaei N. Fatigue crack growth behavior of additively manufactured 17-4 PH stainless steel: Effects of build orientation and microstructure. *International Journal of Fatigue*. 2019 Jun 1;123:168-79
- Daniewicz SR, Shamsaei N. An introduction to the fatigue and fracture behavior of additive manufactured parts. *International Journal of Fatigue*. 2017;2(94):167.
- Herzog D, Seyda V, Wycisk E, Emmelmann C. Additive manufacturing of metals. *Acta Materialia*. 2016 Sep 15;117:371-92.
- Yadollahi A, Shamsaei N. Additive manufacturing of fatigue resistant materials: Challenges and opportunities. *International Journal of Fatigue*. 2017 May 1;98:14-31.
- Yang KV, Rometsch P, Jarvis T, Rao J, Cao S, Davies C, Wu X. Porosity formation mechanisms and fatigue response in Al-Si-Mg alloys made by selective laser melting. *Materials Science and Engineering: A*. 2018 Jan 17;712:166-74.
- Romano S, Nezhadfar PD, Shamsaei N, Seifi M, Beretta S. High cycle fatigue behavior and life prediction for additively manufactured 17-4 PH stainless steel: Effect of sub-surface porosity and surface roughness. *Theoretical and Applied Fracture Mechanics*. 2020 Apr 1;106:102477
- Kardomateas GA, Geubelle PH. Fatigue and fracture mechanics in aerospace structures. *Encyclopedia of Aerospace Engineering*. 2010 Dec 15.
- Stanzl-Tscheegg SE. When do small fatigue cracks propagate and when are they arrested?. *Corrosion Reviews*. 2019 Oct 1;37(5):397-418.
- Schütz, W. Fatigue life prediction of aircraft structures—Past, present and future. *Eng. Fract. Mech*. 1974, 6, 745–762.



Structural Integrity and Reliability of Advanced Materials obtained through Additive Manufacturing (SIRAMM23)

Highlights on the Influence of Thermal Reprocessing of PLA on Mechanical Properties

Dan Ioan Stoia^a, Gerlinde Rusu^a, Anghel Cernescu^{a*}

^aPolitehnica University of Timisoara, Mihai Viteazul no.1, Timisoara 300222, Romania

Abstract

FDM is one of the most popular additive manufacturing techniques through 3D printing. Within this technique, one of the intensively studied subjects is the analysis of the factors that influence the mechanical behavior of the 3D printed parts. However, despite numerous studies that show the influence of parameters such as raster orientation, layer height/thickness, build orientation, number of layers, there are some other process parameters which are less analyzed. Due to some interactions between the effects due to different parameters, it becomes challenging to analyze influences on the mechanical behavior of 3D printed materials. Less studied subject is the mechanical behavior of the extruded filament through the nozzle and the interaction between deposited traces. The mechanical behavior of the air extruded filament, the one trace, two traces and fourteen traces deposition were experimentally analyzed in the paper by tensile testing. Also, the mechanical behavior of the raw filament was checked. In addition, the differential scanning calorimetry (DSC) was conducted on raw filament and extruded filament in order to identify the relation between the crystallinity of the polymer after thermal reprocessing with the mechanical properties. The raw filament is typically a continuous and homogenous material with consistent diameter and structure. However, when the filament is extruded through the nozzle its mechanical behavior will significantly change due to thermal reprocessing. Among the factors that influence the properties are: extruder temperature, platform temperature, extruding velocity, cooling, flow rate of the extruded filament. All can affect the crystallinity of the polymer on one hand and the strength of the adhesion between the consecutive traces on the other hand, as the results are quantifying it.

© 2023 The Authors. Published by Elsevier B.V.

This is an open access article under the CC BY-NC-ND license (<https://creativecommons.org/licenses/by-nc-nd/4.0>)

Peer-review under responsibility of the SIRAMM23 organizers

Keywords: PLA, FDM, Tensile testing, Printing traces, Fillers, DSC.

*Corresponding authors. E-mail address: anghel.cernescu@upt.ro

1. Introduction

3D printing technology is an additive manufacturing process by which a digital model is transposed into a physical model. Fused Deposition Modeling (FDM) is one of the most used 3D printing technologies, by which a thermoplastic filament is melted, extruded and deposited in layers to build the geometry of the printed model [1, 2]. As much as it is used due to its multiple advantages such as low cost of the printers and the raw material respectively the good quality of the printed products, FDM is a highly accessed research topic. One of the subjects analyzed in many studies is the effect of the process parameters on the mechanical behavior of the printed parts. There are many parameters that influence the mechanical properties of the 3D printed parts, such as, [3]: extrusion temperature, print speed, infill pattern and density, build orientation, raster orientation and width, layer thickness and color, [4]. Due to the large numbers of parameters, which require a large volume of experiments, different experimental strategies have been developed such as full-factorial design [5], Taguchi method [6], ANOVA [7], path planning strategies [8], automated neural network search [9], and fuzzy logic [10]. These strategies lead to identification of the best combinations of parameters that improve the mechanical properties of the printed materials, with a reduced volume of experimental tests.

A less studied subject, and which is the objective of this paper, is the mechanical behavior of the adhesion between the consecutive traces of the deposited material and also of the air extruded filament. So, the aim of the paper is to conduct tensile tests on the following extruded samples: air extruded, one trace deposited on the platform, two consecutive traces deposited on the platform and fourteen consecutive traces deposited on the platform and also for the raw filament (Figure 1). In addition, in order to establish the relation between the degree of the crystallinity of the polymer and the mechanical properties, differential scanning calorimetry tests were conducted.

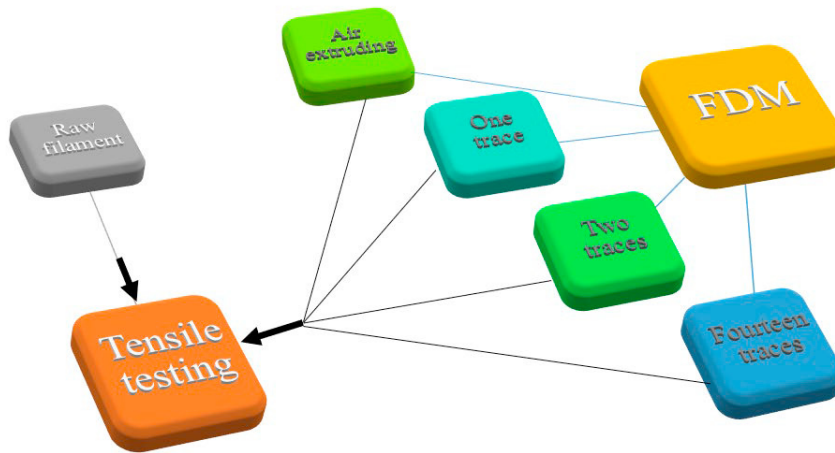


Fig. 1. Block illustration of the study

Nomenclature

Φ_1	diameter of the filament
Φ_2	diameter of the air extruded PLA
d	thickness of the deposited trace
b_1	width of the deposited material (one trace)
b_2	width of the deposited material (two traces)
b_3	width of the deposited material (fourteen traces)

2. Material and methods

The investigated material is a yellow color polylactic acid (PLA) filament with a diameter of 1.75 mm. The PLA filament is a semi-crystalline and recyclable thermoplastic polyester that is derived from renewable resources such as corn starch or sugar cane. The filament is biodegradable with high heat capacity and good mechanical strength.

The analysis carried out in the paper is based on tensile tests on the following types of samples: raw filament; air extruded filament, one trace deposited on the platform, two consecutive traces deposited on the platform and fourteen consecutive traces deposited on the platform (figure 2).

The printing was done on a Makerbot Sketch 3D printer, keeping the printing parameters constant: build plate temperature + 50°C; extruder temperature + 220 °C; extruder print speed – 35 mm/s. In order for the filament to be easily removed from the platform's surface, the platform was covered with adhesive tape. The deposition consists only in 1 layer.

After printing the samples were subjected to microscopical examination in order to identify defects in adhesion between traces, in the purpose of removing those samples from the mechanical testing. In the figure 3 it can be observed at 5:1 scale, the image of the raw filament and the sample that consist in fourteen deposited traces.

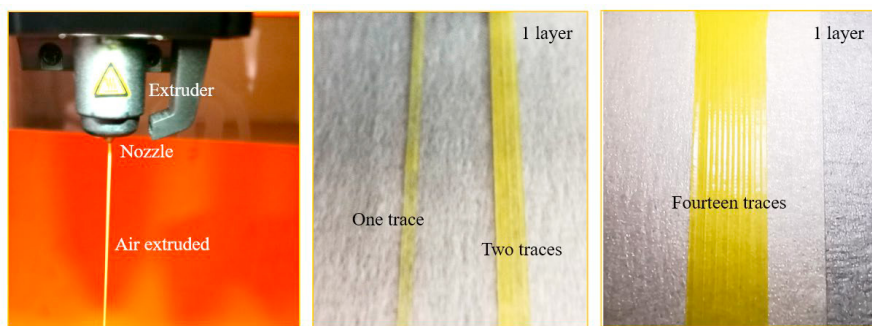


Fig. 2. Air extruded and filament deposition on the platform.

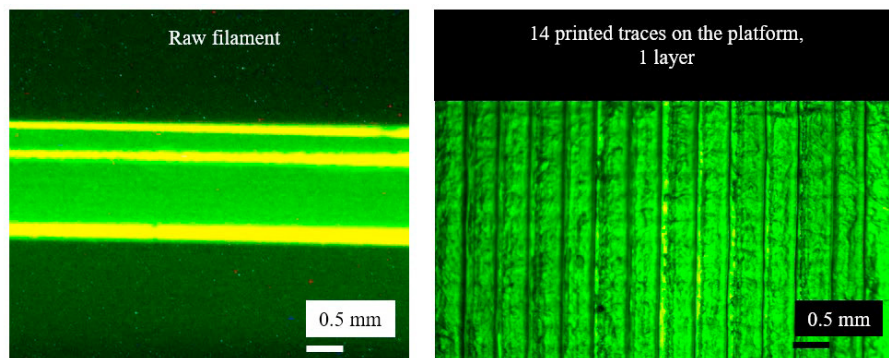


Fig. 3. Microscopic images of (a) raw filament and (b) 14 printing traces, 40X.

The filaments were tested on a Metrotec universal testing machine (figure 4), with a load rate of 2 mm/min. Two load cells of 50 N and 1000 N respectively, same accuracy, were used. The cross-sections of the original and air-printed filaments are circular, with diameters of $\Phi_1 = 1.75$ mm and $\Phi_2 = 0.5$ mm, respectively. The cross-sections of the deposited traces were microscopically measured and approximated to an elliptical shape for one deposition trace,

and rectangular shape for two traces and fourteen traces. The dimensions considered for determining the sections are presented in the figure 5. The resulted sections were used in computing the tensile stresses.

Differential Scanning Calorimetry analysis were performed using DSC 204 F1 Phoenix equipment (Netzsch) on two types of samples: raw filament and extruded filament. Curves were recorded under nitrogen to prevent moisture and oxidative degradation and under dynamic conditions from room temperature to 300°C with 10 K/min heating rate. The samples (around 5 mg) were placed in closed aluminum crucibles (average mass 39±0.2 mg). Data were analyzed using Proteus Analysis 6.1.0 software.

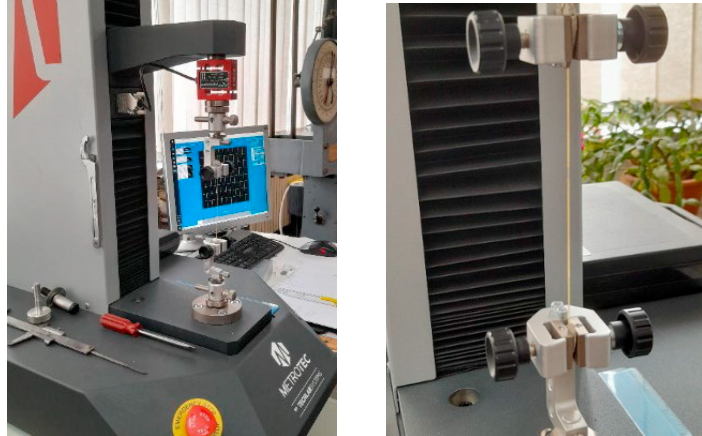


Fig. 4. Filament test stand and machine.

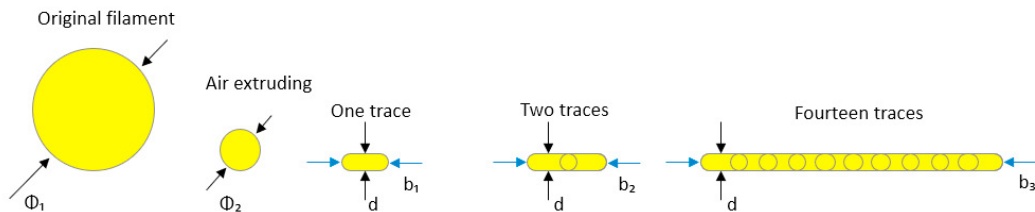


Fig. 5. Characteristic dimensions of the considered cross sections

3. Results and discussions

The analysis of the tensile tests results followed a chain approach. In the figure 6 are presented all stress-strain curves according to the sample types. All curve follows the same trend until a maximum stress is recorded, followed by a drop in the curve to a stabilization level, where the stress remains constant and the material elongates until breaking.

The behavior of the for raw filament and air extruded filament are similar in terms of tensile strength and elongation at break, meaning that the internal structure of the polymer remains similar after thermal reprocessing. The fine details in property difference will be further explained by DSC analysis.

In the case of fourteen traces samples, only the elongation at breaks shows a reduction compared to the air-printed filament. This can be put on slower cooling rate to solidification due to the heated platform. The cooling rate is directly influencing the crystallinity of the polymer, slow cooling leading to high crystallinity and therefore smaller elongation at break. In addition, the adhesion between the filaments helps in maintaining a high tensile strength.

A notable drop in properties can be observed for the one trace and two traces samples (figure 6 d and e). This low tensile strength and elongation compared to the air-printed and raw filament can be explained as a combined effect of faster cooling rate of the samples (due to their sizes) and the deformed shape of the cross section and overall texture.

Table 1 shows the tensile strength and elongation at break for all specimen types as average and standard deviation. The higher standard deviation for one and two deposition traces shows a large variability of the testing data, which is an indicator of a low process stability when comes to only one or two printed traces. The very low elongation at break in one and two traces compared to the raw filament is the indicator of rapid cooling of these samples.

In conclusion, the material printed on the build platform has lower mechanical properties compared to the raw filament and respectively to air-printed one.

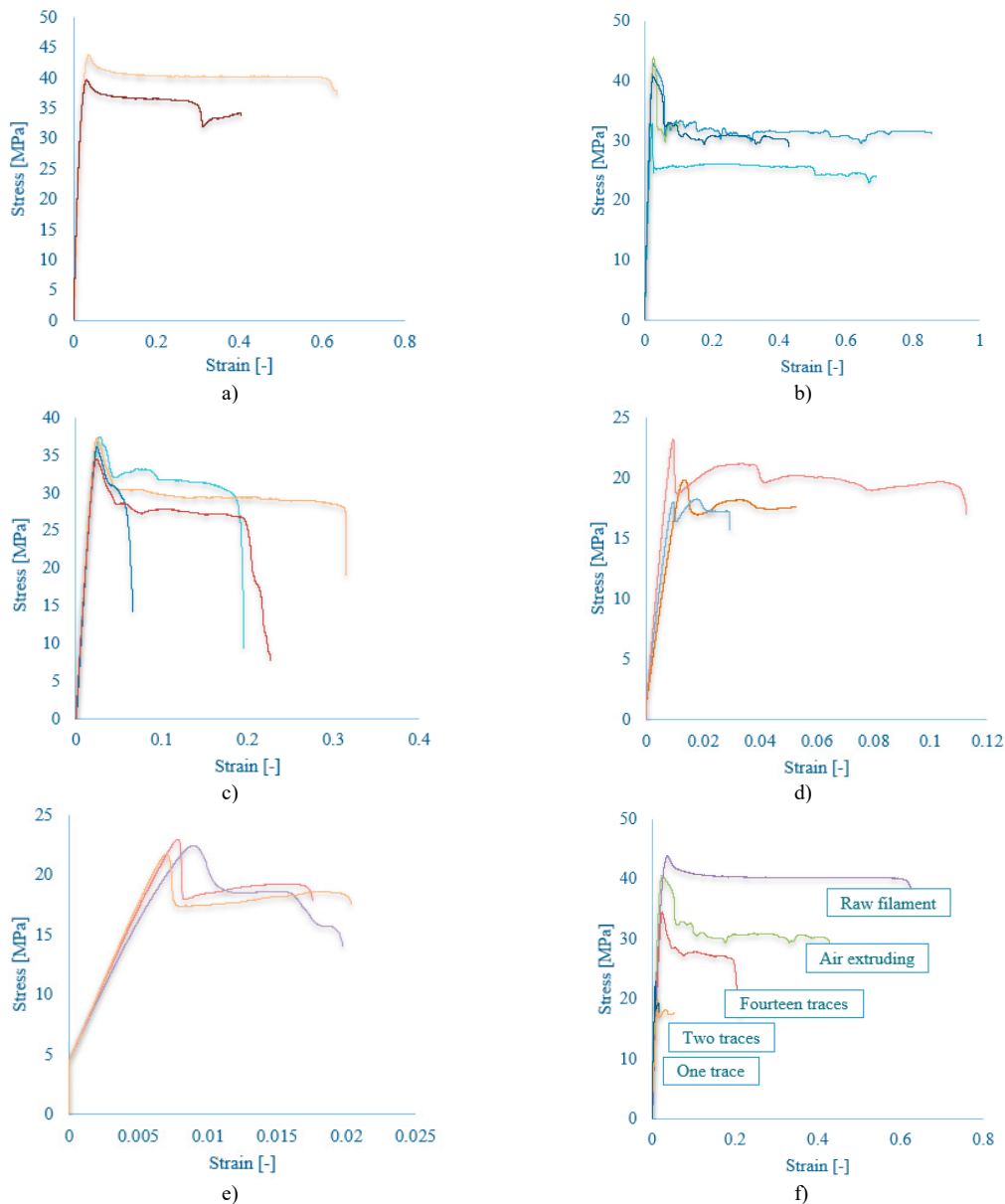


Fig. 6. Stress strain curves for tensile tested (a) raw filament; (b) air extruded; (c) fourteen deposited traces; (d) two deposited traces; (e) one deposited trace; (f) representative curves for all samples.

Table 1. Mechanical properties of the samples.

Sample type	Maximum Tensile Strength [MPa]	Elongation at break [%]
Raw filament	41.18 ± 1.86	54.71 ± 12.44
Air extruded	40.06 ± 4.97	51.94 ± 32.80
Fourteen deposited traces	36.35 ± 1.35	24.88 ± 6.49
Two deposited traces	33.18 ± 10.46	6.05 ± 3.86
One deposited trace	31.88 ± 10.64	2.72 ± 1.60

The thermal reprocessing of the polymer may lead to different degree of crystallinity. This phenomenon was evidenced by the DSC analysis of the raw and extruded filament (figure 7). The two polymers exhibit similar glass transition temperatures and cold crystallization peaks and slightly different melting peaks. The melting area instead are significant different, which lead us to the conclusion that the reprocessed polymer has a lower crystallinity and therefore a higher amorphous structure. The curves in the figure 7 were shifted in order to be more visible.

In conclusion, the crystallinity of the raw filament is higher (the area of the melting peak is 12.67 J/g) than the extrude PLA (which has a melting area of 8.646 J/g), the last one having an increased percentage of amorphous structure. The DSC analysis is sustaining from the structural point of view the mechanical properties determined by tensile testing.

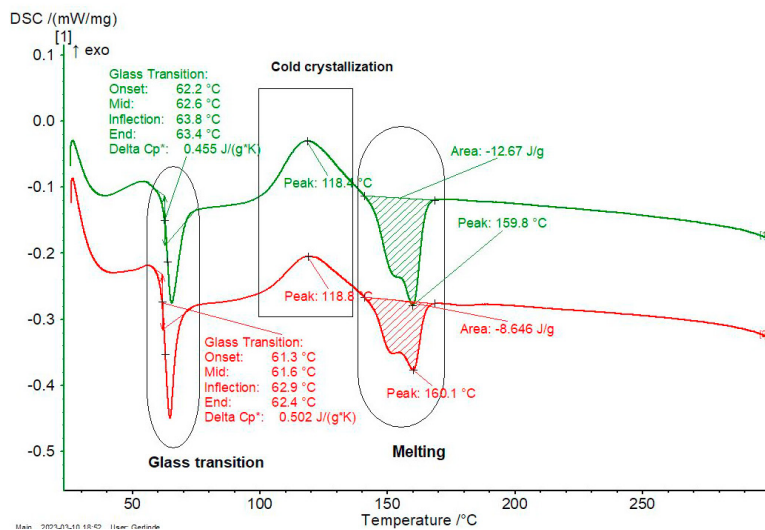


Fig. 7. DSC curves for raw and extruded PLA filament

4. Conclusions

The paper presents an experimental study on the mechanical behavior of the PLA in tensile testing in different conditions of obtaining the samples: raw filament; air extruded filament, one trace deposited on the platform, two consecutive traces deposited on the platform and fourteen consecutive traces deposited on the platform.

The material printed on the build platform has lower mechanical properties compared to the raw filament and respectively to air-printed one, the best results (41.18 ± 1.86 MPa tensile strength and 54.71 ± 12.44 % elongation at break) being obtained for raw material (the filament extracted directly from the roll).

The higher standard deviation for one and two deposition traces indicates a low process stability when it comes to only one or two printed traces. The very low elongation at break in this case indicate a rapid cooling of this samples.

The crystallinity of the raw filament is higher (12.67 J/g) than the extruded PLA (8.646 J/g), the last one having an increased percentage of amorphous zones.

The DSC analysis are sustaining the mechanical properties determined by tensile testing.

References

- [1] L. Marşavina, C. Vălean, M. Mărghitaş, et al., Effect of the manufacturing parameters on the tensile and fracture properties of FDM 3D-printed PLA specimens, *Engineering Fracture Mechanics* 274, 2022, 108766.
- [2] C. Vălean, L. Marşavina, M. Mărghitaş, et al., The effect of crack insertion for FDM printed PLA materials on Mode I and Mode II fracture toughness, *Procedia Structural Integrity* 28, 2020, 1134-1139.
- [3] L. Auffray, P-A. Gouge, L. Hattali, Design of experiment analysis on tensile properties of PLA samples produced by fused filament fabrication, *The International Journal of Advanced Manufacturing Technology*, 118:4123-4137, 2022;
- [4] G. Gao, F. Xu, J. Xu, Z. Liu, Study of material color influences on mechanical characteristics of fused deposition modeling parts, *Materials*, 15: 7039, 2022;
- [5] S.-H. Ahn, M. Montero, D. Odell, S. Roundy, P. K. Wright, Anisotropic material properties of fused deposition modeling ABS, *Rapid Prototyping Journal*, 8(4): 248-257, 2002;
- [6] X. Deng, Z. Zeng, B. Peng, S. Yan, W. Ke, Mechanical properties optimization of poly-ether-ether-ketone via fused deposition modeling, *MDPI Materials*, 11, 216, 2018;
- [7] T. Nancharaiyah, Optimization of process parameters in FDM process using design of experiments, *International Journal on Emerging Technologies*, 2(1): 100-102, 2011;
- [8] J. Jiang, Y. Ma, Path planning strategies to optimize accuracy, quality, build time and material use in additive manufacturing: a review, *MDPI Micromachines*, 11(7), 633, 2020;
- [9] A. Boschetto, V. Giordano, F. Veniali, Surface roughness prediction in fused deposition modelling by neural networks, *The International Journal of Advanced Manufacturing Technology*, 67: 2727-2742, 2013;
- [10] R. K. Sahu, S.S. Mahapatra, A. K. Sood, A study on dimensional accuracy of fused deposition modeling (FDM) processed parts using fuzzy

Structural Integrity and Reliability of Advanced Materials obtained through Additive Manufacturing (SIRAMM23)

Impact of Electron Beam Melting process recycling on defects and microstructure of Ti-6Al-4V powders

Costanzo Bellini^a, Filippo Berto^b, Rosario Borrelli^c, Vittorio Di Cocco^a, Stefania Franchitti^c, Francesco Iacoviello^a, Larisa Patricia Mocanu^{a*}, S. M. Javad Razavi^d

^aUniversity of Cassino and Southern Lazio, via G. Di Biasio 43, 03043 Cassino, Italy

^bSapienza University of Rome, Piazzale Aldo Moro, 5, 00185 Roma, Italy

^cCIRA - Italian Aerospace Research Centre, 81043 Capua, Italy;

^dNorwegian University of Science and Technology (NTNU), 7491 Trondheim, Norway

Abstract

Metal powders are used as the feedstock material during the Electron Beam Melting processes. The process involves using an electron beam as the energy source to produce intricate parts with complex shapes in a layer-by-layer production system. The electron beam is directed by information from an STL file, and the process takes place in a pre-heated chamber that is maintained under vacuum. Once the production cycle is complete, the process yields the desired components along with a certain amount of residual powders that were not melted.

To improve process efficiency and reduce costs associated with powder atomization, it is feasible to reuse the excess powder for subsequent production cycles. Prior to starting a new cycle, the excess powder is initially sieved to ensure a more uniform powder batch, and subsequently, the sieved powder can be mixed with other virgin powder to decrease oxygen content.

This study examines the microstructure and defects present in a batch of virgin powders produced through plasma atomization and a batch of powders that were reused five times and mixed with Ti-6Al-4V grade 23 (ELI powders) at each cycle. The ELI powders are characterized by a low oxygen content.

The results of the analysis indicate a connection between the powder atomization process and the formation of porosities in virgin powders resulting from trapped gas, as well as surface irregularities, including the presence of satellites. With an increase in the number of reuses, there is a reduction in the number of satellites, potentially due to surface partial melting due to the pre-heating of the EBM chamber, leading to rougher surfaces on the recycled particles.

The microstructure of virgin powders is predominantly characterized by a fine acicular α' phase, known as martensitic, formed due to the rapid cooling rate during the atomization process. Conversely, recycled powder tends to exhibit a coarser grain microstructure

* Corresponding author.

E-mail address: larisapatricia.mocanu@unicas.it

due to lower cooling rates. However, it is common to observe particles with a microstructure similar to that of newly manufactured powders, indicating that each individual particle has undergone a distinct thermal history.

© 2023 The Authors. Published by Elsevier B.V.

This is an open access article under the CC BY-NC-ND license (<https://creativecommons.org/licenses/by-nc-nd/4.0>)

Peer-review under responsibility of the SIRAMM23 organizers

Keywords: Additive Manufacturing; Ti-6Al-4V; Electron Beam Melting; powder recycling; internal porosity; microstructure; external defects.

1. Introduction

The ISO/ASTM52900 standard (ISO/ASTM, 2015) defines Powder Bed Fusion (PBF) as an Additive Manufacturing (AM) process in which specific regions of a powder bed are selectively fused by thermal energy. PBF techniques are regarded as the most effective approach to achieve high reproducibility and dimensional accuracy, and this is why these processes have been extensively studied in both the industrial and academic fields (Mostafaei et al., 2022). The most well-known processes under this category for producing metallic components are Electron Beam Melting (EBM) and Selective Laser Melting (SLM).

These two technologies are primarily distinguished by their ability to produce highly intricate shapes such as medical instruments and customized implants (Ishfaq et al., 2022), complex lattice structures (Bellini et al., 2021), aerospace components with high precision (Gardan & Schneider, 2015), and even custom-shaped jewelry (Cooper, 2016), through the addition of materials layer-by-layer in a single production cycle. EBM processes are primarily distinguished from SLM processes by the utilization of an electron beam instead of a laser as the heat source, and by taking place in a hermetically sealed chamber under vacuum to prevent the dissipation of the electron beam. Conversely, SLM processes occur in a controlled environment (Gordeev & Valentine, 2018). Furthermore, it is worth noting that the production chamber in EBM undergoes preheating at a specific temperature depending on the type of material used, such as approximately 1000°C for nickel-based alloys (Chandra et al., 2018) and approximately 400°C for pure copper (Guschlbauer et al., 2018). The preheating step represents a crucial aspect to take into account in EBM processes. The preheating process is crucial as it allows for the initial formation of sintering bridges between particles, preventing individual particles from becoming negatively charged and generating repulsive forces that would lead to the production chamber being filled with suspended powder, commonly referred to as the "smoke effect" (Milberg & Sigl, 2008).

With the exception of these minor differences, EBM and SLM are quite similar. Both methods start with an initial quantity of metallic powder that is selectively melted. At the end of the process, the desired product and some unmelted powders are obtained, which represents the production waste. Due to the high production costs associated with powders, which can also vary depending on the type of metal used (Hann, 2016), it is possible to reuse this waste powder in the subsequent production process (Bellini et al., 2022) (Foti et al., 2022). Currently, there are no established guidelines that govern recycling methodology, and thus, powder recycling is primarily based on user experience (Powell et al., 2020). Therefore, recycling procedures may vary, although typically the powder is initially sieved and, if required, may be combined with additional virgin powder of the same or different types before being introduced into the subsequent manufacturing cycle (Filipovic, 2016).

However, depending on the number of reuse cycles, recycled powders may not exhibit the same properties as virgin powders, primarily due to oxygen contamination and preheating, and can lead to worsened mechanical properties of components manufactured from these recycled powders. Hence, comprehending the alterations in powder properties is crucial to minimize the decline in the performance of the produced components. In fact, several studies have investigated the differences between unused and recycled powders, as well as the dissimilarities in the components produced from these powders. Typically, recycled powders exhibit inferior quality compared to virgin powders.

Specifically, according to research conducted by (Tang et al., 2015) and (Emminghaus et al., 2022), recycled powders in Ti-6Al-4V alloy generally exhibit elevated oxygen levels in comparison to virgin powders, whereas the concentrations of other elements such as V and Al are consistent. The increased oxygen content in recycled powders is primarily attributed to repeated circulation of powder in the process zone, leading to higher oxidation levels. Additionally, another reason is that when removed from the EBM machine, the powder is exposed to moisture and the surrounding atmosphere, which further contributes to oxygen absorption (Shanbhag & Vlasea, 2021).

Regarding the morphology, studies by (Carrion et al., 2019), (Emminghaus et al., 2021) and (Gatto et al., 2021) all suggest that recycled powders exhibit fewer satellites than their as-received counterparts, which is beneficial because it can significantly improve particle flowability. Moreover, several studies including (Carrion et al., 2019), (Yusuf et al., 2020) and (Nie et al., 2021), have reported that recycled powders demonstrate a narrower particle size distribution than unused powders when particle size is examined. Possible reasons for this change include particles sticking together during the manufacturing process to form larger clumps (Carrion et al., 2019), particles remaining suspended in the chamber and not being reusable (Seyda et al., 2012), and small particles sticking to larger ones, making them difficult to count (Sutton et al., 2016), although it should be noted that other research has shown that reused powders can sometimes have a broader size range than virgin powders (Gatto et al., 2021).

No differences were found in the microstructure of Ti-6Al-4V powders between virgin and reused powders, consisting mostly of acicular α' martensite (Emminghaus et al., 2022) (Sun et al., 2018). Components produced from new or reused powders showed, as well, no dissimilarities in the microstructure, displaying slender acicular α' within the columnar prior- β grains oriented in the same direction as the building process (Carrion et al., 2019) (Strondl et al., 2015). In addition, recycled powders generally have a coarser microstructure compared to virgin ones due to slower cooling rates during manufacturing cycles (Opatová et al., 2020). However, the microstructure is also highly dependent on process parameters such as laser power and scanning speed (Emminghaus et al., 2021).

2. Experimental

In this study, plasma-atomized Ti-6Al-4V powders grade 5 and grade 23, both provided by Advanced Powders and Coatings, Inc. (AP&C), were utilized; more specifically, a batch of virgin powder grade 5 and another batch of powder that had been recycled 5 times. AP&C utilized their proprietary Advanced Plasma Atomization process (APATM) which is distinguished for its capability to generate highly spherical powders with accurate size distributions, minimal oxygen content, and low internal porosity (Capus, 2017).

The batch of recycled powder began with grade 5 powder during the first production cycle, and then, in each of the following cycles, grade 23 powder was added. Since it is not possible to attribute the recycled powder to specific regions within the building chamber, the percentage of powder reused can be regarded as a mixture of particles originating from both the pre-sintered and surrounding regions.

Table 1 below presents preliminary information regarding the chemical composition of both powders.

Table 1. Chemical composition of the Ti-6Al-4V powder particles

	% Al	% V	% C	% N	Fe %	% O	% Ti
Virgin	6.50	4.03	0.01	0.02	0.205	0.11	Remaining
Recycled 5 times	6.48	4.02	0.01	0.02	0.196	0.19	Remaining

ASTM F2924 (Ghods et al., 2020) specifies that the permissible limit for oxygen content in aerospace applications is 0.2%. It is noteworthy that the use of grade 23 Ti-6Al-4V powders enables the oxygen content to remain below this limit.

To investigate the morphology in virgin powders and after recycling, which include changes in shape, surface roughness, and imperfections, the FEI Quanta 650 Scanning Electron Microscope (SEM) was employed.

In order to analyze the porosity and voids within the particles, the powder particles were embedded into phenol-formaldehyde resin, creating cylindrical molds with a diameter of 30 mm that made the powder easier to handle. To polish the resin/powder samples, porous woven wool felt and 1 μm and 0.3 μm Alumina solutions were used exclusively, while grinding procedures were avoided due to their aggressive nature, which can increase the number of particles escaping from the resin during the process. The polished samples were then examined for any internal porosities using a Nikon Epithot inverted Metallurgical Microscope.

Starting from the optical microscope images of the powder cross-section, the ImageJ software was utilized to provide the trend of change in internal porosity. However, it should be noted that these values underestimate the actual values as it is not known whether the diameter being considered is actually the maximum.

Finally, the analyzed particles were used to observe their microstructure and possible changes in the present phases. This was done by performing a chemical etching using a 0.1 Molar hydrofluoric acid (HF) solution, followed by rinsing under running water, and then observing them using the same optical microscope.

3. Results and Discussions

Based on the SEM images displayed in *Fig. 1*, it was observed that both types of powders were mainly spherical in shape. However, a closer inspection revealed some notable differences between the two batches. Specifically, the virgin powder exhibited significantly higher concentration of fine particles, also known as satellites, compared to the recycled batch, where most of them were absent. The reason for the disappearance of the small particles was the pre-heating process that occurred inside the EBM chamber, during which the tiny particles fused onto the surface of the larger particles. The removal of satellites was found to enhance the flowability of the material (Seyda et al., 2012).

Furthermore, while the surface of the virgin powder appeared to be smooth and largely devoid of imperfections, the recycled powder exhibited some indications of degradation. For instance, a few broken particles were observed in the recycled powder, possibly due to the sieving procedures employed during the recycling process. In addition, the surface of the recycled powder appeared to be slightly rougher than that of the virgin powder, which could be attributed to the presence of the melted satellites.

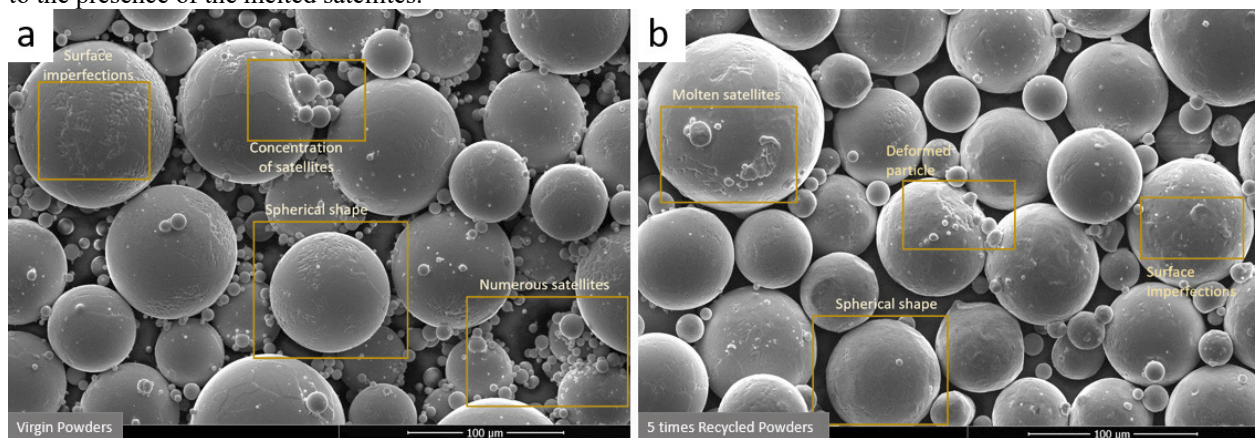


Fig. 1. SEM observation of virgin (a) and recycled (b) Ti-6Al-4V powder particles.

As shown in *Fig. 2*, both types of powders exhibited internal defects in the form of pores caused by entrapped gases during the atomization process, which is a phenomenon also reported by other authors (Chen et al., 2018). Porosities in powders typically have a spherical morphology, which is a result of the high pressure inside the liquid droplets that acts on the gas bubbles. It should be noted that these pores can potentially affect the performance of the final parts, particularly in terms of their mechanical properties. Therefore, it is important to carefully examine and control the porosity levels of powder materials during the manufacturing process.

From these images, it is almost impossible to express opinions regarding the particle size, as they are embedded in resin, and the maximum observable diameter is unknown. The same applies to the pores, as they are spherical.

However, a qualitative analysis can be performed using the commercial software ImageJ with the purpose of showing the trend of how internal porosity varies as the number of reuses changes. With the use of this software, it was possible to observe that the virgin powder holds a defect percentage of 3.72%, while the recycled powder presents a defect percentage of 2.76%. It can be observed that internal defects in the recycled powder have decreased, and this is also consistent with findings from other authors (Bellini et al., 2022).

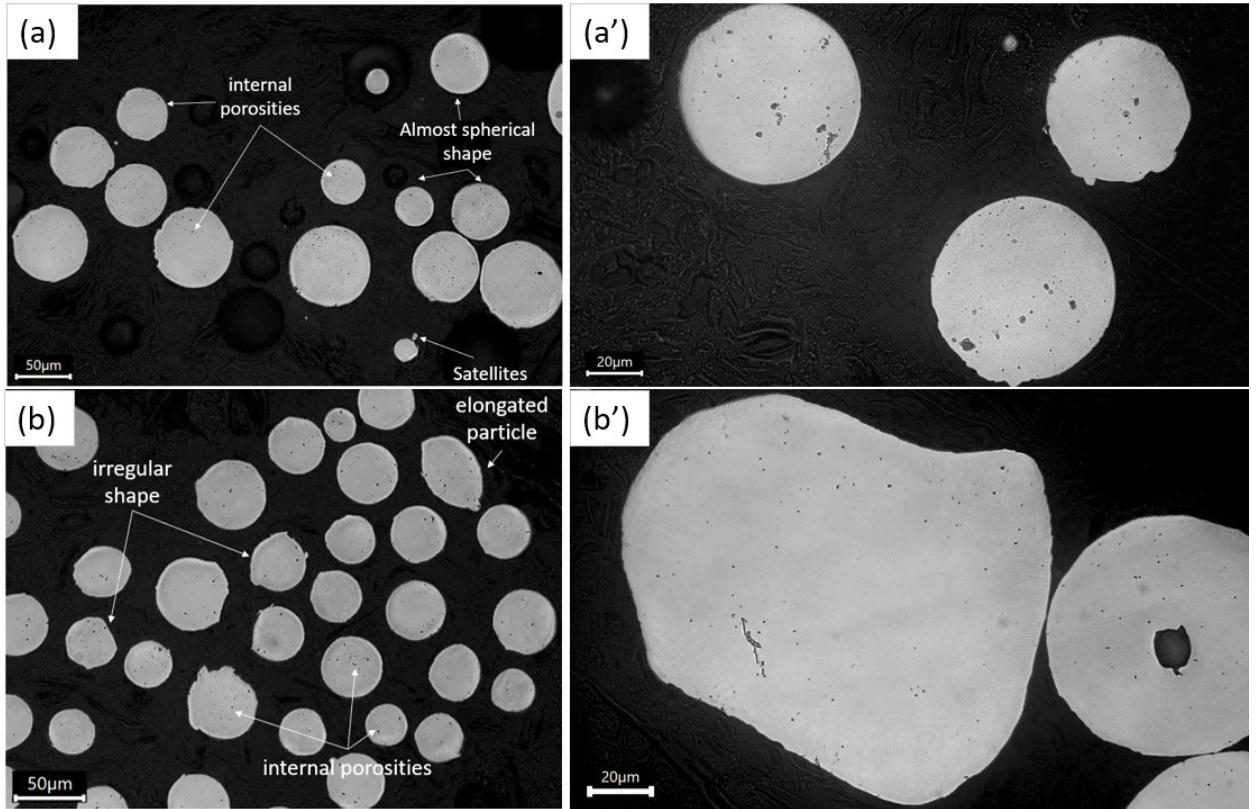


Fig. 2. Optical images of (a) virgin powders low magnification; (a') virgin powders high magnification; (b) recycled powders low magnification; (b') recycled powders high magnification.

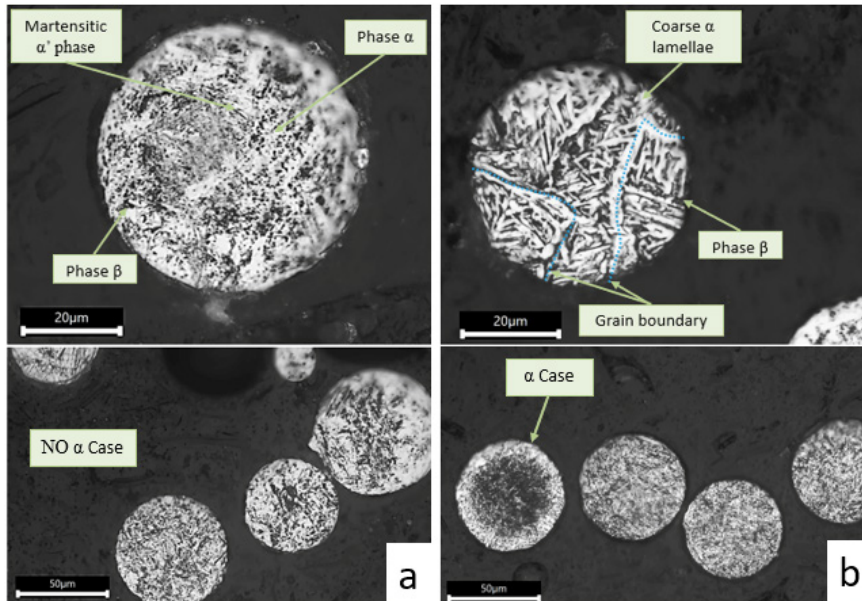


Fig. 3. Optical micrographs showing the microstructure of virgin (a) and recycled (b) powders.

The etching process revealed that the microstructure of virgin powders was predominantly characterized by a fine and martensitic structure. This microstructure was primarily comprised of the α' phase, which was distinguished by

finely dispersed acicular grains of the α phase. It was also noted that this unique microstructure was a direct consequence of the rapid cooling of the β phase that occurred during the atomization process.

Upon examining the powder that had undergone recycling for five cycles, it was found that the microstructure of most particles closely resembled that of the virgin powder exhibiting a martensitic structure. However, a few particles displayed coarser grains in comparison to the original microstructure due to the slower cooling rate during the production cycle.

Furthermore, the recycled powders were found to exhibit the so-called alpha-case phenomenon, which refers to an oxygen-rich layer formed around the particles at high temperatures due to the diffusion of oxygen into the metal, resulting in the creation of a hard interstitial layer. This layer is harder than the particle core, and thus more brittle, often becoming the site of micro-cracks that can degrade the corrosion and fatigue resistance of the metal.

Importantly, this oxygen-rich layer was exclusively observed in the recycled powders and not in the virgin ones.

4. Conclusions

This study aimed to investigate the impact of the recycling process on powder morphology, internal defects, and powder microstructure, analyzing two batches of Ti-6Al-4V powder particles. One batch consisted of virgin powders produced by plasma atomization, while the other batch consisted of powders recycled five times after the Electron Beam Melting process, with ELI powders (Ti-6Al-4V grade 23) added at each cycle.

The results of the investigation revealed the following:

- The virgin powders were found to have a considerable number of satellites, which are known to reduce the flowability of the particles. On the other hand, the powders that had undergone five cycles of recycling showed a reduced number of satellites, possibly due to pre-heating inside the Electron Beam Melting chamber, resulting in improved flowability. Nonetheless, it is important to note that the recycling process did cause some particle damage such as broken particles and increased roughness surface.
- The virgin powders were found to have a high number of internal micro porosities, specifically 3.72%, which was attributed to the entrapment of gas during the atomization process. Such porosities are known to be detrimental to the properties of components manufactured from these powders. On the other hand, the powders that had undergone five cycles of recycling showed a lower number of internal voids, equal to 2.76%. This could be due to pre-heating inside the EBM chamber.
- The microstructure analysis revealed that the virgin powders had a martensitic microstructure, which was a result of the fast cooling rate during the plasma atomization process. On the other hand, the 5-times recycled powders exhibited a mixed microstructure, where some particles had a similar microstructure to the virgin ones, while others had a coarser microstructure. Furthermore, an oxygen-rich layer, commonly known as Alpha case, was observed in the recycled powders.

5. References

- Bellini, C., Berto, F., Cocco, V. Di, Franchitti, S., Iacoviello, F., Mocanu, L. P., & Javad Razavi, S. M. (2022). Effect of recycling on internal and external defects of Ti-6Al-4V powder particles for electron beam melting process. *Procedia Structural Integrity*, 41(June), 175–182. <https://doi.org/10.1016/j.prostr.2022.05.019>
- Bellini, C., Borrelli, R., Di Cocco, V., Franchitti, S., Iacoviello, F., Mocanu, L. P., & Sorrentino, L. (2021). Failure energy and stiffness of titanium lattice specimens produced by electron beam melting process. *Material Design and Processing Communications*, 3(6). <https://doi.org/10.1002/mdp2.268>
- Capus, J. (2017). Titanium powder developments for AM – A round-up. *Metal Powder Report*, 72(6), 384–388. <https://doi.org/10.1016/j.mprp.2017.11.001>
- Carrion, P. E., Soltani-Tehrani, A., Phan, N., & Shamsaei, N. (2019). Powder Recycling Effects on the Tensile and Fatigue Behavior of Additively Manufactured Ti-6Al-4V Parts. *Jom*, 71(3), 963–973. <https://doi.org/10.1007/s11837-018-3248-7>
- Chandra, S., Tan, X., & Wang, C. (2018). Additive manufacturing of a single crystal nickel-based superalloy using selective electron beam melting Conference. May. <https://doi.org/10.25341/D4V30K>
- Chen, G., Zhao, S. Y., Tan, P., Wang, J., Xiang, C. S., & Tang, H. P. (2018). A comparative study of Ti-6Al-4V powders for additive manufacturing by gas atomization, plasma rotating electrode process and plasma atomization. *Powder Technology*, 333(2017), 38–46. <https://doi.org/10.1016/j.powtec.2018.04.013>

- Cooper, F. (2016). Sintering and additive manufacturing: ““ additive manufacturing and the new paradigm for the jewellery manufacturer .”” *Progress in Additive Manufacturing*, 85–87. <https://doi.org/10.1007/s40964-015-0003-2>
- Emminghaus, N., Bernhard, R., Hermsdorf, J., & Kaieler, S. (2022). Residual oxygen content and powder recycling: effects on microstructure and mechanical properties of additively manufactured Ti-6Al-4V parts. *International Journal of Advanced Manufacturing Technology*, 121(5–6), 3685–3701. <https://doi.org/10.1007/s00170-022-09503-7>
- Emminghaus, N., Hoff, C., Hermsdorf, J., & Kaieler, S. (2021). Residual oxygen content and powder recycling: Effects on surface roughness and porosity of additively manufactured Ti-6Al-4V. *Additive Manufacturing*, 46. <https://doi.org/10.1016/j.addma.2021.102093>
- Filipovic, V. P. (2016). Powder recyclability in electron beam melting for aeronautical use *Aircraft Engineering and Aerospace Technology : An International Journal Article information : January*. <https://doi.org/10.1108/AEAT-11-2013-0212>
- Foti, P., Mocanu, L. P., Razavi, S. M. J., Bellini, C., Borrelli, R., Di Cocco, V., Franchitti, S., Iacoviello, F., & Berto, F. (2022). Effect of recycling powder on the fatigue properties of AM Ti6Al4V. *Procedia Structural Integrity*, 42, 1436–1441. <https://doi.org/10.1016/j.prostr.2022.12.183>
- Gardan, N., & Schneider, A. (2015). Topological optimization of internal patterns and support in additive manufacturing. *Journal of Manufacturing Systems*, 37, 417–425. <https://doi.org/10.1016/j.jmsy.2014.07.003>
- Gatto, M. L., Groppo, R., Bloise, N., Fassina, L., Visai, L., Galati, M., Iuliano, L., & Mengucci, P. (2021). Topological, mechanical and biological properties of Ti6Al4V scaffolds for bone tissue regeneration fabricated with reused powders via electron beam melting. *Materials*, 14(1), 1–20. <https://doi.org/10.3390/ma14010224>
- Ghods, S., Schultz, E., Wisdom, C., Schur, R., Pahuja, R., Montelione, A., Arola, D., & Ramulu, M. (2020). Electron beam additive manufacturing of Ti6Al4V: Evolution of powder morphology and part microstructure with powder reuse. *Materialia*, 9(February), 100631. <https://doi.org/10.1016/j.mta.2020.100631>
- Gordeev, E. G., & Valentine, P. (2018). An In-Depth Review on Direct Additive Manufacturing of Metals An In-Depth Review on Direct Additive Manufacturing of Metals. <https://doi.org/10.1088/1757-899X/328/1/012005>
- Guschlbauer, R., Momeni, S., Osmanlic, F., & Körner, C. (2018). Materials Characterization Process development of 99 . 95 % pure copper processed via selective electron beam melting and its mechanical and physical properties ☆. *Materials Characterization*, March, 0–1. <https://doi.org/10.1016/j.matchar.2018.04.009>
- Hann, B. A. (2016). Powder Reuse and Its Effects on Laser Based Powder Fusion Additive Manufactured Alloy 718. <https://doi.org/10.4271/2016-01-2071>
- Ishfaq, K., Rehman, M., Khan, A. R., & Wang, Y. (2022). A review on the performance characteristics, applications, challenges and possible solutions in electron beam melted Ti-based orthopaedic and orthodontic implants. *Rapid Prototyping Journal*, 28(3), 525–545. <https://doi.org/10.1108/RPJ-03-2021-0060>
- ISO/ASTM. (2015). ISO/ASTM 52900-Standard Terminology for Additive manufacturing–general principles–terminology. i, 1–9.
- Milberg, J., & Sigl, M. (2008). Electron beam sintering of metal powder.
- Mostafaei, A., Zhao, C., He, Y., Reza Ghiaasiaan, S., Shi, B., Shao, S., Shamsaei, N., Wu, Z., Kouraytem, N., Sun, T., Pauza, J., Gordon, J. V., Weblar, B., Parab, N. D., Asherloo, M., Guo, Q., Chen, L., & Rollett, A. D. (2022). Defects and anomalies in powder bed fusion metal additive manufacturing. *Current Opinion in Solid State and Materials Science*, 26(2). <https://doi.org/10.1016/j.cossms.2021.100974>
- Nie, Y., Tang, J., Huang, J., Yu, S., & Li, Y. (2021). A study on internal defects of prep metallic powders by using x-ray computed tomography. *Materials*, 14(5), 1–11. <https://doi.org/10.3390/ma14051177>
- Opatová, K., Zetková, I., & Kučerová, L. (2020). Relationship between the size and inner structure of particles of virgin and re-used ms1 maraging steel powder for additive manufacturing. *Materials*, 13(4). <https://doi.org/10.3390/ma13040956>
- Powell, D., Rennie, A. E. W., Geekie, L., & Burns, N. (2020). Understanding powder degradation in metal additive manufacturing to allow the upcycling of recycled powders. *Journal of Cleaner Production*, 268, 1–29. <https://doi.org/10.1016/j.jclepro.2020.122077>
- Seyda, V., Kaufmann, N., & Emmelmann, C. (2012). Investigation of Aging Processes of Ti-6Al-4 v Powder Material in Laser Melting. *Physics Procedia*, 39, 425–431. <https://doi.org/10.1016/j.phpro.2012.10.057>
- Shanbhag, G., & Vlasea, M. (2021). Powder reuse cycles in electron beam powder bed fusion— variation of powder characteristics. *Materials*, 14(16). <https://doi.org/10.3390/ma14164602>
- Strondl, A., Lyckfeldt, O., Brodin, H., & Ackelid, U. (2015). Characterization and Control of Powder Properties for Additive Manufacturing. *Jom*, 67(3), 549–554. <https://doi.org/10.1007/s11837-015-1304-0>
- Sun, Y., Aindow, M., & Hebert, R. J. (2018). The effect of recycling on the oxygen distribution in Ti-6Al-4V powder for additive manufacturing. *Materials at High Temperatures*, 35(1–3), 217–224. <https://doi.org/10.1080/09603409.2017.1389133>
- Sutton, A. T., Kriewall, C. S., Leu, M. C., & Newkirk, J. W. (2016). Powders for additive manufacturing processes: Characterization techniques and effects on part properties. *Solid Freeform Fabrication 2016: Proceedings of the 27th Annual International Solid Freeform Fabrication Symposium - An Additive Manufacturing Conference, SFF 2016*, 1004–1030.
- Tang, H. P., Qian, M., Liu, N., Zhang, X. Z., Yang, G. Y., & Wang, J. (2015). Effect of Powder Reuse Times on Additive Manufacturing of Ti-6Al-4V by Selective Electron Beam Melting. *Jom*, 67(3), 555–563. <https://doi.org/10.1007/s11837-015-1300-4>
- Yusuf, S. M., Choo, E., & Gao, N. (2020). Comparison between virgin and recycled 316l ss and als10mg powders used for laser powder bed fusion additive manufacturing. *Metals*, 10(12), 1–18. <https://doi.org/10.3390/met10121625>

Structural Integrity and Reliability of Advanced Materials obtained through Additive Manufacturing (SIRAMM23)

Influence of heat treatment on welding process of electron beam welded joint of Ti6Al4V parts manufactured via laser powder bed fusion

Anand Kumar S^{1*}, Damodran², Randhir Kumar Singh³, R.K. Kumar⁴, S. Cyril Joseph Daniel², Adarsh K. Hegde⁵, BK Nagesha⁶

¹ Additive Manufacturing Research Laboratory, Dept of Mechanical Eng., Indian Institute of Technology Jammu, Jammu - 181 221, India.

² Department of Mechanical Engineering, Sri Sivasubramaniya Nadar College of Engineering, Chennai - 603110, India.

³ Dept. of Metallurgical & Materials Engineering, Malaviya National Institute of Technology Jaipur, Rajasthan-302017, India

⁴ Material Technology Division, Central Power Research Institute (CPRI), Bangalore 560080, India

⁵ Center for Sensors, Vision Technology and Controls, Central Manufacturing Technology Institute, Bengaluru – 560022, India

⁶ Gas Turbine Research Establishment, Defense Research and Development Organization, Karnataka, Bangalore- 560093, India

Abstract

The present work was conducted to determine the effect of welding as-printed selective laser melting samples and fabricated samples welded with stress-relieved conditions. The research aimed to study the influence of heat treatment on welding parameters and weldability. Additive manufacturing by selective laser melting can achieve near-net shape and complex structure. It has been widely used in manufacturing aerospace components, in the automobile sector and other fields. Ti6Al4V is the most commonly used and researched alloy in additive-manufactured alloys. The microstructure of Ti-6Al-4V is diverse and consists of acicular martensite α' phase with prior β grains. The results showed the formation of α -phase around the β grains in the heat-affected zone where the temperature reached above the T_0 [$<893^\circ\text{C}$], the β -phase recrystallization during the welding process. The primary α -phase develops and forms along the grain boundaries and was more prominent in the stress-relieved specimens. The microhardness decreases in the weld of stress relieved condition compared to weld as-printed condition.

© 2023 The Authors. Published by Elsevier B.V.

This is an open access article under the CC BY-NC-ND license (<https://creativecommons.org/licenses/by-nc-nd/4.0>)

Peer-review under responsibility of the SIRAMM23 organizers

Keywords: Ti-6Al-4V, laser powder bed fusion, electron beam welding, microstructure, microhardness

1. Introduction

Laser powder bed fusion (LPBF) technology emerged as one of the most widely used additively manufactured (AM) techniques that can be applied to most non-volatile metals. It is a layer-based deposition method using a laser to selectively melt successive layers of metal powder in an inert-gas-filled chamber [1-2]. The benefit of this process

^{1*} Corresponding author. Tel.: +91-9036624149; fax: NA.

E-mail address: anandkumarait@gmail.com; anand.subramaniyan@iitjammu.ac.in

is best realized when applied to metals which are difficult to process through other techniques [3]. Any complex-shaped metallic components can be produced by the LPBF process on the LPBF equipment through 3D CAD data. It provides a better alternative manufacturing route than traditional manufacturing techniques in aspects like high flexibility, high material use efficiency and near-net-shape geometries [4]. LPBF has been widely used in medical, military, aerospace, and automobile manufacturing. LPBF represents the advantageous process. However, some problems with large thermal gradients exist due to considerable heat input and short interaction. The influence of various parameters is still a matter of interest for research for its biological and biomechanical compatibility.

Titanium alloys comprising high fracture toughness, high strength-to-weight ratio and superior mechanical properties have been widely used in the biomedical and aerospace industries [5]. Ti6Al4V using conventional processing methods limits its extensive application due to poor machinability and high cost. Moreover, high energy consumption and material wastage occur during the production of titanium alloys through conventional methods. Consequently, researchers have been studying the non-conventional processing of titanium alloys through AM route. AM process through LPBF techniques offers more excellent benefits when compared to the conventional process. Thijs *et al.* studied the microstructural evolution of Ti6Al4V during the LPBF process. Due to the higher temperature gradient during the LPBF process epitaxial growth, elongated grains emerge and acicular martensitic phase formed in Ti6Al4V alloy [6]. Losertová *et al.* [7] focused on the properties of porous Ti6Al4V specimens processed by selective laser melting. The material was tested in tension and compression with and without heat treatment. The as-built stage consisted of prior- β grains filled with acicular α' martensite and displayed high yield strength but limited ductility. In similar work by Naeem Eshawish *et al.* [8], the microstructure, even after stress relieving (SR) at 704°C for two h, shows fine α' martensitic phase.

Most research and development on Ti-6Al-4V fabricated by LPBF has focused on the microstructure of the as-built samples and the adjustment of the process parameters to increase the quality of products [9-10]. This research studies the influence of heat treatments i.e. SR, on the microstructure and hardness on electron beam (EB) welded joint of Ti6Al4V alloy processed by selective laser melting (LPBF). It is reported that the acicular martensite α' phase is formed during the LPBF process which changes to a lamellar mixture of $\alpha+\beta$ after heat treatment below the critical temperature (T_0 at approximately 893°C) [11]. In the present study, the welding process was optimized and welds were analyzed to study the microstructure and its effects on the mechanical properties.

Nomenclature

T_0	critical temperature
α'	martensitic phase
α	hcp phase
β	bcc phase

1. 2. Material and methods

The welding was carried out on two state-of-condition samples, i.e. (i) as-printed (AP) Ti6Al4V parts were welded (AP+AP), and (ii) stress relieving (SR) Ti6Al4V LPBF parts were welded with as-printed LPBF processed parts (SR+AP). The LPBF process parameters included a laser power range of 170 to 200W, a scanning speed of 500 to 1250mm/s, a controlled layer thickness of 0.03 mm, a hatch distance of 0.1mm, a laser beam diameter of 0.1mm, a beam offset of 0.015mm, a stripe width of 5mm and a 67° rotation scanning strategy. The thickness of the as-printed sample is 10x30x5 mm³. The stress relieving heat treatment was performed by heating to 650°C and holding for three h, followed by furnace cooling in an inert atmosphere by maintaining Argon gas supply. The preliminary edge preparations and cleaning with acetone were performed before welding. The welding was performed using a 6 kW, 60-kV electron beam welding (EBW) setup. A circular beam oscillation at 200 Hz having a diameter of 100 μ m was used and surface focus condition was maintained during welding. The welding speed of 1500 mm/min with a beam current of 20 mA was employed. The power density was in the range of 1.525×10^5 W/mm². The weld samples shown in Fig.1 were analyzed and compared regarding weld microstructures, bead profile, microhardness

and macro examination. The microstructure characterization of welded samples was carried out using an OM Leica DMI3000 at different locations on the specimens.

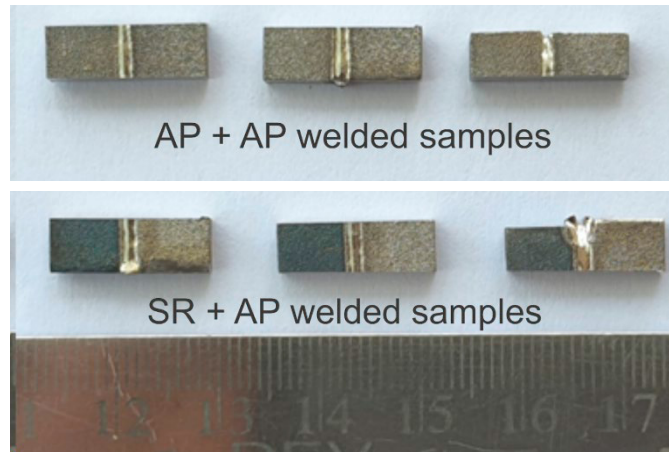


Fig.1 Welded samples of Ti6Al4V alloy

3. Results and Discussion

3.1 Microstructure of welded joint in as-printed condition

The microstructure characterization was carried out at different locations on the welded specimen. Figure 2 describes the microstructure of the welded specimen of LPBF fabricated specimen with LPBF fabricated specimen. The LPBF samples were characterized by the microstructure forming the acicular α' martensitic phase [8]. The reason for developing the acicular α' martensitic phase is that the temperature of the Ti6Al4V alloy is exceptionally high under the laser action. This most likely forms the diffusionless α' phase due to the subsequent rapid cooling process. The cooling rate within LPBF processing exceeds a crucial cooling rate of 410 K/s, which is suggested as a martensite α' formation rate [12]. Consequently, acicular α' martensite forms rather than equilibrium α and β phases in Ti-6Al-4V manufactured by LPBF (Fig. 2a). It is observed from the microstructure that the grains were surrounded by the bright α phase. In the HAZ region shown in Fig. 2b, it is observed that the presence of α phase around the grains increased and there was a clear distinction between the base and weld zone. In the weld zone, columnar grains are observed growing towards the centre of the weld, as evident from Fig. 2c. Zhan-Yong Zhao et. al.[7] had reported the interior of the equiaxed grains mainly consisted of acicular martensite α' phase and the β phase was not detected by XRD in the TC4 alloy fabricated by LPBF. Bey et al.[8] also identified the absence of β phase in as-built TC4 alloys. The microstructure in as-built condition usually has low ductility and high strength [13-14]. Thus, significant effort has been exerted to comprehend the process parameters on microstructures and mechanical properties in optimising the as-built conditions.

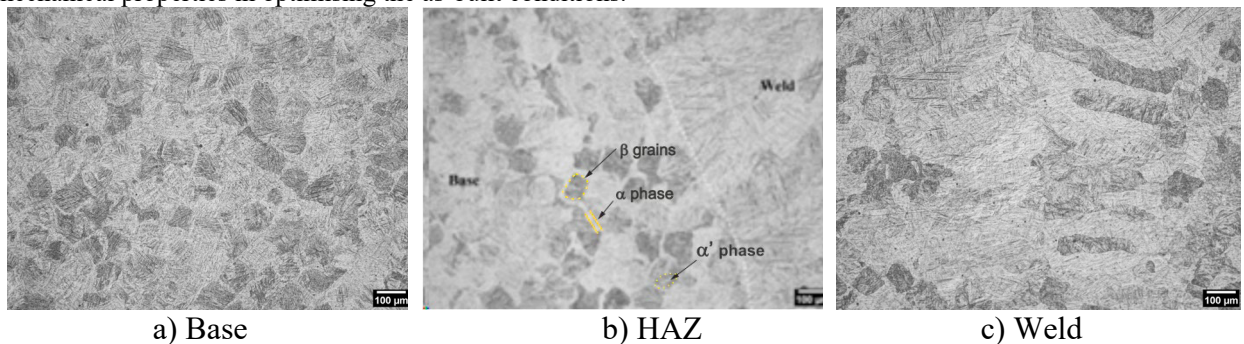


Fig. 2 The optical microstructure of welded joint in as-printed condition

3.2 Influence of heat treatment temperature on microstructure morphology

Improvement in the ductility with strength reduction in LPBF-fabricated Ti6Al4V can be achieved by successive heat treatments involving the transformation of the non-equilibrium phase (acicular α' martensite) into near equilibrium phase (lamellar $\alpha+\beta$ phases) [15]. Most of the research focused on the microstructure of the as-built samples and adjustment of the process parameters to increase the quality of as-built products by LPBF technique [16]. Ali et. al. [17] utilised a greater bed preheating temperature of 570°C to eliminate the in-built residual stresses and improve ductility. Meanwhile, others have optimized the mechanical properties by applying only one heat treatment stage at different temperatures on the as-built samples [18]. In the present study, the stress relieving was carried out at a temperature of 650°C and holding for three h to optimize the microstructure and mechanical properties. The stress-relieving heat treatment was carried out in an inert atmosphere by purging Argon gas to avoid oxidation.

The optical microstructure of welded joint in fabricated and stress relaxed (SR) condition is shown in Fig.3. The microstructure reveals that α phase surrounding the grains are comparatively more in the sample of SR condition than in the as-fabricated condition. The weld region also shows large columnar grains compared to the sample where both built samples are welded.

The sample's SR condition microstructure reveals a comparatively brighter α phase surrounding the prior β grains. The length and width of the prior β grains increase in the SR condition compared to the built-in condition. It is now approximately 1.1-1.8 μm wide and roughly 0.9-1.2 μm for the SR one. The acicular martensite α' phase formed in Ti-6Al-4V alloy developed by LPBF is because of the alloy's high transient temperature under the laser's action during the process. Initially, β phase formation is preferred, which then transforms to α' phase by non-diffusion shear process during the subsequent rapid cooling.

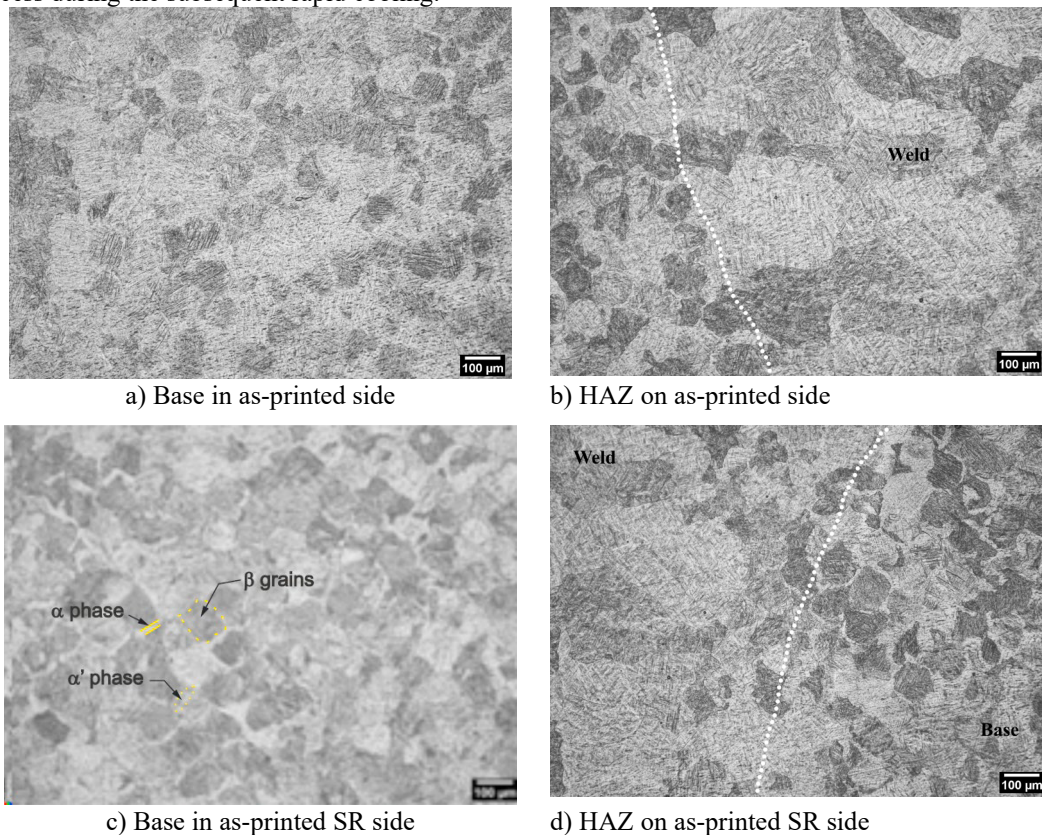


Fig. 3 The optical microstructure of welded joint in as-printed condition and SR condition

3.3 Microhardness

The size of the prior β grains of the Ti6Al4V gradually grows with the stress-relieving heat treatment process. The hardness profile across the welded samples in the as-built condition and the stress-relieving state is shown in Fig. 4. From the hardness profile, the hardness of the as-built sample is higher than that of the stress-relieved samples. Hence, the SR treatment helped relieve the residual stresses in the material due to the LPBF process.

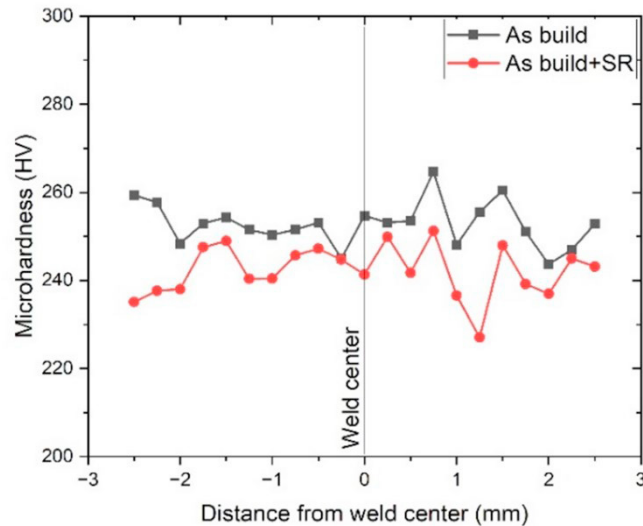


Fig. 4 Microhardness profile of the as-printed condition and SR condition

4. Conclusions

1. The as-built sample produced by the LPBF reveals long columnar grain in the weld regions, which grow by cladding multiple layers and are oriented in the buildup direction.
2. In the SR heat treatment, the microstructure reveals a bright α phase along the grain boundaries.
3. The hardness was found to decrease with SR heat treatment. The hardness in the AP+SR welded samples was lower when compared to the AP+AP welded samples.

References

- [1] Herzog, D.; Seyda, V.; Wycisk, E.; Emmelmann, C.; Additive manufacturing of metals. *Acta Mater.* 2016, 117, 371–392.
- [2] Kumar SA, Prasad RVS (2021) Chapter 2 - Basic principles of additive manufacturing: different additive manufacturing technologies. In: Manjaiah M, Raghavendra K, Balashanmugam N, Davim JP (eds) *Additive Manufacturing*. Woodhead Publishing, pp 17–35.
- [3] Pathania A, Anand Kumar S, Nagesha BK, et al (2021) Reclamation of titanium alloy based aerospace parts using laser based metal deposition methodology. *Materials Today: Proceedings* 45:4886–4892. <https://doi.org/10.1016/j.matpr.2021.01.354>.
- [4] Kiel-Jamrozik, M.; Szweczenko, J.; Basiaga, M.; Nowinska, K. Technological capabilities of surface layers formation on implants made of Ti-6Al-4V ELI alloy. *Acta Bioeng. Biomech.* 2015, 17, 31–37.
- [5] Kiel-Jamrozik, M.; Jamrozik, W.; Witkowska, I.; The heat treatment influence on the structure and mechanical properties of Ti6Al4V alloy manufactured by LPBF technology. *Innov. Biomed. Eng.* 2018, 623, 319–327.
- [6] Thijs, L.; Verhaeghe, F.; Craeghs, T.; Humbeeck, J.V.; Kruth, J. A study of the microstructural evolution during selective laser melting of Ti-6Al-4V. *Acta Mater.* 2010, 58, 3303–3312.
- [7] M Losertová and V Kubeš; Microstructure and mechanical properties of selective laser melted Ti6Al4V alloy, *Materials Science and Engineering* 266 (2017) 012009.
- [8] Naeem Eshawish, Savko Malinov, Wei Sha, and Patrick Walls; Microstructure and Mechanical Properties of Ti-6Al-4V Manufactured by Selective Laser Melting after Stress Relieving, Hot Isostatic Pressing Treatment, and Post-Heat Treatment, *Journal of Materials Engineering and Performance*, 5290 - Volume 30(7) July 2021.
- [9] D. Agius, K.I. Kourousis, and C. Wallbrink, A Review of the As-Built LPBF Ti-6Al-4V Mechanical Properties Towards Achieving Fatigue Resistant Designs, *Metals (Basel)*, 2018, 8(1), p 75.

- [10] M. Simonelli, Y.Y. Tse, and C. Tuck, The Formation of $\alpha + \beta$ Microstructure In as-Fabricated Selective Laser Melting Of Ti-6Al-4V, *J. Mater. Res.*, 2014, 29(17), p 2028–2035.
- [11] Zhan-Yong Zhao, Liang Li, Pei-Kang Bai, Yang Jin, Li-Yun Wu, Jing Li, Ren-Guo Guan 2 and Hong-Qiao Qu ; The Heat Treatment Influence on the Microstructure and Hardness of TC4 Titanium Alloy Manufactured via Selective Laser Melting, *Materials* 2018, 11, 1318.
- [12] T. Ahmed and H.J. Rack, Phase Transformations During Cooling in $\alpha+\beta$ Titanium Alloys, *Mater. Sci. Eng. A*, 1998, 243(1–2), p 206–211
- [13] X. Tan, Y. Kok, Y.J. Tan, G. Vastola, Q.X. Pei, G. Zhang, Y.-W. Zhang, S.B. Tor, K.F. Leong, and C.K. Chua, An Experimental and Simulation Study on Build Thickness Dependent Microstructure For Electron Beam Melted Ti–6Al–4V, *J. Alloys Compd.*, 2015, 646, p303–309.
- [14] Q. Yan, B. Chen, N. Kang, X. Lin, S. Lv, K. Kondoh, S. Li, and J.S. Li, Comparison Study on Microstructure and Mechanical Properties of Ti-6Al-4V Alloys Fabricated by Powder-Based Selective-Laser-Melting and Sintering Methods, *Mater. Charact.*, 2020, 164, p 110358.
- [15] W. Xu, S. Sun, J. Elambasseril, Q. Liu, M. Brandt, and M. Qian, Ti-6Al-4V Additively Manufactured by Selective Laser Melting with Superior Mechanical Properties, *JOM*, 2015, 67(3), p 668–673.
- [16] D. Agius, K.I. Kourousis, and C. Wallbrink, A Review of the As-Built LPBF Ti-6Al-4V Mechanical Properties Towards Achieving Fatigue Resistant Designs, *Metals (Basel)*, 2018, 8(1), p 75.
- [17] H. Ali, L. Ma, H. Ghadbeigi, and K. Mumtaz, In-Situ Residual Stress Reduction, Martensitic Decomposition and Mechanical Properties Enhancement Through High Temperature Powder Bed Pre-Heating of Selective Laser Melted Ti6Al4V, *Mater. Sci. Eng. A*, 2017, 695, p211–220.
- [18] G. Nicoletto, S. Maisano, M. Antolotti, and F. Dall'aglio, Influence of Post Fabrication Heat Treatments on the Fatigue Behavior of Ti-6Al-4V Produced by Selective Laser Melting, *Procedia Struct. Integr.*, 2017, 7, p 133–140.



Structural Integrity and Reliability of Advanced Materials obtained through Additive Manufacturing (SIRAMM23)

Layer thickness influence on impact properties of FDM printed PLA material

Aleksa Milovanović^{a*}, Sergiu-Valentin Galațanu^b, Aleksandar Sedmak^c, Liviu Marșavina^b, Isaak Trajković^a, Cosmin-Florin Popa^b, Miloš Milošević^a

^aUniversity of Belgrade, Innovation Center of the Faculty of Mechanical Engineering, Kraljice Marije 16 Street, Belgrade 11120, Serbia

^bPolytechnic University of Timișoara, Department of Mechanics and Strength of Materials, 1 Mihai Viteazu Avenue, Timișoara 300222, Romania

^cUniversity of Belgrade, Faculty of Mechanical Engineering, Department of Material Science, Kraljice Marije 16, Belgrade 11120, Serbia

Abstract

Polylactic Acid (PLA) is a widely used material in Fused Deposition Modeling (FDM) technology. Additive Manufacturing (AM) parameters are known to have an influence on the mechanical properties of final components. In FDM, the layer thickness is an influencing parameter providing overall better mechanical properties with lower layer thickness values. In that case, the air gaps created between layers and raster lines have a lower share in total volume. However, layer over-compression might be an issue when choosing the lowest layer thickness options. This research paper investigates the impact properties of PLA material with variations in layer thickness namely, 0.1, 0.2, and 0.3 mm are considered here. Charpy tests were used for the impact property assessment, and all specimens were prepared with 100% infill percentage and honeycomb infill structure. Worth mentioning is that specimens have AMed notches. The impact tests were carried out on 7 specimens per batch (a total of 21 specimens). Therefore, obtained impact results from an instrumented pendulum were observed between groups to have an insight into the beneficial influence of lower layer thickness on impact properties and lower result scatter that finer layer resolution should produce.

© 2023 The Authors. Published by Elsevier B.V.

This is an open access article under the CC BY-NC-ND license (<https://creativecommons.org/licenses/by-nc-nd/4.0>)

Peer-review under responsibility of the SIRAMM23 organizers

Keywords: PLA; FDM; Charpy; layer thickness; Instrumented pendulum.

* Corresponding author. Tel.: +381-64-614-8698.

E-mail address: amilovanovic@mas.bg.ac.rs

1. Introduction

At first, AM technology was used for rapid prototyping purposes, because of its faster and cheaper production compared to conventional (subtractive) methods. Over time, with the increase in available production methods and materials, the utilization of this technology in the production of functional components was also taken into consideration. Now, the importance of particular AM technology is not measured only by fabrication time, production energy consumed, and quantity of material used, but also by the potential of a particular AM technology to deliver components for functional applications.

For this estimation material's mechanical properties have to be obtained using standardized tests, and the most probable first choices are tensile, compressive, and flexural tests. Most used are the tensile tests, providing valuable information about the material, utilized in research works by Popović et al. (2023), Pandžić et al. (2019a), Pandžić et al. (2019b), Milovanović et al. (2022a). A comprehensive mechanical property assessment using all three test methods for AMed materials dedicated to dental aligners is shown in Milovanović et al. (2021). Also valuable are the tests from fracture mechanics aspects, as in Milovanović et al. (2022b), and Milovanović et al. (2022c).

For a better insight into the material's behaviour impact properties are also preferable. Standardized impact tests include Charpy and IZOD tests. These two methods differ in specimen geometry and placement on the impact machine, but they both evaluate the same material property, as stated by Popa et al. (2022) and Ailinei et al. (2022).

In FDM, the printing parameters and materials used dictate the mechanical properties of finished components. The proof of the significant influence of the raster angle on impact strength was investigated by Rajpurohit et al. (2020), and Patterson et al. (2021) also investigated build orientation with raster angle on seven different materials. As stated by Patterson et al. (2021), brittle materials (e.g., PLA) have more consistent impact properties. Build orientation influence on impact strength was also a subject in Stoia et al. (2022) research in the case of Polyamide material, used in SLS technology. Popa et al. (2022) investigated the dependence of specimen thickness on IZOD impact strength, for PLA and PETG materials. Here, PLA material has higher impact force values than PETG but has lower overall deflection. A particularly interesting research finding is that higher specimen thicknesses produce a higher value scatter of results. Our research matches the lowest specimen thickness used in the Popa et al. (2022) paper, namely 4 mm.

Except for impact testing of individual materials current research papers cover the properties of composite FDM materials, either as fiber-reinforced or created by stacking layers of different materials. For example, a dual-extruder FDM machine allows for the creation of one layer from one material, and then the other material comes in the next layer. Ahmed et al. (2021) investigated the properties of composites that contain fiber-reinforced PLA in one layer and ABS material in the other. The conclusion here shows that more ABS layers create higher impact strength, and all PLA layers here have brittle fracture surfaces. Ferdinand et al. (2023) used PLA with added synthetic polymer fibers, such as PET and PVA, showing that PVA is a more efficient impact modifier among selected reinforcements. Research shows that fiber characteristics and its adhesion with the matrix material are the main factors for the composite material's impact properties. PLA is a bio-based material, and Tian et al. (2022) focused their research on incorporating nano-fibrillated cellulose into PLA resulting in a 2.3 times higher impact strength of such material.

The subject of this research paper is the influence of layer thickness on the impact properties of PLA material, i.e., impact force-deflection, impact energy-deflection response, maximum impact force value, deflection at the point of break, impact energy, and impact strength values.

Nomenclature

AM	Additive Manufacturing
FDM	Fused Deposition Modeling
PLA	Polylactic Acid
SLS	Selective Laser Sintering
PETG	Polyethylene Terephthalate Glycol
ABS	Acrylonitrile Butadiene Styrene
PET	Polyethylene Terephthalate

PVA Polyvinyl alcohol

2. Materials and Methods

The research covers three different layer thickness values namely, 0.1 mm, 0.2 mm, and 0.3 mm. Specimens were prepared according to ISO 179 standard, with chosen type A notch (see Fig. 1, Left). Specimens' notches were AMed, not machined- as suggested by Valean et al. (2020). All specimens have two outlines and a honeycomb infill structure (see Fig. 1, Right). The honeycomb structure has proven to be the best choice regarding mechanical properties among all available infill patterns in the utilized Simplify3D slicer software (Simplify3D, Cincinnati, OH, USA), as stated by Milovanović et al. (2022d). The infill percentage is set to full (100%).

The tests are conducted on the instrumented pendulum, Instron CEAST 9050 machine (see Fig. 2) with hammer properties listed in Table 1. The sampling rate was set to 1000 Hz, adequate for the interpretation of results. The specimens were tested in an edgewise direction, with a 60 mm span between the anvils. The standard defines five specimens for sufficient repeatability, but just in case two additional specimens were prepared- giving a total of seven specimens per batch.

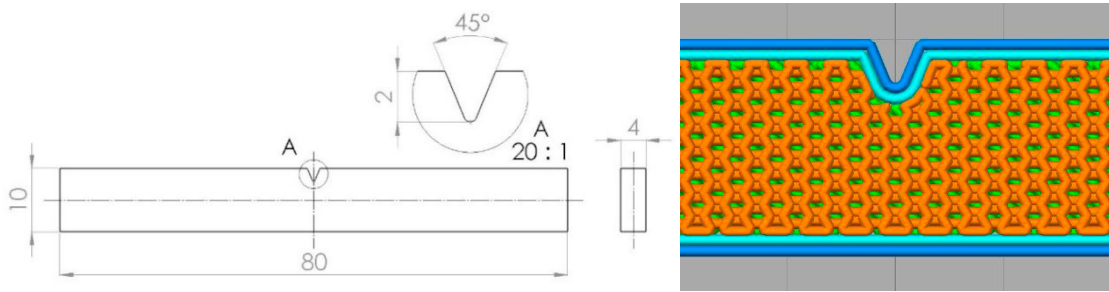


Fig. 1. (Left) Charpy specimen dimensions (in mm); (Right) Layer structure.



Fig. 2. Instron CEAST 9050 Charpy instrumented pendulum.

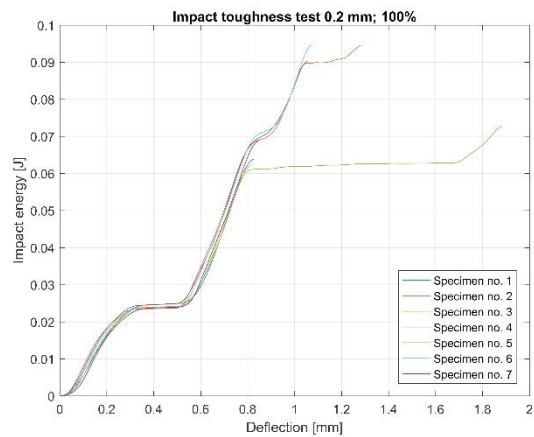
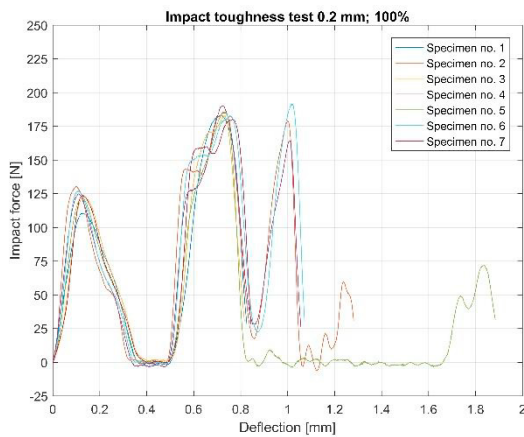
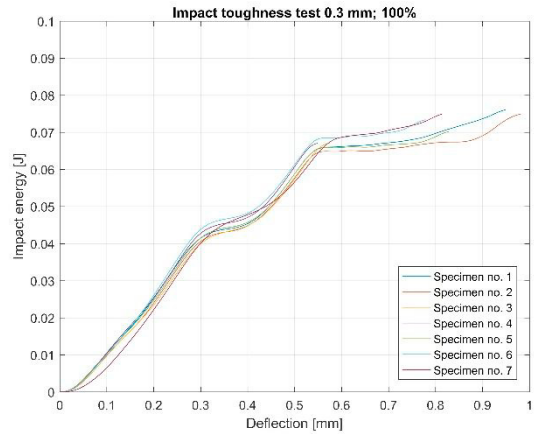
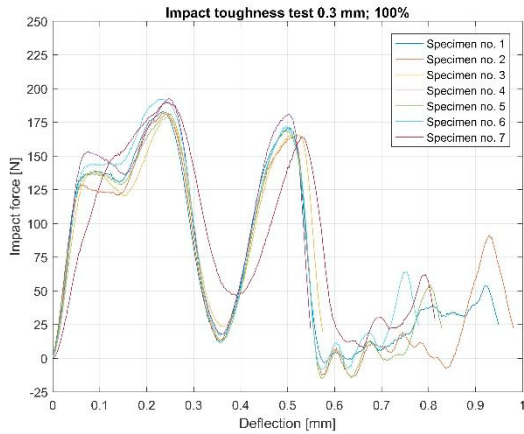
Table 1. Charpy hammer properties.

Parameters	Values
Potential energy	5 J
Impact speed	2.9 m/s

Starting angle	150°
Weight	1.186 kg
Length	229.7 mm

3. Results and Discussion

The impact force and impact energy dependence from deflection are shown for all three chosen layer thicknesses in Fig. 3. Each chart contains seven curves, for all individual specimens.



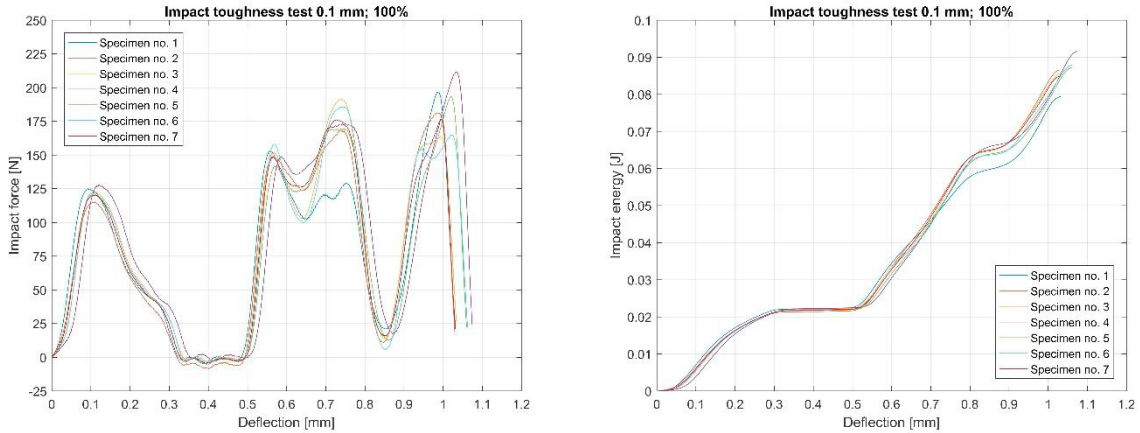


Fig. 3. (Top-Left) Force-deflection for 0.3 mm; (Top-Right) Energy-deflection for 0.3 mm; (Middle-Left) Force-deflection for 0.2 mm; (Middle-Right) Energy-deflection for 0.2 mm; (Bottom-Left) Force-deflection for 0.1 mm; (Bottom-Right) Energy-deflection for 0.1 mm.

The repeatability of impact force and energy response relative to deflection is notable, as can be seen from all the charts in Fig. 3. Especially good repeatability is apparent in the first elastic impact domain (i.e., force increase from zero value until the first peak) and first damage event (i.e., decrease in force after the first peak until the first gradual increase in force). Unlike the batches with lower layer thickness, the 0.3 mm batch contains a distinctive plateau before reaching the first peak (also visible on the average curve chart, Fig. 4- Left).

The similarity in response for the 0.1 mm and 0.2 mm batches can also be seen in Fig. 4, Right (average impact energy-deflection curves). The effect of plastic deformation can be derived from the displacement increase at a constant energy level, as stated by Krausz et al. (2021). The plastic deformation is visible from 0.3 mm until 0.5 mm deflection for 0.1 mm and 0.2 mm layer thickness batches. Unlike these two batches, the 0.3 mm batch has a significantly smaller plateau here. Also, the impact energy value is higher for both lower thickness batches (values are about 0.09 J), and the impact energy value for the 0.3 mm batch is around 0.07 J (see Fig. 4, Right).

In FDM, higher layer thicknesses have lower adhesion between layers and a larger portion of air gaps in the cross-section. For these stated reasons, the 0.3 mm batch differs so much from the other two higher-resolution batches.

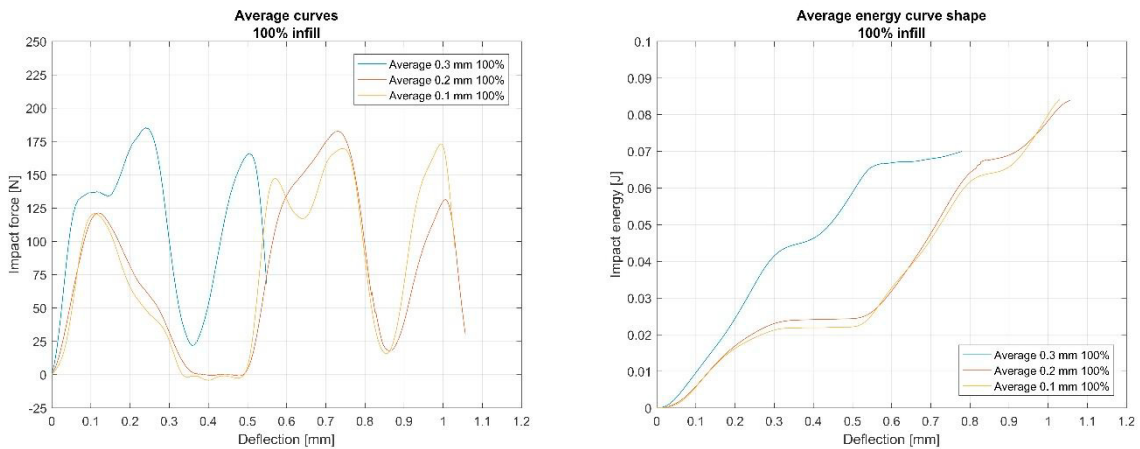


Fig. 4. (Left) Average force-deflection curves; (Right) Average energy-deflection curves.

The maximum impact force and the value of deflection at the break for the observed layer thicknesses are shown in Fig. 5. The maximum impact force is higher in lower layer thicknesses (see trendline, Fig. 5- Left). Unfortunately, the highest value scatter is present in the 0.1 mm batch, due to the presence of the highest peaks later in the propagation phase (see Fig. 3, Bottom-Left). In the 0.3 mm batch, the highest values are located at the first peak, in the 0.2 mm batch the maximum values are mostly placed at the second peak. The maximum impact force value range is 11.489 N and 13.123 N for the 0.2 and 0.3 mm batches, respectively. In the 0.1 mm layer thickness batch the value range is much higher, i.e., 35.24 N. The 0.1 mm batch is unique because it has a considerable number of maximum impact force values located at the last peak. On the one hand, this is an advantage for this layer thickness because it can withstand high forces later in the propagation phase. Unfortunately, this may produce a high scatter of the force values.

The same applies to the deflection at break values (see Fig. 5, Right): the trendline shows higher values for lower layer thicknesses. The highest value scatter is present in the 0.2 mm batch, mostly due to specimens no. 2 and 5 reaching a much higher deflection than the other specimens from the batch (see Fig. 3, Middle-Left). Here, five specimens experienced a break at around 1 mm, the other two failed at around 1.3 mm and 2 mm. Because of that, the deflection at the break range for the 0.2 mm batch is the highest, i.e., 1.068 mm. In the 0.3 mm batch, there were deflection recordings after the last peak, resulting in a 0.432 mm range in break deflection values. In contrast to the mentioned batches, all of the 0.1 mm specimens experienced a break at almost the same location, resulting in a deflection value range of just 0.044 mm.

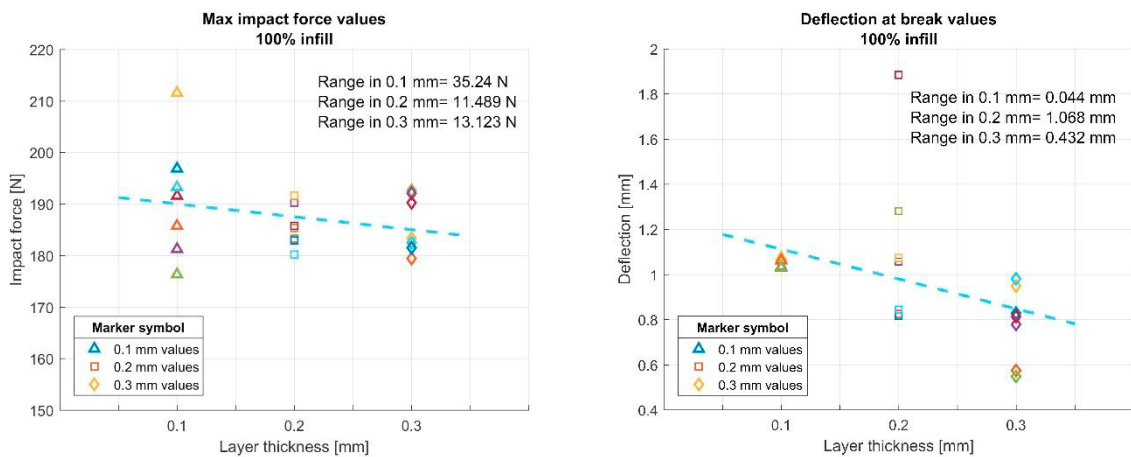


Fig. 5. (Left) Maximum impact force values; (Right) Deflection at break values.

The impact energy and impact strength values are shown in Fig. 6. From both charts the trendline shows that lower layer thicknesses produce higher values. The highest value range is present in the 0.2 mm batch, due to the large difference in deflection at the point of specimen break. Namely, two of the 0.2 mm specimens accumulated more energy because they experienced break much after 1 mm, where almost all of the tested specimens failed. That is the reason why two of the 0.2 mm specimens had much higher values than the rest of the batch. The range in impact energy values is shown in Fig. 6- Left. The range in impact strength values is also the highest in the 0.2 mm batch. The impact strength values (Fig. 6- Right) have a similar trendline and range as impact energy due to the impact energy value being a constituent of the impact strength equation from ISO 179. The average impact strength values for all three chosen layer thicknesses are shown in Table 2.

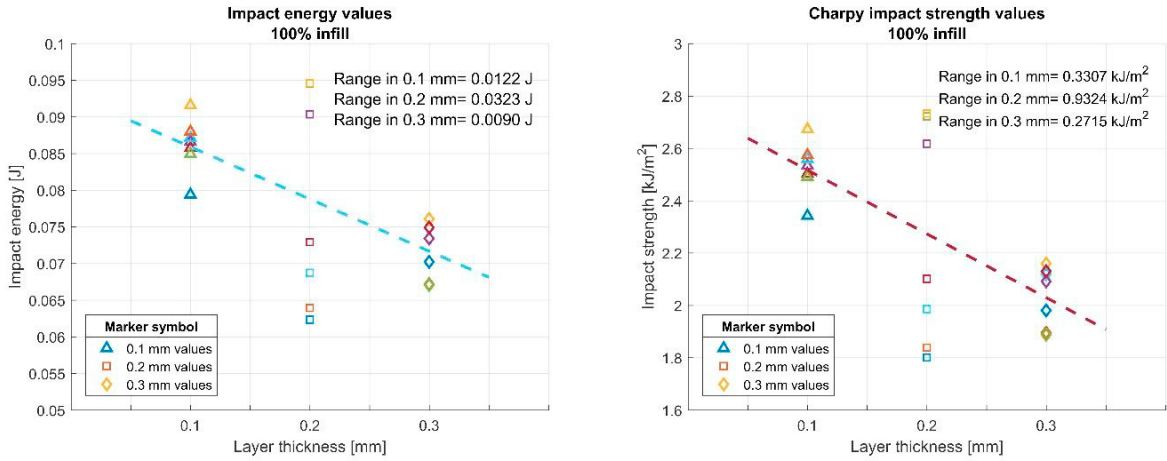


Fig. 6. (Left) Impact energy values; (Right) Charpy impact strength values.

Table 2. Average impact strength values for all three chosen layer thicknesses.

Layer thickness (mm)	0.3	0.2	0.1
Average impact strength (kJ/m ²)	2.0378	2.2572	2.5248

4. Conclusions

The Charpy impact tests were conducted on full infill specimens with different layer thicknesses namely, 0.3 mm, 0.2 mm, and 0.1 mm. All specimens were prepared according to ISO 179 standard, with a type A notch. The notch was directly AMed, not machined. The results are interpreted on impact force/energy-deflection charts and maximal impact force, deflection at the point of break, impact energy, and impact strength value charts relative to specimen thickness. Some conclusions are imposed here:

- High repeatability of results is present concerning impact force/energy response, relative to deflection.
- From average curves the matching between 0.2 mm and 0.1 mm batch is visible.
- Overall, higher impact force, energy, deflection at the point of break, and impact strength are achieved with lower layer thicknesses.
- Average impact strength values here are in the range between 2.0378 and 2.5248 kJ/m².
- The highest overall impact property value range is present in the 0.2 mm layer thickness batch, due to some of the specimens there failing much after the rest of the batch (see the impact force-deflection chart- Fig. 3, Middle-Left).

Acknowledgments

The authors would like to thank the support from the European Union’s Horizon 2020 research and innovation program (H2020-WIDESPREAD2018, SIRAMM) under grant agreement No. 857124.

References

Popović, M., Pjević, M., Milovanović, A., Mladenović, G., Milošević, M., 2023. Printing parameter optimization of PLA material concerning geometrical accuracy and tensile properties relative to FDM process productivity. *Journal of Mechanical Science and Technology* 37(1), pp. 1-10. DOI: 10.1007/s12206-023-0113-6.

Pandžić, A., Hodžić, D., Milovanović, A., 2019a. Effect of Infill Type and Density on Tensile Properties of PLA Material for FDM Process. *Proceedings of the 30th DAAAM International Symposium*, DAAM International. DOI: 10.2507/30th.daaam.proceedings.074.

Pandžić, A., Hodžić, D., Milovanović, A., 2019b. Influence of Material Colour on Mechanical Properties of PLA Material in FDM Technology. *Proceedings of the 30th DAAAM International Symposium*, DAAM International. DOI: 10.2507/30th.daaam.proceedings.075.

- Milovanović, A., Golubović, Z., Babinský, T., Šulák, I., Mitrović, A., 2022a. Tensile properties of polypropylene additively manufactured by FDM. *Structural Integrity and Life* 22(3), pp. 305-308.
- Milovanović, A., Sedmak, A., Golubović, Z., Zelić Mihajlović, K., Žurkić, A., Trajković, I., Milošević, M., 2021. The effect of time on mechanical properties of biocompatible photopolymer resins used for fabrication of clear dental aligners. *Journal of the Mechanical Behavior of Biomedical Materials* 119(104494), pp. 1-9. DOI: 10.1016/j.jmbbm.2021.104494.
- Milovanović, A., Poduška, J., Trávníček, L., Nahlik, L., Sedmak, A., Milošević, M., Berto, F., 2022b. Side-groove effect on fracture mechanical fatigue testing of PLA material. *Procedia Structural Integrity* 42, pp. 847-856. DOI: 10.1016/j.prostr.2022.12.107.
- Milovanović, A., Milošević, M., Trajković, I., Sedmak, A., Razavi, M.J., Berto, F., 2022c. Crack path direction in plane-strain fracture toughness assessment tests of quasi-brittle PLA polymer and ductile PLA-X composite. *Procedia Structural Integrity* 42, pp. 1376-1381. DOI: 10.1016/j.prostr.2022.12.175.
- Popa, C.F., Mărghitaș, M.P., Galațanu, S.V., Marșavina, L., 2022. Influence of thickness on the IZOD impact strength of FDM printed specimens from PLA and PETG. *Procedia Structural Integrity* 41, pp. 557-563. DOI: 10.1016/j.prostr.2022.05.064.
- Ailinei, I., Galațanu, S.V., Marșavina, L., 2022. The effects of layers orientation on impact energy evaluation of FDM printed specimens. *Material Design & Processing Communications* 3(10). DOI: 10.1002/mdp2.267.
- Rajpurohit, S., Dave, H.K., 2020. Impact strength of 3D printed PLA using open source FFF-based 3D printer. *Progress in Additive Manufacturing* 6, pp. 119-131. DOI: 10.1007/s40964-020-00150-6.
- Patterson, A.E., Pereira, T.R., Allison, J.T., Messimer, S.L., 2021. IZOD impact properties of full-density FDM polymer materials with respect to raster angle and print orientation. *Proceedings of the Institution of Mechanical Engineers, Part C: Journal of Mechanical Engineering Science* 235(10), pp. 1891-1908. DOI: 10.1177/0954406219840385.
- Stoia, D.I., Galațanu, S.V., Marșavina, L., 2022. Impact properties of laser sintered polyamide, according to building orientation. *Journal of Mechanical Science and Technology* 37(6), pp. 1-5. DOI: 10.1007/s12206-022-2108-0.
- Ahmed, H., Hussain, G., Gohar, S., Ali, A., Alkahtani, M., 2021. Impact Toughness of Hybrid Carbon Fiber-PLA/ABS Laminar Composite Produced through Fused Filament Fabrication. *Polymers* 13, 3057. DOI: 10.3390/polym13183057.
- Ferdinand, M., Várdai, R., Móczó, J., Pukánszky, B., 2023. A novel approach to the impact modification of PLA. *Engineering Fracture Mechanics* 277, 108950. DOI: 10.1016/j.engfracmech.2022.108950.
- Tian, J., Cao, Z., Qian, S., Xia, Y., Zhang, J., Kong, Y., Sheng, K., Zhang, Y., Wan, Y., Takahashi, J., 2022. Improving tensile strength and impact toughness of plasticized poly(lactic acid) biocomposites by incorporating nanofibrillated cellulose. *Nanotechnology Reviews* 11, pp. 2469-2482. DOI: 10.1515/ntrev-2022-0142.
- Valean, C., Marșavina, L., Mărghitaș, M., Linul, E., Razavi, J., Berto, F., Brighenti, R., 2020. The effect of crack insertion for FDM printed PLA materials on Mode I and Mode II fracture toughness. *Procedia Structural Integrity* 28(10), pp. 1134-1139. DOI: 10.1016/j.prostr.2020.11.128.
- Milovanović, A., Golubović, Z., Trajković, I., Sedmak, A., Milošević, M., Valean, E., Marsavina, L., 2022d. Influence of printing parameters on the eligibility of plane-strain fracture toughness results for PLA polymer. *Procedia Structural Integrity* 41, pp. 290-297. DOI: 10.1016/j.prostr.2022.05.034.
- Krausz, T., Ailinei, I., Galațanu, S.V., Marșavina, L., 2021. Charpy impact properties and numerical modeling of polycarbonate composites. *Material Design & Processing Communications* 3(5), pp. 1-9. DOI: 10.1002/mdp2.260.

Structural Integrity and Reliability of Advanced Materials obtained through Additive Manufacturing (SIRAMM23)

Mechanical behavior of recycled FDM printed parts from PETG in the circular economy

Sergiu-Valentin Galațanu^a, Fátima Nunes Serralha^b, Mihai-Petru Mărghițaș^a, Corina Șoșdean^{c,*}, Cosmin-Florin Popa^a, Linul Emanoil^a and Liviu Marșavina^a

^aDepartment of Mechanics and Strength of Materials, Politehnica University of Timisoara, Mihai Viteazu Bd., 300222 Timisoara, Romania

^bInstituto Politécnico de Setúbal, Campus do IPS – Estefanilha, 2910-761 Setúbal, Portugal

^cDepartment of Mechatronics, Politehnica University of Timisoara, Mihai Viteazu Bd., 300222 Timisoara, Romania

Abstract

The aim of this paper was to observe the behavior of recycled 3D printed polyethylene terephthalate glycol (PETG) specimens and 3D printed raw specimens. In order to extrude the recycled grains into a filament, a Felfil evo filament extruder was used. The recycled filament was extruded from PETG at a temperature of 195°C and with a speed of 7 rpm according to the manufacturers' requirements. Subsequently, different colors of the raw filament were printed on tensile specimens using Prusa i3 MK3S Original to compare the results between the recycled filament and the manufactured one. After printing the samples, the tensile tests were performed on the Zwick machine, with a capacity of 5KN. For the determination of the strain state in the test specimens, digital image correlation was used. A good correlation between the results was observed. Digital image correlation helped to better understand of the distribution of true principal strain in the recycled and raw specimens.

© 2023 The Authors. Published by Elsevier B.V.

This is an open access article under the CC BY-NC-ND license (<https://creativecommons.org/licenses/by-nc-nd/4.0>)

Peer-review under responsibility of the SIRAMM23 organizers

Keywords: polyethylene terephthalate glycol, fused deposition modelling, mechanical behaviour, recycling.

* Corresponding author.

E-mail address: corina.sosdean@upt.ro

1. Introduction

In the last decade, 3D printing technology using Additive Manufacturing (AM) technology, became more and more popular, due to the various industrial applications in the field of rapid manufacturing to fabricate prototypes and concept models. It has several benefits like simpler and reduced supply chain, increased longevity of the product, eradication of tooling need, and shorter assembly chains according to Krishna et al. (2021) and also provides design freedom to the product designer and makes the product more sustainable, Vashi et al. (2021).

Fused deposition modelling (FDM), which is perhaps the most used AM techniques by materials engineers and hobbyists alike, involves the extrusion of a molten filament through a heated nozzle onto a build plate to form a part, which is subsequently built up layer by layer until a finished printed product is completed, Holcomb et al. (2022).

Polyethylene terephthalate glycol (PETG) is an amorphous polymer widely used in 3D printing which performs well mechanically and is far less brittle compared to polylactic acid (PLA) and acrylonitrile butadiene styrene (ABS) (124% elongation at fracture vs. 6% and 100%, respectively). Also, compared to the semi-crystalline polyamide printing polymers, the amorphous PETG shows a lower thermal shrinkage after printing, leading to reduced warping of the printed parts, Rijckaert et al (2022).

A wide range of thermoplastic filaments like PLA, ABS, and PETG are used as a filament in 3D printing according to Ngo et al. (2018), which are non-biodegradable, thus the waste aspect of 3D printed plastic products is a matter of concern due to its impact on the circular economy. Zhu et al. (2021) shown that in order to incorporate sustainability into the process, to minimize negative environmental impact, “the choice of filament-type has an important role in the circular economy of filaments”. Popa et al. (2022, 2023) investigated the impact energy and the impact strength on PLA and PETG specimens, obtained through FDM technology.

Studies have been conducted in order to obtain recycled 3D printed PETG models with high mechanical properties. Schneevogt et al. (2021) shown that a 100% recycled PET (rePET) filament is compared to a conventional PETG filament; tensile tests are furthermore conducted on specimens made from a conventional polymer material and a recycled polymer material. Another study describing the process of printing with 100% recycled PETG using fused FGF (fused granule fabrication) methods examines the extent to which PETG can be recycled and reprinted through the same FGF tool without significant loss to its material properties, Thompson et al. (2022). Kováčová et al. (2020) tried to replace commercial virgin PETG with cheaper recycled PETG whose price is ten times lower, using composite materials for 3D printing technology by FFF (fused filament fabrication), and concluded that replacing virgin PETG with recycled PETG does not significantly change the properties of the filament, just causes a price reduction. Furthermore, research showed that it was possible to recycle and reuse PETG material multiple times, resulting in a significant gain in the mechanical properties of the recycled materials Vidakis et al. (2021).

In this study, we investigated the mechanical properties of raw and recycled PETG materials. The Dantec Digital Image Correlation (DIC) 3D was used to measure the deformation of the specimens in the time of tensile test for a better understanding of their behavior. A good correlation between the results obtained using the raw material and the recycled PETG material was observed. If compute the difference between the movement of the upper and lower point from the specimen in DIC, the maximum displacement in the recycled specimen is 1,39mm and 1,28mm for the raw specimen respectively until the crack appears.

2. Materials and Methods

In the framework of this study, tensile tests were carried out on various specimens. The specimens were manufactured using Prusa MK3 printer. Fused deposit modeling technology, with different colors of the filament: colorless, black, and white, but also filament extruded from recycled pellets, were used.

For the extrusion of the recycled grains into a filament, used in fused deposition modeling (FDM) technology, a Felfil evo filament extruder was used, Figure 1 a. The recycled filament was extruded from polyethylene terephthalate glycol (PETG) at a temperature of 195°C and with a speed of 7 rpm according to the manufacturer's requirements. In order to observe the geometric characteristics of the new extruded filament, the diameter of the wire was measured as follows: from 10 to 10 cm in length, Figure 1b.

To manufacture the specimens from the recycled filament, but also from raw filament infill, speed was set to 80mm/s, with a layer thickness of 0.2mm and 100% rectilinear infill. The nozzle temperature for the first layer was 240°C and 250°C for other layers. The bed temperature was 85°C for the first layer and 90°C for the other layers respectively.



Fig. 1. (a) Felfil evo filament extruder and (b) average of the diameter in length

Tensile test specimens with the following dimensions were used: 2mm in thickness, 5mm in width and the calibrated area of the length 40mm, respectively. The specimens were subjected to tensile testing using a universal testing machine (Zwick Proline Z005, Ulm, Germany), with a maximum force of 5 kN at ambient temperature. To determine Young's Modulus a manual clip-on extensometer was used for some of the tests. The Digital 3D Image Correlation System Q-400 was used for the other tests. In the first step, the calibration procedure was realized. The calibration process was carried out with a BNB9x9. For these tests, the Global Residual was 0.240, and a medium accuracy is between 300 and 500. Images of the specimens were captured at a rate of 1 Hz, one picture for each camera at one second. Next, the specimens were painted with several layers of white paint until the surfaces of the specimens were completely white and without reflectivity. In the end, a second light-speckle pattern of black paint was applied over the area of interest. The specimens were tested as follows: PETG Transparent Recycled specimens, PETG Transparent specimens, PETG White specimens, and PETG Black specimens.

3. Results and discussions

The aim of this paper was to observe the behavior of recycled and raw specimens. In order to understand this behavior, different charts were plotted for each type of specimen. Fig. 2 presents stress–strain curves for the same type of specimens. For a better observation and comparison of the results obtained for each type of material, the stress-strain curves were cut at 0.2 mm/mm. However, some of the specimens failed at much higher strain values, but this aspect can be observed in Fig. 3 c.

Taking into account those results, the average of the maximum stress, the average of the strain at maximum stress, and the average of the ultimate strain were obtained, in Fig. 3. The Young Modulus was determined only for the recycled specimens and for the black specimens.

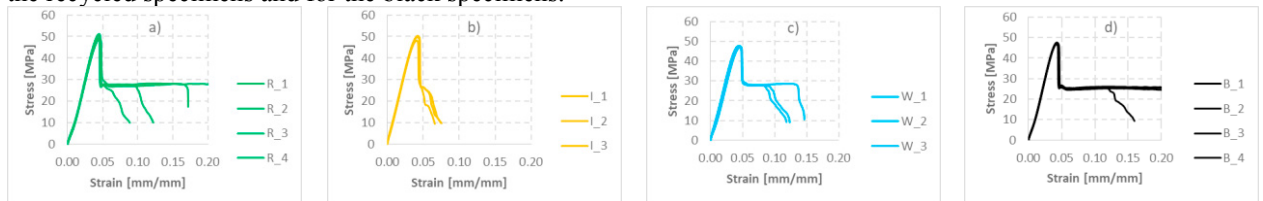


Fig. 2. Stress – strain curves for (a) PETG Transparent Recycled specimens, (b) PETG Transparent specimens, (c) PETG White specimens, and (d) and PETG Black specimens.

It can be seen that the maximum stress average has similar values for all the groups of specimens investigated. Both transparent specimen groups, from recycled material and from raw material, have a maximum stress of about

49 MPa. The white and black specimen groups have lower values of the maximum stress (about 47 MPa in the case of white samples, and about 46 MPa in the case of black samples respectively).

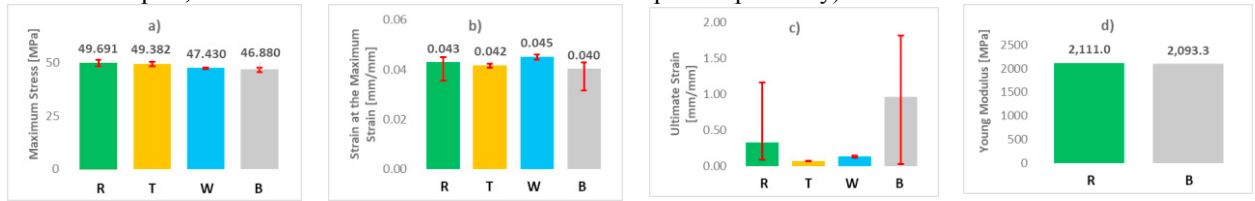


Fig. 3. (a) Average of the maximum stress, (b) Average of the strain at the maximum stress, (c) Average of the ultimate strain, and (d) and Young Modulus.

The highest values of the strain at the maximum stress were observed in the case of white samples, Fig. 3b; they tend to be more ductile than the other samples, even though the difference between the values is subtle. If we analyze the results, we can see that the white samples have the best repeatability, while the recycled samples have a higher spread of values. This may be due to the inhomogeneity, but also to the diameter variation for the extruded recycled wire. At the same time, in the case of the recycled and black samples, the results show us a large dispersion in terms of the ultimate strain. For a better understanding of this behavior, more specimens need to be analyzed in the future. However, with the exception of one specimen, all the black samples presented high ultimate strain values. The observed differences between the results recorded for the group of specimens with different wire colors also confirm that the color influences the mechanical tensile properties, Frunzaverde et al. (2023).

In Fig. 3 d, it can be seen that the Young modulus obtained has similar values to those from the literature (about 2100 MPa both for the recycled and raw specimens).

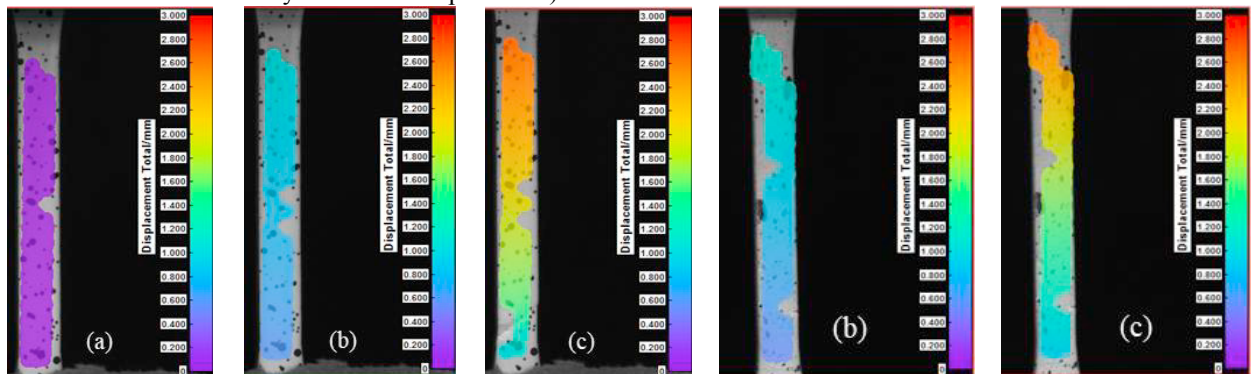


Fig. 4. Displacement from DIC on the recycled specimen

Fig. 5. Displacement from DIC on the raw specimen

In Fig. 4 three displacement phases of the recycled specimen measured with DIC are depicted. The initial phase is presented in (a). This is the reference position for the measurement when the specimen is not loaded. Figure (b) shows an intermediary phase, the specimen was loaded, and the maximum deformation is located in the upper part of the specimen. The last figure shows the last phase before the crack appears; in this phase, the maximum displacement is 2.56 mm in the upper part of the specimen. Fig 5 presents the same thing but for the raw specimen. In this case, the first stage was no longer represented, only the second (b) and third (c) phases are displayed. Similar to the results recorded in the case of the recycled specimen the maximum displacement is about 2.32mm before the crack appears.

If we compute the difference between the movement of the upper and lower point from the specimen in DIC, the maximum displacement in the recycled specimen is 1,39mm and 1,28mm for the raw specimen respectively until the crack appears.

In Fig. 6 and 7 the true principal strain from DIC on the recycled and raw specimens, are presented. The initial phase (presented in Fig. 6a), the intermediate phase (Fig. 6b, Fig. 7b) and a phase close to the appearance of the crack (Fig. 6c and Fig. 7c) are presented. These images provide a better understanding in the distribution of true

principal strain in the recycled and raw specimens. In both cases, Fig. 6c and Fig. 7c already present the appearance of the crack, in the bottom part of the recycled specimen, and in the upper part of the raw specimen.

Experimental testing results showed that fracture occurred in the calibrated area of the specimens.

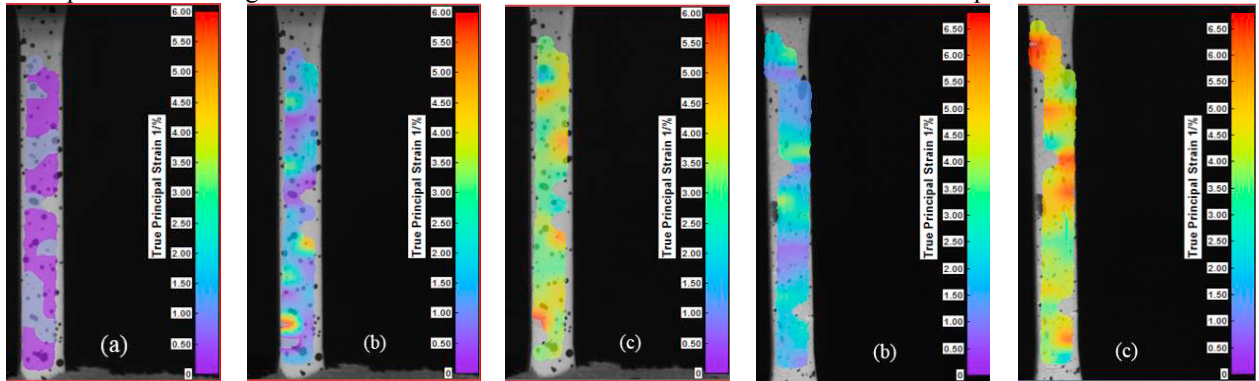


Fig. 6. True Principal Strain from DIC on the recycled specimen

Fig. 7. True Principal Strain from DIC on the raw specimen

4. Conclusions

Taken into account the results of the study, the following conclusions can be drawn:

- Maximum stress presents similar results for the specimens from PETG transparent recycled (R) and PETG transparent (T) from raw wire respectively (R: 49.69 MPa and T:49.38 MPa respectively);
- The results for specimens made from PETG white (W) and PERG Black (B) showed weaker values (W: 47.43 MPa and B: 46.88 MPa respectively). The color of the specimens leading to different results was also observed by other researchers;
- All specimens presented the same behavior in terms of the strain state at the maximum stress value except the results for the white PETG specimens (R:4.3%,T:4.2, B:4% and W:4.5%).
- Ultimate strain presented a major dispersion of results with a high standard deviation for the recycled and black samples. For a better understanding of this behavior, more specimens need to be analyzed.
- Young Modulus has similar values for the specimens, similar to those found in the literature (about 2100 MPa).

Acknowledgements

The authors want to acknowledge the E³UDRES² alliance for supporting this research. This research was supported by the ERASMUS+ Programme [101004069].

References

- Frunzaverde, D., Cojocar, V., Bacescu, N., Ciubotariu, C.-R., Miclosina, C.-O., Turiac, R.R., Marginean, G. 2023. The Influence of the Layer Height and the Filament Color on the Dimensional Accuracy and the Tensile Strength of FDM-Printed PLA Specimens. *Polymers* 2023, 15, 2377. 10.3390/polym15102377 .
- Holcomb, G., Caldona, E. B., Cheng, X., & Advincula, R. C. 2022. On the optimized 3D printing and post-processing of PETG materials. *MRS communications*, 12(3), 381-387.
- Kováčová, M., Kozakovičová, J., Procházka, M., Janigová, I., Vysopal, M., Černičková, I. & Špitalský, Z. 2020. Novel hybrid PETG composites for 3D printing. *Applied Sciences*, 10(9), 3062.
- Krishna LSR, Srikanth PJ, 2021. Evaluation of environmental impact of additive and subtractive manufacturing processes for sustainable manufacturing. *Materials Today: Proceedings* 21; 45:3054–3060.
- Ngo TD, Kashani A, Imbalzano G, Nguyen KTQ, Hui D, 2018. Additive manufacturing (3D printing): A review of materials, methods, applications, and challenges. *Composites Engineering* 2018; 143: Elsevier 172–196.

- Popa C.F., Mărghitaș M.P., Galațanu S.V., Marșavina L., 2023. Influence of thickness on the IZOD impact strength of FDM printed specimens from PLA and PETG, *Procedia Structural Integrity*, Volume 41, Pages 557-563, ISSN 2452-3216, <https://doi.org/10.1016/j.prostr.2022.05.064>.
- Popa C.F., Krausz T., Galațanu S.V., Linul E., Marșavina L., 2022. Numerical and experimental study for FDM printed specimens from PLA under IZOD impact tests, *Materials Today: Proceedings*, Volume 78, Part 2, Pages 326-330, ISSN 2214-7853, <https://doi.org/10.1016/j.matpr.2022.11.501>.
- Rijckaert, S., Daelemans, L., Cardon, L., Boone, M., Van Paepegem, W., & De Clerck, K. 2022. Continuous Fiber-Reinforced Aramid/PETG 3D-Printed Composites with High Fiber Loading through Fused Filament Fabrication. *Polymers*, 14(2), 298.
- Schneevogt, H., Stelzner, K., Yilmaz, B., Abali, B. E., Klunker, A., & Völlmecke, C. 2021. Sustainability in additive manufacturing: Exploring the mechanical potential of recycled PET filaments. *Composites and Advanced Materials*, 30.
- Thompson, N., & Weaver, J. 2022. Closed Loop Recycling of Low Friction Polymers in Fused Granule Fabrication Additive Manufacturing Processes. *Solid Freeform Fabrication Symposium*.
- Vidakis, N., Petousis, M., Tzounis, L., Grammatikos, S. A., Porfyraakis, E., Maniadi, A., & Mountakis, N. 2021. Sustainable additive manufacturing: Mechanical response of polyethylene terephthalate glycol over multiple recycling processes. *Materials*, 14(5), 1162.
- Vashi Y, Anand R, Jayakrishna K, Rajyalakshmi G, Raj SA, 2021. Design and analysis of 3D printed UAV wheel. *Materials Today: Proceedings* 2021; 46: 8307–8312.
- Zhu C, Li T, Mohideen MM, Hu P, Gupta R, Ramakrishna S, Liu Y, 2021. Realization of Circular Economy of 3D Printed Plastics: A Review. *Polymers*. 2021; 13(5):744.



Structural Integrity and Reliability of Advanced Materials obtained through Additive Manufacturing (SIRAMM23)

Numerical and Experimental Analysis of Quilling-Inspired Metamaterials

Vasilica Ioana Cimpoies¹, Mircea Cristian Dudescu^{1*}

¹ Department of Mechanical Engineering, Faculty of Automotive, Mechatronics and Mechanical Engineering, Technical University of Cluj-Napoca, B-dul Muncii 103-105, 400641 Cluj-Napoca, Romania

Abstract

In the current paper is presented the behaviour of a quilling-inspired metamaterial with a nonlinear response to deformation loads. The art of paper quilling relates on curved shapes, circles and spirals that generate 3D multi-layered structures that have the ability to auto-sustain. The study started with models of self-sustaining structures created through paper quilling techniques, further serving as base models for generating 3D metamaterials that resulted in spiral shape layers. These structures have demonstrated the capacity to withstand substantial loads, resulting in high deformation rates and instant shape recovery. The samples of metamaterial have been subjected to compressive loads and the results have been collected through three different methods: experimental testing, digital image correlation and numerical analysis. The purpose of this approach was to find a methodology to investigate the mechanical behaviour of these structures, namely the initial stiffness of the metamaterial. Using these methods of data collection and validation of the results, offers the possibility to research in detail the metamaterial inner structure and to predict the nonlinear displacement generated inside each cell of the layer.

© 2023 The Authors. Published by Elsevier B.V.

This is an open access article under the CC BY-NC-ND license (<https://creativecommons.org/licenses/by-nc-nd/4.0>)

Peer-review under responsibility of the SIRAMM23 organizers

Keywords: Metamaterials ; Quilling ; Spirals ; Digital Image Correlation; Numerical Analysis; Compression Test

* Corresponding author.

E-mail address: mircea.dudescu@rezi.utcluj.ro

1. Introduction

Metamaterials represent a class of materials characterized by the incorporation of structural components that induce alterations in the inherent physical characteristics of the constituent base material. Mechanical metamaterials possess unique and exceptional properties that arise from the relationship between their structural framework and mechanical properties and are able to modify their response to physical phenomena (Findeisen, 2017). These atypical properties may include negative stiffness, compressibility, thermal expansion, and auxeticity, that are rarely seen in nature (Fu, 2018). These characteristics result in advanced functionalities, thus making these materials ideal for a range of specialized applications. The most well-known group of mechanical metamaterials are auxetic systems, which include various geometries that have been established for authenticity (Mousanezhad, 2016). These comprise of re-entrant structure, rotating rigid unit systems, chiral honeycombs, origami/folding patterns, dilatational, and helical systems and have been replicated or detected in sizes that range from the nanoscale to the macroscale (Mizzi, 2021).

By focusing on a particular direction of metamaterials inspired by art, in the last 10 years, has been developed an entire family of metamaterials originating from origami and kirigami (Tachi, 2013). These metamaterials are using the principals of the Japanese art of paper folding and are highly customizable. Their mechanical properties can be altered by changing the geometry and layout of the folded patterns. Researchers have developed a range of groundbreaking and practical origami-based metamaterials, including notable examples such as Ron Resch patterns, Miura-ori structures, and transformable origami metamaterials. (Kshad, 2018) (Zadpoor, 2016). These metamaterials have found applications in robotics, nano and micro mechanisms, aerospace, furniture, and medical devices (Tachi, 2013).

In the context of paper quilling, this area remains relatively underexplored, offering a promising avenue for the development of self-sustaining structures. Paper quilling constitutes an artistic practice wherein strips of paper are meticulously shaped and adhered together to craft ornamental patterns. This process involves the rolling, looping, curling, twisting, and other forms of manipulation of paper strips to fashion various shapes that serve as the building blocks for decorative elements in greeting cards, artwork, containers, as well as in the creation of models, jewelry, figurines, and 3D miniatures, among other applications.

Current research employs paper quilling as a source of inspiration for the development of novel metamaterials. The principal objective of this investigation is to gain insights into the mechanical response of a metamaterial inspired by quilling, particularly one characterized by nonlinear behaviour under deformation loads. The initial section of this paper introduces the structural configuration under scrutiny, elucidating its geometric parameters. A 3D-printed test specimen was employed to subject it to compressive forces while capturing the corresponding force-displacement relationship. The analysis of the inner structural displacements within the metamaterial was conducted using the optical technique known as Digital Image Correlation. Comparative assessments of both experimental datasets were performed in relation to numerical simulations executed via the Finite Element Method. The results convergence and the mechanical stiffness of the structure are presented in the subsequent sections, encompassing the results and conclusions.

2. Materials and Methods

2.1. Design Steps of the Metamaterial

The creation of the metamaterial started from a conceptual design of paper, which was shaped using quilling techniques to create various forms, culminating in interconnected cellular structures comprised of linked spirals. Quilling as a modeling method frequently entails the use of curved, twisted, and spiral shapes, imbuing the model with a fluid quality and enabling the generation of limitless, repetitive patterns.

The second step was the selection of the most suitable model, identified as a geometric configuration consisting of four-armed spirals, which were consistently arranged along both axes (XY). This arrangement led to the formation of layered metamaterial structures.

The third stage of the process entailed the digital transposition of the model. The model was simplified and converted into a stylized digital format to facilitate its compatibility with 3D printing technology, resulting in their final cellular structure. Cellular materials are distinguished for their intrinsic lightweight properties and their exceptional ability to attenuate external forces. Within the domain of cellular materials, those exhibiting periodic

structures have garnered significant attention. This attention is owed to their optimization through the application of minimum weight design principles, comprehensive dynamic and quasi-static experimentation, and the employment of large-scale computer simulations. (Cernescu, 2014).

The provided images below depict the sequential stages involved in achieving the optimal design, progressing from the initial paper concept to the final 3D-printed samples.

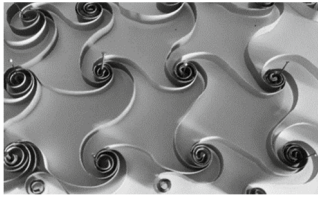


Fig. 1. Paper quilling model

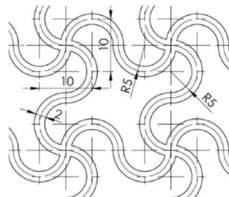


Fig. 2. 2D view of one cell of the metamaterial with geometrical dimensions

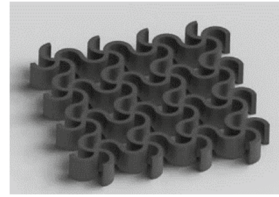


Fig. 3. Geometrical pattern of the metamaterial

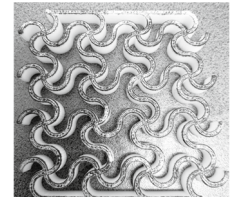


Fig. 4. 3D printed structure of the metamaterial

2.2. Material and Manufacturing Method

In order to create the distinct meso-structure and material design of metamaterials, special manufacturing techniques are necessary. These techniques must be creative and advanced in nature. 3D printing presents a disruptive manufacturing process which combines molding principles with unique benefits such as the ability to create complex geometries, customization, and quick manufacturing. Due to these advantages, 3D printing is increasingly used to fabricate mechanical metamaterials with intricate internal structures (Zhou, 2023).

The manufacturing method selected for all the samples was 3D printing, due to accessibility and ease in creating complicated structures such as spiral patterns. The material chosen for 3D printing was Z-ultrat, an ABS plastic blend filament. When printed this material yields a consistent surface texture and exhibits properties similar to those of models produced through injection molding. Z-ultrat is characterized by its widespread availability, user-friendly nature, and its ability to sustain intricate structures via a single production process. Furthermore, one of the advantages associated with Z-Ultrat is its versatility in conducting a wide range of physical tests, thereby offering precise and relevant information into the response of a component to its environment. (Szykiedans, 2016).

Standard tensile samples of the material were produced for experiments, using similar printing parameters to get the material constants of the 3D printed metamaterial. The specimens printed with 100% infill rate and +45-45 infill pattern, had a cross-sectional area of 9.57 mm by 4 mm. They were tensile tested up to a maximum force of 1,100 N at a speed of 4 mm per minute. Tensile strength testing revealed values of 28.75 MPa, 0.3 for Poisson's ratio, and 1703 MPa for Young's modulus. Due to air to void ratio of the 3D printed materials, the above values were obtained based upon the methodology described by Racz and Dudescu (2022).

2.3. Testing methods

Due to the spiral shapes, when these structures are subjected to loads was observed that the inside cells present in-plane displacements and rotations around the vertices of the spiral centers (denoted in the displacement-load scheme with "O" – Fig. 5). The movements have been visible during the experiment, but we were limited for measuring the displacements on the testing machine. In order to understand the reaction in the structure have been chosen three methods of analyses:

- Physical compression tests of the 3D-printed samples on a universal testing machine;
- Finite Element Method using Ansys Workbench software;
- Digital Image Correlation (DIC) method.

2.4. Structure description

For a better understand of the behaviour of the structure, after developing the model it was found proper to print layers of metamaterials with different number of cells, predicting that the structure will respond with different displacements depending on the number of cells. All the models keep the same dimensions for cells as presented in Fig. 2. For all the models have been added side plates as supports for positioning the samples onto testing machine. The tested samples, as depicted in Fig. 5 and identified by their respective name codes, are as follows:

1. M1X1 – A single cell of the metamaterial featuring side plates, composed of four interconnected spirals.
2. M3X1 – A row of cells with side plates.
3. M3X3 – A square pattern of cells comprising nine complete cells and sixteen spirals, supported by two plates.

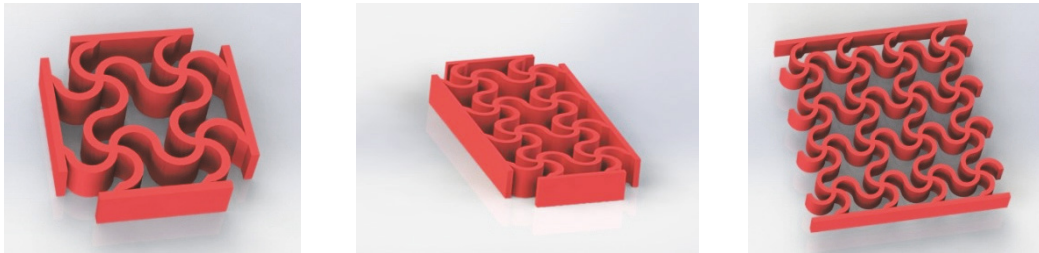


Fig. 5. Samples of the metamaterial used for compressive testing (right - M1X1, center - M3X1, left - M3X3)

2.5. Experimental compression test

Three different 3D printed samples of metamaterial together with the tensile specimens of Z-ultrat (as mechanical properties reference) have been tested on the universal testing machine (Instron 3366, 10 kN). The samples of metamaterial have been subjected to maximum loads that were able to withstand plastic deformation or fracture.

Has been observed that during the experiment the metamaterials have shown a very high extension rate from 8.9% for one-cell model (M1X1), 7.74 % for M3X1 a single row of cells and up to 13.5% for a square pattern with 9 cells (M3X3). All the shapes presented an instant shape recovery of the structure with a precision rate of 99%.

Throughout the testing process, it was observed that the material exhibited deformation in two distinct directions, namely, vertical, and horizontal. The horizontal displacement was primarily induced by the spiral arms, resulting in a rotational deflection around the spiral nodes. Notably, the deformation displayed non-uniform characteristics across all structures, as each spiral arm triggered a cascading effect among its neighbouring counterparts. Consequently, initial observations indicate that these structures demonstrate a nonlinear and hardly predictable response when subjected to applied loads.

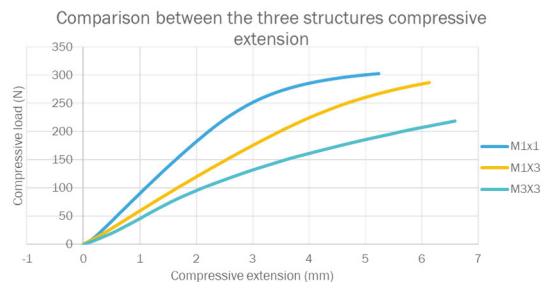


Fig. 6. Comparison of force vs displacement between the three structures (M1X1, M1X3 and M3X3)

The structures have shown that by increasing the number of cells the structure gains significant elasticity. In the graph below (Fig. 6) are presented the compressive load vs compressive extension curves generated by the progressive load for all three models. The extension was captured on the graph up to plastic deformation. Until that point, the structures have an instant recovery behaviour.

2.6. Numerical Analysis

After conducting the physical experiments, the same samples in virtual manner have been tested using the finite element method (as captured in Fig. 7) in Ansys Workbench 2022 (Ansys Inc., USA).

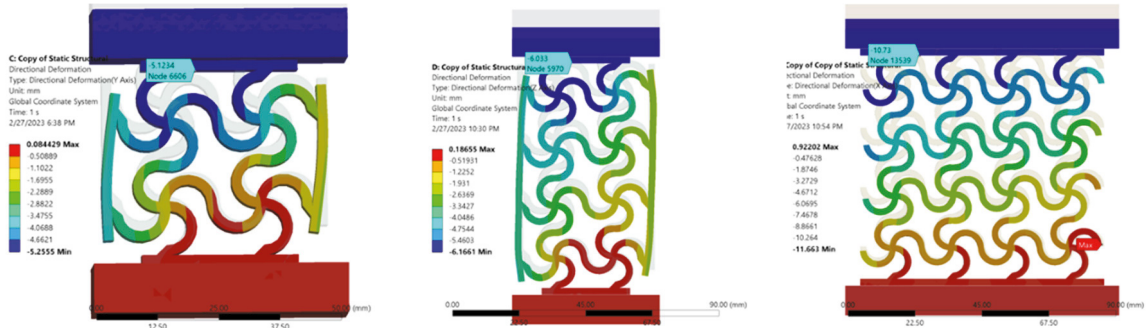


Fig. 7. Samples subjected to compressive tests with FEM (right - M1X1, center - M3X1, left - M3X3)

First the samples have been subjected to the maximum loads resulting from physical experiments by recreating the conditions of the compressive tests. When creating the finite element (FE) models, the material constants were incorporated, including a Young's modulus of 1703 MPa, a Poisson's ratio of 0.3, and a tensile strength derived from experimental testing, amounting to 28.75 MPa. Only geometrical nonlinearities have been considered in the simulation. Subsequently, all FE models were subjected to a uniform load of 150 N, a choice made to ensure elastic behavior and avoidance of the contact interactions between the spiral arms. The focus of the finite element analysis (FEM) was restricted to computing initial stiffness of the metamaterial, including only a linear elastic material model.

The results deviation between the experimental test and FEM was around 3%. Considering that the observed deviation falls within the margin of 5%, signifying a close alignment in results, it can be inferred that the two methods mutually validate each other.

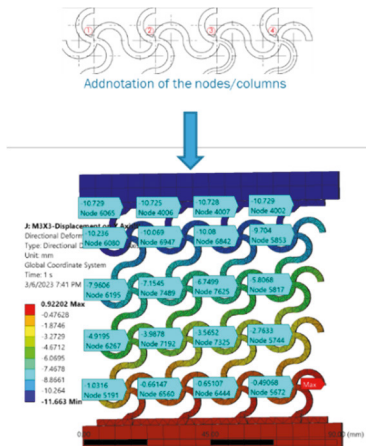


Fig. 8. Directional displacement on Y-axis inside M3X3 model.

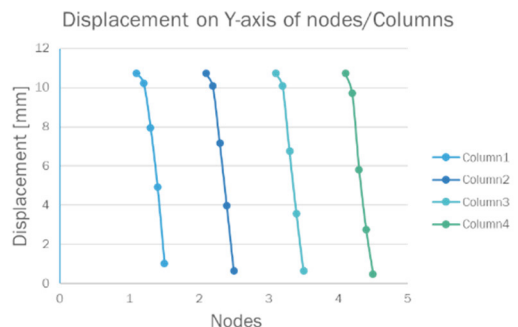


Fig. 9. Graph of the directional displacement on Y-axis

The finite element method offers the possibility to study in detail the structures and the research went further by retrieving the data of compressive extension inside the structures, which conducted to the second step. By collecting the data from inside each of the spiral's nodes gave us an overview of the influence of each individual spiral arm on the displacement of these nodes

If we compare the vertical reaction per column of a square pattern, the nodes tend to present a patterned displacement, that is illustrated in the graph (Fig. 9) attributed to the structure from Fig. 8. For a more comprehensive understanding of the displacement in nodes per each column, presented in Fig. 8, the row of 2D spirals indicates the numbering of columns from the structure.

2.7. Digital Image Correlation Method (DIC)

Due to the fact that in classical compression tests cannot determine the displacement of each node, was found digital image correlation as an appropriate method for data validation of FEM. This method offered the possibility to view in detail and measure the displacements generated by the applied loads inside the structures (Moreira, 2012). For Digital Image Correlation (DIC) method the software used was VEDDAC (Chemnitzer Werkstoffmechanik GmbH, Germany). This method relates to pixels movement from successive frames (Pan, 2011) and the software has the ability to recognize each new position of pixels, tracking their 2D displacements.

During the compression testing of the metamaterial, have been caught scenes of each movement in the structures. The DIC testing starts with a digitized pattern of the undeformed sample, as a reference. On the reference scenes are selected a convenient set of pixels that will change their position when the load is applied (first picture – left from Fig. 10-12).

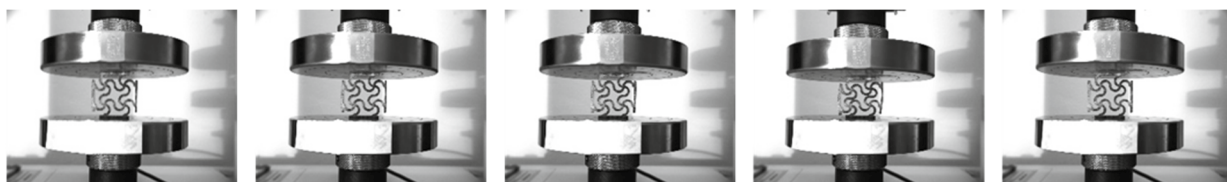


Fig. 10. DIC images corresponding to different loading steps of compressed sample M1X1



Fig. 11. DIC sequence corresponding to different loading steps of compressed sample M3X1



Fig. 12. DIC sequence of the test specimen subjected to a compressive load and unloading (M3X3)

The reference image of the structure is followed by a set of frames (Fig. 10-12) that caught every movement of the

elements during experimental testing. The full-field in-plane displacements inside each sample have been obtained by quantitatively correlating the chosen set of points on each node, given by the group of pixels. The deformations have been identified by the software, in the next scenes, through the displacement path of the pixels and reporting back the extent of deformation between each frame and the reference (Hursa, 2009), (Vanlanduit, 2009).

The measured displacement of the pixels have been compared with the displacement of nodes from FEM simulations as shown in the Fig. 13.

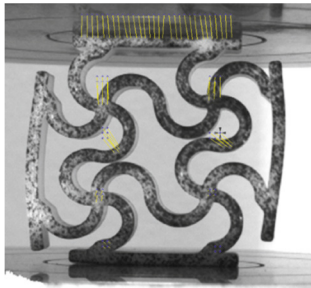


Fig. 13. Displacements vectors of specific points obtained by DIC

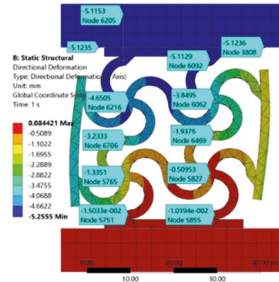


Fig. 14. FEM results of a cell, highlighting the node's displacement

3. Results

In Table 1, a comparison between the compressive experimental testing and numerical analysis for all three models subjected to a load of 150 N is presented. The choice of a consistent load across all models allows for a comprehensive overview of their stiffness characteristics. Consequently, we were able to understand the changes in stiffness given by an increase in the number of cells. As illustrated in the graph (Fig. 15) is clear that having a greater number of cells in both directions results in a substantial reduction in stiffness. For instance, in a square pattern, the stiffness decreases by approximately 60% when compared to a single cell with similar dimensions and subjected to an identical load.

Table 1. The stiffness and strain comparison resulted from experimental testing and numerical analysis.

Structure Type	Experimental Testing		Numerical Analysis	
	Strain at a load of 150 N ($\Delta L/L$) %	Stiffness (N/mm)	Strain at a load of 150 N ($\Delta L/L$) %	Stiffness (N/mm)
M1X1	4.28	60.762	4.55	75.37
M1X1	3.24	46.374	4.4	49.18
M3X3	4.39	31.132	2.6	29.41

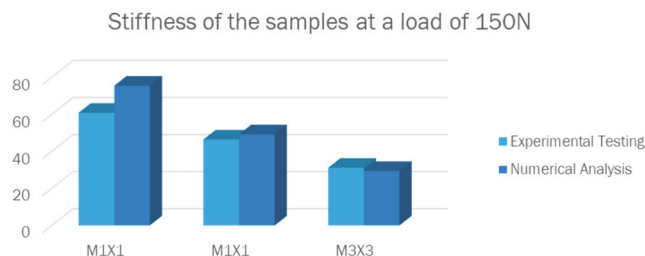


Fig. 15. Comparison of stiffness between the three structures

In the following tables (Table 2, 3 and 4) are captured all the data obtain through two of the selected methods. Digital Image Correlation (DIC) and numerical analysis have provided information about the displacements that occurred at each node, organized by rows (denoted by first digit) and columns (denoted by second digit). From the experimental testing can be exposed only the direct displacement of the entire structure. The experimental tests primarily established the baseline for the displacement all over the structures and served as a reference in comparison with the other methods.

For Sample M1X1 through experimental testing has been obtained a maximum displacement of 5.23 mm, which closely aligns with the values generated through DIC (5.249 mm) and numerical analysis (5.12 mm). The same trend is observed for sample M3X1, where the direct displacement obtained through conventional compression testing is 6.13 mm, and for sample M3X3 the amount of 10.98 mm.

The comparison purpose is to demonstrate that the discrepancies in the data obtained are minimal, under 5% for the majority of the data points. This validates the results obtained through all three methods as complementary and consistent with each other.

Table 2. The results comparison of vertical displacements obtained through numerical analysis and experimental testing for samples M1X1

Sample	Model M1X1							
Points/Rows	1.1	1.2	1.3	1.4	2.1	2.2	2.3	2.4
DIC [mm]	5.249	4.296	3.248	1.251	4.359	3.2	1.494	0.25
Numerical Analysis [mm]	5.12	4.65	3.23	1.34	5.12	3.85	1.94	0.51

Table 3. The results comparison of vertical displacements obtained through numerical analysis and experimental testing for samples M3X1

Sample	Model M3X1									
Points/Rows	1.1	1.2	1.3	1.4	1.5	2.1	2.2	2.3	2.4	2.5
DIC [mm]	5.07	4.1	2.4	1.45	0.33	5.07	4.88	3.8	2.9	0.9
Numerical Analysis [mm]	6.03	5.74	4.38	3.130	1.13	6.03	4.83	2.83	1.60	0.28

Table 4. The results comparison of vertical displacements obtained through numerical analysis and experimental testing for samples M3X3

Sample	Model M3X3									
Points/Rows	1.1	1.2	1.3	1.4	1.5	2.1	2.2	2.3	2.4	2.5
DIC [mm]	10	9.8	7.5	3.2	0.85	10	9.8	7.1	3.3	0.9
Numerical Analysis [mm]	10.729	10.24	7.96	4.92	1.03	10.73	10.07	7.15	3.99	0.66
Points/Rows	3.1	3.2	3.3	3.4	3.5	4.1	4.2	4.3	4.4	4.5
DIC [mm]	10	9.9	7	2.3	1.6	10	10	6	1.9	0.68
Numerical Analysis [mm]	10.73	10.08	6.75	3.57	0.65	10.73	9.70	5.81	2.76	0.49

4. Conclusions

For all the samples subjected to compressive loads each of the three evaluation methods provide highly congruent results. It can be concluded that these methods can be used together to validate the testing results, as the deviations among them remain consistently below 5%

The two different experimental methods used in this case, direct load-displacement measurement and full-field 2D digital image correlation may serve as complementary tools. This proves particularly valuable assessing the behavior of internal points within a structure, a task that may be otherwise challenging to accomplish using alternative instrumentation.

The tested samples have demonstrated that an increasing in the number of cells, whether it occurs in the rows or columns, results in a significant enhancement of the structure's elasticity and a corresponding reduction of its stiffness. It has been validated that the most significant increase is achieved by incorporating symmetrical layers of spiral patterns.

As future perspectives will be developed a mathematical model for this type of structure, with the focus on identifying the potential applications for these metamaterials. It is likely that applications will gravitate towards domains that require high elasticity and instant shape recovery. Evaluation of these structures will imply implementation in the numerical models of both geometrical and material nonlinearities and contact between members of quilling-inspired metamaterials. Considering the observed behavior and properties of this metamaterial, exhibits the potential to function as a substitute for conventional spring mechanisms and can also find application in impact-absorbing panels and protective plates.

References

- Cernescu, A., Romanoff, J., Remes, H., Faur, N., Jelovica, J., 2014, Equivalent mechanical properties for cylindrical cell honeycomb core structure, *Composite Structures*, vol. 108, 866-875.
- Findeisen, C., Hohe, J., Kadic, M., Gumbsch, P., 2017, Characteristics of mechanical metamaterials based on buckling elements, 2017, *Journal of the Mechanics and Physics of Solids*, vol. 102, 151-164.
- Fu, M., Liu, F., Hu, L., 2018, A novel category of 3D chiral material with negative Poisson's ratio, *Composites Science and Technology*, vol. 160, 111-118.
- Kshad, M.A.E., Popinigisa, C., Naguib, H.E., 2018, 3D printing of ron-resch-like origami cores for compression and impact load damping, *Smart Materials and Structures*, vol. 28, no. 1.
- Mizzi, L., Spaggiari, A., 2021, Chiralisation of Euclidean polygonal tessellations for the design of new auxetic metamaterials, *Mechanics of Materials*, vol. 153, 2021, 103698.
- Moreira, D. C., Sphaier, L. A., Reis, J.M.L., Nunes, L.C.S., 2012, Determination of Young's modulus in polyester-Al₂O₃ and epoxy-Al₂O₃ nanocomposites using the Digital Image Correlation method, *Composites Part A: Applied Science and Manufacturing*, vol.43, issue 2, 304-309.
- Mousanezhad, D., Haghpanah, B., Ghosh, R., Hamouda, A. M., Nayeb-Hashemi, H., Vaziri, A., 2016, Elastic properties of chiral, anti-chiral, and hierarchical honeycombs: A simple energy-based approach, *Theoretical and Applied Mechanics Letters*, vol. 6, issue 2, 81-96.
- Pan, B., Li, K., 2011, A fast digital image correlation method for deformation measurement, *Optics and Lasers in Engineering*, vol. 49, issue 7, 841-847.
- Racz, L., Dudescu, M. C., 2022, Numerical Investigation of the Infill Rate upon Mechanical Properties of 3D-Printed Materials, *Polymers*, 2022, vol. 14, issue 10.
- Szykiedans, K., Credo, W., 2016, Mechanical Properties of FDM and SLA Low-cost 3-D Prints, *Procedia Engineering*, Vol. 136, 257-262.
- Tachi, T., 2013, Designing Freeform Origami Tessellations by Generalizing Resch's Patterns, *Journal of Mechanical Design*, vol. 135, issue 11.
- Tachi, T., 2017, Characteristics of mechanical metamaterials based on buckling elements, *Journal of the Mechanics and Physics of Solids* 102, 151-164.
- Vanlanduit, S., Vanlanduit, J., Guillaume, P., 2009 A digital image correlation method for fatigue test experiments, *Optics and Lasers in Engineering*, vol. 47, issues 3–4, March–April, 371-378.
- Zadpoor, A.A. 2016 Mechanical meta-materials, *Materials Horizon*, vol. 3, 371-381.
- Zhou, X., Ren, L., Song, S. et al., 2023, Advances in 3D/4D printing of mechanical metamaterials: From manufacturing to applications, *Composites Part B: Engineering*, vol. 254, 110585.



Structural Integrity and Reliability of Advanced Materials obtained through Additive Manufacturing (SIRAMM23)

Numerical evaluation of the infill pattern upon mechanical proprieties of 3D printed materials

Laszlo Racz^a, Mircea Cristian Dudesca^{a*}

^a*Department of Mechanical Engineering, Faculty of Automotive, Mechatronics and Mechanical Engineering, Technical University of Cluj-Napoca, 103-105 B-dul Muncii, 400641 Cluj-Napoca, Romania*

Abstract

The effect of the structure that is printed inside an object, known as infill pattern, on mechanical proprieties of ABS specimens was investigated in this paper. Numerous studies demonstrated that parts created with fused deposition molding (FDM) technology present inferior mechanical properties due to additional porosity and anisotropy caused by the nature of the manufacturing process. In this regard the influence of printing parameters may be analyzed for correct evaluation of mechanical behavior and material constants. The methodology proposed in this paper consists of a numerical simulation of the fused deposition moulding 3D printed specimen, identification of the real cross-sectional area and evaluation of the strain-stress curves of the materials. There are several infill pattern geometries, each with benefits and compromises between material usage, printing time or mechanical strength of the obtained part. The current paper analysed specimens with 100% density (infill rate) but having different infill patterns: grid 0°-90° and ±45°, triangular 60°, fast honeycomb, full honeycomb and wiggle. The results are showing the dependence of the specimen's E modulus with the infill pattern and comparison of the strain-stress curves drawn with full cross-section and numerically calculated ones.

© 2023 The Authors. Published by Elsevier B.V.

This is an open access article under the CC BY-NC-ND license (<https://creativecommons.org/licenses/by-nc-nd/4.0>)

Peer-review under responsibility of the SIRAMM23 organizers

Keywords: Type your keywords here, separated by semicolons ;

* Corresponding author. Tel.: +40-264-401663; fax: +40-264-415490.

E-mail address: mircea.dudesca@rezi.utcluj.ro

1. Introduction

Manufactured parts by fused deposition molding encounter several uncertainties regarding their mechanical properties, in fact due mainly to the formation of voids in the structure and inefficient bonding of layers. These aspects increase the damage probabilities in polymeric structures, the mechanical properties of the part being one of main disadvantages of this technology (Singh et al., 2020, Lalegani Dezaki et al. 2021). The most relevant factors that influence the mechanical characteristics of polymeric printed materials by FDM technology are related to the manufacturing parameters (infill rate, infill pattern, raster orientation, number of shells, layer height, speed while travelling, speed while extruding), the position of the element in relation to the printing platform, properties of the filament and other design characteristics of the 3D printer. In the literature there are several studies presenting the influence of printing parameters, such as infill ratio, infill pattern, layer thickness, layer height and other printer settings on the mechanical behavior of parts made by FDM technology (Bakır et al. 2021, Khan et al., 2021, Popescu et al. 2018, Dudescu and Racz 2017, Sajjad et al., 2023, Lalegani Dezaki et al. 2020).

The accurate estimation of bonding between the filaments within a layer (termed "intra-layer bonding") and bonds formed between the filaments of the two succeeding layers (termed "inter-layer bonding") is essential to a reliable material model and strength evaluation of the parts made by FDM. The mechanical properties of such components are significantly influenced by the bonding quality between the filaments (Gurralla, et al. 2014, Sun et al. 2008). Theoretical calculations of the ultimate strength and E-modulus of printed structures typically need meso-structure information and void density analyses. Additionally, the mechanical behavior of the FDM prototypes can be predicted using finite element analysis (Garg et al., 2017, Górski et al. 2015, Paul 2021). An FE model to evaluate inter-layer and intra-layer necking of the filaments during the diffusion of the raster layers throughout the printing process is presented by A. Garg et al. 2017. Another method proposed by Racz and Dudescu (2022) modelled the single filaments by a script using the G-code of the 3D printer. The connection between the filaments is established based on experimental analysis of the cross-sectional geometry of a printed tensile specimen and allows the estimation of the flattening effects of the filaments. The technique enables quantification of the E-modulus of a printed tensile specimen with varying deposition densities (infill rate) as well as numerical estimation of the real cross-sectional area of a specimen and correction of the experimental stress-strain curves.

The current study describes an experimental-numerical approach for simulating FDM 3D printed tensile specimens. To create the numerical model based on single filaments deposition, the approach relies on the 3D printer's original g-code. The bonding between the filaments is experimentally estimated by image analysis of the specimen's cross section and allows the evaluation of the flattening effect that occurs during the deposition process. To evaluate the mechanical properties of the 3D printed material, uniaxial tensile tests are performed. When the material/airgap ratio is ignored the stress calculation can be easily done using the exterior dimensions of the tensile specimen. The presence of voids and the flattening effect of the filaments will generate a slightly different cross-sectional area and will influence the engineering stress value computed after the tensile test. The presented methodology ensures a much accurate estimation of the real cross-section, tensile strength, and E-modulus of the investigated printed samples when the infill pattern inside it is changing. The current study analyses six different patterns which are mainly implemented in the printer's software.

2. Materials and methods

To determine the real cross-sectional area of the specimens with different infill rates, a numerical method has been employed (Racz, 2022, Garg et al., 2017). To create a realistic 3D model of the specimens, g-codes of the printed parts were used to build up the geometrical model. Based on the G-code, which was used for printing the specimens, a geometrical model was constructed in ANSA 17.1.2 (BetaCae, Greece). The virtual (CAD) tensile specimen (according to ISO 527-2-2012) was constructed in ANSA according to the process described above for six cases with the following infill patterns: grid 0°-90° and ±45°, triangular 60°, fast honeycomb, full honeycomb, and wobble (Fig. 1). All models correspond to 100 % infill rate, so theoretical have full density.

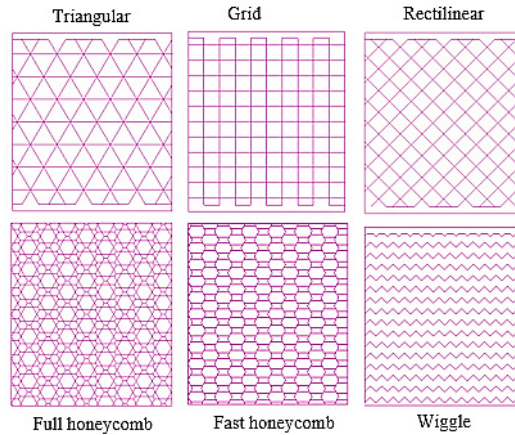


Fig. 1. Investigated infill patterns.

Test specimens made of acrylonitrile butadiene styrene ABS (Plasty Mladeč, Czech Republic) were manufactured horizontally on the build-plate of the 3D printer (Wanhao Duplicator I3) controlled by Simplify 3D software. Directions 0° and 90° are considered along and perpendicular to the longitudinal symmetry axis of the specimen, all layers of a specimen were built in the x-y plane (x, y and z axes defined according to ISO/ASTM 52900:2015). The specimens were manufactured by first building a parametric wall, called shell, that is created by the printer to reach the required dimensional precision and to create the inner pattern.

The meso-structure of the printed specimen’s cross section was analyzed under a microscope to establish the real shape and structural interaction of the filaments. The structure of the fibers in the cross-section from the numerical model was compared to the detailed pictures of the printed specimens. It can be noticed that the extruded filament is in a semi-molten state, and it would flatten slightly when deposited onto the previous layer as indicated in Fig. 2.a.

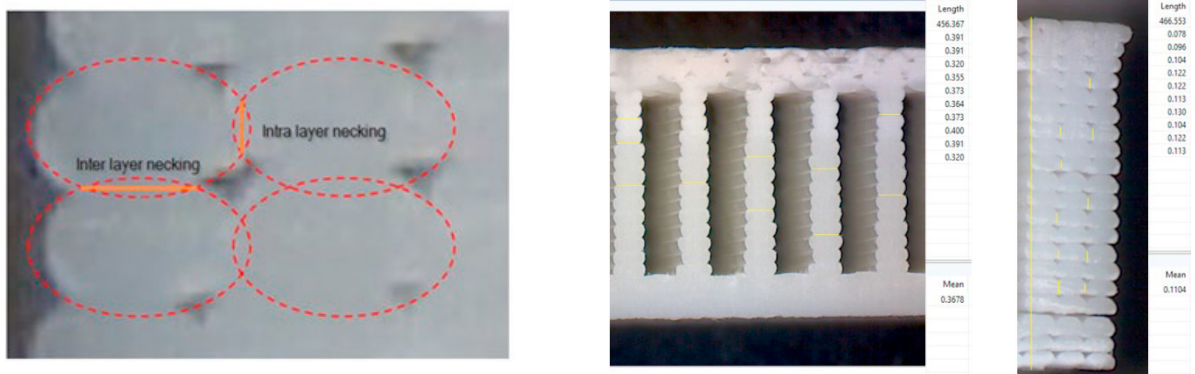


Fig.2. Determination of the contact area between the filaments a) inter layer and intra layer necking, b) optical measurement.

This flattening effect leads to the formation of a larger contact area between the filaments, known as intra and inter layer necking as presented in Fig. 2a. To determine the real size of the contact area between the layers, marked with lighter lines (Fig. 2b), microscopic pictures were analyzed with Digimazer software (MedCalc Software Ltd,

Belgium), where the length of the contact areas, both inter layer and intra layer necking was measured as presented in Figure 2.b.

In the CAD model, considering the flattening effect, the shape of the filaments (ellipsoidal section) is adjusted with the overlapping necking areas, to adjust the perfect geometrical model to a more realistic model. To extract the cross-section area of the tensile specimens, the created geometry was meshed with Tetra 2nd order elements. Finite element analysis (Epilysis solver) that simulates a tensile test is conducted on the different numerical specimens corresponding to the 6 analyzed infill patterns. The same boundary conditions were applied to the FE model as for the real specimens during the tensile test. The selected material model considered in the simulation of individual filaments was isotropic elasticity model, the goal of the research being the evaluation of E-modulus change with the infill pattern. The simulations were run for a tensile force producing only elastic deformations.

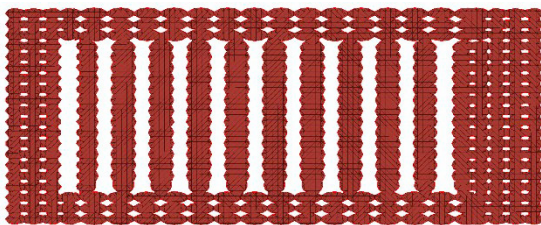
3. Results and discussions

To validate the method, real life tensile tests are necessary, where the experimentally determined tensile strain will be compared to the result of numerical simulation. If they are comparable, the area of the cross-section is correctly established and can be used for further computations. Uniaxial tensile tests on standard ISO 527-2-2012 specimens (type 1A, featuring a gauge length of 75 mm with a 4 mm thickness) with different infill patterns were carried out on a universal testing machine type INSTRON 3366, 10 kN capacity at a loading speed of 1 mm/min, a uniaxial extensometer being used to measure the tensile strain. The results are summarized in Table 1 where the experimentally measured strain is compared to the results of the FE simulations, the results were selected from the elastic domain of the stress-strain curve.

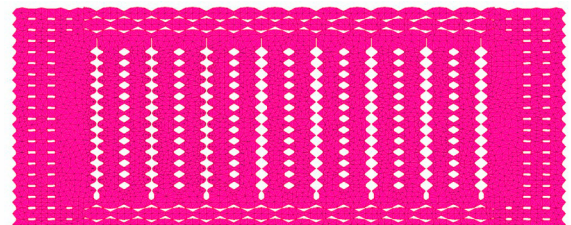
Table 1. Strain values obtained by numerical simulations vs experimentally determined.

Specimen's infill pattern	Strain EXP (mm/mm)	Strain FEA (mm/mm)	Relative Dev. FEA-EXP (%)
Grid 0-90	0.00259	0.00277	6.95
Grid +45-45	0.00267	0.00269	0.75
Fast Honeycomb	0.00279	0.00285	2.15
Full Honeycomb	0.00333	0.00351	5.40
Triangular 60°	0.00274	0.00294	7.2
Wiggle	0.00223	0.00205	8

The results showed a range of minimum 0.75% and maximum 8 % difference, fact that validate the proposed methodology for simulation of 3D printed specimens. In Fig. 3 the cross-section of the tensile specimens is presented for grid 0°-90° and ±45°, triangular 60°, fast honeycomb, full honeycomb and wiggle infill patterns.



a)



b)

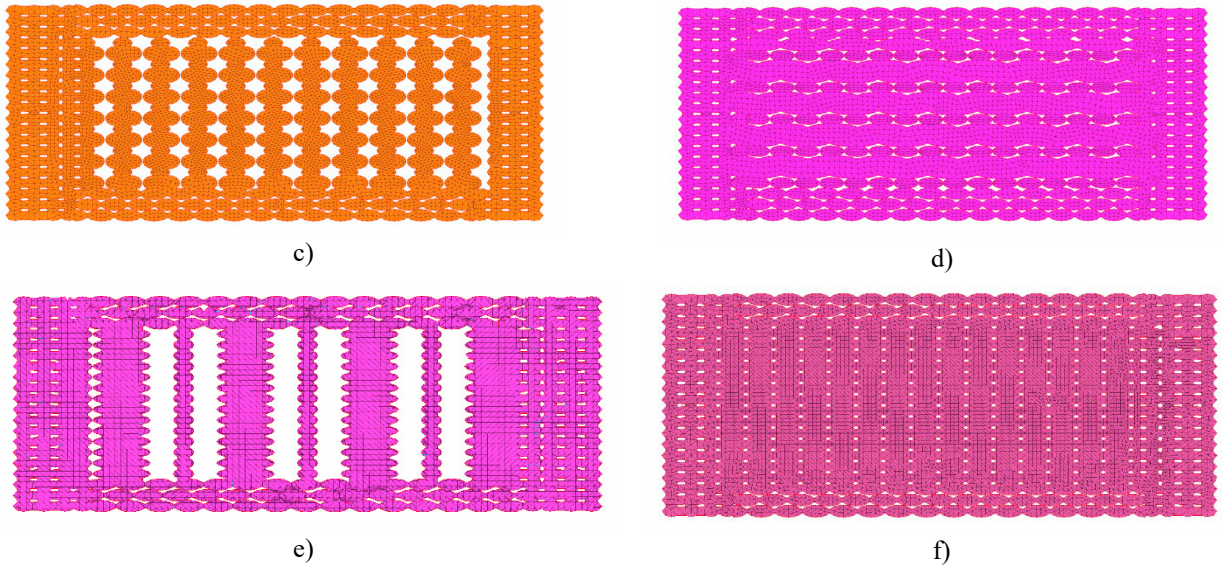


Fig. 3. Cross-section of the tensile specimens for infill pattern: a) grid 0° - 90° b) grid $\pm 45^{\circ}$, c) fast honeycomb, d) full honeycomb, e) triangular 60° and f) wiggle

It can be observed that presence of voids in the cross-section is reduced for grid $\pm 45^{\circ}$, full honeycomb and wiggle infill patterns in comparison with grid 0 - 90° , fast honeycomb and triangular 60° , fact that will influence the stress-strain curves accuracy of the specimens. The shell of the parts is the same, independent of the selected infill pattern. The numerically calculated cross sectional area is presented in Table 2, with that mention that a full cross section has 40mm^2 . In all the six analyzed infill patterns, the extraction position of the cross section was done in the same place for all specimens.

Table 2. Numerically calculated cross-sectional area of the tensile specimens

Specimen's infill pattern	Calculated cross-sectional area (mm^2)
Grid 0° - 90°	28.75
Grid $+45^{\circ}$ - 45°	33.65
Fast Honeycomb	31.75
Full Honeycomb	36.45
Triangular 60°	29.43
Wiggle	37.15

The cross-section extracted from the geometric model was reintroduced into the testing machine software and the stress results were recalculated according to the new value. Comparative strain-stress curves for all analyzed infill patterns are depicted in Fig. 4. The experimental curves (denoted EXP) are based on a constant cross-sectional area of 40mm^2 given by the outside dimensions of the specimens and those denoted FEA consider the real cross-sectional area presented in Table 2 for each infill pattern. It can be observed that even for a 100% infill rate, there are significant differences between infill patterns, the calculation based on full cross-section will not deliver a result within an expectable error range for some patterns like grid 0 - 90° , fast honeycomb and triangular 60° , the differences in terms of ultimate tensile strength being 28.1%, 20,6% and 26.4% respectively.

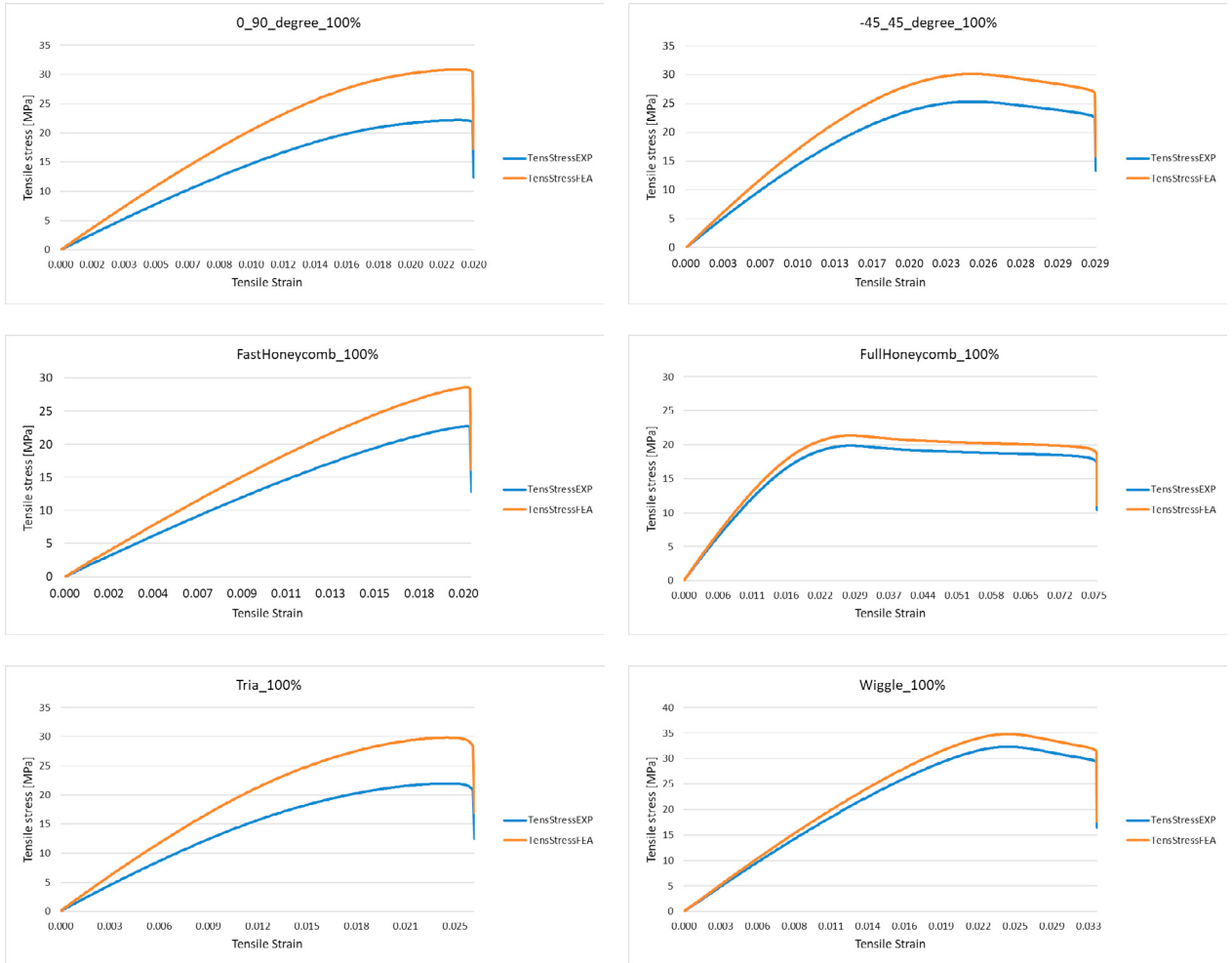


Fig. 4. Comparative strain-stress curves for all analyzed infill patterns.

Based on the adjusted stress-strain curves the value of the E-modulus for each infill pattern was recalculated, their values comparative with the initial ones based on full cross-section are presented in Table 3.

Table 3. Values of E-modulus for different infill patterns

Specimen's infill pattern	E-modulus (MPa)		Relative deviation (%)
	Calculated (numerical)	Full cross-section	
Grid 0°-90°	2049.00	1523.7	25,4
Grid +45-45°	1631.00	1545.2	5,3
Fast Honeycomb	1892.04	1484.0	21,6
Full Honeycomb	1272.20	1188.6	6,6
Triangular 60°	2055.26	1502.8	26,88 %
Wiggle	1877.49	1733.5	7,7 %

As expected, patterns like grid 0-90°, fast honeycomb and triangular 60° have a difference upon E-modulus when full cross-section is used of around 25%.

In Fig. 5 are presented the comparative results in shape of bar graph of the tensile moduli for different infill patterns. The value of E modulus (denoted E_Fcs) represents the measured tensile modulus of the specimen utilizing the full cross-section (Fcs) of the sample and the other one is the E modulus (denoted E_Calc) based on corrected cross-sectional area. It can be concluded that utilizing the full cross-section of the 3D printed specimens, even for a 100% infill rate, will not deliver for the E-modulus and ultimate tensile strength a result within a reasonable error range especially for patterns like grid 0-90°, fast honeycomb and triangular 60°.

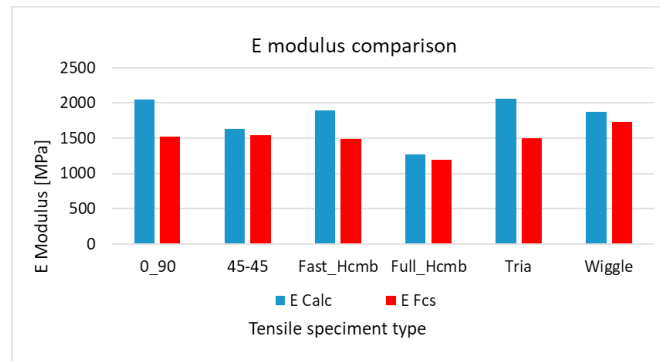


Fig. 5. Comparative results of the tensile moduli with and without adjusted cross-sectional area for different infill patterns.

4. Conclusion

In this paper 3D printed tensile specimens with different infill patterns were analyzed to understand the effect of internal structure on the mechanical behavior. An original approach, based on the printer generated G-code, to create numerical models of the parts was presented, that assists finite element analysis and assessment of the air gap - material ratio problem. The tensile strain resulted from the simulation were compared to experimental result, which confirmed that the area of cross-section extracted from the geometric model is predicted with reliable accuracy. Establishing of the E moduli of different infill patterns implied adjustment of the experimentally determined strain-stress curves with the numerical calculated cross-section of the specimens. The obtained E moduli for different infill patterns can be used for FE simulation where the microstructure no longer must be modeled because the E modulus also contains the correct airgap- material ratio.

The findings presented in this paper allow the following overall conclusions to be drawn:

- The proposed methodology on building a finite element model starting from the printer generated G-code is a reliable method to evaluate the influence of inner structure given by the infill pattern upon mechanical behavior of the FDM printed parts.
- Adjustments to represent the intra and inter layer necking are necessary for accurate results and must be done on real printed specimens.
- Cross-sectional area of a tensile specimen extracted from the numerical mode is predicted with good accuracy and allows estimation of strain-stress curves and E-moduli closer to reality.
- Patterns like grid $\pm 45^\circ$, full honeycomb and wiggle have a higher material to airgap ratio and proved reasonable results in terms of tensile strength and E-modulus comparative with those obtained using full material assumptions, so it would be recommended to be used for parts undergoing mechanical loads.
- Patterns like grid 0-90°, fast honeycomb and triangular 60° have difference in terms of ultimate tensile strength and E-modulus when full cross-section more than 20%, which cannot be neglected in case of parts under mechanical loading.

Acknowledgements

Computations were done on the computing infrastructure of the CLOUDUT Project, cofunded by the European Fund of Regional Development through the Competitiveness Operational Programme 2014-2020, contract no. 235/2020.

References

- Singh, S., Singh, G., Prakash, C., & Ramakrishna, S. (2020). Current status and future directions of fused filament fabrication. *Journal of Manufacturing Processes*, 55, 288-306.
- Lalegani Dezaki, M., Mohd Ariffin, M. K. A., & Hatami, S. (2021). An overview of fused deposition modelling (FDM): Research, development and process optimisation. *Rapid Prototyping Journal*, 27(3), 562-582.
- Bakır, A. A., Atik, R., & Özerinç, S. (2021). Mechanical properties of thermoplastic parts produced by fused deposition modeling: a review. *Rapid Prototyping Journal* 27(3), 537-561.
- Khan, I., & Kumar, N. (2021). Fused deposition modelling process parameters influence on the mechanical properties of ABS: A review. *Materials Today: Proceedings*, 44, 4004-4008.
- Popescu, D., Zapciu, A., Amza, C., Baci, F., & Marinescu, R. (2018). FDM process parameters influence over the mechanical properties of polymer specimens: A review. *Polymer Testing*, 69, 157-166.
- Dudescu, C., & Racz, L. (2017). Effects of raster orientation, infill rate and infill pattern on the mechanical properties of 3D printed materials. *Acta Universitatis Cibiniensis. Technical Series*, 69(1), 23-30.
- Sajjad, R., Butt, S. U., Saeed, H. A., Anwar, M. T., & Rasheed, T. (2023). Impact of multiple infill strategy on the structural strength of single build FDM printed parts. *Journal of Manufacturing Processes*, 89, 105-110.
- Lalegani Dezaki, M., & Mohd Ariffin, M. K. A. (2020). The effects of combined infill patterns on mechanical properties in fdm process. *Polymers*, 12(12), 2792.
- Gurralla, P. K., & Regalla, S. P. (2014). Part strength evolution with bonding between filaments in fused deposition modelling: This paper studies how coalescence of filaments contributes to the strength of final FDM part. *Virtual and Physical Prototyping*, 9(3), 141-149.
- Sun, Q., Rizvi, G. M., Bellehumeur, C. T., & Gu, P. (2008). Effect of processing conditions on the bonding quality of FDM polymer filaments. *Rapid prototyping journal*, 14, 72-80.
- Garg A, Bhattacharya A. An insight to the failure of FDM parts under tensile loading: finite element analysis and experimental study. (2017) *International Journal of Mechanical Sciences*, 120, 225-36
- Górski, F., Kuczko, W., Wichniarek, R., & Hamrol, A. (2015). Computation of mechanical properties of parts manufactured by fused deposition modeling using finite element method. In *10th International Conference on Soft Computing Models in Industrial and Environmental Applications* (pp. 403-413). Springer, Cham.
- Paul, S. (2021). Finite element analysis in fused deposition modeling research: A literature review. *Measurement*, 178, 109320.
- Racz, L., & Dudescu, M. C. (2022). Numerical Investigation of the Infill Rate upon Mechanical Properties of 3D-Printed Materials. *Polymers*, 14(10).



Structural Integrity and Reliability of Advanced Materials obtained through Additive Manufacturing (SIRAMM23)

On the mixed mode fracture of DLP manufactured SCB specimens

Mihai Marghitas^a, Liviu Marsavina^{a*}, Cosmin-Florin Popa^a, Roberto Brighenti^b

^aDepartment of Mechanics and Strength of Materials, Politehnica University of Timisoara, 1st Mihai Viteazu Bd., Timisoara, 300222, Romania

^bDepartment of Engineering and Architecture, University of Parma, Parco Area delle Scienze 181/A, 43124 Parma, Italy

Abstract

The scope of this study is to investigate the mixed mode fracture of components manufactured from photo-polymerized resin using the Digital Light Processing (DLP) additive manufacturing technology.

The mixed mode tests were performed on Semi Circular Bend (SCB) specimens loaded under symmetric Mode I, asymmetric mixed mode and mode II loading, respectively. The specimens manufactured via DLP have a crack introduced during the manufacturing process. Tests were performed at room temperature using a universal testing machine with three point bending grips at a constant loading speed. Four tests were carried on for each supports position.

The experimental results expressed as K_{II}/K_{IC} versus K_I/K_{IC} are plotted by adopting four fracture criteria, namely the Maximum Tensile Stress (MTS), the Strain Energy Density (SED), the Maximum Energy Release Rate (G_{max}), and the Equivalent Stress Intensity Factor (ESIF). Most of the experimental results fall in the range of fracture envelope curves.

© 2023 The Authors. Published by Elsevier B.V.

This is an open access article under the CC BY-NC-ND license (<https://creativecommons.org/licenses/by-nc-nd/4.0>)

Peer-review under responsibility of the SIRAMM23 organizers

Keywords: Semi Circular Bend specimens; fracture toughness; mixed mode

1. Introduction

Additive Manufacturing (AM) technologies start to be developed at the end of 20th Century and have had a great impact on the fabrication directly from a 3D model of objects with complex geometries, Wong and Hernandez (2012).

Digital Light Processing (DLP) is a 3D printing technology used to quickly manufacture polymeric components by photo-polymerization. It belongs to the family of additive manufacturing technologies known as vat photo-

* Corresponding author. Tel.: +40726397635.

E-mail address: liviu.marsavina@upt.ro

polymerization. They use a light source (laser beam or projector) to cure a liquid resin into a hardened plastic solid. Brighenti et al. (2021) presented a comprehensive review on processes and mechanical models on laser-based additively manufacturing of polymeric materials, while the influence of the manufacturing parameters on the obtained mechanical properties of additively manufactured photo-polymerized polymers is shown in Brighenti et al. (2022). The exposure time and the layer thickness have been considered as the main fabrication parameters to be used as design variables for controlling the mechanical characteristics of the obtained AM components. It has been shown that the exposure time represents the main parameter affecting the mechanical properties on tensile strength, while the influence of the layer thickness appeared to be less important.

The influence of the printing angle and load direction on flexure strength of two commercial resins obtained through Stereolithography (SLA) used for dental restorations is presented in Derban et al. (2000). The results show that the smallest flexural properties were obtained when the printing angle equals 45°. On the other hand, higher values of the flexural modulus and flexure strength were obtained when the applied load is parallel to the AM growing direction.

So far, a limited number of studies on the fracture toughness of vat photo-polymerization components is available. Brighenti et al (2023) presented a study of the influence of curing and printing angle on the fracture toughness of DPL specimens. Single Notched Bend specimens loaded in three point bending were tested. Three printing angles (0° , 45° and 90°), and three curing treatments were considered: 1) 5 minutes maintained in Isopropyl Alcohol (IPA) and then cured for 5 minutes; 2) cleaned in hot water ($60-70^{\circ}\text{C}$) and 30 minutes ultrasonic curing; 3) cleaned for 5 minutes maintained in IPA and 30 minutes ultrasonic curing. The highest fracture toughness was obtained for 0° printing angle and 5 minutes maintained in Isopropyl Alcohol (IPA) and then cured for 5 minutes. For all the tested specimens, for which a plain strain condition was fulfilled, a brittle fracture was observed.

The present study investigates the mixed mode fracture of DLP manufactured specimens and compares this response with classical fracture criteria. The Semi Circular Bend (SCB) specimen loaded asymmetric was adopted for mixed mode loading. Previous studies on different materials showed that this specimen could produce different ranges of mixed modes, ranging from pure mode *I* to pure mode *II* only by changing the position of one support, Marsavina et al. (2023), Ayatollahi et al. (2011).

Nomenclature

a	crack length
K_I	mode I stress intensity factor
K_{II}	mode II stress intensity factor
K_{IC}	fracture toughness
R	specimen radius
S_1, S_2	spans
t	specimen thickness
θ_c	crack initiation angle

2. Experimental tests

Mixed mode fracture tests were performed using Semi-Circular Bend (SCB) specimens loaded asymmetric, Fig. 1.

The specimens were printed using a 3D LCD printer (Anycubic Photon[®]), based on DLP technology. The SCB specimens were manufactured using an UV-sensitive resin “translucent green” (curing UV light wavelength 405 nm) with the following parameters: light exposure time 20 s for each layer, layer thickness 0.05 mm, and printing orientation 0° . Post printing process consisted in 5 minutes in Isopropyl Alcohol (IPA) and then cured for 5 minutes in Anycubic[®] wash and post-cure machine 2.0. These manufacturing parameters were the optimal ones for obtaining the highest fracture toughness in our previous studies, Brighenti et al. (2023).

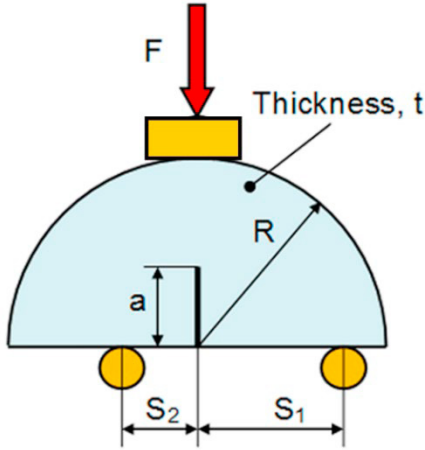


Fig. 1. The Semi-Circular Bend (SCB) specimen.

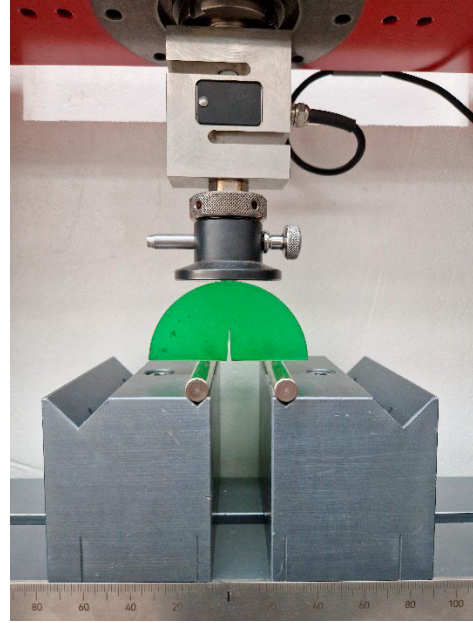


Fig. 2 The SCB specimen in three-point bending grips.

Mixed mode fracture tests were performed using Semi-Circular Bend (SCB) specimens loaded asymmetrically. The SCB specimens having radius R and thickness t have an edge crack of length a oriented normal to the specimen edge, inserted during the printing process, Fig. 1. The specimens were loaded in a three point bend fixture, which was proved to give a wide range of mixed modes, Fig. 2, from pure mode I ($S_1 = S_2$), mixed modes ($S_1 \neq S_2$) and to pure mode II , only by changing the position of one support, Lim et al. (1994), Ayatollahi et al (2011), Negru et al (2014). The specimen dimensions where: radius $R=40$ mm, thickness $t=3-6$ mm, crack length $a \approx 18$ mm, and spans $S_1=30$ mm, respectively $S_2=30, 12, 8, 6, 4, 2.66$ mm. The crack was introduced directly during the 3D printing process as a very sharp notch.

The Stress Intensity Factors (SIFs) solutions for the SCB specimen loaded asymmetric were provided in Marsavina et al. (2014):

$$K_i = \frac{P_{\max}}{2Rt} \sqrt{\pi a} f_i(a/R, S_1/R, S_2/R), \quad i = I, II \quad (1)$$

where, the non-dimensional SIFs, $f_i(a/R, S_1/R, S_2/R)$, were determined by finite element analysis using FRANC2D software, Marsavina et al. (2014):

$$\begin{aligned} f_I(S_2/R) &= 6.235(S_2/R)^3 - 15.069(S_2/R)^2 + 17.229(S_2/R) - 1.062 \\ f_{II}(S_2/R) &= 1.884(S_2/R)^5 - 7.309(S_2/R)^4 + 5.037(S_2/R)^3 + 2.77(S_2/R)^2 - 5.075(S_2/R) + 1.983 \end{aligned} \quad (2)$$

Four tests were performed, for each combination of S_1, S_2 positions, on a Zwick/Roell 5 kN testing machine at room temperature with a loading rate of 2 mm/min. Brittle fracture was observed for all tests and mode mixities, Fig. 3. The fracture load increases with decreasing the span S_2 from 30 (pure Mode I) mm to 2.66 mm (pure Mode II), respectively with increasing the mode II.

3. Results and discussions

Relations (1) and (2) were used to estimate the stress intensity factors K_I and K_{II} . The obtained experimental results are shown in Table 1. The average value of symmetric loading was considered the mode I fracture toughness of the additive manufactured resin, $K_{IC} = 1.012 \pm 0.057 \text{ MPa m}^{0.5}$.

Table 1. Experimental results

Specimen	R [mm]	t [mm]	a [mm]	S_1 [mm]	S_2 [mm]	P_{max} [N]	K_I [MPa m ^{0.5}]	K_{II} [MPa m ^{0.5}]
2.6-1	40.02	6.30	17.7	30	2.66	1160	0.000	0.904
2.6-2	40.10	6.24	17.3	30	2.66	1070	0.000	0.831
2.6-3	40.00	4.33	17.3	30	2.66	875	0.000	0.981
2.6-4	39.92	3.91	17.5	30	2.66	739	0.000	0.924
4.0-1	40.17	4.40	16.3	30	4	957	0.312	0.923
4.0-2	40.03	5.30	17	30	4	1000	0.280	0.820
4.0-3	40.00	5.89	16.5	30	4	1100	0.273	0.800
4.0-4	40.10	4.35	17.6	30	4	803	0.277	0.815
6.0-1	39.98	6.28	17.4	30	6	927	0.519	0.557
6.0-2	40.02	6.30	16.3	30	6	903	0.486	0.523
6.0-3	39.97	6.24	17.4	30	6	947	0.534	0.573
6.0-4	40.10	6.35	17.7	30	6	817	0.453	0.489
8.0-1	40.16	3.57	17.8	30	8	520	0.780	0.474
8.0-2	40.09	5.22	17	30	8	839	0.844	0.511
8.0-3	40.04	3.23	17.1	30	8	419	0.686	0.414
8.0-4	40.06	3.76	17.5	30	8	469	0.666	0.403
12.0-1	40.00	4.42	17.7	30	12	535	1.040	0.283
12.0-2	40.06	2.96	17.5	30	12	335	0.965	0.263
12.0-3	43.74	3.77	17.5	30	12	425	0.803	0.261
12.0-4	40.10	6.33	17.7	30	12	715	0.966	0.264
30-1	40.17	3.37	18	30	30	200	1.054	0.000
30-2	40.00	4.32	18	30	30	224	0.927	0.000
30-3	40.00	4.32	16.8	30	30	257	1.028	0.000
30-4	40.12	3.40	17.3	30	30	203	1.041	0.000

Generally, fracture criteria for mixed mode loadings provide:

- a combination of the stress intensity factors (K_I and K_{II}) and fracture toughness (K_{IC}), i.e.:

$$F(K_I, K_{II}, K_{IC}) = 0 \quad (3)$$

- the crack initiation angle θ_c .

For comparison in the case of plane mixed mode fracture, four classical fracture criteria are considered, namely the Maximum circumferential Tensile Stress (MTS), the Minimum Strain Energy Density (SED), the Maximum energy release rate (G_{max}), and the Equivalent Stress Intensity Factor (ESIF); their mathematical formulation is provided in Table 2.

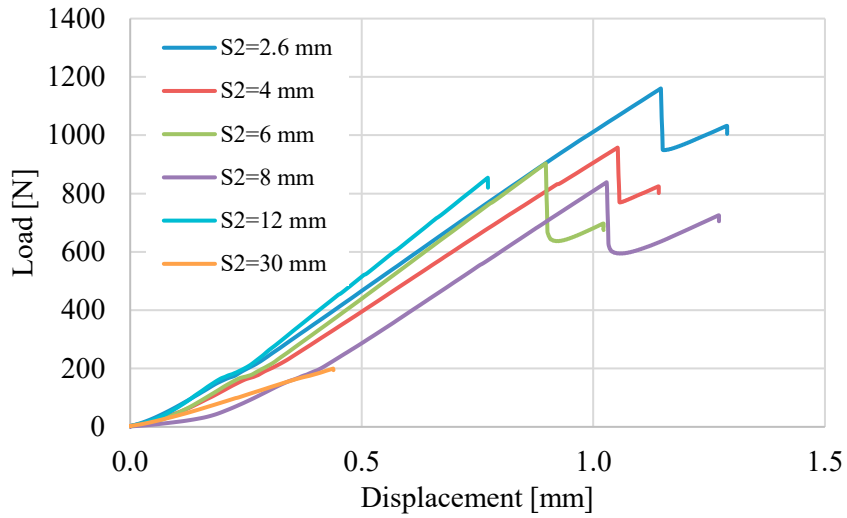


Fig. 3. Load – displacement curves for mixed mode loading.

Fig. 4 shows one cracked specimen for each of the tested modes. It could be observed a curvilinear crack trajectory for mixed mode and pure mode II loading. The crack initiation angle θ_c is increasing with increasing the mode II.

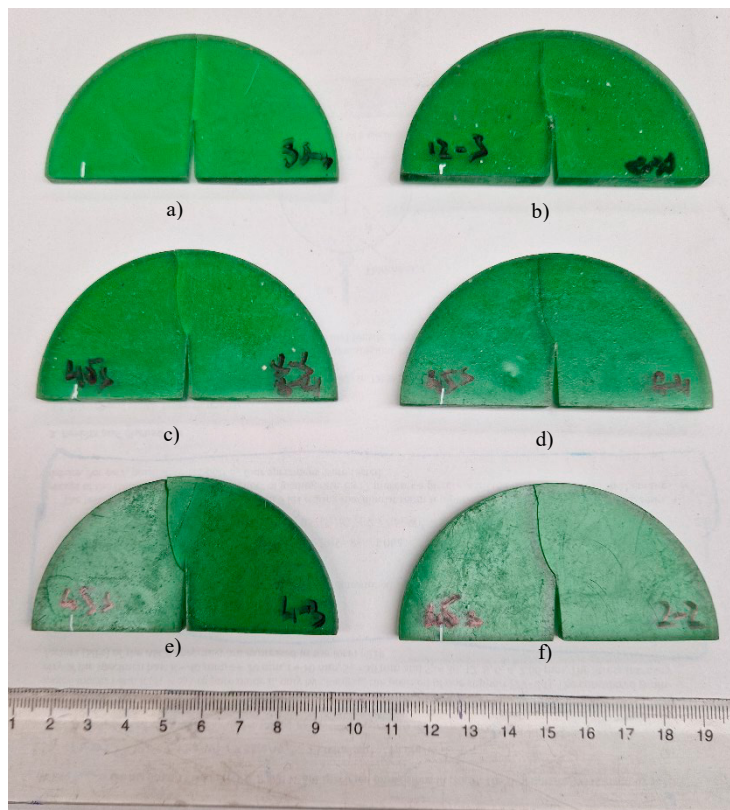


Fig. 4. Fractured specimens: a) $S_1=S_2=30$ mm; b) $S_1=30$ mm, $S_2=12$ mm; c) $S_1=30$ mm, $S_2=8$ mm; d) $S_1=30$ mm, $S_2=6$ mm; e) $S_1=30$ mm, $S_2=6$ mm; f) $S_1=30$ mm, $S_2=2.66$ mm;

The experimental results expressed in terms of K_{II} / K_{IC} versus K_I / K_{IC} for the different fracture criteria reported in Table 2 are plotted in Fig. 5. It could be observed that the SED, MTS and ESIF criteria are in good agreement with the experimental results.

Table 2. Mixed mode fracture criteria

Fracture criterion	Formulation	Eq. (3)
MTS Erdogan – Sih (1963)	$\sigma_{\theta\theta, \max} = \sigma_{cr} = \frac{K_{IC}}{\sqrt{2\pi r}}$	$F = \cos \frac{\theta_c}{2} \left(K_I \cos^2 \frac{\theta_c}{2} - \frac{3}{2} K_{II} \sin \theta_c \right) - K_{IC}$
SED Sih (1974)	$S = S_{cr} = \frac{(\kappa - 1)}{8\pi\mu} K_{IC}^2$	$F = \frac{1}{2(\kappa - 1)} \left[(1 + \cos \theta_c)(\kappa - \cos \theta_c) K_I^2 + 2 \sin \theta_c (2 \cos \theta_c - \kappa + 1) K_I K_{II} + ((\kappa + 1)(1 - \cos \theta_c) + (1 + \cos \theta_c)(3 \cos \theta_c - 1)) K_{II}^2 \right] - K_{IC}^2$
Gmax Hussain (1974)	$G(\theta_c) = G_{IC} = \frac{K_{IC}^2}{E}$	$F = 4 \left(\frac{1}{3 + \cos^2 \theta_c} \right)^2 \left(\frac{1 - \frac{\theta_c}{\pi}}{1 + \frac{\theta_c}{\pi}} \right)^\pi \cdot \left[(1 + 3 \cos^2 \theta_c) K_I^2 + 8 K_I K_{II} \sin \theta_c \cos \theta_c + (9 - 5 \cos^2 \theta_c) K_{II}^2 \right] - K_{IC}^2$
ESIF Richard (1985)	$K_{eq} = K_{IC}$	$F = \frac{K_I}{2} + \frac{1}{2} \sqrt{K_I^2 + 4(\alpha K_{II})^2} - K_{IC}$

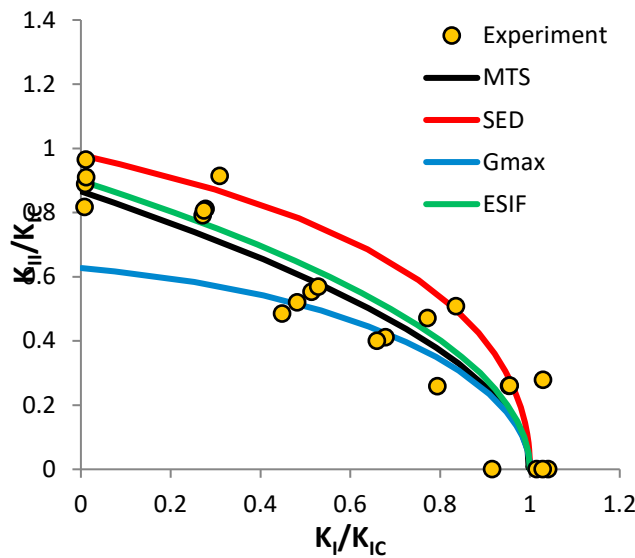


Fig. 5. The fracture criteria and experimental results.

4. Conclusions

The following conclusions of this study could be drawn:

- The semi-circular bend specimen loaded asymmetric was adopted to investigate mixed mode fracture of DLP additive manufactured specimens made of translucent green photo-polymerization resin. The advantages of this specimen are the simple geometry, the use of classic bending fixtures for loading the specimens and the ability to produce full range of mixed modes, from pure mode I to pure mode II, only by changing the position of one support.

- The obtained average value of the mode I fracture toughness is $1.021 \text{ MPa m}^{0.5}$ and is in agreement with those obtained on Single Edge Notched Bend specimens for different curing process $0.64 - 1.31 \text{ MPa m}^{0.5}$, Brighenti et al. (2023). The mode II fracture toughness has an average value of $0.895 \text{ MPa m}^{0.5}$.
- The four classical fracture criteria were assessed to characterize the failure of mixed mode loaded DLP resins. The experimental results proof that the SED, MTS and ESIF are the most suitable, Fig. 5. With the mention that the ESIF is the only criteria criterion which takes into account the ratio between mode I and mode II fracture toughness, $\alpha = K_{IC}/K_{IIC}$.

Acknowledgements

This paper was financially supported by the European Union's Horizon 2020 research and innovation program (H2020-WIDESPREAD-2018, SIRAMM) under grant agreement no. 857124.

References

- Ayatollahi, M.R., Aliha, M.R.M., Aghafi, H., 2011. An improved semi-circular bend specimen for investigating mixed mode brittle fracture, *Engineering Fracture Mechanics*, 78,110-123.
- Brighenti, R., Cosma, M.P., Marsavina, L., Spagnoli, A., Terzano, M., 2021. Laser-based additively manufactured polymers: a review on processes and mechanical models. *Journal of Materials Science*, 56(2), 961-998.
- Brighenti R., Marsavina L., Marghitas M.P., Cosma M.P., Montanari M., 2022 Mechanical characterization of additively manufactured photopolymerized polymers. *Mech. of Advanced Materials & Structures*,
- Brighenti R., Marsavina L., Marghitas M.P., Montanari M., Spagnoli A., Tatar F., 2023. The effect of process parameters on mechanical characteristics of specimens obtained via DLP additive manufacturing technology, *Materials Today: Proceedings*, 78 (2), 331-336.
- Derban, P., Negrea, R., Rominu, M., Marsavina L., 2020. Influence of the printing angle and load direction on flexure strength in 3D printed materials for provisional dental restorations, *Materials*, 14, 3376.
- Erdogan, F., Sih, G. C., 1963. On the crack extension in plates under plane loading and transverse shear, *J Basic Engng*, 85, 519-525.
- Hussain, M. A., Pu, S. L., Underwood, J., 1974. Strain energy release rate for a crack under combined mode I and mode II. In: *Fracture analysis*, P.C. Paris, G.R. Irwin (Edts), ASTM STP560, Philadelphia, 2-28.
- Lim, I.L., Johnston, I.W., Choi, S.K., Boland, J.N., 1994. Fracture Testing of a Soft Rock with Semi-circular Specimens Under Three-point Bending. Part 2--Mixed-mode, *Int. J. Rock Mech. Min. Sci. & Geomech. Abstr.*, 31(3), 199-212.
- Marsavina L., Valean C., Marghitas M., Linul E., Javad Razavi S.M., Berto F., Brighenti R., 2022. Effect of the manufacturing parameters on the tensile and fracture properties of FDM 3D-printed PLA specimens, *Engineering Fracture Mechanics*, 274, 108766.
- Negru, R., Marsavina, L., Filipescu, H., Pasca, N., 2013. Investigation of mixed mode I/II brittle fracture using ASCB specimen. *International Journal of Fracture*, 18:155-161.
- Richard H. A., *Bruchvorhersagen bei uberlagreter normal- und schubbeanspruchung von rissen*, VDI-Verlag, Dusseldorf, 1985.
- Sih, G. C., 1974. Strain-energy-density factor applied to mixed mode crack problems, *I J Fract*, 10, 305-321.
- Wong, K. V., Hernandez, A., 2012. A Review of Additive Manufacturing. *ISRN Mechanical Engineering*, 2012, 1–10.



Structural Integrity and Reliability of Advanced Materials obtained through Additive Manufacturing (SIRAMM23)

Optimization of the numerical homogenization method for cellular structures manufactured by Selective Laser Melting

Kevin Moj^{a*}, Grzegorz Robak^a, Robert Owsinski^a

^a Faculty of Mechanical Engineering, Opole University of Technology, Opole 45-271, Poland,

Abstract

Rapid development of additive technologies presents enormous opportunities, associated with the production of complex geometries. For this reason, the field of 3D printing has become an ideal technique for producing cellular structures. The paper addresses the issue, related to the determination of the minimum number of unit cells, at which the structure is characterized by a constant effective Young's modulus. Currently, it is not possible to state unequivocally what number of individual cells is needed. For this reason, the paper proposes an algorithm by which the minimum number of unit cells can be determined. The parameters of the structure, such as the relative density and the topology of a single cell, have an important influence. It is worth noting that the base material also plays an important role. Various methods are used for numerical analysis of cellular structures, such as finite element-based analysis, numerical homogenization and beam-based analysis. Nevertheless, each of them has its own advantages as well as disadvantages. This paper proposes to optimize the numerical homogenization of cellular structures, using models consisting of a minimum number of unit cells and a 3D representation of actual printed models of cellular structures. Based on these optimizations, better agreement with experiment was obtained.

© 2023 The Authors. Published by Elsevier B.V.

This is an open access article under the CC BY-NC-ND license (<https://creativecommons.org/licenses/by-nc-nd/4.0>)

Peer-review under responsibility of the SIRAMM23 organizers

* Corresponding author. .

E-mail address: k.moj@doktorant.po.edu.pl

Keywords: Selective Laser Melting. Computer Tomography. Finite Element Method. Numerical Homogenization;

1. Introduction

Metal additive manufacturing is the process of creating three-dimensional objects from metal by applying successive layers of material. It enables the production of complex geometries and structures that would be difficult or impossible to achieve using traditional manufacturing methods. Among other applications, the technology is widely used in the aerospace, medical and automotive industries.

During recent years, additive manufacturing has become a promising technique for creating cellular structures with customized geometries and properties. Using 3D printing technology, complex internal architectures can be created that cannot be achieved by traditional manufacturing methods. Such cellular structures have potential applications in various fields, such as biomedical engineering, aerospace and energy storage (Al-Ketan, Rowshan, and Abu Al-Rub 2018; Maconachie et al. 2019; Zadpoor 2019).

However, there is still no clear consensus on the minimum number of cells at which the structure exhibits a constant effective Young's modulus. This is especially important for experimental studies. The optimal number of cells depends on the specific application and the material used. Other key parameters are the relative density, i.e. the degree of filling with the material, and the topology of the unit cell (Cantaboni et al. 2022; Mehboob et al. 2018; Mines 2019; Yan et al. 2021).

Cellular structures can be simulated using three basic methods: solid-based analysis, homogenization and beam-based analysis. In solid-based analysis, a cellular structure is modeled as a solid object, and its mechanical behavior is analyzed using finite element analysis. Such an approach allows a detailed understanding of the mechanical properties of a lattice structure, including its deformation, stresses and strains. However, it can be computationally expensive and time-consuming, especially for complex structures. Beam-based analysis is a simplified method for analyzing cellular structures that treats the structure as a collection of interconnected beams. This simplifies the geometry of the structure and reduces computational time significantly. Numerical homogenization is a method of analyzing the effective mechanical behavior of cellular structures by considering them as homogeneous materials. This method simplifies the complexity of the lattice structure and allows for faster simulations and simpler analysis. The homogenization technique involves determining the mechanical properties of a lattice structure using an effective material model. This model captures the overall mechanical behavior of the structure, including its stiffness and strength. However, the accuracy of numerical homogenization can be improved by using a model obtained by CT scanning (Cantaboni et al. 2022; Chatzigeorgiou et al. 2022; Doroszko, Falkowska, and Seweryn 2021; Jiang et al. 2021; Mehboob et al. 2018; Yan et al. 2021).

The purpose of this study was to determine an algorithm that would allow the determination of the minimum number of individual cells at which the cell structure exhibits a constant effective Young's modulus. In addition, a homogenization method was optimized for cell structures (Al-Ketan et al. 2020).

2. Methods

2.1. Design and production of the cellular structures

Cellular structures were designed using nTopology software, which is specifically tailored to create advanced geometries. The implicit modeling method allows the generation of more complex shapes, and the available design methodology makes it possible to control different variants of the design using formulas, tests, simulations and other data. The detailed design process is presented in (Moj et al. 2022). In Figure 1, the tested specimens are presented. It was determined to print samples with a variety of single cell topologies, changing both the size of a single cell and the

relative density. All the parameters of the structures are shown in Table 1. With the help of such selected parameters of the cell structure, a wide range of properties can be estimated without printing every set with the given parameters.

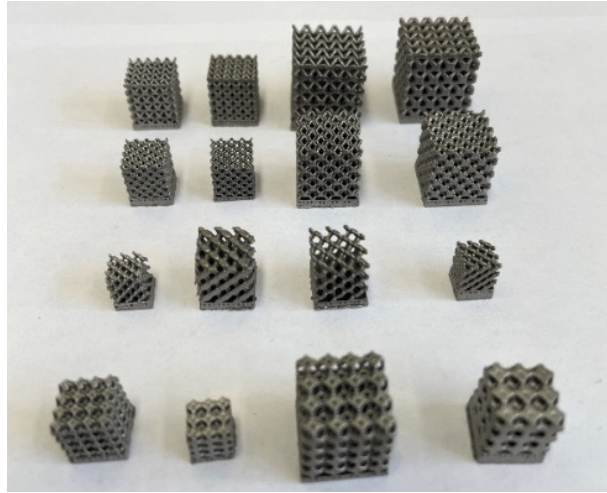


Fig. 1. Printed cellular structures using Selective Laser Melting.

Table 1. Overview of the investigated cellular structures with their parameters.

No.	Single cell topology	Size of a single cell (mm)	Designed relative density (%)	Specimen dimensions (mm)
1	Body Centered Cubic	2	25	10x10
2			50	
3		3	25	15x15
4			50	
5	Diamond	2	25	6x6
6			50	
7		3	25	9x9
8			50	
9	Fluorite	2	25	8x8
10			50	
11		3	25	12x12
12			50	
13	Kelvin	2	25	8x8
14			50	6x6
15		3	25	12x12
16			50	9x9

2.2. Effect of the unit cell number on the mechanical properties of the structures

Finite element models of cellular structures were designed using nTopology software, and simulations were performed using commercial ANSYS software. To evaluate the effect of the number of cells on mechanical

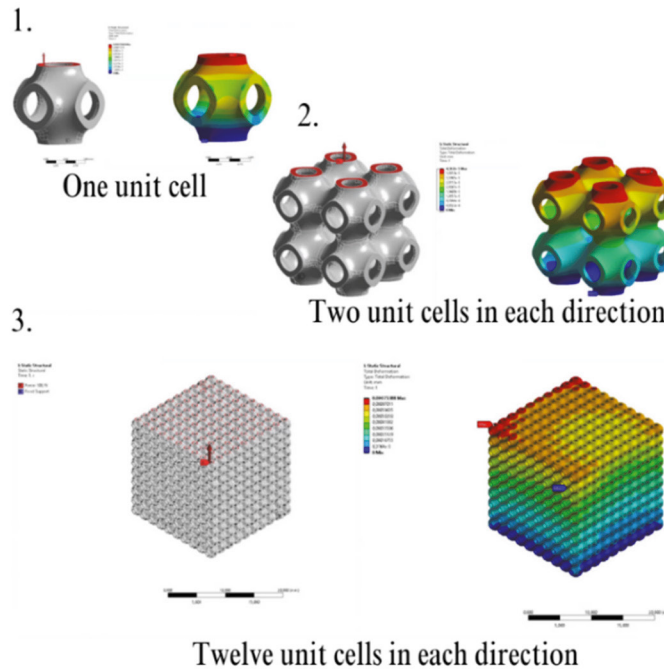


Fig. 2. Numerical analysis of cellular structures - study of the effect of the number of cells on strength properties.

properties, different models were developed, beginning with a cell structure consisting of one cell and ending with a structure containing twelve cells in one direction in space. The purpose of this analysis was to determine the number of cells at which the cell structure exhibits a stable effective Young's modulus. In defining effective values, it is assumed that the material is homogeneous and constant. A cellular structure composed of a sufficient number of unit cells is treated as a homogeneous material, and voids in the form of pores are not taken into account in determining the cross-sectional area required for calculating effective stresses. Effective strains are estimated from equation (1), which takes into account the difference between the measured length after deformation and the initial measured length. Effective stresses, on the other hand, are calculated from equation (2), accounting for the applied force and the initial cross-sectional area of the specimen.

$$\varepsilon_{eff} = \frac{\Delta l}{l_0} \quad (1)$$

$$\sigma_{eff} = \frac{F}{A_0} \quad (2)$$

The simulation included a uniaxial compression test. In general, two analysis concepts can be used. The first is to apply boundary conditions directly to the model, while the second requires creating two rigid plates to simulate contact between the testing machine and the specimen. Due to the significantly increased calculation time, the first option was chosen. Figure 2 shows the method for conducting the analysis based on the Schwarz TMPS cell. The parameters of the material model used were determined from a uniaxial tensile test of the base material. A linear elastic model was used in the numerical analysis.

2.3. Analysis using computed tomography

Due to the complex geometry of cellular structures, their accurate representation using additive manufacturing technology poses a challenge. One of the most reliable technologies for identifying defects and dimensional deviations is computed tomography (CT). Currently, CT has become the only non-invasive method for measuring the internal dimensions of geometric features. Because CT reconstruction creates a complete 3D representation of an object based on a large number of 2D X-ray images, it allows for answering questions about the external and internal structure of an element, as well as its material properties (Wu and Yang n.d.; Zadpoor n.d.).

The study of cellular structures was conducted using the Phoenix V Tome xS system (Fig. 3). The system consists of a detector with a resolution of 1000×1000 px (pixel size of $200 \mu\text{m}$) and a 16-bit grayscale, a rotary table, and an X-ray lamp with microfocus at a maximum accelerating voltage of 240 kV. The data analysis was performed using GOM Volume Inspect software. With this system, a comprehensive analysis of porosity and dimensional deviations was carried out, simultaneously obtaining a 3D representation of the objects, which was necessary for the issue related to numerical homogenization.

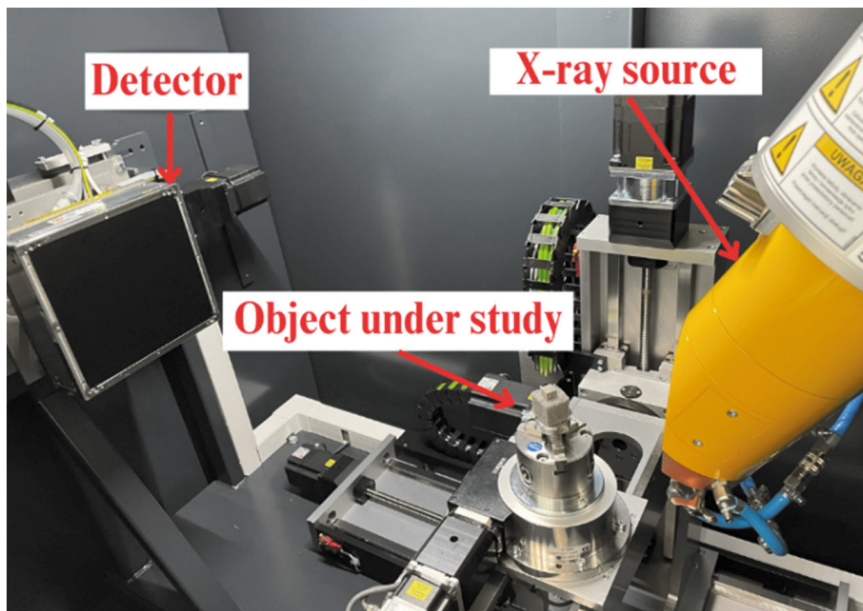


Fig. 3. Examination of cellular structures by computed tomography.

2.4. Determination of the stiffness matrix

In order to evaluate the mechanical properties of cellular structures, nTopology software was used to create a representative stiffness matrix for each cell type or several cells using homogenization techniques. This makes it possible to determine the variation of strength properties depending on the number of cells, dimensional deviations and internal defects. The tool provides valuable support for the design of materials with specific mechanical properties, enabling the design of materials with new and unique properties based on structural analysis of cells.

3. Results

3.1. Effect of the unit cell number on the mechanical properties of the structures

The findings indicate that the effective Young's modulus of the cell structure increases with the number of cells. However, the growth rate decreases as the number of cells increases and reaches a plateau at some point. Depending on the two key parameters of the structure, the relative density and the topology of a single cell, each structure has a different stability. To better interpret this phenomenon, an algorithm was developed (Fig.4). Based on such methodology, a numerical analysis was carried out for different single cell shapes and relative densities. Based on preliminary results, the effect of single cell size was found to be negligible. The whole algorithm was divided into two stages. The first criterion refers to the dependence of the change in effective Young's modulus on the number of cells $\Delta E_{eff} = f(N)$. Based on this function, a power approximation was estimated. If the correlation coefficient is greater than or equal to 0.85, the criterion of the power approximation of the relationship $\Delta E_{eff} = f(N)$, was applied. If the correlation coefficient is less than 0.85, a criterion based on the logarithmic approximation of the dependence of the effective Young's modulus on the number of cells $E_{eff} = f(N)$ was used. More significance was assigned to the

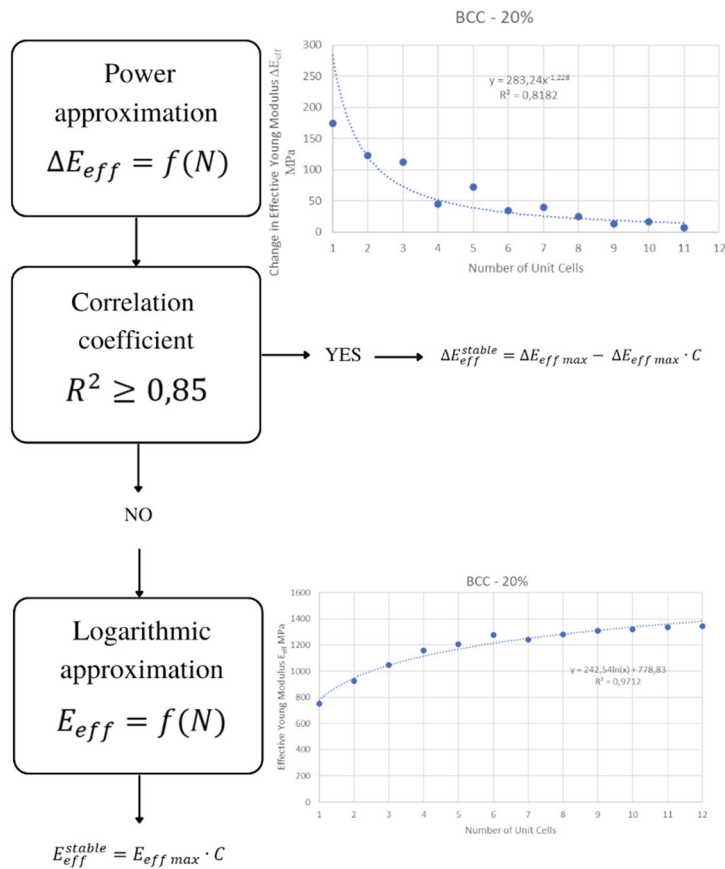


Fig. 4. Algorithm for determining the number of minimum single cells.

power approximation due to the fact that this function is characterized by the presence of a horizontal asymptote. In addition, a stability parameter of $C = 0.85$ was introduced into the equations, which are presented in Figure 4.

Based on the algorithm, the minimum number of cells for a given unit cell and relative density were defined. The results for each set of parameters are shown in Table 2.

Table 2. The minimum number of cells for selected examples.

The type of cell	Minimum number of cells		Stability criterion
BCC (20%.50%)	5	5	change in effective Young's modulus
Diamond (20%.50%)	2	3	effective Young's modulus
Kelvin (25%.50%)	4	3	change in effective Young's modulus
Fluorite (25%.50%)	3	4	effective Young's modulus

3.2. Geometric and porosity analysis using Computer Tomography

The use of computed tomography makes it possible to evaluate the actual relative density, porosity, average defect size and average dimensional deviation from the designed model. Using a three-dimensional representation of real objects, the relative density was determined (Karme et al. 2015). The data on this is illustrated in Table 3, where the other test results are also summarized. Based on the collected data, it can be seen that in all cases where the cell size in the cellular structure was 2 mm and the relative density was designed at 25%, there were slight positive differences. Nevertheless, based on the data obtained, it can be concluded that good compliance with the designed relative density was achieved. The highest porosity was observed for a cellular structure consisting of a 2 mm Fluorite cell and a relative density of 25%. The maximum porosity value is 0.22%.

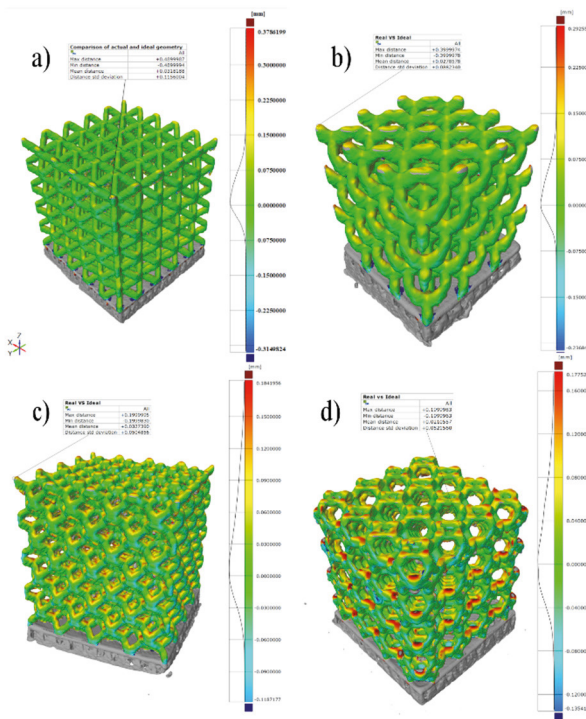


Fig. 5 Analysis of dimensional deviations.

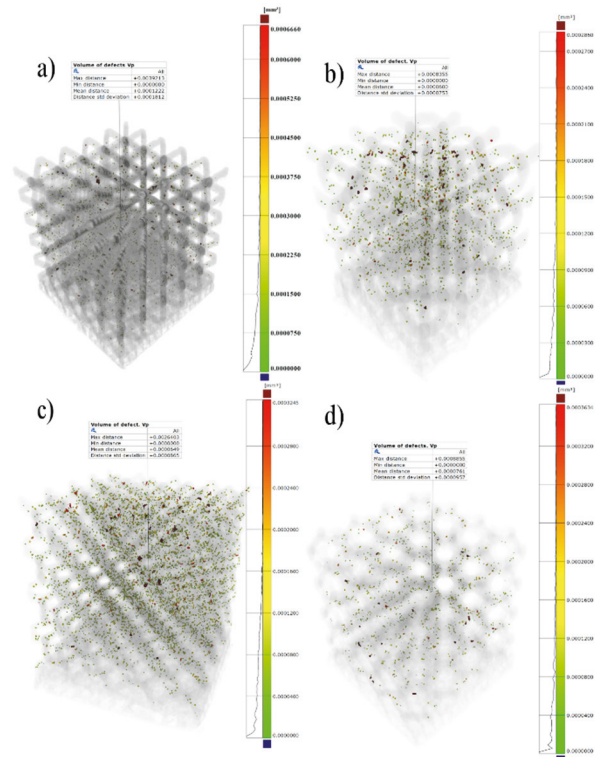


Fig. 6. Analysis of the volume of defects.

Table 3. Overview of results from dimensional deviation and porosity analysis.

No.	Porosity (%)	Average defect volume (mm ³)	Average dimensional deviation (mm)	Real relative density (%)
1	0.096	0.00012	0.032	28.17
2	0.0332	0.00009	0.0092	48.78
3	0.04	0.00065	0.0035	24.58
4	0.01	0.00025	0.0037	47.82
5	0.17	0.00006	0.028	27.59
6	0.12	0.000067	0.024	50.28
7	0.1	0.000083	0.0037	24.97
8	0.06	0.00012	0.003	48.04
9	0.22	0.000065	0.033	29.73
10	0.13	0.000093	0.016	50.59
11	0.05	0.00015	0.018	26.96
12	0.05	0.00014	0.0016	49.33
13	0.05	0.000076	0.021	27.1
14	0.17	0.000049	0.01012	48.31
15	0.04	0.0001	0.0093	24.31
16	0.05	0.00013	0.00041	48.03

3.3. Numerical homogenization of cellular structures

Numerical homogenization consists in determining the effective elastic parameters based on knowledge of the properties of a representative volume. In the case of cellular structures, such a representative volume can be defined as a cell. However, a single cell may be too simplified. Therefore, a simulation was performed using the homogenization method to determine the effect of the number of cells on the resulting mechanical response. The analysis was carried out using a predefined minimum number of cells at which the structure behaves stably. An additional optimization would be a model obtained from a CT scan, which includes information on the actual relative density or porosity.

For estimation of the properties of individual cells, a linear model of isotropic elasticity was used, assuming a constant Young's modulus of 163 GPa and a Poisson's ratio of 0.3. Figure 7 depicts the stiffness distribution in red, which indicates the direction of higher stiffness in a cell, while the blue color represents the direction of lower stiffness. For an ideal isotropic material, the stiffness matrix would be represented by a homogeneous sphere.

Analysis of the data presented in Table 4 shows that the difference between the distribution of stiffness for one unit cell and the minimum number of cells is not significant. Mostly, the distribution of stiffness for the minimum number of cells is slightly higher. However, in the case of a structure with a Diamond unit cell, the situation changes. This is due to the fact that this topology is not symmetrical, and only using the minimum number of cells will allow to estimate the correct stiffness matrix. It can be seen that there is a close correlation between the actual relative density and the stiffness distribution for models obtained using CT. It is the relative density, rather than the porosity present in the models, that has a greater influence on the formation of cellular properties. Nonetheless, taking all factors into account, in the form of defects or deviations, will allow a more accurate numerical analysis.

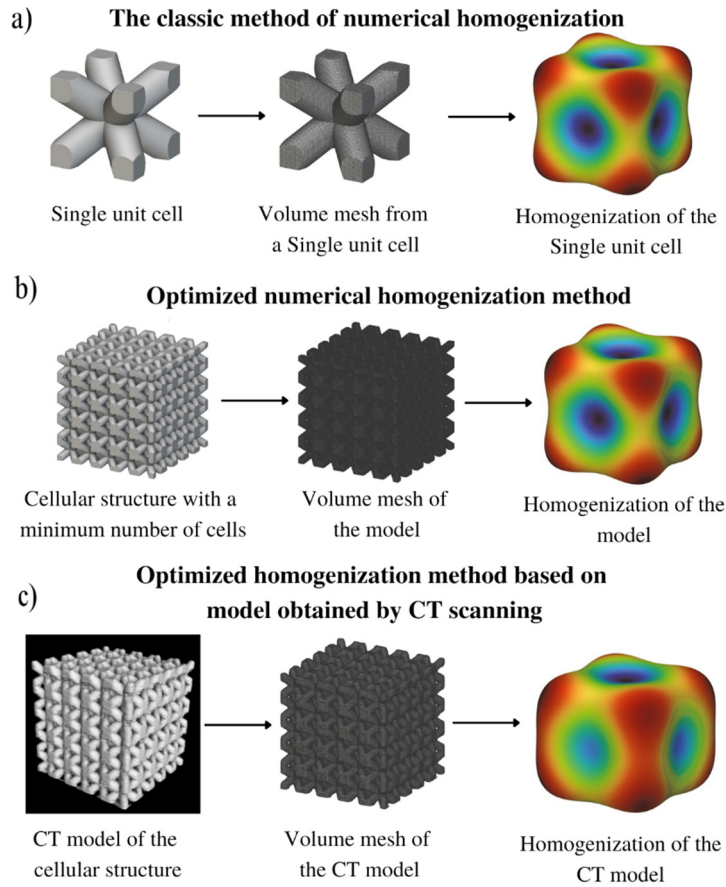


Fig. 7. Methodology for performing homogenization analysis: (a) Classical; (b) Optimized based on minimum number of cells; (c) Optimized based on model with CT.

4. Conclusion

The study investigates the effect of the number of cells on the effective Young's modulus of cellular structures. The two key parameters of the structure, the relative density, and topology of a single cell, are considered for stability analysis. The purpose of the study was to develop a procedure for determining the minimum number of cells that is required for a structure to exhibit a constant effective Young's modulus. Based on the literature review, it was not possible to clearly specify how many cells such a structure should contain. The study also proposed an optimization of the homogeneous method for cell structures.

- The study revealed that the effective Young's modulus of cellular structures increases with the number of cells, but the growth rate decreases and reaches a plateau at some point. The size of a single cell has an insignificant effect on mechanical properties. An algorithm was developed to determine the minimum number of cells for a given cell and relative density.
- The power approximation was found to be a better criterion for the relationship between the change in effective Young's modulus and the number of cells. A stability parameter $C=0.85$ was entered.
- The relative density, rather than porosity, has a greater influence on the formation of cellular properties. However, taking into account all factors, such as defects or deviations, would allow a more accurate numerical analysis. The stiffness distribution for the minimum number of cells is slightly higher, but for

non-symmetrical topologies like the Diamond unit cell. using the minimum number of cells is essential to estimate the correct stiffness matrix.

Overall, the study provides insights into the effect of the number of cells on the mechanical properties of cellular structures and proposes an algorithm for stability analysis. The findings can be useful for designing and optimizing cellular structures for various applications.

Table 4. Comparison of results from homogenization analysis.

No.	Directional maximum Young's modulus E_{\max} (GPa)		
	One Unit Cell	Minimum number of cells	CT Model
1	15.75	15.78	18.12
2	41.97	42.36	41.85
3	15.73	15.77	15.15
4	41.52	41.82	40.17
5	7.07	13.4	16.25
6	25.76	43.9	45.18
7	6.86	13.17	12.81
8	25.39	43.53	41.43
9	11.48	11.93	22.83
10	43.9	44.32	52.25
11	11.13	11.24	13.77
12	42.86	43.69	44.24
13	12.68	13.32	17.25
14	46.85	46.76	45.65
15	12.6	12.83	12.96
16	46.34	46.51	44.22

References

- Al-Ketan, Oraib, Dong Wook Lee, Reza Rowshan, and Rashid K. Abu Al-Rub. 2020. "Functionally Graded and Multi-Morphology Sheet TPMS Lattices: Design, Manufacturing, and Mechanical Properties." *Journal of the Mechanical Behavior of Biomedical Materials* 102:103520. doi: 10.1016/j.jmbbm.2019.103520.
- Al-Ketan, Oraib, Reza Rowshan, and Rashid K. Abu Al-Rub. 2018. "Topology-Mechanical Property Relationship of 3D Printed Strut, Skeletal, and Sheet Based Periodic Metallic Cellular Materials." *Additive Manufacturing* 19:167–83. doi: 10.1016/J.ADDMA.2017.12.006.
- Cantaboni, F., P. Ginestra, M. Tocci, A. Colpani, A. Avanzini, A. Pola, and E. Ceretti. 2022. "Modelling and FE Simulation of 3D Printed Co-Cr Lattice Structures for Biomedical Applications." *Procedia CIRP* 110(C):372–77. doi: 10.1016/J.PROCIR.2022.06.066.
- Chatzigeorgiou, Chrysoula, Boris Piotrowski, Yves Chemisky, Pascal Laheurte, and Fodil Meraghni. 2022. "Numerical Investigation of the Effective Mechanical Properties and Local Stress Distributions of TPMS-Based and Strut-Based Lattices for Biomedical Applications." *Journal of the Mechanical Behavior of Biomedical Materials* 126:105025. doi: 10.1016/J.JMBBM.2021.105025.
- Doroszkowski, M., A. Falkowska, and A. Seweryn. 2021. "Image-Based Numerical Modeling of the Tensile Deformation Behavior and Mechanical Properties of Additive Manufactured Ti–6Al–4V Diamond Lattice Structures." *Materials Science and Engineering: A* 818:141362. doi: 10.1016/J.MSEA.2021.141362.
- Jiang, Weimin, Wenhe Liao, Tingting Liu, Xin Shi, Cong Wang, Junfeng Qi, Yi Chen, Zhen Wang, and Changdong Zhang. 2021. "A Voxel-Based Method of Multiscale Mechanical Property Optimization for the Design of Graded TPMS Structures." *Materials & Design* 204:109655. doi: 10.1016/J.MATDES.2021.109655.
- Karme, Aleksis, Aki Kallonen, Ville Pekka Matilainen, Heidi Piili, and Antti Salminen. 2015. "Possibilities of CT Scanning as Analysis Method in Laser Additive Manufacturing." *Physics Procedia* 78:347–56. doi: 10.1016/j.phpro.2015.11.049.
- Maconachie, Tobias, Martin Leary, Bill Lozanovski, Xueze Zhang, Ma Qian, Omar Faruque, and Milan Brandt. 2019. "SLM Lattice Structures: Properties, Performance, Applications and Challenges." *Materials & Design* 183:108137. doi: 10.1016/J.MATDES.2019.108137.
- Mehboob, Hassan, Faris Tarlochan, Ali Mehboob, and Seung Hwan Chang. 2018. "Finite Element Modelling and Characterization of 3D Cellular Microstructures for the Design of a Cementless Biomimetic Porous Hip Stem." *Materials & Design* 149:101–12. doi: 10.1016/J.MATDES.2018.06.066.

10.1016/J.MATDES.2018.04.002.

Mines, Robert. 2019. "Metallic Microlattice Structures." doi: 10.1007/978-3-030-15232-1.

Moj, Kevin, Grzegorz Robak, Robert Owsiński, Andrzej Kurek, Krzysztof Żak, and Dawid Przysiężniuk. 2022. "A New Approach for Designing Cellular Structures: Design Process, Manufacturing and Structure Analysis Using a Volumetric Scanner." *Journal of Mechanical Science and Technology*. doi: 10.1007/s12206-022-2107-1.

Wu, Yan, and Li Yang. n.d. "Modeling and Analysis of Material Anisotropy-Topology Effects of 3D Cellular Structures Fabricated by Powder Bed Fusion Additive Manufacturing." 197:106325. doi: 10.1016/j.ijmecsci.2021.106325.

Yan, Chunze, Liang Hao, Lei Yang, Ahmed Yussuf Hussein, Philippe G. Young, Zhaoqing Li, and Yan Li. 2021. "Numerical Analysis on the Mechanical Properties of Uniform TPMS." *Triply Periodic Minimal Surface Lattices Additively Manufactured by Selective Laser Melting* 183–217. doi: 10.1016/B978-0-12-824438-8.00006-6.

Zadpoor, Amir A. 2019. "Mechanical Performance of Additively Manufactured Meta-Biomaterials." *Acta Biomaterialia* 85:41–59. doi: 10.1016/J.ACTBIO.2018.12.038.

Zadpoor, Amir A. n.d. "Mechanical Performance of Additively Manufactured Meta-Biomaterials." 85:41–59. doi: 10.1016/j.actbio.2018.12.038.



Structural Integrity and Reliability of Advanced Materials obtained through Additive Manufacturing (SIRAMM23)

Temperature and Thermal Aging Effects on the Mechanical Response of Polycarbonate Materials

Tamas Krausz^{a*}, Cosmin-Florin Popa^b, Cosmin-Denis Topircean^c, Lucian Rusu^d, Liviu Marsavina^e

^a*Mechanics and Strength of Materials, Politehnica University of Timisoara, 1st Mihai Viteazu Bd., Timisoara, 300222, Timis, Romania*

Abstract

Thermoplastic materials, due to their nature, are sensible to temperature variations. This sensibility restrains their usage to a limited number of applications, such as interior automotive products, household, and consumer electronics, where temperature and humidity conditions are limited to a certain range, thus ensuring their structural stability.

The polycarbonate grades from the Makrolon family are frequently met in various automotive electronic products, therefore their mechanical parameters must be thoroughly investigated before designing the mechanical components these materials will be used for.

The scope of this study is to investigate the variation of the mechanical properties of the unreinforced Makrolon 2405, and of the glass fibre reinforced Makrolon 9415 and Makrolon 8035 polycarbonate grades, in terms of elasticity modulus, tensile strength and Poisson's ratio, by subjecting standard, dogbone type specimens, to traction tests combined with various temperature loads. In addition, the long-term effect of the thermal cycles is also analyzed by conducting a material aging test for the proposed polycarbonate grades. Measurements are done using video extensometer and digital image correlation techniques.

© 2023 The Authors. Published by Elsevier B.V.

This is an open access article under the CC BY-NC-ND license (<https://creativecommons.org/licenses/by-nc-nd/4.0>)

Peer-review under responsibility of the SIRAMM23 organizers

Keywords: Makrolon; thermal aging; Poisson's ratio; digital image correlation

* Corresponding author. Tel.: +4-0256-403570.

E-mail address: tamas.krausz@student.upt.ro

1. Introduction

Thermal loads and their long-term effects often lead to certain material failures or defects, which despite not resulting in structural damage, might end up as a claim of the customer towards the manufacturer of the specific product.

In general, engineers and material specialists limit the use cases of these temperature sensitive materials to applications which are meant to function in controlled environmental conditions. However, during the lifetime of these products, they can still be subjected to various extreme temperatures. For this reason, there are several international standards (*ISO 16750-4, Road Vehicles - Environmental Conditions and Testing for Electrical and Electronic Equipment - Part 4: Climatic Loads*, 2010), specifying that all the electronic products, which rely on the usage of such thermoplastics, must withstand high numbers of thermal cycles, within the -40°C to $+85^{\circ}\text{C}$ temperature range, without producing mechanical failures.

Polycarbonate is one of the most widely used thermoplastic materials, from the amorphous polymer category, which offers several benefits due to its physical properties which make it the material of choice for a wide variety of applications. These include low density, transparency, high impact resistance, chemical stability, and ease of processing (Allen et al., 1973; Davis & Golden, 1969; Shah, 2009). Although the very good properties it possesses, longer exposure of polycarbonate to temperature will alter its chemical, thermal, and mechanical properties (Jiang et al., 2018; Redjala et al., 2019, 2021).

The aim of this paper is to investigate the variation of the elastic properties of the proposed polycarbonate grades, such as Young's modulus, yield strength and Poisson's ratio, during quasi-static tensile testing of thermally aged and non-aged samples. For the non-aged samples, the effect of the temperature increase over the mechanical behavior in tension of the materials has been studied (Cao et al., 2014; Krausz et al., 2021). The investigation concludes with the comparison of both test cases with the tensile behavior of the materials at room temperature condition.

Nomenclature

MK2405	Makrolon 2405, polycarbonate material without glass fiber reinforcement
MK9415	Makrolon 9415, polycarbonate material with 10% glass fiber
MK8035	Makrolon 8035, polycarbonate material with 30% glass fiber

2. Experimental investigations

2.1. Specimen preparations

The specimens used for the experiments were produced by injection molding, directly in their final, dogbone shape, and kept at room temperature (22°C) and normal humidity conditions ($\sim 50\%$).

The shape and dimensions of the specimens were selected according to the ISO 572-2 tensile testing standard (*ISO 527-2, Plastics - Determination of Tensile Properties - Part 2: Test Conditions for Moulding and Extrusion Plastics*, 2012), with a total length of 150 [mm], a gauge length of 60 [mm], a width of 10 [mm] and a thickness of 4 [mm].

The thermal aging of the specimens has been conducted in a Vötsch VT3 7006 S2 type thermal shock test system. The system consists of two low and high temperature chambers, which permit very rapid temperature changes in the range of -80°C to $+220^{\circ}\text{C}$.

The specimens were placed on the shelves inside the cradle, which makes a translatory movement between the top (hot) and bottom (cold) chambers during the thermal cycles applied. The type and number of the cycles has been selected according to the IEC 60068-2-14 international standard (*IEC 60068-2-14, Environmental Testing - Part 2-14: Tests - Test N: Change of Temperature*, 2009), applicable to environmental testing. (Fig.1).

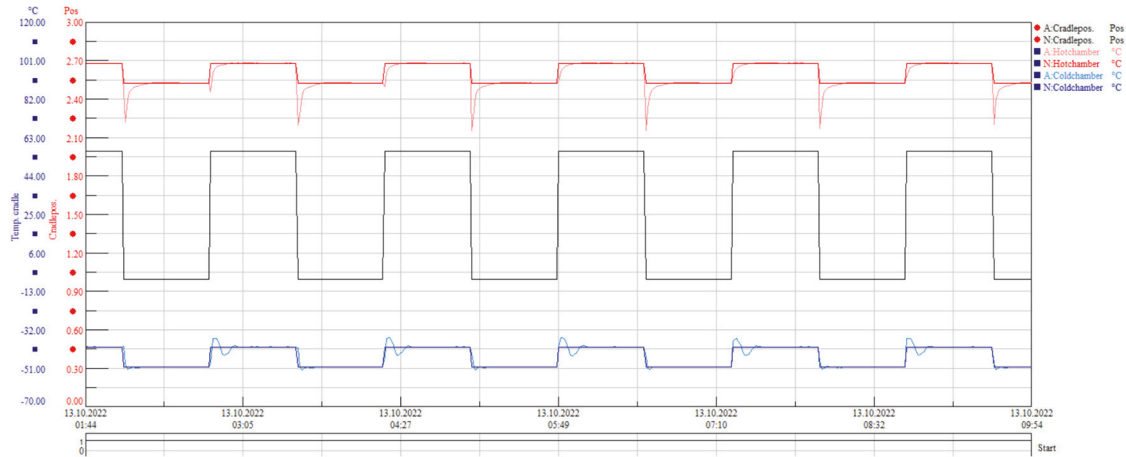


Fig. 1. Aging of samples – 100 cycles of thermal load varying between -40°C and $+85^{\circ}\text{C}$.

The fans mounted in both chambers ensured the high flow rate and even air distribution, and thus the homogenization of the temperature in the test space.

2.2. Tensile testing of non-aged samples at elevated temperatures

For the tensile testing in the temperature range of 20°C - 80°C of the non-aged samples an Instron 8874 multiaxial test machine with hydraulic control has been used. The machine was equipped with an environmental chamber controlled by a resistance-wire heater and with a video-extensometer to capture the longitudinal and transversal displacements of four circular spots marked on the specimens.

The tests were conducted with a constant loading rate of 50 mm/min . The temperature of the specimens inside the chamber has been monitored with a thermocouple to ensure the even distribution of the thermal load before the tensile tests.

2.3. Tensile testing of aged samples

The tensile testing of the aged samples at room temperature and normal humidity conditions (20°C , 50%) has been conducted using a Zwick-Roell Z005 universal machine, equipped with a 5 kN load cell, in combination with a clip-on extensometer for strain recording, having a gauge length of 30 mm . Tests were performed with a constant cross head velocity of 2 mm/min .

In addition to the clip-on extensometer, a Dantech Dynamics Digital Image Correlation system has also been utilized to capture the transversal deformations of the specimens during tension and hence to allow the calculation of the Poisson's ratio of the thermally aged samples.

3. Results and discussions

3.1. The influence of uniform, constant heating

It is generally known that the tensile response of polycarbonate, as of most polymeric materials, is highly dependent on strain rate and temperature, as confirmed by several studies (Cao et al., 2010, 2014).

Figure 2 shows the engineering stress-strain response in monotonic tension of the neat and fiber reinforced polycarbonate grades as function of three different temperatures (22°C, 40°C, 80°C).

The curves for the individual materials are having the same shape, differentiated by the shifts caused by the temperature conditions. These reflect an elastoplastic behavior which consists of a viscoelastic region followed by the yield point (considered as the local maximum point on the stress-strain curve), then by the plastic or flow region and concludes with the end point where the material failure occurs. Similar nonlinear material deformation tendency under quasi-static monotonic tension conditions is described by several studies in the literatures (Krausz et al., 2021), (Autade & Pawar, 2015).

In case of the MK8035, however, the curves are only characterized by non-linear elasticity, as due to the brittleness of the material this will fail without any significant softening after reaching the maximum stress value that the material can still withstand, independent of the temperature variations.

One common observation for all the studied material grades is the yield stress showing a strong temperature dependency.

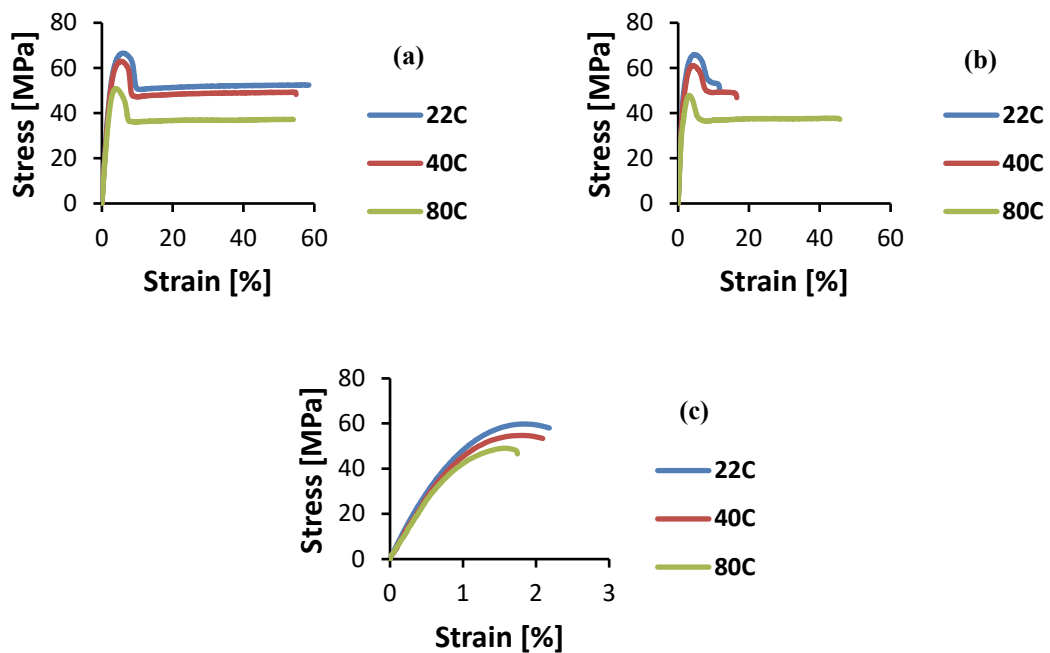


Fig. 2. Force-deflection curves as function of temperature of the three polycarbonate grades: (a) MK2405, (b) MK9415 and (c) MK8035.

Table 1 summarizes the average and standard deviation values of the elastic modulus of the materials in terms of the three temperature levels that have been selected for the study. Like the flow stress, the elastic modulus is also highly influenced by temperature. This undergoes a decrease of up to 13% for the MK2405 and for the MK9415, and a slightly lower decrease of 7.5% for the MK8035.

Table 1. The average and standard deviation values of the elastic modulus as function of temperature.

	Makrolon 2405		Makrolon 9415		Makrolon 8035	
	Average [MPa]	St. dev. [MPa]	Average [MPa]	St. dev. [MPa]	Average [MPa]	St. dev. [MPa]
22°C	2600	305.16	4104	131	5723	469.88
40°C	2480	98.11	3930	275.45	5680	200.44
80°C	2260	184.73	3571	177.93	5295	118.32

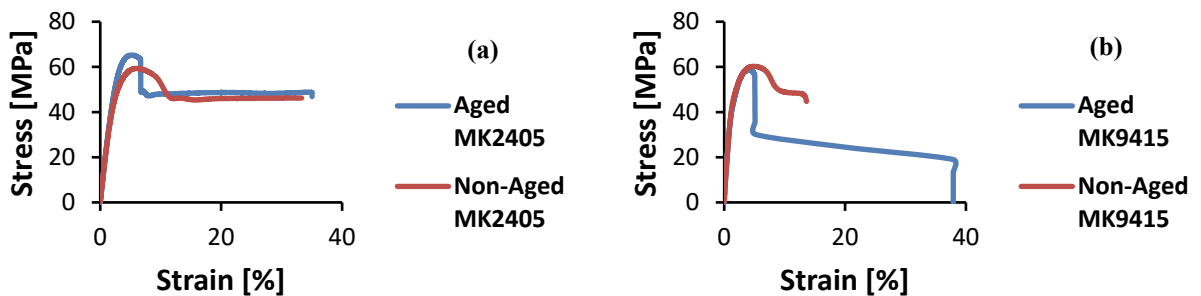
In terms of the Poisson's ratio one can observe that all three material grades show stability although the temperature increases (Table 2). There is a variation of about 3% for each grade, but there is no clear indication of negative temperature impact.

Table 2. The average and standard deviation values of the Poisson's ratio as function of temperature.

	Makrolon 2405		Makrolon 9415		Makrolon 8035	
	Average [-]	St. dev. [-]	Average [-]	St. dev. [-]	Average [-]	St. dev. [-]
22°C	0.418	0.067	0.414	0.014	0.343	0.083
40°C	0.43	0.041	0.421	0.03	0.336	0.086
80°C	0.431	0.02	0.403	0.041	0.332	0.06

3.2. The effects of thermal aging

Figure 3 represents the engineering stress - strain curves in monotonic tensile testing of aged and non-aged polycarbonate, from all three selected grades. The curves of the aged specimens do respect the same tendency as the ones for the non-aged samples, however, high degrees of similarity can only be observed up to the yield limit (elastic region). Beyond this point the aged samples exhibit a sudden drop in terms of stresses opposed to the non-aged materials where the softening of the material happens more slowly. A flow of the material can then be observed for both specimen types until the deformations reach their maximum values before fracture occurs.



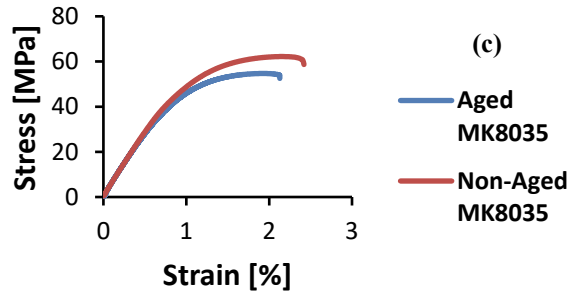


Fig. 3. Force-deflection curves of aged and non-aged specimens for the three polycarbonate grades: (a) MK2405, (b) MK9415 and (c) MK8035.

Table 3 groups the values of the elastic modulus and yield strength of the aged and non-aged polycarbonate materials at room temperature conditions. From the values shown one can observe a slight increase (1.2%) in Young's modulus and in yield strength (10%) in favor of the aged samples, but only for the unreinforced grade.

In the case of the fiber reinforced materials the tendency will change, making the non-aged materials more stable for loads with magnitudes close to the yield limit.

Table 3. The variation of the elastic modulus and of the yield strength due to the aging of the specimens.

	Makrolon 2405		Makrolon 9415		Makrolon 8035	
	Elastic modulus [MPa]	Yield strength [MPa]	Elastic modulus [MPa]	Yield strength [MPa]	Elastic modulus [MPa]	Yield strength [MPa]
Aged	2487.45	65.21	4215.37	58.53	5846.45	54.69
Non-aged	2457.84	59.33	4042.02	60.26	5960.54	58.83

Although the behavior shown by the aged specimens is different from the one observed by Sonja et al. (Redjala et al., 2019), the sudden drop is expected to be due to the physical and chemical aging of the materials at microscale level, resulting in bond breakages which make room for degradations.

4. Conclusions

Uniaxial monotonic tension behavior of unreinforced and reinforced polycarbonate grades was investigated at three temperatures - 22°C, 40°C and 80°C. The experimental findings demonstrated once again the temperature dependency of the material. The elastic modulus and yield stress values are decreasing with the increasing temperature, whereas the Poisson's ratio remains stable, with almost insignificant variations, throughout the entire tested temperature range.

In addition, thermal aging of the specimens from the selected polycarbonate grades has been conducted. After aging, the specimens have been tested for uniaxial tensile loading and compared to non-aged material behavior. The aging had an impact upon the base polycarbonate, by increasing its mechanical properties by up to 10%, however, with the increasing fiber ratio, the stiffening effect of the aging has been canceled. The specimens for the two reinforced grades showed a drop of up to 7% compared to the non-aged materials. Both the temperature dependency and the possibility of negative impact of aging should be considered before the selection of a specific polycarbonate grade for a certain engineering application.

Acknowledgments

This paper was financially supported by the Project “Network of excellence in applied research and innovation for doctoral and postdoctoral programs” / InoHubDoc, project co-funded by the European Social Fund financing agreement no. POCU/993/6/13/153437 and by the European Union's Horizon 2020 research and innovation program (H2020-WIDESPREAD-2018, SIRAMM) under grant agreement no. 857124.

References

- Allen, G., Morley, D. C. W., & Williams, T. (1973). The impact strength of polycarbonate. *Journal of Materials Science*, 8(10), 1449–1452.
- Autade, P. G., & Pawar, D. S. (2015). *Effect of Temperature and Strain Rate on the Mechanical Properties of Polycarbonate and Polycarbonate/Thermoplastic Polyurethane Blend*. 2(3), 60–65.
- Cao, K., Ma, X., Zhang, B., Wang, Y., & Wang, Y. (2010). Tensile behavior of polycarbonate over a wide range of strain rates. *Materials Science and Engineering: A*, 527(16–17), 4056–4061.
- Cao, K., Wang, Y., & Wang, Y. (2014). Experimental investigation and modeling of the tension behavior of polycarbonate with temperature effects from low to high strain rates. *International Journal of Solids and Structures*, 51(13), 2539–2548.
- Davis, A., & Golden, J. H. (1969). Stability of Polycarbonate. *Journal of Macromolecular Science, Part C*, 3(1), 49–68.
- IEC 60068-2-14, *Environmental testing - Part 2-14: Tests - Test N: Change of temperature*. (2009).
- Jiang, L., Zhou, M., Ding, Y., Zhou, Y., & Dan, Y. (2018). Aging induced ductile-brittle-ductile transition in bisphenol A polycarbonate. *Journal of Polymer Research*, 25(2).
- Krausz, T., Serban, D. A., Negru, R. M., Radu, A. G., & Marsavina, L. (2021). The effect of strain rate and temperature on the mechanical properties of polycarbonate composites. *Materials Today: Proceedings*, 45, 4211–4215.
- ISO 527-2, *Plastics - Determination of tensile properties - Part 2: Test conditions for moulding and extrusion plastics*. (2012).
- Redjala, S., Azem, S., & Ait Hocine, N. (2021). The effect of the thermal aging on polycarbonate. *Materials Today: Proceedings*, 47, 3073–3076.
- Redjala, S., Ferhoum, R., Ait Hocine, N., & Azem, S. (2019). Degradation of Polycarbonate Properties Under Thermal Aging. *Journal of Failure Analysis and Prevention*, 19(2), 536–542.
- ISO 16750-4, *Road vehicles - Environmental conditions and testing for electrical and electronic equipment - Part 4: Climatic loads*. (2010).
- Shah, Q. H. (2009). Impact resistance of a rectangular polycarbonate armor plate subjected to single and multiple impacts. *International Journal of Impact Engineering*, 36(9), 1128–1135.



Structural Integrity and Reliability of Advanced Materials obtained through Additive Manufacturing (SIRAMM23)

The influence of contour on FDM parts for the Shear Test

Cosmin Florin POPA^a, Tamas KRAUSZ^a, Sergiu-Valentin GALATANU^{a,*} and Liviu MARSAVINA^a

^aUniversity Politehnica Timisoara, Department of Mechanics and Strength of Materials, 1 Mihai Viteazul Blvd., 300222, Timisoara, Romania

Abstract

Additive manufacturing (AM) is a process that can achieve many complexities in the production of parts. The most important aspect of AM is that there is no more material wastage, so costs are reduced. Additive manufacturing is starting to be used in many fields, including medicine, automotive, aircraft, etc. The method of adding layer by layer is used for a wide range of materials: plastics, metals, and ceramics.

This paper investigated the influence of nutshells on shear specimens. To obtain the specimens Prusa 3D printer and PETG filament were used. The specimens were built using Fused Deposition Modeling (FDM) technology. The shear properties were investigated in-plane, where the force was measured with a load cell, and the displacement was measured with Dantec Q400 digital image correlation. The difference between nutshell and without nutshell specimens in the shear strength was investigated. It has been seen that the specimens behave differently when the nutshell exists or not. On the other hand, digital image correlation (DIC) was used to calibrate the strain that appears on the fracture.

© 2023 The Authors. Published by Elsevier B.V.

This is an open access article under the CC BY-NC-ND license (<https://creativecommons.org/licenses/by-nc-nd/4.0>)

Peer-review under responsibility of the SIRAMM23 organizers

* Corresponding author.

E-mail address: sergiu.galatanu@upt.ro

Keywords: PETG, SHEAR, DIC

1. Introductions

Additive manufacturing is the process that can build complex parts layer by layer without wasting material and having a fast building speed. The 3-D printing employs an additive manufacturing process whereby products are built on a layer-by-layer basis, through a series of cross-sectional slices, Barry (2012). On the other hand, the only material waste is a few rows of material, the contour of the printed specimens. The AM technology is used for complex parts without any other operations, Zhang et al. (2018). AM technology is used in different fields, such as mechanical Henriques et al. (2018), biomechanical Malik et al. (2015), Mulford et al. (2016), aeronautical engineering Ahmed et al (2013), Kroll et al (2011)), and so on.

The first 3D printer based on Fused Depositing Modelling was made in the USA in the 1980s; this technology is used much more than other technologies, Dudek et al. (2013). To use the FDM technology, it is necessary to define a 3D model and import it into a 3D printer software to establish the parameters and export it into a G-code file. The parameters that can be established in the software are printing speed, layer thickness, bed temperature, and nozzle temperature.

FDM is an additive manufacturing method and is the most widely used because of its ease of use. Materials used in the FDM method are thermoplastic polymers. Although some experts in the field would restrict 3-D printing to units with inkjet-based print heads that create an object on a layer-by-layer basis, others would apply this term to office or consumer versions of rapid prototyping machines that are relatively low-cost and easy to use Casey (2009). The filament is heated until the material is melted and can be deposited on the other layer. The specimens were made according to the ASTM B 831-5 standard, which is used for thin sheet metal specimens to characterize the mechanical properties in shear specimens. For printed specimens, there is no specific standard for in-plane shear properties.

Valean et al. (2020) and Marsavina et al. (2022) investigated the influence of manufacturing parameters on the tensile properties, respectively fracture toughness of FDM specimens made of PLA. Ziemian et al. (2012) studied the dependence of the mechanical properties of ABS parts produced by FDM on raster orientation and the conclusion of the paper is mechanical properties display anisotropic behavior with the orientation of raster and the directionality of polymeric molecules.

In order to identify additional material parameters, Rauch et al. (1992) made many studies of the constitutive behavior during shear deformation, especially for the examination of large strains. Bouvier et al. (2006) analyzed the homogeneity of the shear zones depending on the geometric ratio of the shear gauge. The in-plane simple shear with a single shear zone is a very efficient technique for evaluating the shear properties and for analyzing the in-plane plastic anisotropy of metals Rauch et al. (1998) For those types of specimens which are in-plane loaded is easy to use digital image correlation DIC to measure the strains during the test, Liew et al. (2018). DIC is a non-contact optical digital method to measure specimen deformation Casey et al (2009). The method was used instead of the extensometer, which can influence the fracture zone. DIC uses 2 cameras positioned at 700 mm by the specimen and an angle of 60 degrees, so it is not necessary to touch the specimen. The DIC accuracy is very high, and the computational efficiency has been improved.

Song et al. (2017) found that polylactic acid (PLA) specimens had three different strengths in three directions, and the strength along the build direction had the smallest value. Popa et al. (2022) investigated the influence of thickness under the Izod impact test and observed that PETG specimens have better accuracy in results and a brittle fracture.

The objective of this study was to investigate the difference in shear behavior between specimens with and without contour. For this investigation, specimens adhering to ASTM 831-5 specifications, utilized polyethylene terephthalate glycol (PETG).

2. Material and methods

The specimens were made from blue PETG, the color has a characteristic that has been shown to have an impact on the material's behavior. Shear specimens were 3D printed using a Prusa MK3 printer with a 2 mm nozzle and 1.75 mm filament diameter. Printing parameters included a nozzle temperature of 230°C and a bed temperature of 85°C, adhering to ASTM 831-5 specifications for shear specimen geometry.

Simultaneously, blue PETG was characterized using tensile specimens, which were manufactured and subjected to experimental investigation. Post-testing, Young's modulus and ultimate strength were determined.

The shear specimens were produced in two configurations: the first with two layers contour and the second without contour. Both configurations were printed with the same raster orientation at 0 degrees. Six specimens of each type were printed, as depicted in Fig. 1. Fig. 1 a) displays a specimen without a contour, revealing an irregular outline and rough filament ends. In contrast, Fig. 1 b) illustrates a specimen with a contour, displaying a smooth surface without any roughness. These observations highlight the influence of contour presence, on the final surface quality of the 3D-printed PETG specimens.

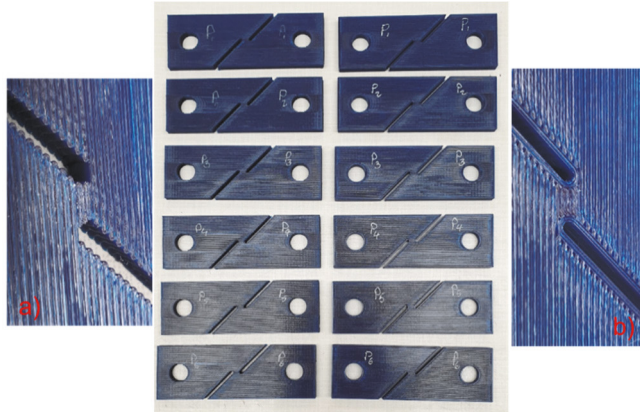


Fig. 1 The printed specimens a) without contour and b) with contour.

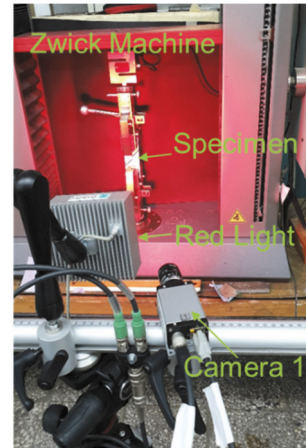


Fig 2 The test setup used for the experiment.

The specimens were measured before the painting, the dimensions are shown in Table 1.

Table 1 The specimen dimensions

Specimens without contour			Specimens with contour		
Specimen	Width	Thickness	Specimen	Width	Thickness
P1	5.10	6.35	P1c	5.09	6.35
P2	4.99	6.29	P2c	5.06	6.35
P3	5.00	6.32	P3c	5.11	6.36
P4	4.89	6.29	P4c	5.02	6.38
P5	5.03	6.33	P5c	5.03	6.37
P6	4.78	6.35	P6c	5.06	6.38

The Dantec Q-400 Digital Image Correlation (DIC) system comprises two 5-megapixel greyscale cameras strategically positioned on either side of the red-light source, precisely at the center of the specimen. For illumination, Dantec HILIS LED technology was employed, ensuring better precision in measurements. Data acquisition was facilitated through a trigger unit, offering both analog and digital input/output channels. Instron4D software was employed for data processing and visualization purposes. First, to conduct the tests, a meticulous calibration procedure was executed to ensure the accuracy of the measurements. Calibration involved the use of a BNB 9x9 plate. During these tests, the Global Residual was determined to be 0.240. Image capture occurred at a rate of 1 Hz, for each camera. To optimize visibility and minimize reflectivity, the specimens were meticulously prepared. They were coated with multiple layers of white paint until the surfaces achieved complete whiteness. Subsequently, a light-speckle pattern, created using black paint, was applied over the area of interest on the specimens.

The tests were performed on the Zwick tensile machine with a 5 kN load cell. The specimens were clamped in each half of the specimen, remaining in the interest area of the specimen. The specimen was loaded with a speed of 5 mm/min in displacement control. The collection of the necessary strain data was accomplished through the use of DIC

The DIC strain measurement on both sides of the specimen also compensates for any twisting or rigid body motion during loading, since the strain values collected on either side are averaged together for the subsequent material property calculations.

3. Results and discussion

The purpose of this paper was to observe the difference in behavior between specimens made with contour and those without contour in shear. The first step involved defining the mechanical properties of the PETG material. For this study, the specimens were designed with a contour. Tensile specimens were then manufactured and tested using the same Zwick machine, with a loading rate of 2 mm/min. Figure 3 illustrates the Force-Displacement graph obtained from the tensile testing.

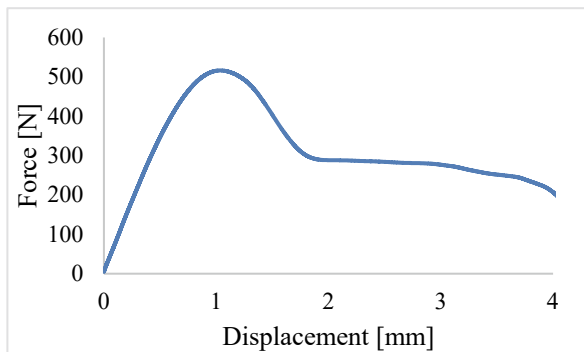


Fig. 3 The Force - Displacement curve at tensile test

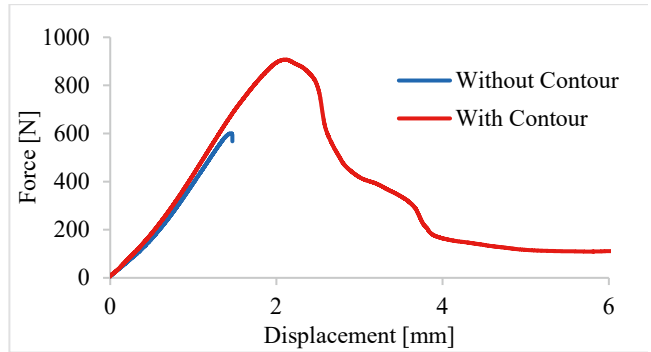


Fig. 4 The Force – Displacement curves at shear test

The second step involved conducting shear tests on the Zwick machine. For each specimen, images were captured using DIC. With the help of Instra4D software, the position of maximum shear stress was detected, allowing for a comparison between the strain shape and the experimental values. Once a test was completed, the process was repeated six times for each type of specimen.

Fig. 4 shows the Force-Displacement curves for both specimens, the red curve is for the specimen with contour and the blue curve is for the specimen without contour. The difference between curves is about 30% in maximum force. Specimens without contour highlighted a more brittle behavior compared with those with contour.

To compute the displacements measured by DIC, two points were fixed on the specimens, Fig. 5. First point 1 was fixed on the upper side of the specimen and the second point 2 was fixed on the bottom side of the specimen. With Instra4D software it was possible to measure the displacement and extract the measurement data. For both specimens, the points were fixed at the same distance.

In Fig. 5, the displacements provided by the DIC from the two points near the shear zone are shown. On the graph are overlapped pictures in 3 stages. The pictures were taken in the first step where the force and displacement were 0. The second picture is in an intermediate stage, the value of displacement corresponding to point 1 is 0.38 mm. On the graph, the same picture is around 0.8 mm taken from the machine, and for this, the force is 295 N. The third stage was just before the fracture, the value of displacement is around 1.4 mm (for point 1) and the force is 592 N.

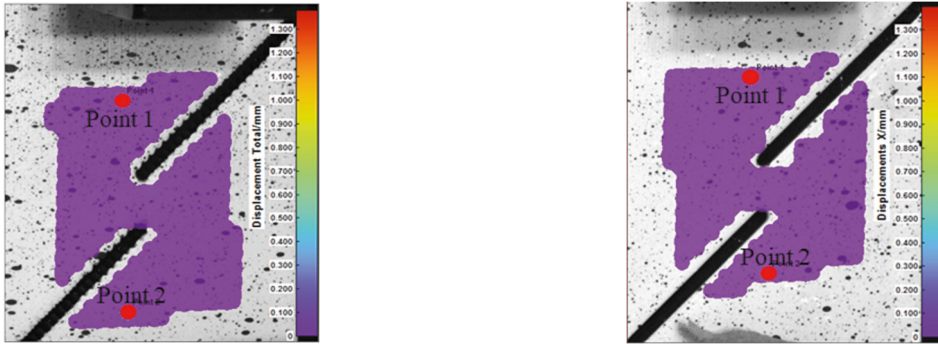


Fig. 5 The points measured by DIC

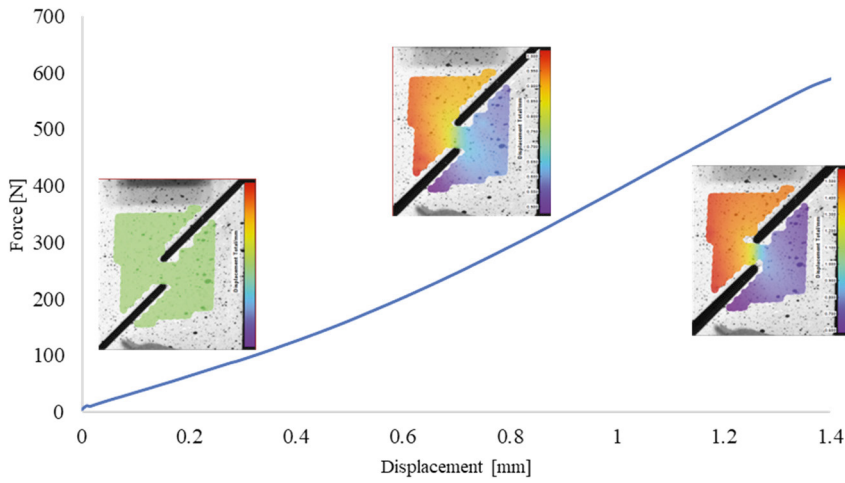


Fig. 6 Un-contour specimen phases overlapped over Force - Displacement graph

Fig. 7 depicts three stages of displacement on a contour specimen measured with DIC. The stages were taken in the same order and at the same time as in the previous Fig. 6. The first picture shows the incipient phase, which is the reference position on the measurement when the specimen is not loaded. The second figure shows an intermediary stage of 1 mm displacement (recording by DIC), where 1.3 mm and 587 N according to the Zwick, and the maximum displacement is located in the upper part of the specimen. The last picture shows the last stage before crack propagation, where the maximum displacement is 1.55 mm according to Dantec and 1.8 mm and 829 N according to Zwick.

It is worth noting that the force for specimens with contour is higher than that those specimens without contour. The contours provide higher strength to the specimens and higher elongation.

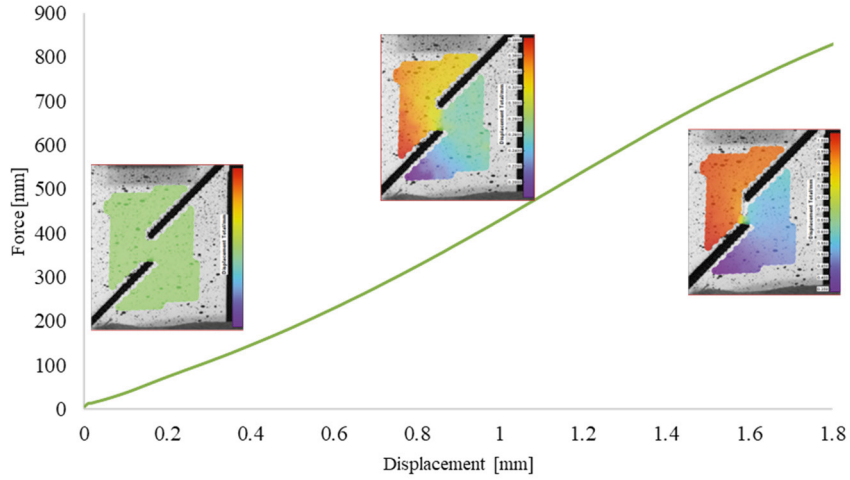


Fig 7 Contour specimen phases overlapped over Force - Displacement graph

The engineering shear strain is depicted in Fig. 8, which shows the displacement measurements in three phases: the incipient phase and two final stages, before and after fracture. In the second phase, before fracture, the distribution of the engineering shear strain along the crack and is highly concentrated in that area. The maximum value of the engineering shear strain is 5.5%

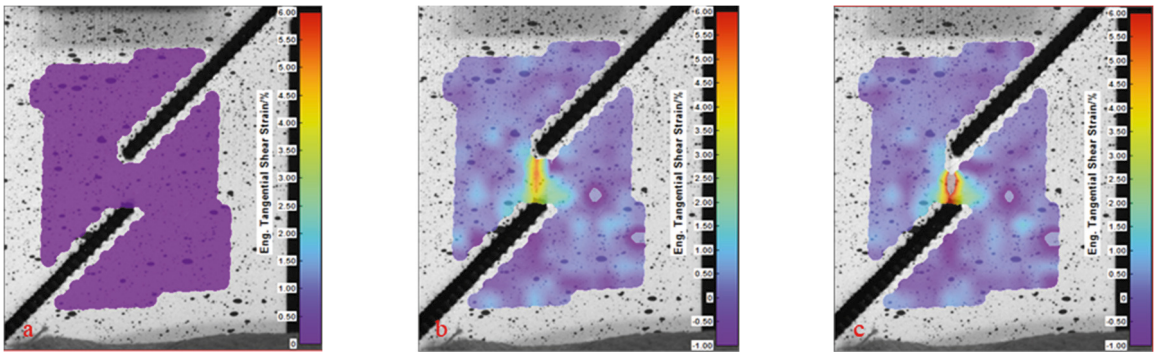


Fig. 8 Engineering Shear Strain on specimen without contour

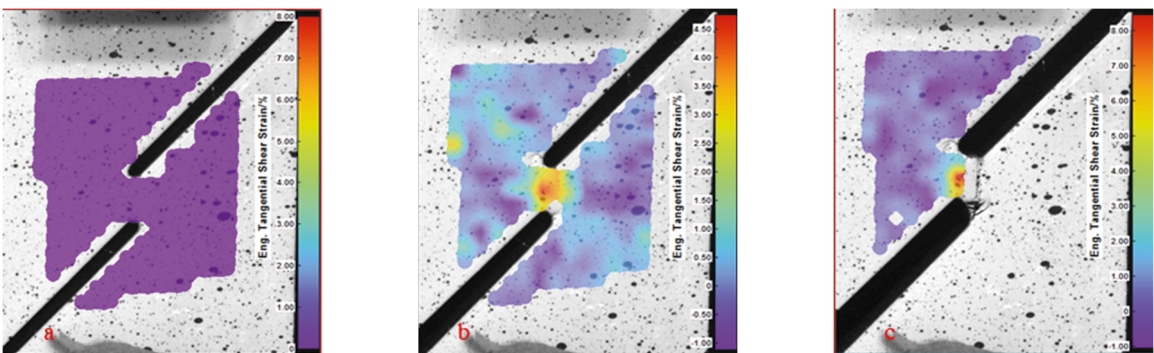


Fig. 9 Engineering Shear Strain on the specimen with contour

In the other specimen in stage 2 Fig. 9 b), the engineering shear strain is distributed in a circle area, the cracks appeared on both sides of the fracture area, which can be seen in the last stage, Fig. 9 c). The maximum value is above the 5% strain due to the contour layers.

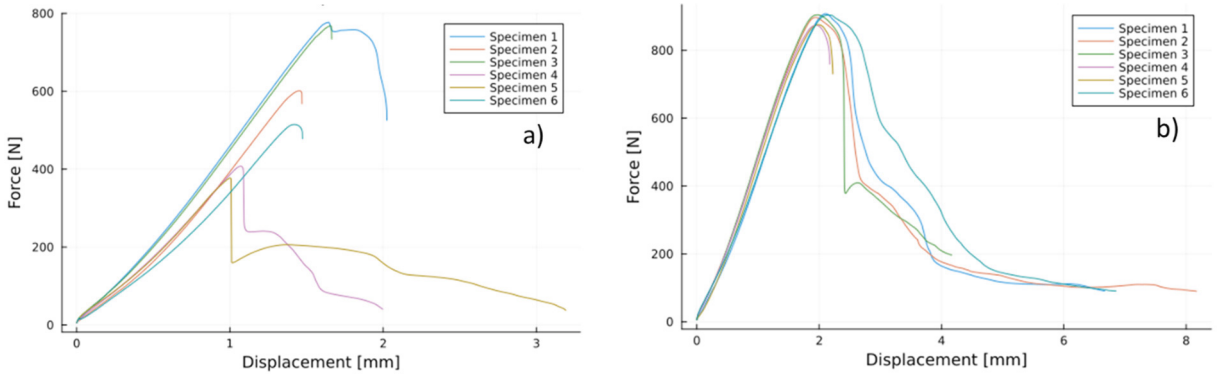


Fig. 10 Force - Displacement curves for a) specimens without contour and b) for specimens with contours

Fig. 10 depicts the force-displacement graph for both specimen types. In Fig 10.a, the results for the specimens contour it could be observed that the values of force are scattered. The results are clustered in groups of two, this behavior may be due to the printing process or microcracks, which initiate at the layers interface. On the other hand, for the specimens with contour, the results are very close to each other, and the behavior is the same for all specimens.

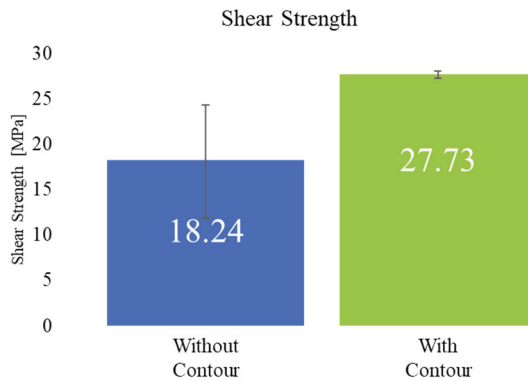


Fig. 11 Comparison of shear strength between the two types of specimens

Fig. 11 presents a comparison of the shear strength between two types of specimens. The contour specimens exhibited a 34% higher shear strength than the specimens without contour. The contour has a significant influence on the results. The error bars indicate that the values for specimens without contour are highly scattered, whereas the values of specimens with contour are much less scattered.

4. Conclusions

The objective of this study was to investigate the difference in shear behavior between specimens with and without contour. The contoured specimens exhibited a shear strength of 27.73 MPa, which is 34% higher than that of the un-contoured specimens (18.24 MPa). Additionally, the contoured specimens showed a greater elongation at fracture. These results suggest that contouring should not be ignored when designing and manufacturing 3D-printed parts.

Using digital image correlation, the engineering shear strain distribution was observed in a circular area for the contoured specimens. Cracks appeared on both sides of the fracture area. In contrast, for the specimens without contour, the engineering shear strain distribution was along the ligament of the specimen.

Acknowledgments

The project leading to this application has received funding from the European Union's Horizon 2020 research and innovation program under grant agreement No. 857124

References

- Ahmed N.A., J. Page, Manufacture of an unmanned aerial vehicle (UAV) for advanced project design using 3D printing technology, *Applied Mechanics and Materials*, Trans Tech Publ (2013), pp. 970-980
- Barry B., 3-D printing: The new industrial revolution, *Business Horizons*, Volume 55, Issue 2, March–April 2012, Pages 155-162, <https://doi.org/10.1016/j.bushor.2011.11.003>
- Bouvier S., H. Haddadi, P. Levée, C. Teodosiu, Simple shear tests: experimental techniques and characterization of the plastic anisotropy of rolled sheets at large strains, *J. Mater. Process. Technol.*, 172 (2006), pp. 96-103
- Casey L., Prototype pronto, *Packaging Digest*, 46 (8) (2009), pp. 54-56
- Popa C. F., Marghitas M. P., Galatanu S. V., Marsavina L., Influence of thickness on the IZOD impact strength of FDM printed specimens from PLA and PETG, *Procedia Structural Integrity* 41(6) (2022), pp. 557-563
DOI: 10.1016/j.prostr.2022.05.064
- Dudek P., FDM 3D printing technology in manufacturing composite elements, *Arch. Metall. Mater.*, 58 (4) (2013), pp. 1415-1418
- Henriques B., P. Pinto, F. Silva, M. Fredel, D. Fabris, J. Souza, O. Carvalho, On the mechanical properties of monolithic and laminated nanoceramic resin structures obtained by laser printing, *Compos. Part B*, 141 (2018), pp. 76-83
- Kroll E., D. Artzi, Enhancing aerospace engineering students' learning with 3D printing wind-tunnel models, *Rapid Prototype. J.*, 17 (5) (2011), pp. 393-402
- Liew L.A., Read D.T., White R.M., Barbosa N.: U.S. Army ARDEC Joint Fuze Technology Program (JFTP) Task 2 report: quasi-static tensile tests of microfabricated electrodeposited (LIGA) Ni alloys. NIST interagency report 8182, (2018).<https://doi.org/10.6028/NIST.IR.8182>
- Malik H.H., A.R. Darwood, S. Shaunak, P. Kulatilake, A. Abdulrahman, O. Mulki, A. Baskaradas, Three-dimensional printing in surgery: a review of current surgical applications, *J. Surg. Res.*, 199 (2) (2015), pp. 512-522
- Marsavina L., Valean C., Marghitas M., Linul E., Javad Razavi S.M., Berto F., Brighenti R., 2022. Effect of the manufacturing parameters on the tensile and fracture properties of FDM 3D-printed PLA specimens, *Engineering Fracture Mechanics*, 274, 108766.
- Mulford J.S., S. Babazadeh, N. Mackay, Three-dimensional printing in orthopaedic surgery: review of current and future applications, *ANZ J. Surg.*, 86 (9) (2016), pp. 648-653
- Rauch E.F., The flow law of mild steel under monotonic or complex strain path, *Solid State Phenom.*, 23–24 (1992), pp. 317-333
- Rauch E.F., Plastic anisotropy of sheet metals determined by simple shear tests, *Mater. Sci. Eng. A*, 241 (1998), pp. 179-183
- Song Y., Li Y., Song W., Yee K., Lee K.Y., Tagarielli V.L., Measurements of the mechanical response of unidirectional 3D-printed PLA, *Mater Des*, 123 (2017), pp. 154-164
- Valean C., Marsavina L., Marghitas M., Linul E., Javad Razavi S.M., Berto F., 2020. Effect of manufacturing parameters on tensile properties of FDM printed specimens, *Procedia Structural Integrity*, 26, 313-320.
- Ziemian C, Sharma M, Ziemian S. Anisotropic mechanical properties of ABS parts fabricated by fused deposition modelling. In: Gokcek M, editor. *Mechanical engineering*, InTech, 2012 159–180
- Zhang P., D.J. Arceneaux, Z. Liu, P. Nikaen, A. Khattab, G. Li, A crack healable syntactic foam reinforced by 3D printed healing-agent based honeycomb, *Compos. Part B*, 151 (2018), pp. 25-34



Structural Integrity and Reliability of Advanced Materials obtained through Additive Manufacturing (SIRAMM23)

The influence of wall thickness on the fracture toughness of short fiber reinforced polymers obtained using single edge cracked test specimens

Alexandru Isaincu^{a,*}, Dan Micota^b, Liviu Marsavina^b, Viorel Ungureanu^a

^aPolitehnica University of Timișoara, Department of Steel Structures and Structural Mechanics, Ioan Curea, No. 1, Timișoara 300224, Romania

^bPolitehnica University of Timișoara, Department of Mechanics and Strength of Materials, Mihai Viteazul Blvd, No. 1, Timișoara 300222, Romania

Abstract

In this paper, the fracture behavior of two short fiber reinforced polymers is discussed. The two investigated materials are polyphthalamide (PPA) with glass fiber inclusions of 33% (GF33) and polyphenylene sulfide (PPS) with glass fiber inclusions of 40% (GF40). Due to the highly anisotropic behavior of these types of materials, most of the mechanical properties, including fracture toughness, are dependent on the fiber orientation. One parameter that directly affects the fiber orientation is the wall thickness. Single edge crack (SEC) test specimens were used to determine the cracking force under mode I (opening mode) loading conditions. The specimens were milled from plates at different orientations. Three fiber orientations were considered: 0°, 45° and 90°. Two different thicknesses of the plates were used: 2.0 mm and 3.2 mm.

© 2023 The Authors. Published by Elsevier B.V.

This is an open access article under the CC BY-NC-ND license (<https://creativecommons.org/licenses/by-nc-nd/4.0>)

Peer-review under responsibility of the SIRAMM23 organizers

Keywords: Fracture toughness; short fiber reinforced polymers; polyphthalamide; polyphenylene sulfide.

* Corresponding author. Tel.: +40-720-75-7935.

E-mail address: Alexandru.isaincu@student.upt.ro

1. Introduction

High performance engineering polymers with glass fiber reinforcement are more often than ever used in the automotive industry. The harsh requirements arising from the automotive industry are transferred to the material manufacturer. One of the main advantages of these types of materials is good mechanical properties compared with the density. A lightweight component can result in the end. A second advantage is that mass scaled production using complex shapes and low production costs can be achieved. These materials can be seen in chassis and suspension load bearing applications as well as traditional powertrain component applications.

Understanding how these types of materials work and what are the limitations in terms of performance is required for an efficient design.

Nomenclature

PPA	polyphthalamide
GF33	33% glass fiber inclusions
PPS	polyphenylene sulfide
GF40	40% glass fiber inclusions
SEC	single edge crack
SFRP	short fiber reinforced polymers
t	thickness of the single edge notch specimen
L	length of the single edge notch specimen
b	width of the single edge notch specimen
a	notch length/depth
h	gripping distance of the single edge notch specimen
SIF	stress intensity factor of a crack
K_I	mode I stress intensity factor
K_{Ic}	mode I fracture toughness

The aim of this work is to investigate the influence of fiber orientation and material thickness on the fracture toughness of PPA GF33 and PPS GF40 materials determined on SEC specimens. The effects on the mechanical behavior due to the fiber orientation was studied extensively in Holmström, Hopperstad and Clausen (2020), Bernasconi et al. (2007) and many others.

When it specifically comes to fracture toughness, a small number of studies were published for SFRP. For PPS, some values of fracture toughness can be found in Friedrich (1985); Karger-Kocsis and Friedrich (1987), Tanaka, Kitano and Egami (2014). Determining and understanding fracture toughness is extensively presented in Nelson, Li and Kamada (2002) Ramirez, Carlsson and Acha (2009), Soderholm (2010), Limited (2012) Garcia-Manrique et al. (2018). The fracture toughness of these two particular materials was previously determined using edge crack triangular specimen in Isaincu, Micota and Marsavina (2022).

In this paper, the fracture toughness of PPA GF33 and PPS GF40 is studied by means of physical testing and analytical interpretation.

2. Experimental details

2.1. Materials

Two SFRP are considered for this study: a PPA with 33% glass fiber content and a PPS with 40% glass fiber. The materials are provided by the Solvay Group and can be found on the market under the trade name Amodel AE-4133 and Ryton R-4-270 respectively. The amount of fiber, in terms of percentage, refers to the weight of the composite. The average dimension of a fiber, according to the material supplier, is in the range of 10 μm for the diameter and 200 μm for the length. The distribution fiber length probability density versus fiber length for a similar material can be

seen in Fu et al. (2001). The shape of the fibers was presented in Isaincu, Micota and Marsavina (2022) by using a scanning electron microscope. Both materials are part of the thermoplastic branch of polymers. A semi-crystalline structure can be found in both materials.

2.2. Sample preparation

Single Edge Crack (SEC) specimens were prepared for the fracture tests. They were obtained by water jet cutting from injected larger plates. The nominal dimensions of 3.2 mm (1/8 of an inch) thick plates are 100 mm length by 100 mm width. The nominal dimensions of 2.0 mm thick plates are 100 mm length by 80 mm width. These plates were directly delivered by the Solvay Group. The plates were obtained by injection molding with the aim of achieving a good and uniform fiber orientation in the middle of the plate. This is required in order to obtain specimens at different fiber orientation angles.

The dimensions of SEC specimens, together with the dimensions of the plates from where they were obtained, are presented in Fig. 1.

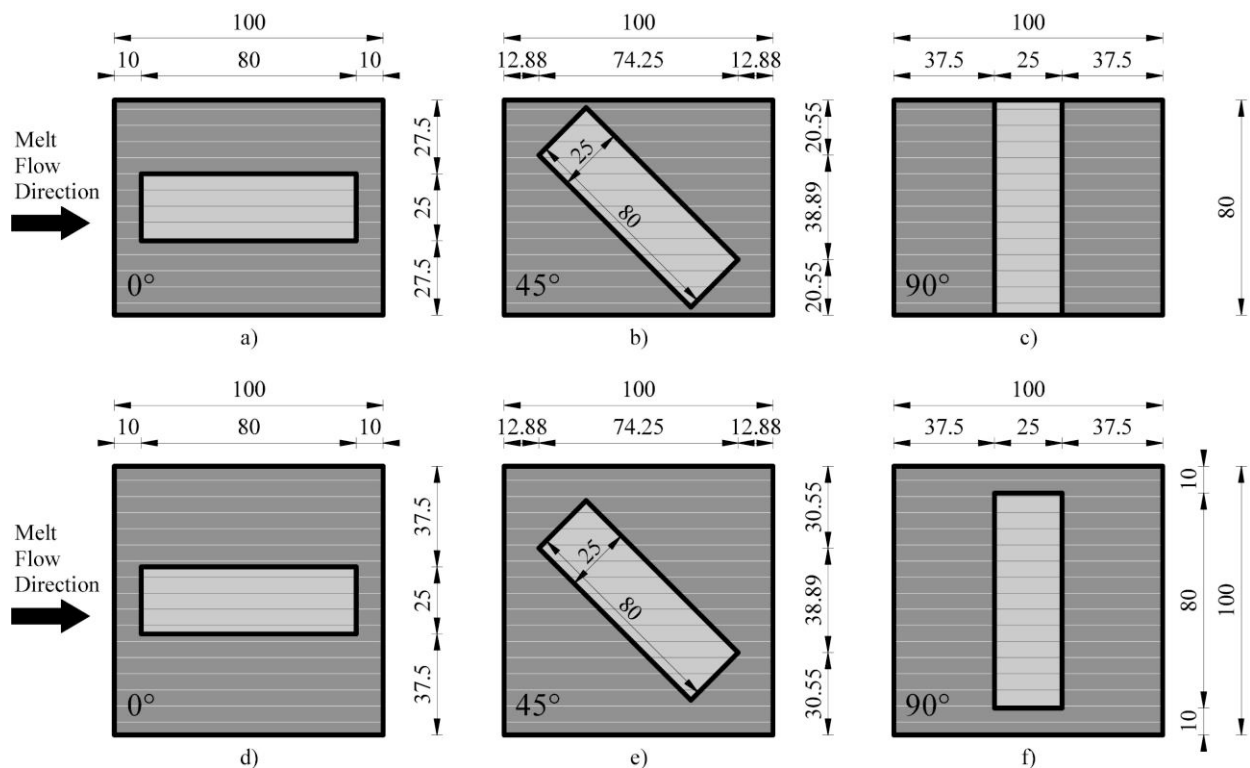


Fig. 1. Specimen cutting from the original plates considering an orientation angle of (a)/(d) 0°, (b)/(e) 45° and (c)/(f) 90°. The first row of plates corresponds to 2.0 mm thickness. The second row of plates corresponds to 3.2 mm thickness.

For both thicknesses (t), the nominal length (L) of SEC specimen is 80 mm. The width (b) is 25 mm. The notch was manually cut using a vertical bandsaw machine. The depth/length of the notch (a) is 15 mm. A cutter was used to create a sharp indentation insight the specimen (in order to facilitate a better stress concentrator). An important aspect for SEC test specimens is the ratio between a and b . In the current study, this value was kept constant at 0.6 ($a=15$ mm / $b=25$ mm). The final shape and dimensions of the specimens are depicted in Fig. 2.

Note that there is a difference between the probe fiber orientation angle, relative to the melt flow and probe fiber orientation angle to the crack orientation. In this study, the orientation is described as the angle between fiber

orientation and crack orientation. This remark is important if the results are compared with different shapes of the specimen in which the fiber orientation angle relative to the melt flow is not visible.

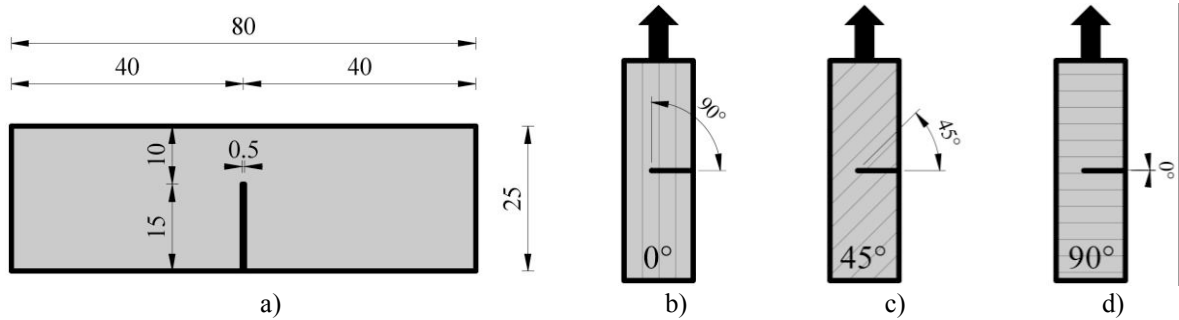


Fig. 2. a) SEC specimen dimensions and the fiber orientation angle in relation to crack orientation for 90° in b), for 45° in c) and for 0° in d).

2.3. Tensile tests on dog bone specimens

To characterize the behavior of the two materials, tensile tests were performed on dog bone specimens. The testing was performed according to ISO 527. Type 1BA specimens were cut from the previous mentioned plates as for SEC specimens. The tensile tests were performed for both thicknesses of the materials. The following orientation angles were considered for testing: 0°, 15°, 30°, 45°, 60° and 90°. An overview of the mechanical properties can be found in Micota, Isaincu and Marşavina (2021). The main properties are presented in Table 1.

Table 1. Mechanical properties for PPA GF33 and PPS GF40 for two thicknesses (2.0 mm and 3.2 mm).

Material	Thickness [mm]	Orientation Angle [°]	Young's Modulus [MPa]	Tensile Strength [MPa]	Strain at break [%]
PPA GF33	2.0	0	11698	186.4	2.20
		45	6510	110.4	5.13
		90	5616	96.0	5.02
	3.2	0	8996	146.6	2.83
		45	6980	125.2	3.74
		90	6363	111.3	3.57
PPS GF40	2.0	0	15923	194.6	1.56
		45	8649	121.2	2.17
		90	7385	98.4	1.79
	3.2	0	11693	134.1	1.45
		45	9051	105.8	1.45
		90	9191	98.3	1.28

A clear decrease in rigidity, resistance and ductility in between the two thicknesses can be distinguished for both materials.

2.4. Tensile tests on SEC specimens

To investigate the toughness of the two materials, a series of tensile tests were performed on SEC specimens. These tests were conducted under mode I (crack opening) loading conditions. All tests were conducted at room temperature ($\approx 20^\circ\text{C}$) and in normal humidity conditions (50% R.H.). A vertical tensile force (F) was applied up to fracture. A

universal testing machine, Zwick Roell Z005, was used. The speed of the testing equipment was set to 5 mm/min. The distance in between the jaw grips was kept around 50 mm. The test setup is presented in Fig. 3 a).

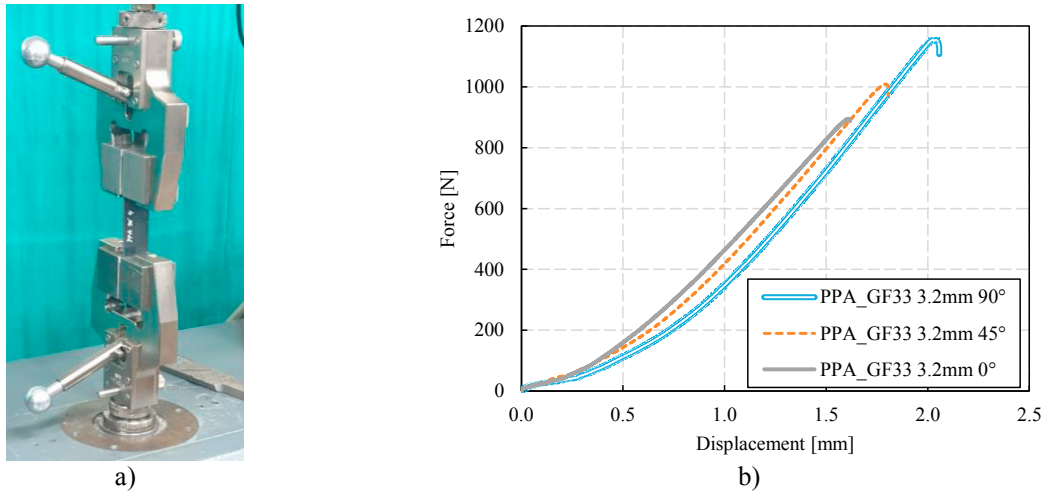


Fig. 3. Test setup of SEC specimen a) and typical force-displacement curves b).

Two materials (PPA GF33 and PPS GF40), with two thicknesses (2.0 mm and 3.2 mm) and three orientations (0° , 45° and 90°) were considered. For each case, a set of 5 specimens were investigated. In the end, a set of 60 specimens were tested.

3. Experimental results and analytical interpretation

The main parameter that was measured during testing was the breaking force. For both materials and both thicknesses, the failure is brittle. This aspect can also be noticed in Fig. 5 b). In the beginning of the test, there is a slight slippage until the force increases and the jaws grip the probe more firmly. After that point, a linear behavior can be seen until failure. This is similar for both materials. An overview of all breaking forces is presented in Fig. 4.

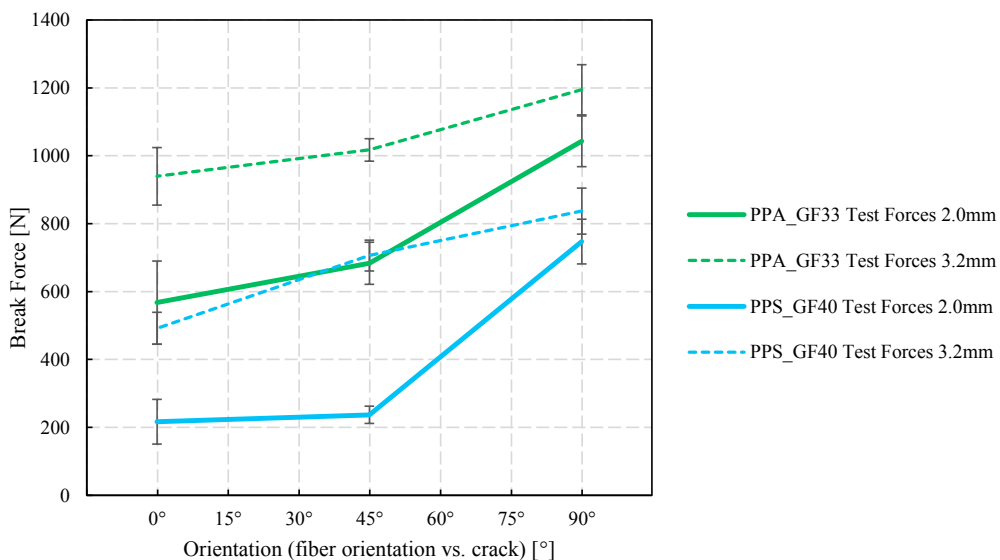


Fig. 4. Breaking force for PPA GF33 and PPS GF40 function of material thickness.

The breaking forces are increasing with the orientation angle. Lower forces are obtained when the crack is parallel with the fibers (0° orientation). An increase in force can be observed, in all orientations, if a higher thickness is considered. A more constant transition can be seen in terms of force for a higher thickness. This aspect is due to a higher randomized fiber orientation in the specimens that will provide a higher isotropic behavior. The fibers are strongly orientated for the 2.0 mm case and will lead to a higher orthotropic behavior. This is especially visible for PPS GF40 with 2.0 mm thickness. A substantial change in force obtained for 0° and 45° to 90° orientation can be distinguished. All previously mentioned trends can be noticed for both materials. Overall, higher forces can be seen for PPA GF33, in comparison with PPS GF40.

The Stress Intensity Factors (SIF's) solution in mode I (K_I) are defined as follows:

$$K_I = \sigma \sqrt{\pi a} \cdot F\left(\frac{a}{b}\right) \tag{1}$$

In formula (1), σ is the applied stress and $F(a/b)$ is a geometrical function that depends on notch length/depth (a) and the width of SEC specimen (b). The maximum breaking force was used to compute the applied stress. For the geometrical function, many variations can be observed in the literature. In this study, the following formula was used:

$$F\left(\frac{a}{b}\right) = \sqrt{2b/\pi a \cdot \tan(\pi a/2b)} \cdot \frac{0.752 + 2.020 \cdot (a/b) + 0.370 \cdot (1 - \sin(\pi a/2b))^3}{\cos(\pi a/2b)} \tag{2}$$

The formula references derive from Tada, Paris and Irwin (2000), they suggested that relation (2) applies also for anisotropic materials in order to estimate the stress intensity factors. Based on the breaking force, the fracture toughness (K_{Ic}) was computed for different orientations. The obtained results are presented in Fig. 5 for both materials.

The influence of fiber orientation relative to crack orientation can be noticed for both materials and thicknesses. A decrease in fracture toughness with the decrease in orientation angle can be distinguished. This outcome is due to the higher degree of energy required by the crack to develop at 90° in order to fracture, split and pull the fibers. For the 0°, the crack develops through the matrix and the fibers have a lower contribution.

The amplitude of the orientation decrease is dependent on the material thickness. This situation is explained by the level of isotropy in the specimens. The 3.2 mm thick specimens are closer to an isotropic behavior than the 2.0 mm specimens. This aspect occurs due to the injection molding process that will align the fibers in a more uniform direction if the thickness is smaller, Amjadi and Fatemi (2020).

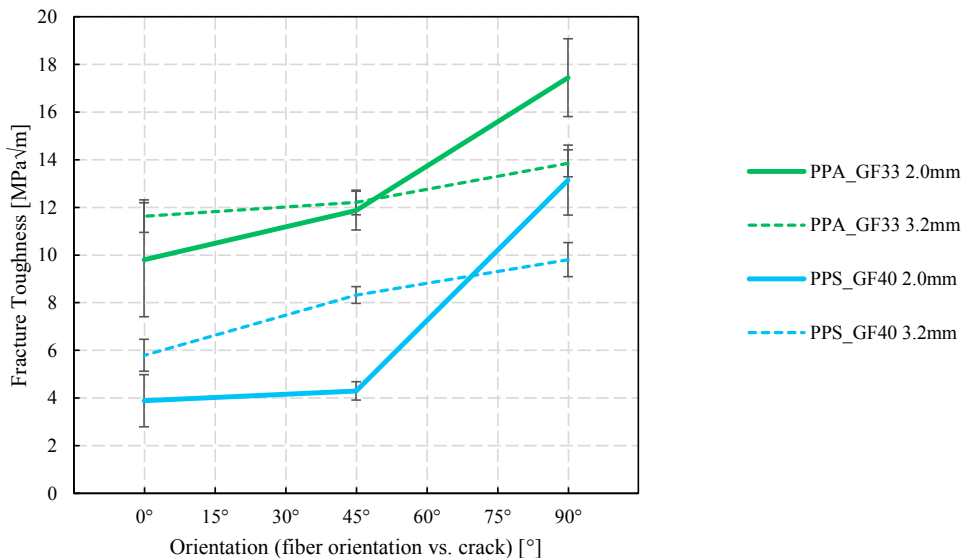


Fig. 5. Fracture toughness function of orientation and thickness.

With the increase of material thickness, a smoothing effect of the fracture toughness along the orientation (the variation in between 0° and 90° orientation is smaller for the 3.20 mm thick specimens) can be distinguished. The difference between the 0° and 90° orientation will decrease and will tend to converge to a single value (similar to an isotropic material), if the thickness increases further. For both materials, the average fracture toughness (computed using the 0°, 45° and 90° orientation) has similar values regardless of the thickness (PPA GF33: for 2.0 mm thickness, the value is 13.04 MPa √m and for 3.2 mm thickness, the value is 12.57 MPa √m; PPS GF40: for 2.0 mm thickness, the value is 7.11 MPa √m and for 3.2 mm thickness, the value is 7.97 MPa √m). Based on these values, it can be concluded that the fracture toughness tends to flatten out around the average value obtained using the 0°, 45° and 90° orientation with the increase of material thickness.

The orientation effect is much stronger for higher fracture of glass fiber content. This can be seen especially for the PPS GF40, when considering the 2.0 mm thickness. The values obtained for the 0° and 45° orientation are much closer. A significant increase for the 90° orientation can be noticed afterwards. For both materials, the predictions arising from 2.0 mm thick specimens do not coincide with the ones arising from 3.2 mm. For PPA GF33, an overlap at 45° orientation can be noticed. This statement is not valid for PPS GF40, the value at 3.2 mm is approximately two times higher, compared to the value at 2.0 mm (8.3 MPa √m, compared to 4.3 MPa √m). The fracture toughness will be higher for 3.2 mm thick specimens, at 0° and 45° orientation and lower for 90° orientation, in comparison with 2.0 mm thick specimens.

Equation (3) was used to predict and compare the fracture toughness at 45° orientation, based on the 0° and 90° values. The formula is raised in (Kfoury 1996).

$$\frac{1}{K_{IC}(\theta)^2} = \frac{\cos^2 \theta}{K_{IC}(0^\circ)^2} + \frac{\sin^2 \theta}{K_{IC}(90^\circ)^2} \quad (3)$$

The results are presented in Table 2. Different results for the two materials were obtained. In the case of PPA GF33, the results match precisely with the values obtained using equation (1). Differences of 2% - 3% can be seen for both thicknesses. For PPS GF40, the prediction is not reliable. For 2.0 mm thickness, an overestimation of 23% can be distinguished. For 3.2 mm thickness, an underestimation of 15% can be distinguished.

Table 2. Fracture toughness comparison for 45° orientation.

Material	Thickness [mm]	Eq. (1) [MPa√m]	Eq. (3) [MPa√m]	Difference [%]
PPA GF33	2.0	11.9	12.1	2%
	3.2	12.2	12.6	3%
PPS GF40	2.0	4.3	5.3	23%
	3.2	8.3	7.1	-15%

4. Conclusions and discussions

The current paper investigated the effects of thickness and orientation of two short fiber reinforced polymers (PPA GF33 and PPS GF40) on fracture toughness. In this direction, a set of tensile tests on SEC specimens were performed to determine the breaking force. An analytical approach was used to determine the fracture toughness of the materials based on the test results.

The main conclusions that can be deduced from this study are the following:

- The results in terms of breaking force have a relatively high spread. The notch was manually cut using a vertical bandsaw machine, that led to an inconsistent and irregular crack on all specimens. Nevertheless, both effects of thickness and orientation can be noticed in terms of reaction forces for both materials.
- Increasing the material thickness of the specimen will lead to uneven change in fracture toughness at different orientations. For 0° and 45° orientations, an increase in fracture toughness can be identified, opposite to the case for 90° orientation, where a decrease trend can be observed. This phenomenon is similar for both

materials. A higher thickness of the material will tend to flatten the curve around the average value. Considering the plain strain theory for the fracture toughness, an increase in thickness should provide lower values. For this type of materials, an increase in thickness will be followed by a differential change in material properties at different orientations (check Table 1 for values). Therefore, there is an inconsistent decrease in fracture toughness when comparing the results obtained for 2.0 mm and 3.2 mm.

- The trend of the fracture toughness is to increase with the increase in orientation angle. This aspect occurs regardless of thickness. The orientation effect has a substantial contribution for the specimens with 2.0 mm thickness, in comparison with the 3.2 mm thickness specimens. This remark is especially visible for PPS GF40. The values obtained at 0° and 45° orientations are particularly similar.
- As a general tendency, by increasing the specimen thickness, the amount of anisotropy ($K_{Ic,90} - K_{Ic,0}$) is decreasing for both materials.

Acknowledgement

The work leading to this paper was partially supported by InoHubDoc project POCU/993/6/13/153432 and by the European Union's Horizon 2020 research and innovation program (H2020-WIDESPREAD-2018, SIRAMM), under grant agreement no. 857124. Results were disseminated in the SIRAMM project, final conference SIRAMM 23 in Timisoara, Romania. Special acknowledgement to the Solvay Group for providing the two materials and support. Recognition is also extended to Vitesco Technologies company for support in specimen elaboration.

References

- Amjadi, Mohammad, and Ali Fatemi. 2020. "Tensile Behavior of High-Density Polyethylene Including the Effects of Processing Technique, Thickness, Temperature, and Strain Rate." *Polymers* 12(9).
- Bernasconi, A., P. Davoli, A. Basile, and A. Filippi. 2007. "Effect of Fibre Orientation on the Fatigue Behaviour of a Short Glass Fibre Reinforced Polyamide-6." *International Journal of Fatigue* 29(2): 199–208.
- Friedrich, K. 1985. "Microstructural Efficiency and Fracture Toughness of Short Fiber/Thermoplastic Matrix Composites." *Composites Science and Technology* 22(1): 43–74.
- Fu, Shao Yun, Chee Yoon Yue, Xiao Hu, and Yiu Wing Mai. 2001. "Characterization of Fiber Length Distribution of Short-Fiber Reinforced Thermoplastics." *Journal of Materials Science Letters* 20(1): 31–33.
- Garcia-Manrique, J., D. Camas-Peña, J. Lopez-Martinez, and A. Gonzalez-Herrera. 2018. "Analysis of the Stress Intensity Factor along the Thickness: The Concept of Pivot Node on Straight Crack Fronts." *Fatigue and Fracture of Engineering Materials and Structures* 41(4): 869–80.
- Hiroshi Tada, Paul C. Paris, and George R. Irwin. 2000. "Stress Analysis Results for Common Test Specimen Configurations." In *The Stress Analysis of Cracks Handbook, Third Edition*, ASME Press, 39–80.
- Holmström, Petter Henrik, Odd Sture Hopperstad, and Arild Holm Clausen. 2020. "Anisotropic Tensile Behaviour of Short Glass-Fibre Reinforced Polyamide-6." *Composites Part C: Open Access* 2: 100019.
- Isaincu, Alexandru, Dan Micota, and Liviu Marsavina. 2022. "On the Fracture Toughness of PPS and PPA Reinforced with Glass Fiber." *Procedia Structural Integrity* 41(C): 646–55. <https://doi.org/10.1016/j.prostr.2022.05.073>.
- Karger-Kocsis, J., and K. Friedrich. 1987. "Microstructural Details and the Effect of Testing Conditions on the Fracture Toughness of Injection-Moulded Poly(Phenylene-Sulphide) Composites." *Journal of Materials Science* 22(3): 947–61.
- Kfour, A. P. 1996. "CRACK EXTENSION UNDER MIXED-MODE LOADING IN AN ANISOTROPIC MODE-ASYMMETRIC MATERIAL IN RESPECT OF RESISTANCE TO FRACTURE." *Fatigue & Fracture of Engineering Materials & Structures* 19(1): 27–38. <https://onlinelibrary.wiley.com/doi/10.1111/j.1460-2695.1996.tb00929.x>.
- Limited, Woodhead Publishing. 2012. "Fracture Toughness Properties of Aerospace Materials." *Introduction to Aerospace Materials*: 454–68.
- Micota, Dan, Alexandru Isaincu, and Liviu Marşavina. 2021. "Experimental Testing of Two Short-Fiber Reinforced Composites: PPA-GF33 and PPS-GF40." *Material Design and Processing Communications* 3(6): 2–8.
- Nelson, Patricia Kim, Victor C. Li, and Toshiro Kamada. 2002. "Fracture Toughness of Microfiber Reinforced Cement Composites." *Journal of Materials in Civil Engineering* 14(5): 384–91.
- Ramirez, F. A., L. A. Carlsson, and B. A. Acha. 2009. "A Method to Measure Fracture Toughness of the Fiber/Matrix Interface Using the Single-Fiber Fragmentation Test." *Composites Part A: Applied Science and Manufacturing* 40(6–7): 679–86.

<http://dx.doi.org/10.1016/j.compositesa.2009.04.011>.

Soderholm, Karl Johan. 2010. "Review of the Fracture Toughness Approach." *Dental Materials* 26(2): 63–77.

Tanaka, Keisuke, Takuya Kitano, and Noboru Egami. 2014. "Effect of Fiber Orientation on Fatigue Crack Propagation in Short-Fiber Reinforced Plastics." *Engineering Fracture Mechanics* 123: 44–58.



Structural Integrity and Reliability of Advanced Materials obtained through Additive Manufacturing (SIRAMM23)

Thermo-Mechanical Simulation of the Powder Bed of Polyamide 12 during the Selective Laser Sintering Process

Hanane YAAGOUBI^{*}, Hamid ABOUCHADI¹, Mourad TAHA JANAN¹

¹Laboratory of Applied Mechanics and Technologies (LAMAT), ENSAM, ST21 Research Center Mohammed V University, Rabat, Morocco

Abstract

The selective laser sintering process is considered to be a new process among the most innovative techniques in the field of additive manufacturing, to facilitate the development and the technical improvement of this process, Thermo-mechanical investigation is necessary to control the SLS process, in this paper a thermo-mechanical simulation of selective laser sintering of polyamide 12 will be presented., this thermo-mechanical simulation was made under the COMSOL Multiphysics software, using Hook's law with the equilibrium and accounting equations for the calculation of the residual stresses appearing in the sintered layer of polyamide 12, this simulation was made for the prevention of deformations appeared in the final printed parts. The calculation of von Mises stress and the calculation of the magnitude of displacement within a sintered layer of polyamide 12 was done, with the analysis of the volumetric strain and the calculation of the volume: stress tensors, principal strain directions.

© 2023 The Authors. Published by Elsevier B.V.

This is an open access article under the CC BY-NC-ND license (<https://creativecommons.org/licenses/by-nc-nd/4.0>)

Peer-review under responsibility of the SIRAMM23 organizers

Keywords: Thermo-mechanical simulation, Polyamide12, Non linear Mechanical Model, Selective Laser Sintering, Stress, strains.

1. Introduction

An additive manufacturing process called Selective Laser Sintering (SLS) uses a laser to selectively fuse layers of polyamide 12 powder to quickly produce plastic parts directly from a CAD model Amado A.all (2016), Dong, L.all (2007),(2009), Elham.all (2020), Li J (2020), Nevertheless, a melting of the powder layer or thermal stresses caused by large temperature gradients during part construction can lead to residual stresses and defects in SLS parts, Ganci M. all (2017), Nelson, J.all (1993), Xiaoyong (2018), Paolucci F, (2020), Mechanical models of SLS process are rarely found in the literature Roberto.all (2021), To ensure the quality of part production and to enable the use of new materials and designs, without resorting to experimental needs, an accurate thermo-mechanical model of the SLS process is required. In this article, mechanical analysis of the polyamide 12 layer during the laser sintering is carried out using the COMSOL Multiphysics software. a transient three-dimensional finite element thermo-mechanical model is created, in this paper, the results of the mechanical analyses of the polyamide layer sintered by CO₂ laser will be

* Corresponding author.

E-mail address: hanane.yaagoubi@um5s.net.ma

presented.

II. Mechanical Modelling

Solving a thermal problem in the selective laser sintering of polyamide 12 has already been done in our previous articles Yaagoubi.all (2019,2020,2021,2022) , the objective in this study is to solve a mechanical problem amounts to determining the displacement field responding to equilibrium equations and the law of behavior while taking into account the different boundary conditions ,these conditions can be a constraint or an imposed displacement, The equilibrium equations of static coupled with the divergence theorem allow us to obtain Roberto.all (2021):

Nomenclature

SLS Selective laser sintering
 PA12 polyamide 12
 ϵ^e Elastic strains
 ϵ^p Inelastic strains
 E Young's modulus
 ν Poisson rate
 FE Finite Element
 AM Additive Manufacturing

$$\text{div}\sigma(u) + f = 0 \quad (1)$$

With:

- σ : symmetric second-order tensor of Cauchy constraints
- f : vector of internal volume forces.

The boundary conditions as for them, depend on the modelled case. By considering that the strains are infinitesimal, it is possible to use the assumption of additive partition to describe the constitutive laws.

Thus, the tensor of the deformations follows the following equation, Roberto.all (2021):

$$\epsilon = \epsilon^e + \epsilon^{vp} + \epsilon^p + \epsilon^{th} + \epsilon^{pt} \quad (2)$$

With ϵ^e , ϵ^{vp} , ϵ^p , the elastic and inelastic strains respectively, and ϵ^{th} the strain caused by volume changes due to temperature and phase changes. This can be defined using the following formula, Paolucci F.all (2020):

$$\epsilon^{th} = \beta \Delta T \quad (3)$$

Where β is the coefficient of thermal expansion of polyamide.

Table 1. Model parameters using in COMSOL software (yaagoubi.all (2021))

Material property	Value
E Young's modulus	2. 10 ⁹ Pa
Poisson rate ν	0.3
Density ρ	1030 kg/ m ³
Heat capacity Cp	1090 J/kg/K
Thermal conductivity Ke	0.28 W / m k
Power of laser P	1.8 W
Temperature Prehating T ₀	130C°
Convection coefficient h	15 j/sm ² k
Laser radius	1.2 10 ⁻⁴ m

III. Result & Discussion

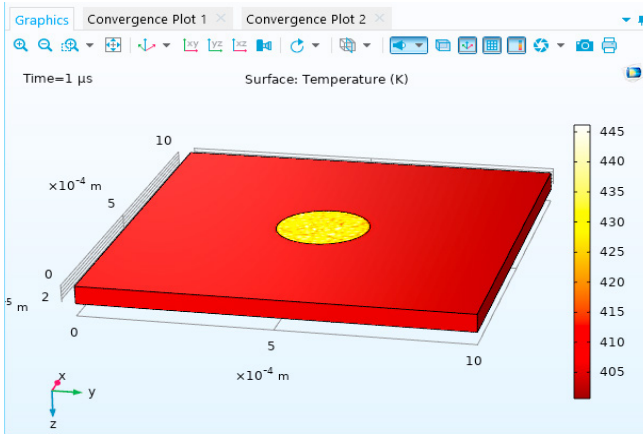


Figure 1 The maximum temperature within a layer of polyamide 12 (K)

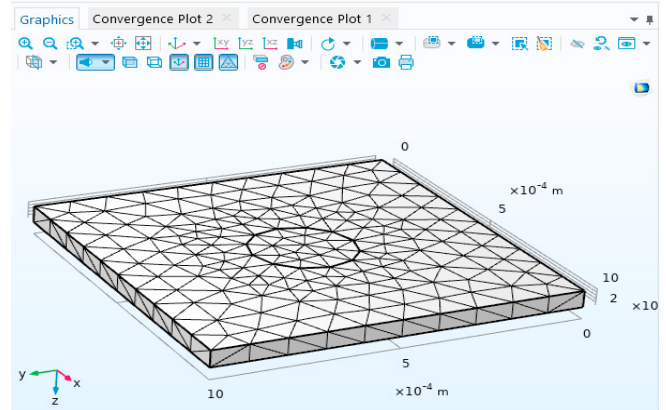


Figure 2 Mesh

The plate is considered to be thick and therefore in a state of plane strain. A layer of polyamide 12 is modelled with a size of $0.001 \text{ m} \times 0.001 \text{ m} \times 0.00005 \text{ m}$ heated by a laser spot with a radius of $1.2 \cdot 10^{-4} \text{ m}$ (figure 1), the coefficients of the physical properties are constant. The physical properties are shown in Table 1 and the mesh statistic are shown in Table 2.

Table 2. Mesh statistics

Mesh statistics	
Description	Value
Minimum element quality	0.2186
Average element quality	0.7054
Tetrahedron	96179
Triangle	13268
Edge element	452
Vertex element	12

Figure 1 shows the maximum temperature within a layer of polyamide 12 which is equal to 445K (170C°) for an instant $t=1\mu\text{s}$, with a preheating temperature of 403K (130C°), this layer is heated by a CO2 laser 1.8W. The geometry of the investigated part is illustrated in Fig. 2 with mesh using a solid mechanics module integrated into COMSOL Multiphysics software.

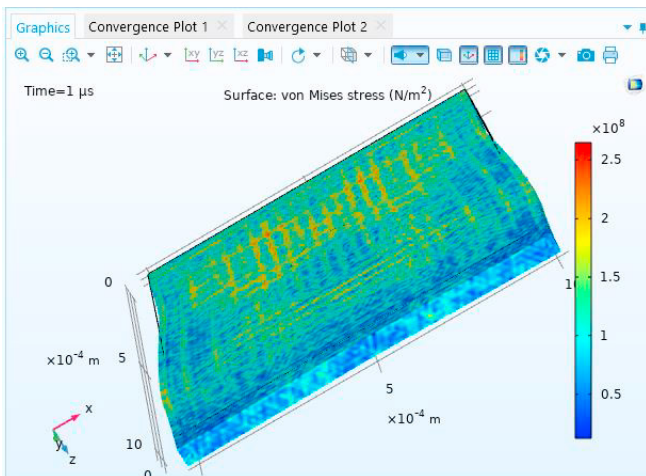


Figure 3 Calculation of von Mises stress

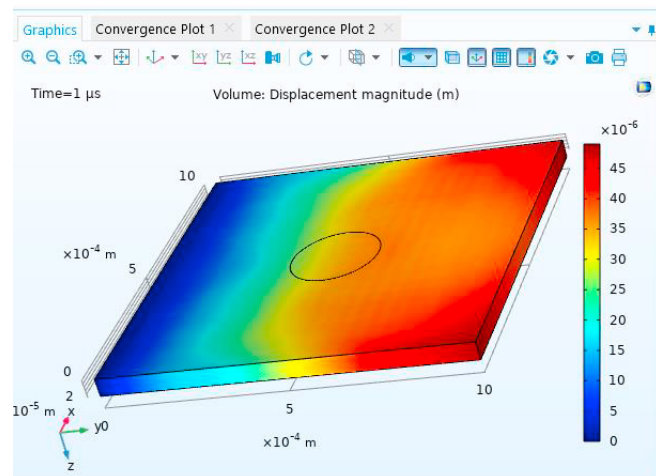


Figure 4 Calculation of the magnitude of displacement (m)

Figure 3 shows the design stress of von Mises stress in a layer of polyamide 12 after laser projection, this value is equal to $2.5 \cdot 10^8 \text{ N/m}^2$.

Figure 4 shows the magnitude of displacements within a layer of polyamide 12 which is equal to $45 \cdot 10^{-6} \text{ m}$.

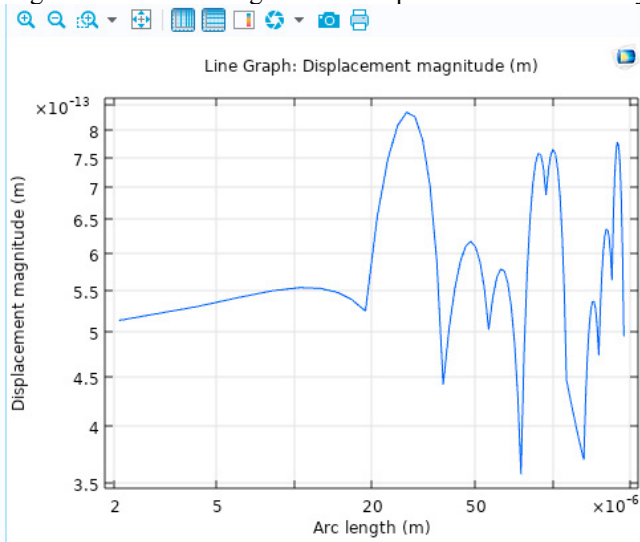


Figure 5 Calculation of displacement on the arc length of the spot laser (m)

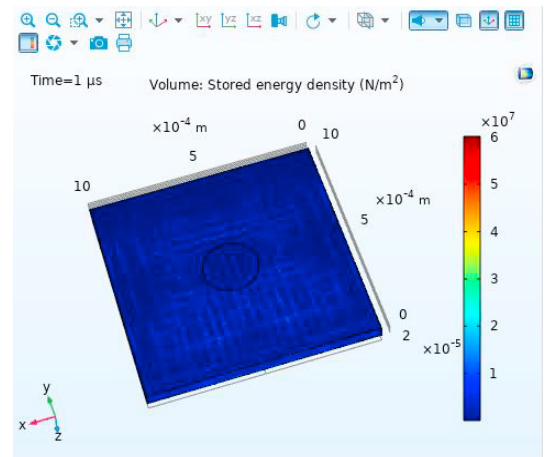


Figure 6 Calculation of stored energy density (N/m²)

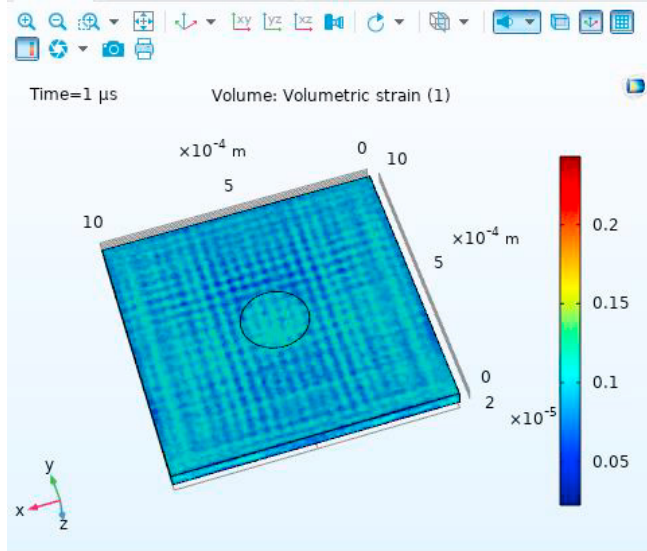


Figure 7 Calculation of the volumetric strain

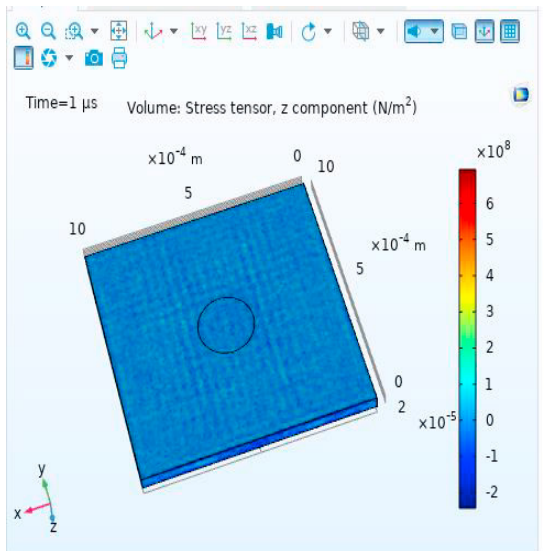


Figure 8 Calculation of the volume: stress tensor, z component (N/m²)

Figure 5 shows analyses of displacement on the arc length of the spot laser. Figure 6 shows the calculation of stored energy density (N/m²) which is equal to $6 \cdot 10^7 \text{ N/m}^2$ Figure 7 shows the calculation of the volumetric strain which is equal to 0.2, figure 8 shows the calculation of the volume: stress tensor, z component (N/m²). Which is equal to $6 \cdot 10^8 \text{ N/m}^2$.

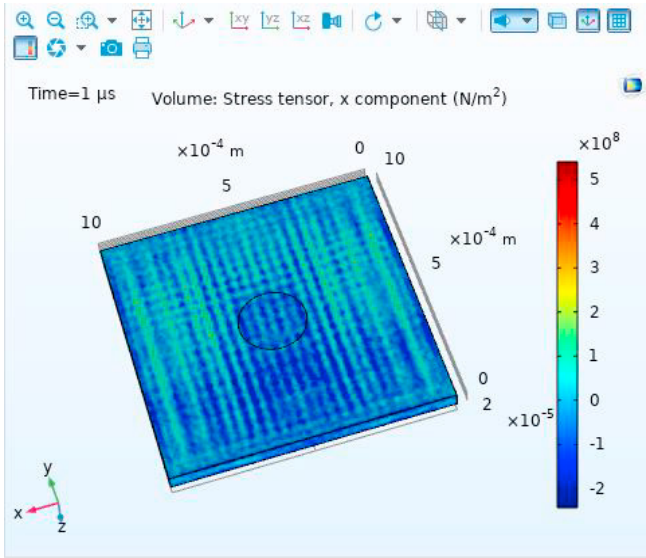


Figure 9 Calculation of the volume: stress tensor, x component (N/m²)

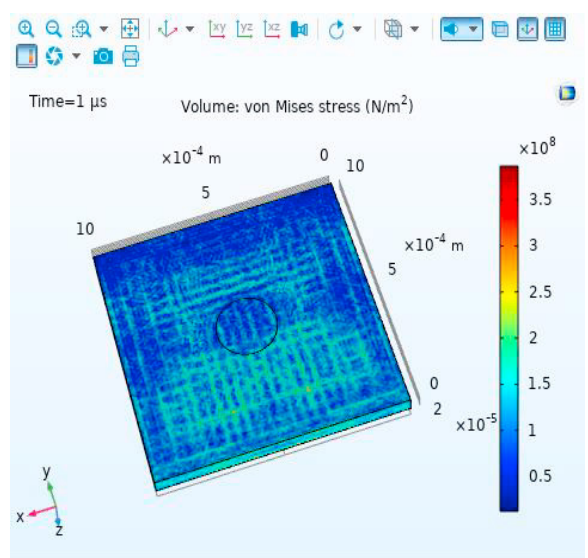


Figure 10 Calculation of the volume of von Mises stress (N/m²)

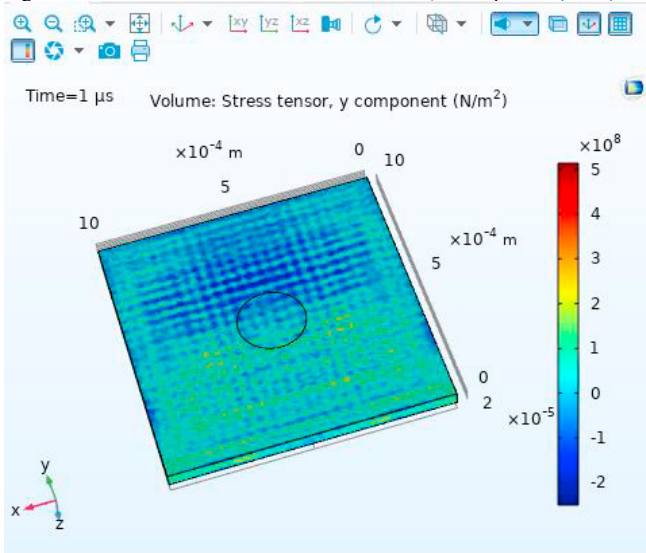


Figure 11 Calculation of the volume: stress tensor, y component (N/m²)

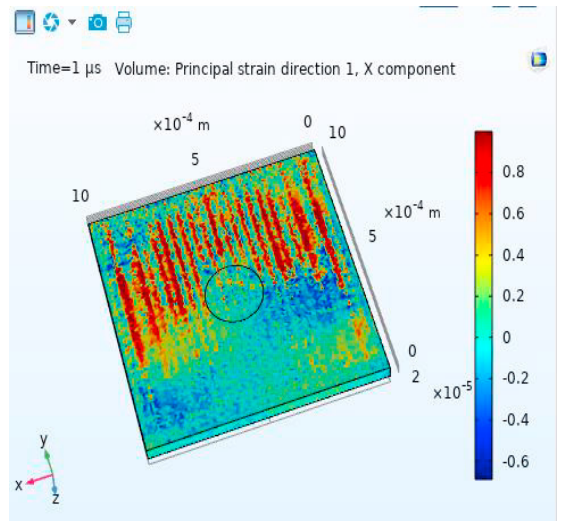


Figure 12 Calculation of the volume: direction of principal strain direction 1, component X.

Figure 9 shows the calculation of the volume: stress tensor, x component, which is equal to $5 \cdot 10^8 \text{ N/m}^2$. Figure 10 shows the calculation of the volume of von Mises stress which is equal to $3.5 \cdot 10^8 \text{ N/m}^2$, figure 11 shows the calculation of volume: stress tensor, y component which is equal to $5 \cdot 10^8 \text{ N/m}^2$. Figure 12 shows the calculation of volume: direction of principal strain direction 1, component X. which is equal to 0.8.

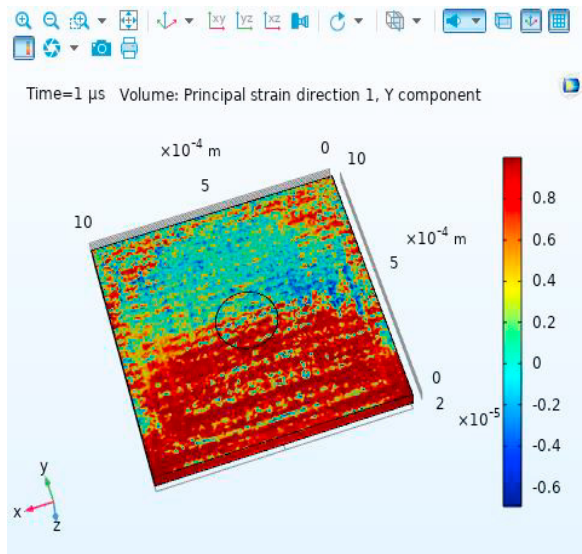


Figure 13 Calculation of the volume: principal strain direction 1, y component

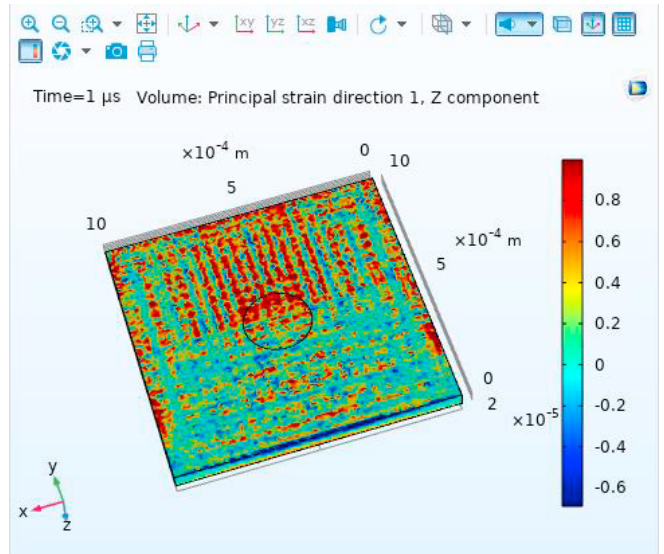


Figure 14 Calculation of the volume: principal strain direction 1, z component

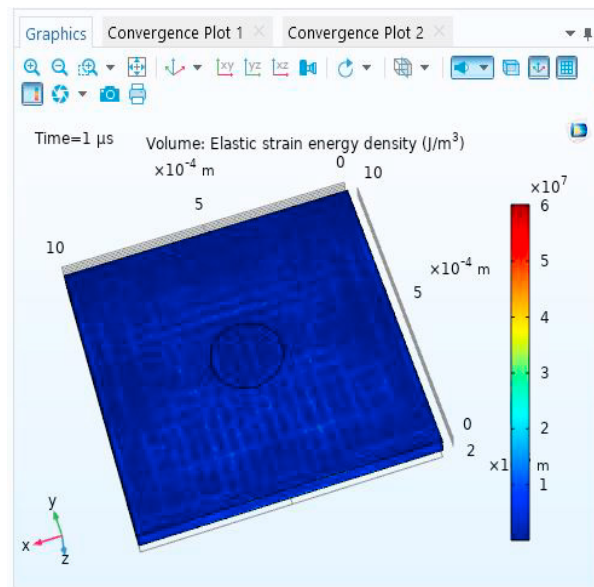


Figure 15 volume: Elastic strain energy density(J/m^3) Component

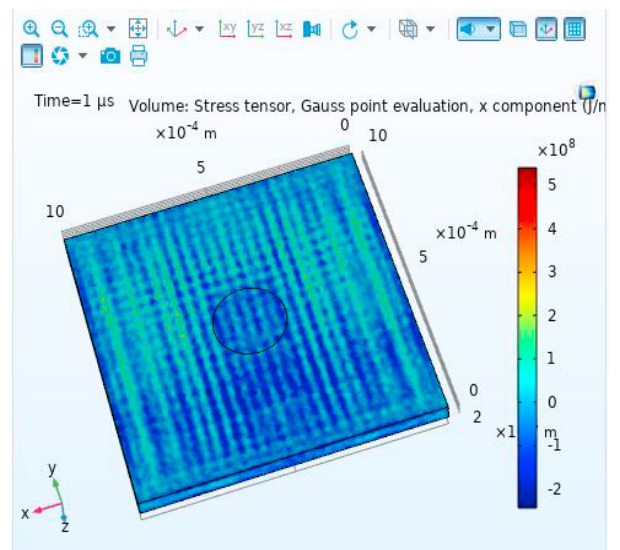


Figure 16 Volume: Stress tensor, Gauss point evaluation $x (J/m^3)$

Figure 13 shows the calculation of volume: principal strain direction 1, y component that is equal to 0.8 figure 14 shows the calculation of volume: principal strain direction 1, z component that is equal to 0.8 Figure 15 shows the calculation of volume: Elastic strain energy density which is equal to $6 \cdot 10^7 J/m^3$. Figure 16 shows volume calculation: Stress tensor, Gauss point evaluation component, which is equal to $5 \cdot 10^8 J/m^3$.

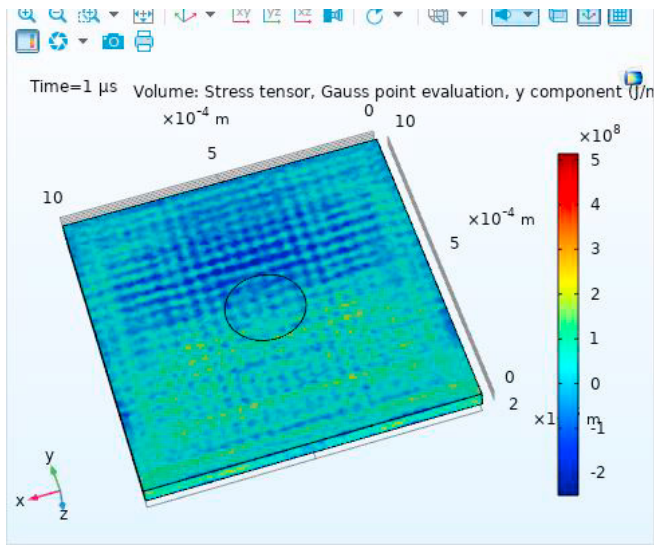


Figure 17 Volume calculation: Stress tensor, Gauss point evaluation, Y component (J/m^3).

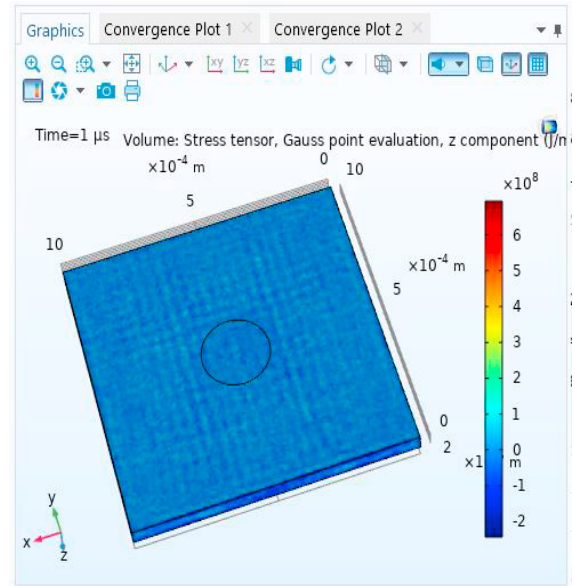


Figure 18 Volume calculation : Stress tensor, z component (N/m^2) stresses, Z component (J/m^3)

After our analysis, we remark when the temperature decreases the magnitude of displacement and the stress of von Mises also decreases. In our results, the von Mises stresses and the magnitude of displacement in a polyamide 12 layer heated by a CO_2 laser was calculated using the COMSOL V5.6 software. The proposed simulation is extremely valuable as it provides a fast and accurate prediction of the stress state in construction. This modelling aims to predict the stresses in the polyamide 12 layer. The proposed thermo-mechanical simulation will be validated by experimental work in the future. This study shows that thermal stresses appear during the laser projection; in particular when the laser beam heats the surface, as known the thermal stresses are in compression (negative values) due to the thermal expansion of the upper part of the layer and during cooling, the thermal stresses become in tension (positive values) due to removal of the upper part Elham.all (2020), The normal stress component (σ_{yy}) (Fig 17) and the longitudinal stress components (σ_{xx}) is small compared to transverse (σ_{zz}) stress components; we show the numerical results of the longitudinal (σ_{xx}) and transverse transient (σ_{zz}) stresses over the surface (Fig. 16, 18), the maximum values during the time history (1us) are $5 \cdot 10^8$ (J/m^3) for the longitudinal direction and $6 \cdot 10^8$ (J/m^3) for the transverse direction transforming into compressive stresses at approximately 0.8 mm deep (Fig. 12).

IV. Conclusion

A physics-based numerical model is proposed to quickly and accurately calculation the stress state and displacement in the additively manufactured part (selective laser sintering of polyamide12, the high computational efficiency of the proposed model makes it a powerful and useful tool for the development of new materials, creation of the new designs, it also allows effective control and optimization of the process parameters to obtain a produced part with high quality. In this modelling, the state of stress is obtained by importing the thermal history as input for residual stress prediction in which in-plane residual stress distributions are obtained from the incremental plasticity and kinematic work hardening behaviour of polyamide12, in coupling with equilibrium and compatibility conditions integrated in mechanics solid module in the COMSOL Multiphysics software. As the rapid irradiation of the laser and the rather low thermal conductivity of the polyamide material, this material undergoes a high-temperature gradient. In this work, the displacement magnitude field is predicted in the polyamide 12 layer, with a calculation of von Mises stresses and different residual stresses, this thermo-mechanical simulation will be used to reduce the deformations that appeared in the final part produced by the SLS process.

References

- Amado A , 2016, Characterization and prediction of SLS processability of polymer powders with respect to powder flow and part warpage. PhD thesis, ETH Zurich.
- Dong, L., Makradi, A., Ahzi, S., & Rémond, Y., 2007, "Finite Element Analysis of Temperature and Density Distributions in Selective Laser Sintering process," Materials Science Forum – Diffusion in Solids and Liquids II, Vol. 553 , pp. 75–80.
- Elham Mirkoohi , Dongsheng Li, Hamid Garmestani , and Steven Y. Liang, 2020 Analytical Modeling of Residual Stress in Selective Laser Melting Considering Volume Conservation in Plastic Deformation, Journal Modelling, Mdpi , 1, 242-259.
- Eyring H (1936) Viscosity, plasticity, and diffusion as examples of absolute reaction rates. J Chem Phys 4(4):283–291.
- Hanane Yaagoubi, Abouchadi Hamid, Mourad Taha JANAN. 2021, " Numerical simulation of heat transfer in the selective laser sintering process of Polyamide12", Energy Reports 7(2):189-199, .
- Hanane Yaagoubi, Abouchadi Hamid, Mourad Taha JANAN , 2019, "A three dimensional meshfree-simulation of the selective laser sintering process with constant thermal coefficients applied to nylon 12 powders", in MATEC Web of Conferences 286(12): 04003 · (January 2019) DOI: 10.1051/mateconf/201928604003.
- Hanane Yaagoubi, Abouchadi Hamid, Mourad Taha JANAN , 2020, "Mathematical study on the relation of energy density and other parameters in the selective laser sintering of polyamide12 and their influences on the quality of the final produced part", April 2020 DOI: 10.1109/ICOA49421.2020.9094498.
- H. YAAGOUBI, H. ABOUCHADI, M. TAHA JANAN , 2021, Simulation of the Heat Laser of the Selective Laser Sintering Process of the Polyamide12, January 2021, E3S Web of Conferences (E3S,Scopus).
- Hanane YAAGOUBI, Hamid ABOUCHADI, Mourad TAHA JANAN ,2020, "Topological Optimization By ANSYS 18.1 For The Additive Manufacturing", The International Conference on Advanced Intelligent Systems for Sustainable Development AI2SD, (Springer , Scopus).
- Hanane Yaagoubi, Abouchadi Hamid, Mourad Taha JANAN , 2020 , "A New Method to Analyze the Quality Characteristics Of 3D Printing Technologies: Production, Time, Cost ", March 2020 DOI: 10.1109/ICEIT48248.2020.9113198.
- Hanane Yaagoubi, Abouchadi Hamid, Mourad Taha JANAN , 2019, " A One-Dimensional Meshfree-Method for Solving Thermal Problems Of Selective Laser Sintering Process Of Polymer Powder". DOI: 10.1109/ICOA.2019.8727660 .
- Hanane Yaagoubi, Abouchadi Hamid, Mourad Taha JANAN , 2019, "A New Method to Analyze the Quality Characteristics Of 3D Printing Technologies: Production, Time, Cost ", March 2020 DOI: 10.1109/ICEIT48248.2020.9113198.
- Hanane Yaagoubi, Abouchadi Hamid, Mourad Taha JANAN , 2021, "Review on the modeling of the laser sintering process for Polyamide 12" , January 2021, E3S Web of Conferences 234:00006 , DOI: 10.1051/e3sconf/202123400006.
- H. Yaagoubi, H Abouchadi, MT Janan,, 2021, "Mathematical modeling and numerical thermal simulation of the selective laser sintering, International Journal on "Technical and Physical Problems of Engineering (IJTPE).
- H. Yaagoubi, H Abouchadi, MT Janan ,2022, "3D mathematical thermal analyses of PA12 powder bed on the SLS process by two numerical methods" International Journal on "Technical and Physical Problems of Engineering (IJTPE).
- Isabella Sani , 2020, Selective Laser Melting process simulation: Advancements Towards A Cost-Effective Model A Thesis submitted in Fulfilment of the Requirements for the Degree of Doctor in Philosophy in Computational Mechanics and Advanced Materials at Istituto Universitario degli Studi Superiori di Pavia, Italy.
- Ganci M, Zhu W, Buffa G, Fratini L, Bo S, Yan C , 2017, A macroscale FEM-based approach for selective laser sintering of thermoplastics. Int J Adv Manuf Technol J Mater Sci 91(9–12).
- L. Dong, A. Makradi, S. Ahzi, Y. Remond, 2009, "Three-dimensional transient finite element analysis of the selective laser sintering process", Journal of Materials Processing Technology, 209(2), 700-706.
- Li J, Yuan S, Zhu J, Li S, Zhang W, 2020, Numerical model and experimental validation for laser sinterable semicrystalline polymer: shrinkage and warping. Polymers 12(6):1373.
- Nelson, J. Christian, Samuel Xue, Joel W. Barlow, Joseph J. Beaman, Harris L. Marcus, and David L. Bourell., 1993, "Model of the selective laser sintering of bisphenol-A polycarbonate" , Industrial & Engineering Chemistry Research.
- Paolucci F, Peters GWM, Govaert LE , 2020, Plasticity controlled failure of sintered and molded polyamide 12: influence of temperature and water absorption. J Appl Polym S.
- Roberto Brighenti, Mattia Pancrazio Cosma, Liviu Marsavina, Andrea Spagnoli & Michele Terzano , 2021, Laser-based additively manufactured polymers: a review on processes and mechanical models Published: 29 September 2020 volume 56, pages961–998 (2021).
- Xiaoyong tian, gang peng , 2018, Process prediction of selective laser sintering based on heat transfer analysis for polyamide composite powders, International Journal of Heat and Mass Transfer.



Structural Integrity and Reliability of Advanced Materials obtained through Additive Manufacturing (SIRAMM23)

Unconventional use of FDM printing method for testing the delamination of PVA material for different layer height

Mina Šibalić^{a*}, Aleksandar Vujović^a, Jelena Šaković Jovanović^a

^a*Faculty of Mechanical Engineering, University of Montenegro, Bulevar Džordža Vašingtona bb, 81000 Podgorica, Montenegro*

Abstract

The necessity to alter the material used for producing specific components has arisen in tandem with technological advancements, specifically in the realm of additive manufacturing. The aim is to enhance both the physical and mechanical attributes of these objects. The newly envisaged materials are anticipated to confer increased durability, resilience, and in some cases, elasticity, thus extending the lifespan and bolstering their utility. Furthermore, environmental considerations dictate that these innovative materials should be amenable to recycling. The ultimate objective of this study is to establish a foundational set of optimal parameters for 3D printing with PVA material. This research will unveil the outcomes of material tensile strength in samples produced using the Fused Deposition Modelling (FDM) technique, with variations in layer height. The focal point of this investigation is PVA material, which will subsequently be augmented with particles of biological origin to create a novel polymer with broader applicability and improved mechanical properties, following future tests.

© 2023 The Authors. Published by Elsevier B.V.

This is an open access article under the CC BY-NC-ND license (<https://creativecommons.org/licenses/by-nc-nd/4.0>)

Peer-review under responsibility of the SIRAMM23 organizers

Keywords: Additive manufacturing; PVA material; FDM method

1. Introduction

Anciently utilized items have found a lasting presence in our contemporary lives thanks to innovative modern materials. Polymers have revolutionized the manufacturing of objects once crafted from wood, transforming them into plastic forms. While numerous scientific studies have delved into the mechanical properties of various filaments, the practice of employing PVA material in conjunction with FDM technology remains relatively uncommon. FDM, stands

* Corresponding author. Tel.: +382-069-330-444;

E-mail address: minasibalic@edu.ucg.ac.me

as one of the earliest 3D printing techniques, involving the extrusion and fusion of materials through a nozzle to construct three-dimensional objects. Typically, FDM leverages polymer-based filaments, with PLA, PETG, and ABS being the most prevalent choices, rendering PVA an unconventional option for FDM printing. Consequently, this research aims to lay the foundation for enhancing the suitability of PVA material for FDM printing. PVA material boasts versatility and finds extensive applications, particularly in the fields of medicine and agriculture (Li, H. et al., 2020). Use of PVA material in medical applications, more precisely in the pharmaceutical industry, since the CAD design ensures the opportunity to add drug-releasing holes into the surface of the carrier, produced from PVA material (Basa B, et al., 2021). PVA is characterized by its hydrophilic nature and exhibits a semi-crystalline planar zig-zag structure (Khoramabadi, N. et al., 2020). Furthermore, PVA demonstrates exceptional chemical and thermal stability, resisting degradation within most physiological settings. Its water-soluble properties, enhanced polarity, non-toxicity, and high biocompatibility render it easily workable. PVA material holds great promise for crafting biodegradable films, though its water-solubility remains a challenge in FDM printing, except in specific cases involving dual-head printers where PVA serves as a support material.

As highlighted in the abstract, this paper's objective is to assess FDM-printed PVA specimens to determine the maximum force threshold. These findings are poised to significantly influence future research endeavors, potentially leading to the development of new bio-polymers derived from PVA material.

In the course of printing test specimens, adjustments were made to the layer thickness, while maintaining constant parameters such as the head and bed temperatures, as well as the specimen's orientation. Table 1. Show the printing parameters that were pre-set in the software, which include printing velocity, bed temperature, and head temperature.

Table 1. Pre-defined parameters.

Head temperature (C)	Bed temperature (C)	Specimen orientation	Printing speed (mm/s)
210	30	90°	30
210	30	90°	30
210	30	90°	30

Table 2. shows the defined values for variable parameters for each number of test parameters.

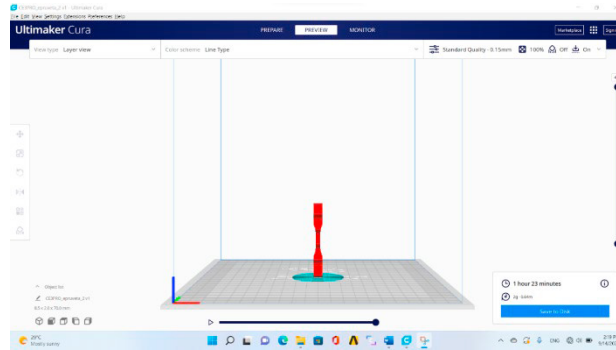
Table 2. Variable parameters for each number of tests.

Number of tests	Layer height (mm)
1	0.1
2	0.15
3	0.2

2. Specimen preparation

The PVA material's susceptibility to instability during FDM printing is evident through increased moisture absorption when exposed to the air for extended periods, resulting in altered mechanical properties. To mitigate this, the material was consistently maintained under similar conditions throughout the testing process. During printing, the filament was stored in a Polybox to maintain a controlled atmosphere. Overnight, the material was subjected to drying at a temperature of 40 degrees Celsius between 6 p.m. and 7:30 a.m. (Šibalić, 2022).

The specimens were printed according to the ISO 527-1:2019 standard, orientation remained consistent to ensure accurate testing, with a focus on determining the maximum force required for the specimen layers to delaminate. As illustrated in Figure 1, the specimens were 3D printed with their layers aligned parallel to the printing bed (the only printing angle that was considered for the testing is 0°). Layer separation, which was observed in this research, referred to as delamination, is a 3D printing issue involving poor layer adhesion.



a)

Fig. 1. Specimen orientation

3. Results

Testing of the adhesion strength between the layers was performed on a stretching machine while the results were digitally recorded and read from the desktop.

Table 3 shows the force values for the layer height of 0.1 mm. For this layer height, five specimens were tested and the maximum force obtained in this case was 118.7113 N.

Table 3. Obtained values for layer height = 0.1 mm.

Specimen number [n]	Force [N]
1.1	111.9711
1.2	118.7113
1.3	112.5498
1.4	116.5833
1.5	111.7161

The next five specimens that were tested, were for layer height of 0.15 mm. In this case, the force was significantly lower, and the results are shown in Table 4.

Table 4. Obtained values for layer height = 0.15 mm.

Specimen number [n]	Force [N]
2.1	88.3261
2.2	86.5460
2.3	90.2472
2.4	98.274
2.5	93.9943

The last five specimens that were tested were for layer height of 0.2 mm. The maximum force obtained in this case is also the overall maximum force, which has the value of 133.1641 N and is shown in Table 5.

Table 5. Obtained values for layer height = 0.2 mm.

Specimen number [n]	Force [N]
3.1	128.9865
3.2	133.1641
3.3	123.4704
3.4	125.3571
3.5	132.9238

4. Conclusion

The objective of this study is to assess the PVA material's performance using different FDM 3D printing parameters. This is intended to establish a baseline for the development of a novel biodegradable material. Based on the findings presented in Tables 3 to 5, it is evident that the maximum force (F) of 133.1641 N is achieved when the layer height is set at 0.2 mm.

Subsequent investigations will explore the variation of other interrelated parameters to determine the ultimate set of optimal conditions at which the mechanical properties of FDM 3D printed PVA material are optimized.

Acknowledgments

The experimental part of this research was done in cooperation with the Faculty of Mechanical Engineering, University of Ljubljana.

References

- Li, H.Q., Liu, X.J., Wang, H., Yang, H., Wang, Z., He J. (2020) Proton exchange membranes with cross-linked interpenetrating network of sulfonated polyvinyl alcohol and poly(2-acrylamido-2-methyl-1-propanesulfonic acid).
- Basa B, Jakab G, Kállai-Szabó N, Borbás B, Fülöp V, Balogh E, Antal I. Evaluation of Biodegradable PVA-Based 3D Printed Carriers during Dissolution. *Materials*. 2021; 14(6):1350. <https://doi.org/10.3390/ma14061350>
- Khoramabadi, H. N., Arefian, M., Hojjati, M., Tajzad, I., Mokhtarzade, A., Mazhar, M., Jamavari, A. (2020) A review of polyvinyl alcohol/carboxymethyl cellulose (PVA/CMC) composites for various applications.
- Jin, M. (2020). Material development for extrusion-based 3D printing.
- Šibalić, M. (2022) Eksperimentalno istraživanje optimalnih parametara za 3D štampanje PVA materijala kontrolom adhezivne snage između slojeva. *Master rad*.

